Robust Guidance for Vision-based Navigation Systems

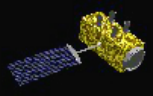

MSc Thesis

N.M. de Korte

Technische Universiteit Delft

TU Delft

Credits for the cover image go to the European Space Agency and M. Bhagat [3].

Robust Guidance for Vision-based Navigation Systems

by

N.M. de Korte

to obtain the degree of Master of Science
at the Delft University of Technology,
to be defended publicly on Tuesday August 24, 2021 at 09:00 AM.

Student number:	4279018	
Project duration:	August 24, 2020 – August 5, 2021	
Thesis committee:	Prof. Dr. E.K.A. Gill,	TU Delft, Chair
	Dr. Ir. A. Menicucci,	TU Delft, Supervisor
	Dr. Ir. E. Mooij ,	TU Delft, Examiner
	Ir. L. Pasqualetto Cassinis,	TU Delft, Additional (daily supervisor)

An electronic version of this thesis is available at `http://repository.tudelft.nl/`.

TU Delft

Preface

Before you lies my Master Thesis 'Robust Guidance for Vision-based Navigation Systems', written in partial fulfilment of the graduation criteria of the Master Track 'Space Exploration' at the Technische Universiteit Delft. I was engaged in researching and writing this thesis from September of 2020, until the beginning of August 2021, having experienced some delays, which was inevitable when continuously working from home.

The idea for the research was formed together with my daily supervisor Lorenzo, whose work on vision-based navigation systems sparked the idea of investigating robust guidance systems that could deal with the challenges observed with monocular cameras as means of relative navigation.

From this position I would like to thank my supervisors for their guidance, especially Lorenzo, to whom I owe much gratitude for his guidance, assistance and availability in the past year. There were many struggles to overcome, but in the end it all worked out. Also I would like to thank Dr. Alessandra Menicucci for supervising this research on behalf of the university.

Finally, it has been an exceptional year, not always in the positive sense. The COVID pandemic has forced me to undertake all the research from behind my laptop at home, which is all the more reason to extend my thanks to my, parents, girlfriend and roommates, who made sure that I did not go mad in the past year, and have made it very agreeable to work at home.

N.M. de Korte
Delft, August 2021

Contents

List of Figures

List of Tables

List of Symbols

$a\delta\boldsymbol{\alpha}$	Relative Orbital Element vector
β	Sun incidence angle on orbit
$\delta\lambda$	Relative argument of longitude
θ	True Anomaly, Quaternion rotation angle
ϑ	Phase angle (relative inclination), Relative azimuth
ρ	Angle between mean and relative orbital plane
σ	(Measurement) standard deviation (Position - σ_{pos}, Attitude - σ_{att})
$\boldsymbol{\sigma}$	Modified Rodriguez Parameter vector
φ	Phase angle (relative eccentricity)
ϕ	Phase angle (spin-axis)
χ_{cam}	Sun-camera angle (angle between sun pointing and camera boresight vector)
χ_{spin}	Angle between sun pointing and spin-axis vector
ψ	Relative elevation
ω	Argument of perigee
$\boldsymbol{\omega}$	Rotation vector
Ω	Right ascension of the ascending node
δa	Relative semi-major axis
a	Semi-major axis
δe	Relative eccentricity
e	Eccentricity
E	Eccentric anomaly
$\boldsymbol{h}$	Angular momentum
δi	Relative inclination
i	Inclination
$\boldsymbol{I}$	Identity matrix
$\boldsymbol{J}$	Inertia
$\boldsymbol{K}_k$	Kalman Gain
m	Mass
M	Mean anomaly
$\hat{\boldsymbol{n}}$	Unit axis of rotation
n	Orbital mean motion
N	Orbit normal
P_{state}	State covariance. (Split into P_{pos}, P_{vel}, P_{att}, P_{rot})
$\boldsymbol{q}_A^B$	Quaternion describing rotation from A to B
$Q_{\text{r,LQR}}$	Tuning parameter for LQR controller, position
$Q_{\text{v,LQR}}$	Tuning parameter for LQR controller, velocity
Q_v	Noise parameter for velocity
Q_ω	Noise parameter for rotation
$\boldsymbol{r}$	Relative position vector
$\dot{\boldsymbol{r}}$	Relative velocity vector
R_{KOS}	Keep-out-sphere radius
R_z	Measurement covariance
$\boldsymbol{R}_A^B$	Rotation matrix from frame A to B
T_{orbit}	Orbital period
u	argument of longitude (defined as $M+\omega$)
$\boldsymbol{u}$	control effort
$\boldsymbol{W}_s$	State noise vector
$\boldsymbol{X}_{xxx}$	Satellite state in the xxx coordinate system
Z_k	Measurement (position + attitude)

List of Abbreviations

ADR	Active Debris Removal
AOCS	Attitude and Orbital Control System
APF	Artificial Potential Function
Att	Attitude
CBF	Chaser Body-Fixed (coordinate system)
CL	Closed-loop
CoM	Centre of Mass
CON	Control system
CWH	Clohessy-Wiltshire-Hill
ECI	Earth Centered Intertial (coordinate system)
ESA	European Space Agency
FF	Formation Flying
FoV	Field-of-View
GEO	Geosynchronous Earth Orbit
GNC	Guidance, Navigation and Control system
GUI	Guidance system
ISAR	Inverse Synthetic Aperture Radar
ISS	International Space Station
KOC	Keep-Out-Coat
KOS	Keep-Out-Sphere
LAR	Launch Adapter Ring (Envisat)
LEO	Low Earth Orbit
LQR	Linear Quadratic Regulator
MEKF	Multiplicative Extended Kalman Filter
MMF	Moving Mean Filter
MPC	Model Predictive Control
MRP	Modifief Rodriguez Parameters
NAV	Navigation system
NASA	National Aeronautics and Space Administration
NORAD	North American Aerospace Defense Command
OCP	Optimal Control Problem
OL	Open-loop
OOS	On-Orbit Servicing
PID	Proportional, Integral, Derivative (controller)
PnP	Perspective-n-Points
Pos	Position
RF	Radio Frequency
ROE	Relative Orbital Element
Rot	Rotation
RTN	Radial, Tangential, Normal (coordinate system)
SLR	Satellite Laser Ranging
SMP	Spacecraft Motion Planning
STM	State Transition Matrix
TBF	Target Body-Fixed (coordinate system)
TLE	Two-Line Element
Vel	Velocity

Summary

The removal of space debris from the most commercial and densely populated areas of space is one of the challenges for the space industry in the upcoming years. The need for Active Debris Removal (ADR) was identified by two NASA scientists, D.J. Kessler and B.G. Cour-Palais [33], who found that, under the right circumstances, a collision between two objects in space could trigger a chain reaction. Such a chain reaction would exponentially increase the amount of space debris in already highly populated regions, and render these regions nearly useless. Removal of space debris is thus required in the future and this research contributes to the realisation of this goal. Multiple independent studies have found the inactive Envisat satellite the single most risk-inducing piece of space debris ([41], [95], [65]) and have identified it as useful target for the first ADR missions.

A critical part of ADR missions is the ability to perform a safe rendezvous with the debris that is to be removed from orbit. The rendezvous problem is represented with two satellites, called target and chaser. The target is the debris to be removed, and is assumed completely passive and uncooperative. The chaser spacecraft is fully operational and controllable. One of the key enabling technologies for ADR missions is the capability of the chaser satellite to perform rendezvous with the target autonomously [99], where autonomy is defined as the absence of human-in-the-loop. Autonomous rendezvous with an uncooperative target requires the chaser satellite to receive (near) real-time information of the relative pose, where the word pose refers to the position and orientation/attitude of the spacecraft. This information is obtained from a set of on-board navigation sensors with the capability to provide this information.

A type of navigation system that has been presented as a promising solution is the so-called vision-based system, which uses solely monocular cameras [10]. These systems show a capability to deliver fast pose solutions under low power and mass requirements, which is valuable given the need for (near) real-time pose estimation and the limited amount of available processing power in orbit. However, although the development and performance of vision-based systems has received a lot of attention from the perspective of navigation, their impact on guidance and control has been neglected. This work therefore aims to investigate the influence of vision-based navigation systems on the performance of guidance systems, centred around the following question:

> *How does the performance of a vision-based pose estimation system influence the ability of the guidance system to calculate a collision-free and fuel-efficient rendezvous trajectory toward a freely tumbling and uncooperative target satellite?*

In order to assess this question a rendezvous process is set up, consisting of three separate phases. The first phase consists of a passively safe, closed orbit around the target for the purpose of observation and characterisation of the target dynamics. In the second phase a nonlinear guidance algorithm is selected, based on a polynomial parameterization of the Clohessy-Wiltshire-Hill (CWH) equations, which is used to optimise a rendezvous trajectory for fuel consumption. This near-optimal trajectory ends at the intersection of the target spin-axis with the target Keep-out-sphere (KOS), the location of which is estimated by forward-integrating the target attitude dynamics over the remaining manoeuvre time. The trajectory is re-evaluated in an iterative process, allowing the optimality of the trajectory to be re-evaluated for the current chaser position and estimated final conditions. Finally, the third phase of the trajectory approaches the target along the spin-axis, up to a distance of 5 meters. During this phase the rotational dynamics of the chaser are also synchronised with those of the target, effectively cancelling the relative rotation between chaser and target. The final approach and docking, as well as the far-range rendezvous, fall outside the scope of this research.

Artificially generated measurements are used, rather than a real pose estimation system. This means that the performance of the pose estimation system is completely dependent on the accuracy that is manually assigned to the measurements, which has both benefits and drawbacks. This approach allows to assess the robustness of the guidance system with respect to errors, and allows to introduce many different scenarios in order to explore the limits and set requirements on the minimal performance of (vision-based) navigation systems, from the perspective of guidance. The main drawback of this approach is the necessity to make assumptions about the relationship between physical parameters, such as inter-satellite distance, illumination

and relative attitude, and the accuracy of the measurements, on the topic of which little research is available.

This research is split into three main parts, the first part of which is concerned with the performance of the guidance system in situations where the performance of the pose estimation system is decreased. Subsequently, the second part of the research is concerned with finding strategies for recognition and mitigation of these undesirable scenarios. The third part of the research is focused on the design of trajectories where the lighting conditions of the vision-based system are optimised, preventing undesirable scenarios as much as possible.

In the first part of the research, multiple scenarios are defined, first of all scenarios with a low to moderate measurement error that last over a long period of time. Such scenarios would be encountered under sub-optimal lighting conditions or with difficult image backgrounds, and are therefore useful for analysis. A second set of scenarios is constructed with a high level of measurement error, only lasting for relatively short periods of time. Such scenarios would be encountered during periods of difficult/ambiguous relative attitudes or for short periods of shadowing. The length of these periods is varied, as is their occurrence at the beginning, middle or end of the optimal trajectory. Furthermore, the influences of position and attitude measurement errors are evaluated separately to isolate their influence on the guidance system.

From this assessment of the performance of the guidance system, under influence of the vision-based system, a number of undesirable scenarios are selected that require further attention. As such, the second part of the research is concerned with finding strategies that allow the recognition of these undesirable periods. This recognition, and subsequently mitigation, is required to allow the guidance system to calculate a collision-free and fuel-efficient trajectory despite the decreased performance of the pose estimation system.

The scenarios that were evaluated in the first phase are divided into two categories. A first category contains scenarios that can be recognised by the navigation system itself, and a second category contains failures that the navigation system does not recognise. In the scenarios from the first category the state covariance, tracked within the navigation Kalman Filter, can be used to recognise the decreased performance of the pose estimation system. In these cases the measurement feedback is a good reflection of the true accuracy, or simply put, if the measurements are not accurate they are correctly perceived as such. The second category is more difficult, as in these scenarios the measurement feedback is not a good reflection of their true accuracy. Simply put, in these scenarios the measurements are not accurate and contain a high degree of error, but are considered to be accurate by the pose estimation system. This overvaluation of the measurements causes problems in the navigation filter, eventually causing a divergence of the state estimate.

Furthermore, the second phase of the research is also concerned with the integration of the target attitude dynamics. This process is required to estimate the final conditions for the optimal trajectory, however, is proven to be very sensitive to error. Especially when longer integration times are considered, the integration process is unreliable and a different strategy is desirable. Therefore the formulation of a more robust method for estimating the desired final state is attempted. This new method should ideally increase both the robustness of the estimate, as well as its accuracy.

Parallel to the investigation of mitigation strategies, the third and final part of this research focuses on designing a trajectory where the lighting conditions of the vision-based system are optimised. This type of trajectory planning should reduce the need for mitigation and allow for optimal illumination, improving the camera images which are dependent on the passive collection of light. The trajectory design is performed using the properties of sun-synchronous orbits, together with a Relative Orbital Element (ROE) state parameterization.

This approach requires a number of assumptions about the relation between the orientation of the sun and the accuracy of the measurements. The trajectory planning is therefore evaluated based on the assumption that the angle between the camera boresight axis and the sun vector is the main driver of measurement accuracy. The magnitude of this angle can be easily calculated and evaluated for a multitude of scenarios. Its value can be assessed for the closed, relative orbit in the first phase of the rendezvous, which allows to find a single best orientation for this relative orbit. Similarly, optimal configurations of the second and third phases of the rendezvous may be discovered, allowing to evaluate the performance of the GNC system for these optimal conditions.

1

Introduction

This chapter introduces the context of the research. Section 1.1 provides some background information and motivation for the subject of this work. Next, Section 1.2 introduces the scope of the research and presents the formal research questions of this thesis work. Finally, Section 1.3 provides an outline of the structure of this work.

1.1. Background

Already as early as 1978, the need for Active Debris Removal (ADR) was identified by two NASA scientists, D.J. Kessler and B.G. Cour-Palais [33]. Analysing the collision probability of space objects they concluded that, under the right circumstances, a chain reaction could be triggered exponentially increasing the amount of space debris in the most densely populated areas of space. Figure 1.1 shows the expected number of space debris in Low Earth Orbit (LEO), which is the most densely populated region in space. The total spacecraft mass is still growing every year, and is expected to grow very rapidly when no ADR is performed [43].

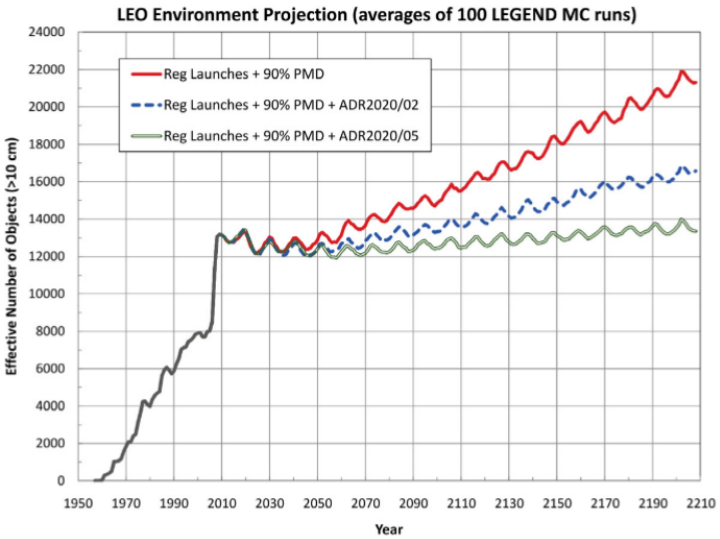

Figure 1.1: Predicted growth of space debris in the LEO environment for three different scenarios. In the first scenario no debris is actively removed from orbit, in the second scenario two pieces of debris are removed yearly and in the third scenario this is increased to five pieces yearly (credit: [43] - NASA Orbital Debris Program Office).

Based on their research, presented in Figure 1.1, Liou, Johnson and Hill conclude that it will be required to remove 5 large objects per year from the LEO environment to keep it stable and usable [42]. This report, written in 2010, assumes the beginning of debris removal in 2020. However, ADR has not commenced and launch traffic is still increasing at a dazzling rate.

Various classifications of orbital debris have been proposed over the years, in an attempt to identify the most promising targets for ADR missions. Using the collision risk as most important metric, Wiedemann [95] identifies the Envisat as the most dangerous piece of space debris. The sudden loss of this satellite in 2012 has led to this large and heavy satellite being still in its nominal orbit, while all ability to control the satellite was lost. Envisat is considered a useful first target for future ADR missions and, consequently, this research.

Autonomy

Autonomous rendezvous, or simply autonomy, has been identified as an enabling technology for future space missions in the field of Active Debris Removal (ADR) and On-Orbit Servicing (OOS) [99]. In this context autonomy is defined as the absence of human-in-the-loop control. It has been employed in many different missions in the past, such as the space shuttle missions (i.e. Challenger, Discovery) [29] and, more recently, on the PRISMA mission [28], in the context of Formation Flying (FF). Autonomy is also presented as a key element for future missions such as the ESA Clean space initiative [97] or the DEOS mission [68] by the German DLR.

An important distinction must be made in the required level of autonomy, based on the target satellite being either cooperative or uncooperative. A clear example of cooperative rendezvous is found in case of the space shuttle missions (i.e. Challenger, Discovery). The intended rendezvous target of these missions, the International Space Station (ISS), actively assisted the rendezvous process by providing range measurements, lights and grappling hardware [29, 99] and passively through high-contrast markings on its surface [85]. Contrarily, targets for ADR are usually passive pieces of debris and provide no cooperation during rendezvous. Rendezvous and docking with a fully uncooperative target has not yet been demonstrated, however, the PRISMA mission [15, 28] has demonstrated the ability to autonomously perform close-proximity operations based on on-board relative navigation. This research limits itself to applications with uncooperative targets, as the Envisat is the intended target and completely uncooperative.

Relative Navigation

Autonomous rendezvous with an uncooperative target requires the chaser satellite to carry a set of navigation sensors that provide real-time information of the relative pose. The word pose refers to the complete set of position, velocity, attitude and rotation. In this context, vision based systems should be preferred over Radio Frequency (RF) systems [10]. Such systems have been proposed in numerous different ways, using both active and passive devices. Active devices require power to function (i.e. LIDAR) while passive devices passively acquire radiation (i.e. monocular cameras).

Navigation systems based on solely monocular cameras are currently under active investigation ([44, 54, 61]), since these systems have a capability for delivering fast pose solutions under low power and mass requirements [72]. This capability is valuable given the need for (near) real-time pose estimation and the limited amount of available processing power in orbit. The main drawback of these systems is the lack of range information from monocular cameras [67], resulting in research into systems that use stereo cameras or LIDAR, sometimes in combination with one or more monocular cameras ([57, 90]). Other solutions for this range ambiguity are found in the application of 3D wire-frame models [10] and the development of more sophisticated image processing (IP) algorithms [34] and even application of neural networks [59, 70].

1.2. Scope of the research

The development and performance of vision-based systems has received much attention from the perspective of navigation. Vision-based navigation systems are under active investigation [10, 57] and even competitions are started to aid in their development [34]. However, the satellite ability to rendezvous safely and perform efficiently is not solely dependent on the navigation system. Rather, this ability is the result of the performance of the Guidance, Navigation and Control (GNC) system as a whole. Within the GNC system the navigation estimates the current state of the satellite, which the guidance system uses to calculate a desired future state, to which the satellite is controlled by the control system.

Whereas vision-based navigation is a widely researched topic, vision-based guidance and control is not. Few authors specifically discuss guidance strategies in combination with vision-based navigation. Barbee et al. [1] present vision-based guidance strategies for satellites in Geosynchronous Earth Orbit (GEO), which has different lighting conditions and longer illuminated times compared to LEO. Furthermore, the authors assume a sensor suite, complete with infrared cameras and range finders, and accurate performance is simply assumed. Volpe et al. [90, 91] present the most relevant work on the subject, evaluating GNC performance for a vision-based system, however, their evaluation is limited to a nominal performance of the navigation

system, not testing limiting cases. More importantly, their research ignores some of the most challenging tasks of the guidance system such as accurately estimating the future state of a rotating target satellite.

Research Questions

This work therefore aims to investigate the influence of vision-based navigation systems on the performance of guidance systems. It does not aim to investigate vision-based navigation, nor does it aim to assess or improve the performance of such systems in any way. The research is centred around the guidance system and its purpose is to answer the following main question:

> *How does the performance of a vision-based pose estimation system influence the ability of guidance to calculate a collision-free and fuel-efficient rendezvous trajectory toward a freely tumbling and uncooperative target satellite?*

To aid in finding the answer to this question, three sets of research questions are formulated to investigate a number of specific cases that explore the limits of navigation performance.

First, it is important to assess the performance of a guidance system with respect to the performance of a vision-based pose estimation system. The aim is to establish a possible correlation between the accuracy of the pose estimate and the ability of the guidance system to accomplish the tasks it is given, such as estimating the desired final state, or calculating an efficient and safe trajectory. The following questions are formulated for this purpose:

1. How is the performance of the guidance system affected when the performance of the pose estimation system decreases?
    - 1.1. What is the influence of the magnitude of the pose estimation error?
    - 1.2. How is guidance affected when pose estimation performance is decreased over extended periods of time?
    - 1.3. How is guidance affected when the decreased performance of the pose estimation system is limited to a single part of the pose (i.e. either position or attitude)?

Second, when a correlation is found, actionable strategies should be investigated to improve the performance of the guidance system in situations where the pose estimation system might fail to provide an accurate estimate. This starts with the recognition of such situation and identification of other data that is available on-board. The following questions aid in this investigation:

2. How can the guidance system mitigate periods in which the performance of the pose estimation system is decreased, and ensure a collision-free and fuel-efficient trajectory during these periods?
    - 2.1. How can the guidance system identify periods of decreased performance of the pose estimation system?
    - 2.2. What data can the guidance system alternatively use during periods of decreased performance of the pose estimation system?
    - 2.3. What strategies can be implemented such that the effect of the decreased performance is minimised?

Thirdly, in parallel with the investigation of mitigation strategies, it is interesting to explore methods of trajectory planning that would reduce the need for such mitigation in the first place. Cameras are passive sensors, as discussed earlier, and depend on the passive collection of radiation. This makes their performance highly dependent on illumination conditions and image background. Also a camera can only register objects in its Field-of-View (FoV) and needs to be carefully pointed at all times. The following questions are formulated to aid in this exploration:

3. How can trajectory planning aid in minimising the expected occurrence of periods where performance of the pose estimation system is decreased?
    - 3.1. How can illumination conditions be integrated in the trajectory planning?
    - 3.2. Are any specific parts of the trajectory sensitive to illumination conditions?

1.3. Thesis outline

In order to provide further details about the research, Chapter 2 describes the context and further narrows the scope of the research, defining the intended target and trajectory, as well as outlining the currently available state-of-the-art guidance systems. Subsequently, Chapter 3 provides some useful background theory, before the research methodology and general assumptions are introduced in Chapter 4. The complete GNC framework is described in Chapter 5, outlining all three subsystems.

The main part of this work consists of Chapters 6 to 8, which each aim to answer a set of questions from Section 1.2. Chapter 6 presents the results from the evaluation of the first set of questions, as it assesses the performance of the guidance system in various situations with high pose error. The second set of questions is discussed in Chapter 7, which presents an overview of available strategies for improving the guidance performance, and discusses their effect. Finally, Chapter 8 aims to answer the third set of questions. It describes how the illumination conditions may be used in trajectory planning and how this impacts the guidance system. The conclusions of the research are presented in Chapter 9, along with answers to the research questions and recommendations for further research.

2

Research Framework

This chapter provides the context for the research. First, Section 2.1 specifies which parts of the rendezvous trajectory are within the scope of this work and which parts are not. Since the Envisat is the intended target, the physical properties of this satellite are presented in Section 2.2, along with the expected orbital properties and attitude dynamics. Next, the chaser baseline is presented in Section 2.3, discussing its physical properties. Finally, Section 2.4 concludes the chapter with an overview of the general structure of vision-based GNC systems. This includes a short outline of pose estimation systems and their expected performance, as well as a discussion about the currently available state-of-the-art guidance systems.

2.1. Rendezvous

The rendezvous problem is represented using two satellites, called target and chaser. Different names for these two satellites can be found, such as chief/deputy [14] or client/servicer [37], sometimes used interchangeably. In this work the satellite being approached (Envisat) is always referenced as target, while the approaching satellite is always referenced as chaser. The complete rendezvous consists of a variety of manoeuvres, depending on the distance to the object with which rendezvous is desired. An overview of a typical rendezvous procedure is shown in Figure 2.1.

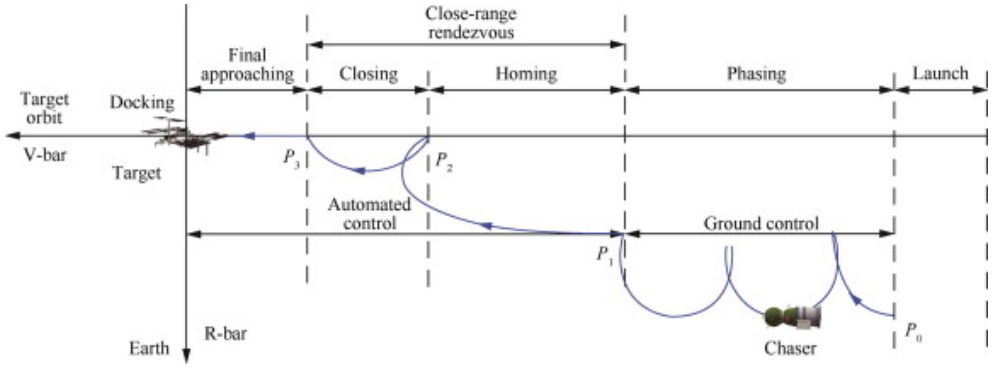

Figure 2.1: Schematic overview of the rendezvous process. The image is representative of rendezvous with the ISS. [48]

This work only considers close-range rendezvous, as cameras can only be used as tool for relative navigation at close distances, also depending on the size of the target. If the inter-satellite distance is too large, no spacecraft features can be distinguished in the images and pose estimation is not possible [57]. During the initial phase of the mission, the chaser is assumed to be in a passively safe, closed orbit around the target. This is consistent with P_1 in Figure 2.1. The complete trajectory consists of:

- **Phase 1: Passive observation** The first phase consists of taking measurements from a passively save orbit. This allows for convergence of the navigation filter, as well as proper characterisation of the target rotational motion. In Figure 2.1 this means that the satellite stays in P_1 for a complete orbital period.

- **Phase 2: Optimal trajectory** The second phase consist of a (near-)optimal trajectory that synchronises the chaser satellite with the spin-axis of the target. This synchronisation means that the desired position of the chaser, at the end of the manoeuvre, is at the intersection of the spin-axis vector with the Keep-Out-Sphere (KOS) of the target. In Figure 2.1 this means that the satellite travels from P_1 to P_2.
- **Phase 3: Approach along spin-axis** The third and final phase uses a forced motion approach to follow the spin-axis while decreasing the inter-satellite distance. In Figure 2.1 this means that the satellite moves from P_2 to P_3. This happens along an approximately straight line when no nutation is present, or along a spiral when a wobbling motion is expected. Furthermore, the chaser synchronises its rotation with the target, bringing the relative rotation to **0**.

In the case of Envisat, the virtual point P_3 in Figure 2.1 is set at a distance of 5 meters from the satellite. Around this distance it is likely that pose estimation will need to be exchanged for a different method of relative navigation, such as feature tracking, which is outside the scope of this research. Both P_1 and P_3 most likely require a shift in GNC methods, marking them as valid begin and end points for the close-range rendezvous process in this research. Everything before P_1 (i.e. far-range rendezvous) and after P_3 (i.e. final approach and docking) is considered outside the scope of this research.

2.2. Envisat

The Envisat has been identified as the single most risk-inducing piece of space debris in multiple independent studies [41, 65, 95]. As Schaub et al. [65] notice, the reasons for removing Envisat from orbit are both technical and political. If the Envisat were to collide with another object, in the worst case another operational satellite, it could cause a massive debris field in the highly commercial sun-synchronous orbit regime. This would make the orbit useless to satellites and the political consequences would be severe.

2.2.1. Physical properties and coordinate system

The Envisat is a satellite with mass 7828kg [87] and plays a key role in this work. Its shape and dimensions are shown in Figure 2.2, as well as its body-fixed coordinate system. This coordinate system is centred in the Centre of Mass (CoM), with the positive x-axis pointing in the direction of the solar panel and the positive z-axis pointing in the direction of the Ka-band antenna, away from the ASAR-antenna. The y-axis completes a right-handed system. The exact orientation of the solar panel is likely to be different from the one presented in Figure 2.2 due to almost a decade of uncontrolled motion and the possibility of small debris impacts. Such impacts might affect the overall Envisat physical and rotational properties, meaning that room for uncertainty must always be present.

The location of the CoM is defined as [87]

$$\begin{aligned} x_{com} &= -3.905 \\ y_{com} &= -0.009 \\ z_{com} &= +0.003 \end{aligned}$$

These values are referenced to the geometrical centre of the Launch Adapter Ring (LAR, Figure 2.2). It is unlikely that these measures are fully accurate, after the satellite has been in an uncontrolled state for several years. The inertia of Envisat around its principal axes is stated in Table 2.1 along with the expected uncertainties.

Table 2.1: Envisat inertia with expected uncertainties [87]. The expected uncertainties stated here account for approximately 2% of the total satellite inertia.

Nominal	**Uncertainty**
$J_{target} = \begin{bmatrix} 17023 & 397.1 & -2171 \\ 397.1 & 124826 & 344.2 \\ -2171 & 344.2 & 129122 \end{bmatrix} kg \cdot m^2$	$dJ_{target} = \pm \begin{bmatrix} 350 & 100 & 250 \\ 100 & 3000 & 150 \\ 250 & 150 & 3000 \end{bmatrix} kg \cdot m^2$

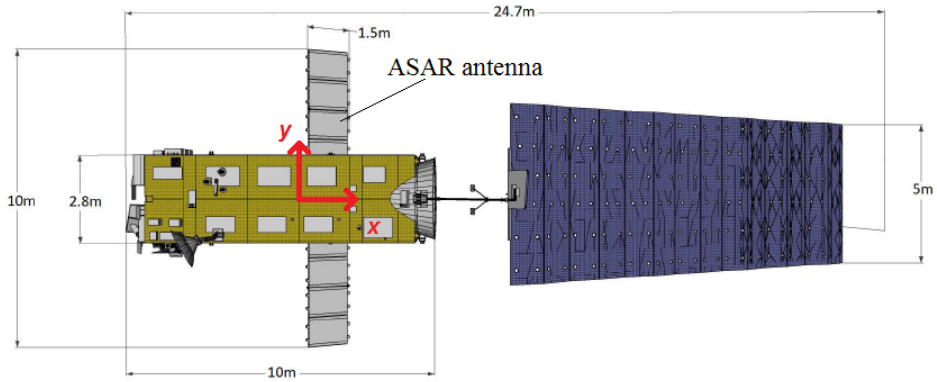

(a) Top view.

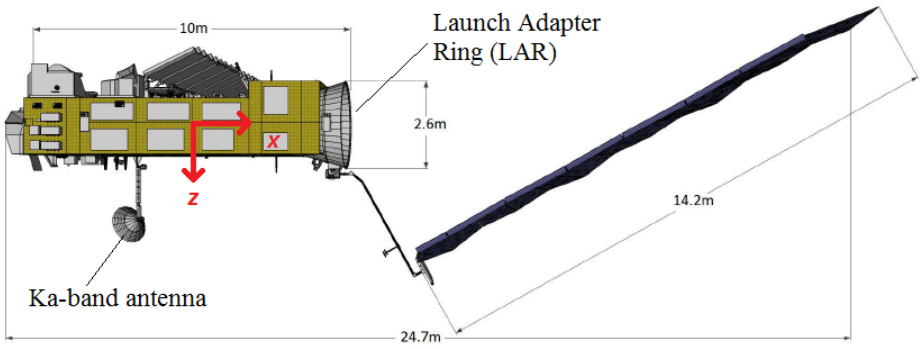

(b) Side view.

Figure 2.2: Envisat model and dimensions [17].

Finally, the assumed solar radiation and drag area for Envisat, as well as its radiation and drag coefficients are presented in Table 2.2. These values are used to integrate the dynamics of the satellite inside the high-fidelity model.

Table 2.2: Assumed Envisat radiation and drag parameters. Subscript t is adopted for 'target'.

Property	Abbreviation	Value	Unit
Solar radiation area	$A_{SR,t}$	110.5	m^2
Drag area	$A_{DR,t}$	62.5	m^2
Radiation coefficient	$C_{r,t}$	1.0	-
Drag coefficient	$C_{d,t}$	2.2	-

2.2.2. Orbital parameters

Because the satellite was suddenly lost in 2012, no highly accurate orbital parameters are available. The North American Aerospace Defense Command (NORAD) keeps a database, Celestrak, with recent Two-Line Elements (TLE's), from which the extraction of the orbital parameters is possible. Recent TLE observations from NORAD indicate the following orbital parameters (Keplerian elements) for Envisat, presented in Table 2.3. These parameters show that Envisat is located in a polar, retrograde (inclination > 90 deg) and near circular (eccentricity ≈ 0) orbit. The altitude of this near-circular orbit is approximately 772 km, with perigee and apogee height estimated to be less than 20km apart [17]. The resulting orbital period is approximately 6030 seconds. Finally, this orbit is sun-synchronous and thus the angle with respect to the sun-vector, an important indicator for lighting conditions, is similar at all times.

Table 2.3: Envisat Orbital parameters on 19 September 2020. [11]

Orbital parameter	Value	Unit
Semi-major axis	7143.16	km
Inclination	98.18	deg
Right Ascension of the ascending node (Ω)	147.84	deg
Eccentricity	0.0013	-
Argument of perigee (ω)	88.50	deg
Mean anomaly (M)	291.29	deg

2.2.3. Attitude dynamics

In order to perform a successful rendezvous and docking manoeuvre with any target satellite, it is necessary to classify the expected attitude dynamics [87]. This becomes even more important as the final approach towards Envisat is envisioned along its spin-axis [8], with several mission concepts having been designed around this approach [4, 24]. As a result, the orientation of the spin-axis fully determines the lighting conditions on the final approach. For these reasons it is important to model realistic attitude dynamics, to validate the performance of a vision-based guidance architecture.

Studies agree that the Envisat is spinning with a main rotational rate somewhere between 2.5-5 degrees per second, gradually slowing down, and that the spin axis is around the Z-axis (Figure 2.2) [6, 87]. Multiple extensive studies of the Envisat rotation were performed around 2013, after the loss of the satellite. Kucharski et al. [36] used Satellite Laser Ranging (SLR) to determine the orbital and rotational properties of Envisat and found an inertial period of 134.7 s, consistent with a rotational velocity of 2.67 deg/s. A second study, performed by ESA [87], used Inverse Synthetic Aperture Radar (ISAR) observations and found an average rotational velocity of 3.5 deg/s. The attitude states, derived independently from ISAR and SLR data, are in good agreement qualitatively, but quantitatively different, most likely due to different assumptions [87]. These two studies both agreed on a likely configuration of the spin-axis, which was found to be inertially stable, making an angle of 61.86deg with the nadir vector and 90.69 deg with the along-track vector [36], as visualised in Figure 2.3.

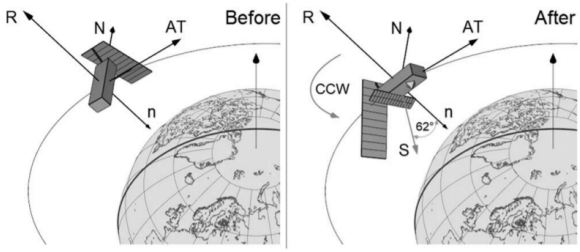

Figure 2.3: Orientation of Envisat. (Left) During the mission, i.e., nadir stabilized. (Right) After May 2013, the satellite spins in the Counter Clockwise (CCW) direction about the spin axis *S*. Vectors: radial *R*, normal to the orbital plane *N*, along-track *AT*, and nadir *n*; a ground track of the polar orbit is marked. [36]

Note that the spin-axis orientation adopted by Kucharski et al. [36] in Figure 2.3 is opposite from the one in this work, shown in Figure 2.2. The spin-axis in this work is defined along the $+z$-axis in Figure 2.2 and the rotation shall be modelled in a clockwise direction around this axis. The above orientation is used as a reference throughout this research, however, the data from different studies is not completely in agreement. This was recently quantified by Sagnières and Sharf [64] in 2019, whose study used various assumptions to construct multiple simulations of the Envisat attitude dynamics. These simulations were compared to the available data from seven studies to identify the most likely scenario of the attitude dynamics.

Sagnières and Sharf [64] present a total of three conclusions. First, the Envisat is subject to precession and this precession moves with the orbital plane. Second, there is a revolution of the angular momentum vector around the orbit normal and, third, a 'wobbling' motion is found of the spin-axis around the angular momentum vector due to the asymmetrical inertia matrix (Table 2.1). Furthermore, a decrease in the angular velocity is found, indicating a possible future increase of the nutation amplitude with respect to the main rotation. This motion is represented schematically in Figure 2.4.
The precession was found to be present in the inertial frame, and concerns the angle between the Envisat

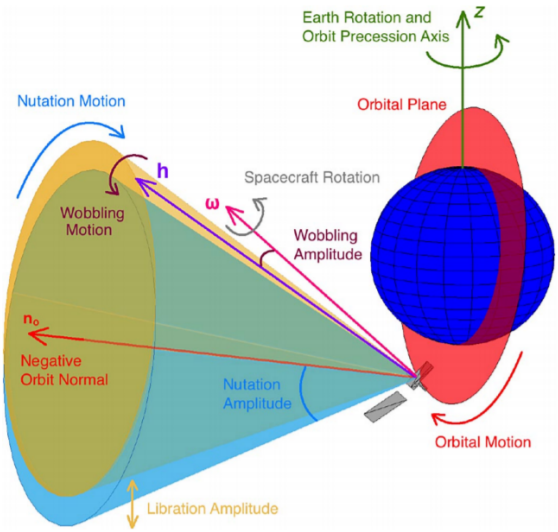

Figure 2.4: Schematic of angular motions experienced by Envisat [64]. h is the angular momentum vector and ω the instantaneous spin-axis.

angular momentum vector h and the X-axis of the inertial frame (pointing in the direction of the vernal equinox). This precession is attributed to the gravity gradient torque and has a period of approximately one year, meaning that the precession of the spin-axis is equal to the precession of a sun-synchronous orbit. This thus ensures that the orientation of h with respect to the orbit is stable, especially over short time intervals.

The revolution of the angular momentum vector around the orbit normal was found to have a period of several days, and is thought to be decreasing. This revolution is the nutation described in Figure 2.4, and concerns the angle between angular momentum h and Earth Rotation Axis Z. The angle of h with the orbit normal is stable at approximately 28-30 degrees, while the angle between h and Z changes between approximately 50 and 110 degrees. The relatively long period of this motion, together with the very slow precession justifies the modelling of the spin-axis orientation as constant in an Earth-centred inertial frame over short instances of time such as one or two orbital periods.

In terms of lighting conditions, this nutation is very beneficial. The precession ensures that the spin-axis remains at the same angle with the orbital plane which, due to the sun-synchronous orbit, is at constant angle with the solar rays. In the absence of the nutation, the spin-axis would experience these same, constant lighting conditions. However, in the presence of a nutation, the lighting condition change over the course of these days, as the spin-axis revolves around N. This means that more, and less, favourable conditions for the approach exist, as a range of scenarios with different lighting conditions is created as a consequence of the nutation. Furthermore, considering the period of the nutation it is reasonable to assume constant lighting conditions for short periods of time such as a single orbital period ($\approx$ 6000s), or a short manoeuvre ($\approx$ 2000s).

Finally, the wobbling motion of the spin-axis was found to be increasing due to the decrease of the main rotational velocity. This decrease removes some of the spin stabilisation, consequently increasing the tumbling motion. It is therefore of high importance to evaluate the performance of the guidance architecture for a significant amount of tumbling to properly assess the performance in this situation.

The conclusions from Sagnières and Sharf [64] justify the selection of several scenarios, required to validate the vision-based guidance architecture for a wide range of possible scenarios. It is decided to evaluate scenarios with the spin-axis at 0, 15 and 30 degree tilt-angles with the orbit normal, since those were all found to be in agreement with the measurements [64]. For the main rotation a worst case scenario is adopted, where the spin rate is 3.5 deg/s around the Z-axis. Furthermore, as both measurements and simulations indicate significant wobbling, non-zero rotations around the other two axes are implemented, similar to [86], where the spin rates around X and Y were set to 0.5 deg/s. Adopting these rotations introduces significant wobbling, thus adding an additional challenge for the vision-based system. The adopted rotational properties are summarised in Table 2.4.

Table 2.4: Envisat rotational properties

Property	Value	Unit
Spin-axis	+z-axis (Figure 2.2)	-
Main rotation	3.5	deg/s
Minor rotation	0.5	deg/s
Angle with N	0, 15, 30	deg

2.3. Chaser baseline

The chaser design is a modified version of the Eurostar3000 platform used by Airbus, presented at an ESA symposium in 2014 [25]. The chaser baseline design is shown in Figure 2.5 and several assumptions are listed in Table 2.5. The design of the chaser is based on the CDF study for the e.Deorbit mission, by ESA in 2013 [4, 17].

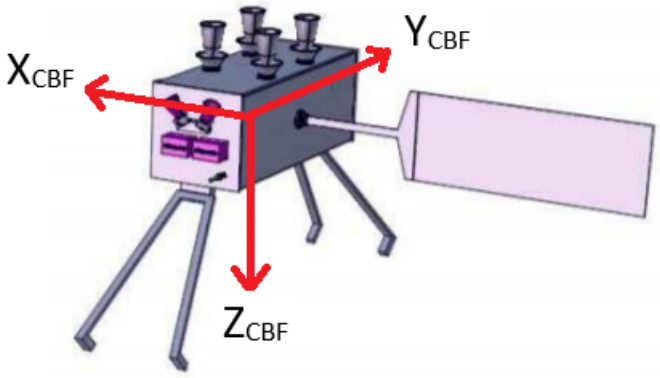

Figure 2.5: Chaser baseline design [4] including the orientation of the Chaser Body-fixed Frame (CBF) coordinate system.

Table 2.5: Chaser technical specifications. [4, 25].

Mass	Dry mass	762 kg
	Propellant mass	826 kg
Sensors	Absolute navigation	3x Star tracker
		2x Sun sensor
		2x IMU
		2x GPS receiver
	Relative navigation	2x Far field camera
		1x Near field camera
Actuators	Reactions wheels	4x (Max.) 40 Nm
	Thrusters	12x 22 N (6-axis)
		12x 22 N (redundant)

The selected chaser design for this research is a design that uses a robotic arm to fix itself to the Envisat for the purpose of deorbiting, as opposed to a design that uses a net. As declared previously, the approach and final docking will occur along the Envisat position Z-axis, reaching a final position as visualised in Figure 2.6. Although the approach and docking is outside the scope of this research, the definition of the reference frames in Figure 2.2 and Figure 2.5, yields a parallel alignment of the X-axes and anti-parallel alignment of the Y- and Z-axes for the desired alignment described in Figure 2.6. This also requires the camera to be aligned with the chaser $+Z$-axis.

The best estimate of the inertia matrix for the chaser is taken from the e.deorbit symposium at ESA from 2014 [25] and is set to

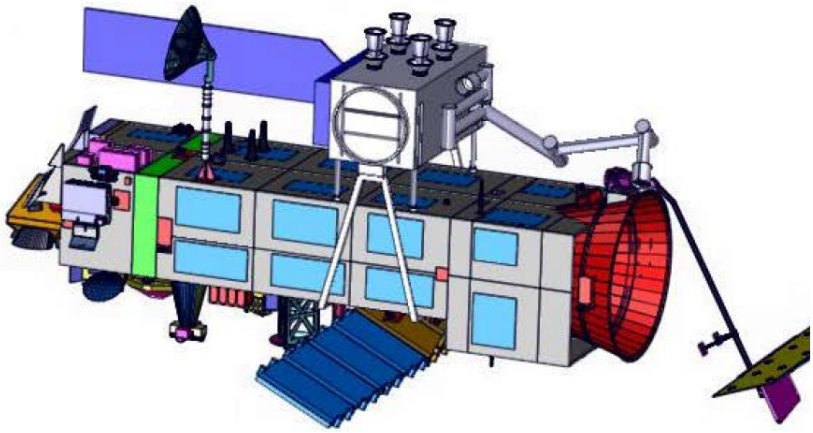

Figure 2.6: Intended docking configuration at the Envisat +Z-axis.

$$J_{chaser} = \begin{bmatrix} 1673 & 130 & 54 \\ 130 & 2040 & 25 \\ 54 & 25 & 2574 \end{bmatrix} kg \cdot m^2$$

Finally, the assumed solar radiation and drag area for the chaser, as well as its radiation and drag coefficients are presented in Table 2.6. These values are used to integrate the dynamics of the chaser inside the real-world model.

Table 2.6: Assumed Chaser radiation and drag parameters. Subscript c is adopted for 'chaser'.

Property	Abbreviation	Value	Unit
Solar radiation area	$A_{SR,c}$	5.5	m^2
Drag area	$A_{DR,c}$	4.0	m^2
Radiation coefficient	$C_{r,c}$	1.1	-
Drag coefficient	$C_{d,c}$	2.0	-

2.4. Vision-based GNC

The top-level flow of a general vision-based GNC system is outlined in Figure 2.7. This shows how state information flows between systems and what top level tasks are performed by each system. Two points of interaction with the real-world are shown, through the camera and actuators, and a distinction is made between the measurement module and other GNC functions. This distinction is made to, again, indicate that this system is outside the scope of this research. In no way this presumes that the measurement module is not part of the spacecraft GNC, which it is. In this research however, the measurements are artificially generated, which is further discussed in Chapter 5. A short description of the function of each system in Figure 2.7 is provided.

Navigation Filter

The navigation system estimates the current spacecraft state, $\boldsymbol{X}_{NAV}$, along with an estimate of the state covariance, $\boldsymbol{P}_{State}$, which is an indication of the accuracy of the state, made by the navigation system itself. The navigation uses a Kalman Filter, which always runs a prediction step. Whenever measurements are available (when $t = k \cdot t_{meas}$, with $k = 0, 1, 2\ldots$), the predicted state can be corrected using the measurement $\boldsymbol{Z}_k$ and its measurement covariance $\boldsymbol{R}_z$. The measurement contains information about the relative position and relative attitude. Measurements may be rejected, resulting in the filter only performing a prediction step. The navigation system is described in more detail in Section 5.2.

Guidance

The task of the guidance system is to provide a desired state, $\boldsymbol{X}_{GUI}$, which the spacecraft must reach in the future. The system calculates a reference trajectory and a reference attitude for the spacecraft to follow, using

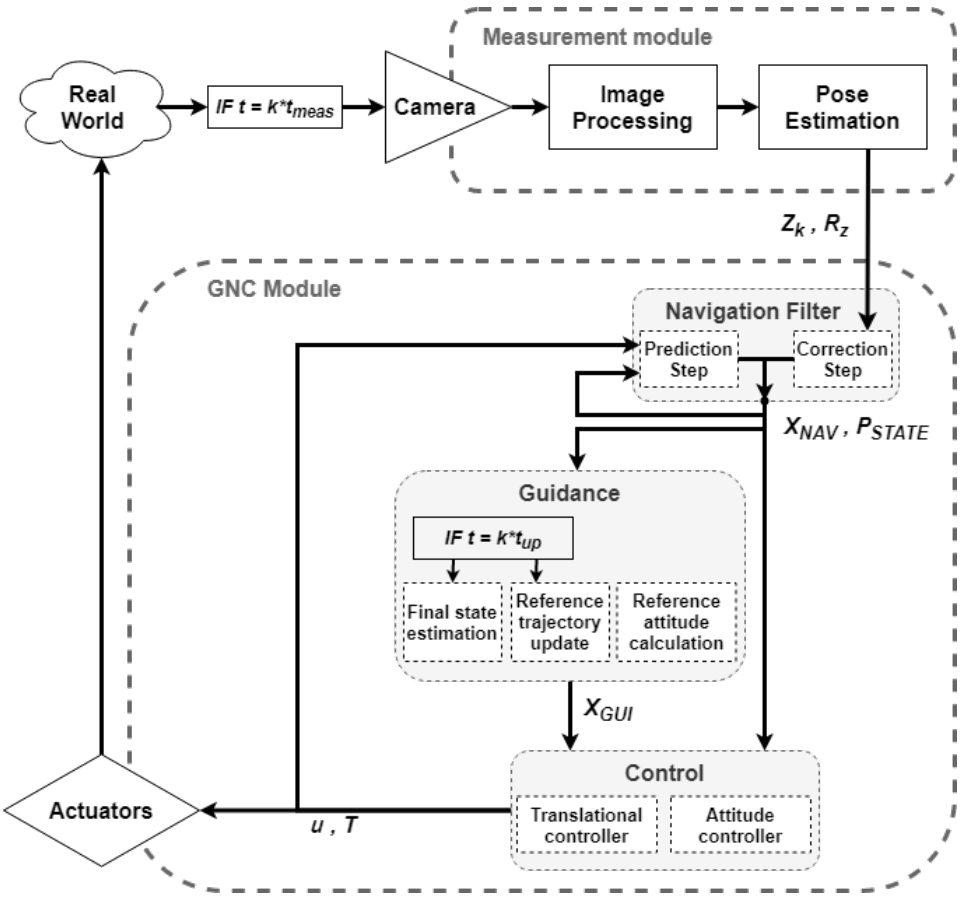

Figure 2.7: Top-level flow of a general vision-based GNC system. The system completes an iterative loop, starting with measurements, obtained from the real world using a monocular camera. These measurements come in the form of images, which are processed in the measurement module and converted to a relative position and attitude, which together form the pose measurement $\boldsymbol{Z}_k$. This measurements is then provided to the navigation filter, which uses it to estimate the current relative state of the chaser. This relative state is used by the guidance system to calculate a desired subsequent state, which is passed to the control system, together with the current relative state. The control system calculates the control effort from the difference between these two states and uses its actuators to influence the real world, upon which a new measurement may be attempted and the iterative loop restarted.

the current estimated state $\boldsymbol{X}_{NAV}$. In the case of rendezvous, this involves making an estimate of the future state of the target, which is a challenging task. The reference trajectory, unlike the reference attitude, does not necessarily need to be recomputed at every step. It might be more beneficial to set an update interval t_{up}, only updating the reference trajectory at integer multiples of this update interval ($t = k \cdot t_{up}$). The guidance system is described in more detail in Section 5.1

Control

The control system controls the satellite, such that it reaches the desired reference state, defined by the guidance system, as quickly or efficiently as possible. The control system receives both the currently estimated state $\boldsymbol{X}_{NAV}$ from navigation, as well as the desired state $\boldsymbol{X}_{GUI}$ from guidance, and uses both to calculate the required control effort to turn the current state into the desired state. This control effort is performed by the actuators in the real world environment, allowing the spacecraft to reach a new state. The control system is described in more detail in Section 5.3.

Measurement module

The measurement module provides the navigation system with recent information from the real world environment. As this system is outside the scope of the research it requires some more attention at this moment, as understanding its challenges and expected performance is crucial to correctly model the artificial measurements.

2.4.1. Monocular, model-based pose estimation

Pose estimation is performed using a single monocular camera. The challenge with using a single monocular camera lies in the lack of range observability. This problem can be at least partially solved by using a 3D wire-frame model to assist in the pose estimation, matching the 3D model with features in the 2D image and solving for the full relative pose [10]. Pose estimation methods that do not use a 3D model are also available and can potentially be applied to a wider range of targets of unknown shape [57]. This research, however, limits itself to the model-based pose estimation methods.

Pose Estimation Theory

In the case of model-based pose estimation, the high level architecture looks as in Figure 2.8. The system receives a 2D image and 3D model as inputs, after which the images are processed and features of the satellite are extracted. These features are then matched with the corresponding parts of the 3D model.

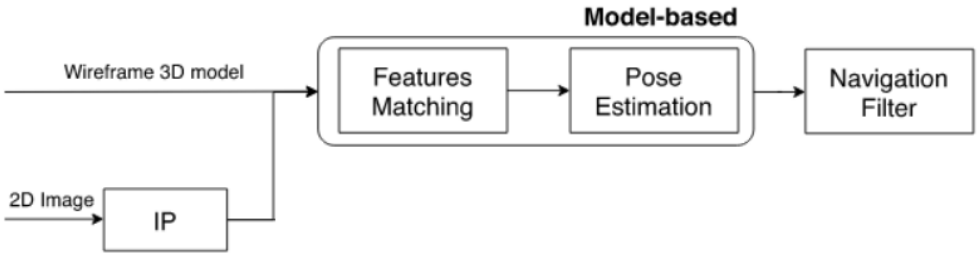

Figure 2.8: Process flow for the model-based pose estimation process [10].

The processing of these features can happen in different ways. Pasqualetto-Cassinis et al. [10] highlight that, in general, key-point detection methods are preferred due to their stability with respect to perspective, scale and illumination changes. However edge/corner detector have shown increased robustness for images with Earth in the background [75] as well as for images where the target is only partially visible [38].

Highly simplifying the process, it can be reasoned that the pose estimation system extracts a number of features from the 2D images and cross-references these with the 3D model to construct the pose estimate. The pose estimation process is schematically represented in Figure 2.9.

This process aims to determine the position of the Centre of Mass (CoM) of the target spacecraft ($\boldsymbol{t}^C$), as well as the target orientation with respect to the camera frame C ($\boldsymbol{R}^{BC}$). This process is described by the following two equations, the so-called Perspective-n-Points (PnP) problem [10]:

$$\boldsymbol{r}^C = \boldsymbol{R}^{BC}\boldsymbol{q}^B + \boldsymbol{t}^C \tag{2.1}$$

$$\boldsymbol{p} = (u_i, v_i) = \left(\frac{x^C}{z^C} f_x + C_x, \frac{y^C}{z^C} f_y + C_y\right) \tag{2.2}$$

where $\boldsymbol{t}^C$ represents the relative position of the CoM of the target in the camera frame (see Figure 2.9), $\boldsymbol{R}^{BC}$ is a rotation matrix, $\boldsymbol{p}$ is a point in the image plane, $\boldsymbol{q}^{\boldsymbol{B}}$ is a point in the 3D model, expressed in the body-fixed frame of the target, f_x and f_y are the camera focal lengths and C_x and C_y are the principal points of the image. The pose estimate is passed to the navigation filter as $\boldsymbol{Z}_k$, along with an estimate of the measurement covariance. Both are used by the filter to estimate the relative state of the two spacecraft.

The pose estimation process only provides the relative position and attitude of the two spacecraft. The navigation filter will need to estimate the relative velocity and rotation from the measurements through integration over time.

Estimation Error

Since the measurements in this research are generated artificially, it is crucial to understand the expected behaviour of the pose estimation system. In order to realistically model measurement error, the errors caused by the pose estimation architecture should be understood first. Extensive research into the availability and capability of pose estimation systems has been performed by Opromolla et al. [57] and Pasqualetto-Cassinis et al. [10], from which a summary of the expected performance of current pose estimation systems can be made.

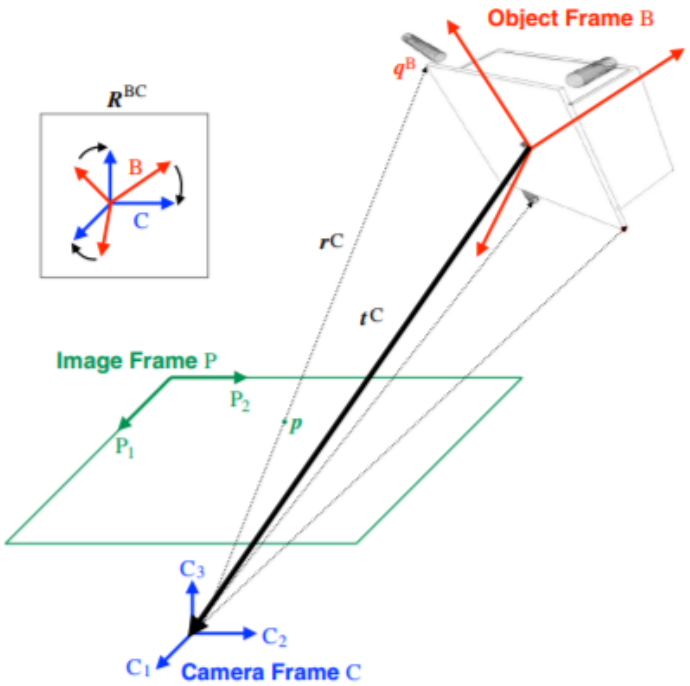

Figure 2.9: Schematic representation of the pose estimation problem using a monocular image [75].

Table 2.7 summarises the findings from this research and shows the expected performance of several pose estimation architectures. It shows the error for measuring both the relative position ($||E_T||$) and attitude ($||E_R||$). The final columns present the robustness with respect to Earth in the background, the robustness with respect to target symmetry and the validation methods used in validating the performance.

As Table 2.7 shows, most authors have not validated the pose estimation architecture with actual space imagery, but rather with synthetic images, which sometimes leads to the omission of the reflectivity of actual space materials [10]. Since space imagery is characterised by lighting conditions that are continuously changing and highly dependent on the orientation of the two spacecraft, adverse lighting conditions can easily decrease the expected accuracy of the pose estimate.

Pasqualetto-Cassinis et al. [10] also assessed the validation of pose estimation systems with respect to Earth in the background of the image and with respect to symmetry of the target spacecraft. A lack of validation was found for most architectures, meaning that the pose estimate could easily become less accurate under these specific conditions.

The results in Table 2.7 should therefore be interpreted as the nominal performance, or an estimate of the highest achievable accuracy of currently available pose estimation systems. The pose estimation error will, however, likely increase when the camera is presented with undesirable viewing and/or lighting conditions. Vision-based guidance systems should thus show sufficient robustness to situations where pose estimation error is increased due to undesirable viewing or lighting conditions. Furthermore, it should aid in the creation of desirable conditions whenever possible.

2.4.2. State-of-the-art Guidance

In the formulation of a guidance law both translational guidance and rotational guidance should be considered. In general, two approaches are possible for the formulation of guidance laws. In the first approach only a final desired state is defined and the spacecraft is free to follow an optimal trajectory to this final destination. This is intended for phase 2 of the rendezvous process, between P_1 and P_2 (see Section 2.1). Contrary to this is the second approach, where the spacecraft is forced to follow a predefined reference at every step. This is intended for phase 3 of the rendezvous process, when following the spin-axis between P_2 and P_3 (see Section 2.1). In the first approach the guidance is required to estimate a final state as well as calculate an optimal trajectory. In the second approach the guidance is only required to estimate the desired state, however,

Table 2.7: Overview of current state-of-the-art pose estimation accuracy. ([10]). When multiple numbers are shown these indicate different scenario's or algorithms that were analysed.

Source:	Tested Range	$\|\|E_T\|\|$ (m)	$\|\|E_R\|\|$ (deg)	Robust w.r.t. Earth	Robust w.r.t. Symmetry	Method of Validation*
[75]	~ 10m	0.23 / 0.3	2.7 / 8.1	Semi	Yes	ASI
[54]	180m - 30 m	2.02 / 2.77	3.65 / 5.64	NA	NA	LP, -, -
	30m - 3m	0.28 / 0.51	5.02 / 5.51	NA	NA	LP, -, -
[19]	5m - 1m	0.03	1.95	NA	NA	SI, RCM, NMR
[44]	40m - 5m	0.03	0.6	NA	Yes	SI, ICM, NMR
[22]	~ 10m	0.2	11.2	NA	No	ASI
[72]	~ 10m	0.1	0.66	-	-	-
[76]	~ 5m	0.32	0.76	-	NA	SI, NCM, NMR
[61]	≤ 30m	0.38	1.47	NA	Yes	-

*NA = Not found, - = No information
ASI = Actual Space Imagery, SI = Synthetic Images, LP = Lab Pictures
RCM = Realistic Camera Model, ICM = Ideal Camera Model, NCM = No Camera Model
NMR = No Materials Reflectivity

this action has to be performed at every step rather than only once.

Translational guidance thus follows an optimal trajectory in phase 2, between P_1 and P_2, and a fixed trajectory in phase 3, between P_2 and P_3. Rotational guidance is required to follow a fixed reference in both phases, as the camera shall be pointed at the target CoM at all times. Additionally the chaser is required to synchronise its rotation with the target rotation in phase 3, between P_2 and P_3. Defining this desired state is the task of the guidance system, while following this reference is related to the control system rather than the guidance system. The estimate of a desired state at every step is highly dependent on the accuracy of the pose estimate, and an elaborate discussion on the calculation of reference state in these cases can be found in Section 5.1. Only the optimal translational guidance, required between P_1 and P_2 is further discussed here, to provide an overview of available solutions.

Optimal Translational Guidance

Throughout the past 50 years many approaches to the translational guidance problem have been considered. The best-known methods are perhaps the traditional V-bar and R-bar approach, adopted in multiple of the space-shuttle missions (i.e. Discovery, Challenger) [29]. These approaches are however inadequate when considering scenarios with time-varying constraints (i.e. in the case of tumbling space debris) and are non-optimal [77]. Therefore alternative techniques have been developed, and a list of the currently available state-of-the-art solutions is provided by Starek et al. [81]. Three most promising methodologies, respectively Model Predictive Control (MPC), Artificial Potential Functions (APF) and Spacecraft Motion Planning (SMP) are summarised shortly.

Model Predictive Control:

This type of guidance law is based on the repeated evaluation of the Optimal Control Problem (OCP). In general, an optimal trajectory is defined by the minimisation of a cost function, using the current state and the final desired state as constraints to the problem. This requires expressing the final state as a function of all previous states and control inputs, i.e. like Breger et al. [9]:

$$\boldsymbol{x}_{\text{final}} = \boldsymbol{A}_{t_0}^{t_f} \boldsymbol{x}_0 + \Gamma_t \begin{bmatrix} \boldsymbol{u}_0 \\ \vdots \\ \boldsymbol{u}_{t-1} \end{bmatrix} \tag{2.3}$$

where $\boldsymbol{x}_{\text{final}}$ is the desired final spacecraft state, $\boldsymbol{A}_{t_0}^{t_f}$ is the State Transition Matrix from t_0 to t_f, $\boldsymbol{u}_t$ represents the control input at time t and Γ_t is a convolution matrix (see [9] for more detail). Using this definition, a cost function J^*, aimed at finding the optimal sequence of control inputs $\boldsymbol{u}_i$ such that the total control effort is minimised, can be written as

$$J^* = \underset{\boldsymbol{u}_0 \cdots \boldsymbol{u}_{N-1}}{min} \sum_{i=0}^{N-1} ||\boldsymbol{u}_i|| \tag{2.4}$$

Although this example uses a linear state representation, non-linear state representations are in no way excluded from this formulation. Once the optimal control effort has been established, the chaser can be controlled to a new position where the optimal trajectory may be re-evaluated based on the new state, iteratively solving the OCP at every step. This approach lends itself very well to vision-based systems, as it allows for the OCP to be continuously re-evaluated with new estimates of the target state. As accuracy is expected to increase over time, when more data becomes available, an increasingly optimal trajectory is expected.

Artificial Potential Functions:

This method is based upon the definition of a function that fills the space around the target with artificial potentials, guiding the spacecraft from regions of high potential to regions of low potential, similar to "a ball moving from a hill to a valley" [98]. The potential assigned to the goal-state should be such that the global minimum is defined at the target. An example potential is provided by Zhang et al. [98]:

$$\varphi_t = \frac{1}{2}\Delta \boldsymbol{x}_v^T \boldsymbol{P}_v \Delta \boldsymbol{x}_v + \frac{1}{2}\Delta \boldsymbol{x}_p^T \boldsymbol{P}_p \Delta \boldsymbol{x}_p \tag{2.5}$$

where $\boldsymbol{P}$ represents a set of tunable potential functions (see Zhang et al. [98] for more detail). The motion within such a potential field can easily be constrained by defining regions of high potential Ψ_o. The system potential function is simply the sum of all potential functions:

$$\phi = \varphi + \sum_{i=0}^{N} \Psi_o \tag{2.6}$$

This approach offers an easy implementation of path constraints, but requires proper tuning of the potential generating functions ($\boldsymbol{P}_v$,$\boldsymbol{P}_p$,Ψ_o) to function correctly. The largest drawback of this method is that it tends to converge to local minima [63]. Another significant problem with the use of potential functions is that an artificial potential force cannot always prevent the chaser from entering regions of high potential when real dynamics are involved [98]. This compromises the safety of the satellite, which is never acceptable.

Spacecraft Motion Planning:

Motion planning is sometimes viewed as a sub-set of MPC and uses algorithms to generate sequences of decisions that safely guide the chaser towards the target. As an example, Biggs and Horri [7] use motion planning to compute optimal rotational guidance using the following kinematic constraint function:

$$\frac{d\boldsymbol{R}(t)}{dt} = \boldsymbol{R}(t)\,(\upsilon \boldsymbol{A} + \Omega \boldsymbol{A}_2 + \Omega_3 \boldsymbol{A}_3) \tag{2.7}$$

where one axis is constrained to spin at a fixed rate υ, R represents the spacecraft orientation and A forms a basis for Lie algebra (see Biggs and Horri [7] for more detail). When aiming to minimise this function, the authors define a subset of allowable and smooth motions by defining the optimal angular velocities (Ω_1^*, Ω_2^*) and quaternion components ($q_0^*, q_1^*, q_2^*, q_3^*$) as functions of three parameters (r, c, β), available for optimization. Using this subset allows the definition of two cost functions J_1 and J_2

$$J_1(t,r,c,\beta) = \left[(q_0(t,r,c) - q_{f0})^2 + (q_1(t,r,c) - q_{f1})^2 + (q_2(t,r,c,\beta) - q_{f2})^2 + (q_3(t,r,c,\beta) - q_{f3})^2\right] \tag{2.8a}$$

$$J_2 = \int_0^{t_f} = ||\boldsymbol{u}(t,r,c,\beta)||dt \tag{2.8b}$$

where $q_{f0}, q_{f1}, q_{f2}, q_{f3}$ correspond to the final rotational orientation and $\boldsymbol{u}$ represents the control effort. These two functions are then combined in a total weighed cost function J which is minimised in the time domain.

The idea is computationally advantageous, but simply solving Equation (2.7) would require an infinite sample set to be able to guarantee an existing solution. Biggs and Horri [7] define a subset which is guaranteed to yield feasible solutions, but such a subset is generally hard to define. Due to this, motion planning has seen

very little application in spacecraft control systems, as feasible plans are more highly regarded than optimal plans [81].

When the drawbacks of both the artificial potential and motion planning methods are considered, compromising either the safety of the spacecraft or feasibility of solutions, the MPC approach is selected as most viable candidate algorithm for this research. Mainly its characteristic to re-evaluate the optimal control problem is of high value when considering vision-based systems. A discussion on the exact problem formulation in terms of dynamics, cost function and constraints is presented in Section 5.1.

3

Theoretical Background

This chapter outlines the theoretical background of the thesis. First, Section 3.1 provides an overview of reference frames. Second, Section 3.2 provides a short note on orbital perturbations, after which a discussion of the translational dynamics follows in Section 3.3, considering both Cartesian and Orbital Element state parameterizations. The chapter is concluded with a discussion on attitude dynamics, presented in Section 3.4.

3.1. Reference Frames

In order to model the dynamics of the spacecraft it is necessary to define the reference frames in which their motion is represented. This section shortly introduces the reference frames that are exploited and discusses their relationship, as well as conversions between frames.

3.1.1. Definitions

The first frame is an inertial frame, which is useful to represent a full-force model for the integration of true dynamics. Next two body-centred reference frames are introduced, one for each spacecraft, which are useful to define satellite properties. Finally, the RTN or Hill frame is introduced, which is especially useful to represent relative motion during the rendezvous process in a comprehensive and intuitive way.

- **Inertial (ECI):** The inertial frame is the Earth Centered Inertial (ECI) frame which has axes pointing to the vernal-equinox (X-axis) and the Earth's north pole (Z-axis). The Y-axis completes the right handed system and lies in the Earth's equatorial plane. The ECI frame is visualised by $\vec{X}$, $\vec{Y}$ and $\vec{Z}$ in Figure 3.1 and, as indicated previously, is especially useful for representing the true, disturbed, non-linear satellite motion.
- **Body-fixed (CBF/TBF):** The second set of frames is fixed with respect to the body features of the spacecraft. For the chaser it is convenient to align the body fixed axes with the camera axes, as one less rotation is required to go from the camera frame to the orbital frame. For the target, the axes are defined by a 3D model of the target body.
  - **Chaser Body-Fixed Frame (CBF):** The CBF frame is fixed to the CoM of the chaser spacecraft. The Z-axis of this frame is aligned with the camera boresight axis. It might be the case that, in reality, the camera frame is not perfectly aligned with CBF. In this case an additional coordinate system will have to be employed to describe the camera frame, but in this work it is assumed that the two coincide. The X and Y axes form a plane perpendicular to this first axis and are oriented as shown in Figure 2.5. As a convention, the Y-axis of the CBF frame is pointed downward in the images taken by the camera, with the X-axis pointed to the right.
  - **Target Body-fixed Frame (TBF):** This frame is fixed to the target's CoM. It is defined to assist in describing the relative attitude and angular motion of the target. The axes are defined by the 3D model as shown in Figure 2.2.
- **Orbital/Hill Frame (RTN):** The final frame is the Hill or Orbital Frame. This frame is centred in the target's CoM and has axes pointing outward along the orbital radius (R-axis) and parallel to the orbital

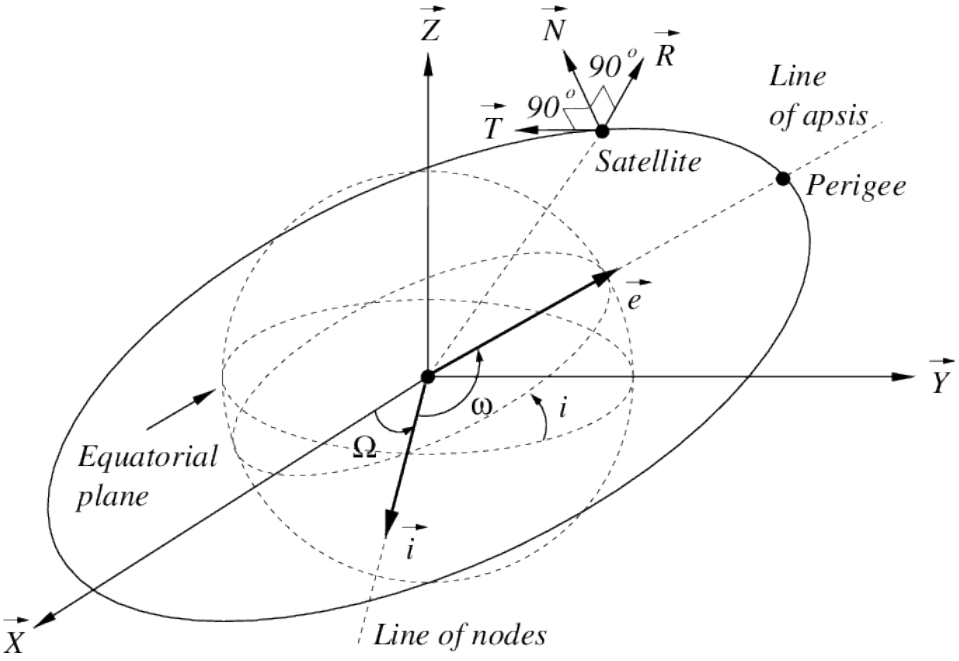

Figure 3.1: Relation of ECI and RTN frames [46].

momentum vector (N-axis), with the final axis (T-axis) completing a right-handed system. In the case of (near-)circular orbits, (T) is tangential to the orbit radius and aligned with the velocity vector **V**. This frame is also called the Radial-Tangential-Normal (RTN) frame and is referenced as such in this work. It is used to represent the relative motion between the chaser and target satellites. The RTN frame is visualised by $\vec{R}$, $\vec{T}$ and $\vec{N}$ in Figure 3.1.

3.1.2. ECI to RTN

A relative vector in the ECI frame, $\boldsymbol{r}_{12}^{I}$ in Figure 3.2, can be transformed into a relative vector in the RTN frame, $\boldsymbol{r}_{12}^{R}$ in Figure 3.2 by using the following relation [96]

$$\boldsymbol{r}_{12}^{RTN} = [\boldsymbol{C}]\boldsymbol{r}_{12}^{ECI} \tag{3.1}$$

$$\dot{\boldsymbol{r}}_{12}^{RTN} = [\dot{\boldsymbol{C}}]\boldsymbol{r}_{12}^{ECI} + [\boldsymbol{C}]\dot{\boldsymbol{r}}_{12}^{ECI} \tag{3.2}$$

where $[\boldsymbol{C}]$ is a 3x3 rotation matrix and $[\dot{\boldsymbol{C}}]$ is its derivative. The matrix $[\boldsymbol{C}]$ is defined as

$$[\boldsymbol{C}] = \begin{bmatrix} e_{RX} & e_{RY} & e_{RZ} \\ e_{TX} & e_{TY} & e_{TZ} \\ e_{NX} & e_{NY} & e_{NZ} \end{bmatrix} = \begin{bmatrix} \boldsymbol{e}_R \\ \boldsymbol{e}_T \\ \boldsymbol{e}_N \end{bmatrix} \tag{3.3}$$

Since $[\boldsymbol{C}]$ is a rotation matrix, the inverse rotation from RTN to ECI can simply be computed using $[\boldsymbol{C}^T]$. The components $\boldsymbol{e}_R, \boldsymbol{e}_T, \boldsymbol{e}_N$ are defined as

$$\boldsymbol{e}_R = \frac{\boldsymbol{r}_{ECI}}{||\boldsymbol{r}_{ECI}||} \tag{3.4}$$

$$\boldsymbol{e}_N = \frac{\boldsymbol{h}}{||\boldsymbol{h}||} = \frac{\boldsymbol{r}_{ECI} \times \boldsymbol{v}_{ECI}}{||\boldsymbol{r}_{ECI} \times \boldsymbol{v}_{ECI}||} \tag{3.5}$$

$$\boldsymbol{e}_T = \boldsymbol{e}_R \times \boldsymbol{e}_N \tag{3.6}$$

with $\boldsymbol{h}$ the orbital momentum vector. Using the chain rule, the derivatives of these vectors, required for $[\dot{\boldsymbol{C}}]$, are computed as

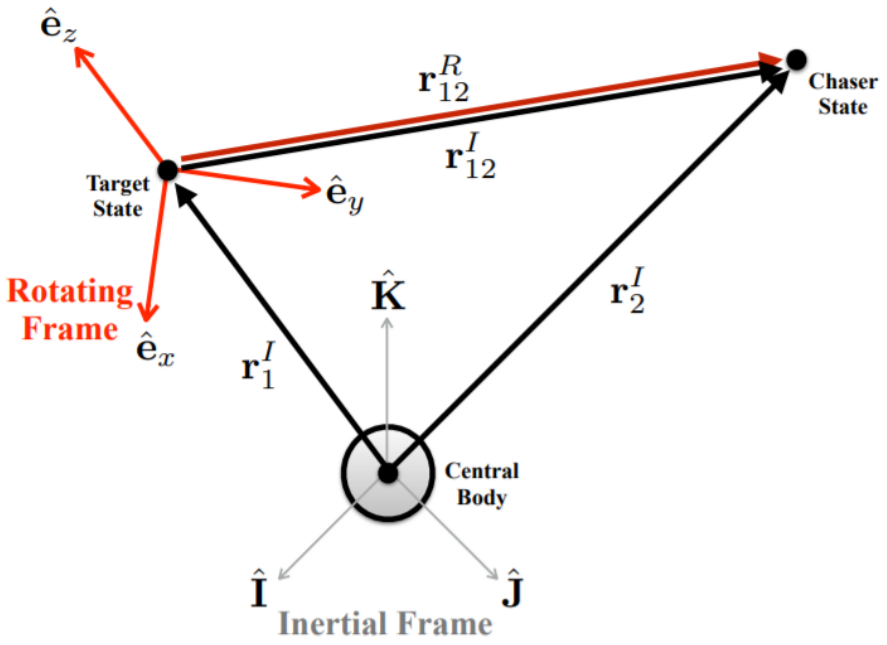

Figure 3.2: Relative vectors in the ECI and RTN frames [96].

$$\frac{d}{dt}\boldsymbol{e}_R = \frac{1}{||\boldsymbol{r}_{ECI}||}\left[\boldsymbol{v} - (\boldsymbol{e}_R \cdot \boldsymbol{v})\boldsymbol{e}_R\right] \tag{3.7}$$

$$\frac{d}{dt}\boldsymbol{e}_T = \left[\frac{d}{dt}(\boldsymbol{e}_R) \times \boldsymbol{e}_N\right] + \left[\frac{d}{dt}(\boldsymbol{e}_N) \times \boldsymbol{e}_R\right] \tag{3.8}$$

$$\frac{d}{dt}\boldsymbol{e}_N = \frac{1}{||\boldsymbol{h}||}\left[\dot{\boldsymbol{h}} - (\boldsymbol{e}_N \cdot \dot{\boldsymbol{h}})\boldsymbol{e}_N\right] = \frac{1}{||\boldsymbol{h}||}\left[(\boldsymbol{r} \times \boldsymbol{a}) - (\boldsymbol{e}_N \cdot (\boldsymbol{r} \times \boldsymbol{a}))\,\boldsymbol{e}_N\right] = \boldsymbol{0} \tag{3.9}$$

This assumes that the satellites move under two-body motion, where $\boldsymbol{r}||\boldsymbol{a}$ and no acceleration outside of the orbital plane is experienced.

3.2. Perturbations

Before looking at available models, it should be clear what perturbations have to be included, as the choice of model depends on this. The rendezvous process is expected to be shorter than 2000 seconds (see Section 4.2), which is a relatively short timescale when considering the effect of perturbations. Most publications that consider a similar rendezvous scenario, simply neglect perturbations [9, 83, 90], assuming unperturbed dynamics. This can easily be justified by considering that the effect of relative perturbations decreases significantly with decreasing inter-satellite separation, as shown in Figure 3.3. In LEO, this means that differential drag and J_2 are usually considered.

Guffanti et al. [30] show that, for LEO, contributions of solar radiation pressure, third body accelerations and higher order gravitational perturbations (J_3 and higher) can be safely ignored, as errors are at cm-level even after 10 complete orbits. The largest contribution of error is due to the J_2 effect, causing errors of 190 m over a period of 10 orbits. This error grows approximately linearly and could already cause errors of several meters in the time span allocated for rendezvous. However, this work considers a combination of linear models with measurements, which are connected to the real world and used to correct the propagation step of linear models. This approach only requires the assumption of linearization to be valid over very short time spans between measurements, in the order of seconds, which it is proven to be [30].

A final note on the inclusion of drag is provided by Sullivan et al. [82], who indicate that this perturbation is usually extremely difficult to model accurately and that in certain scenarios it might be more beneficial to discard the modelling of drag. Including it would only decrease the model accuracy, due to the uncertainty

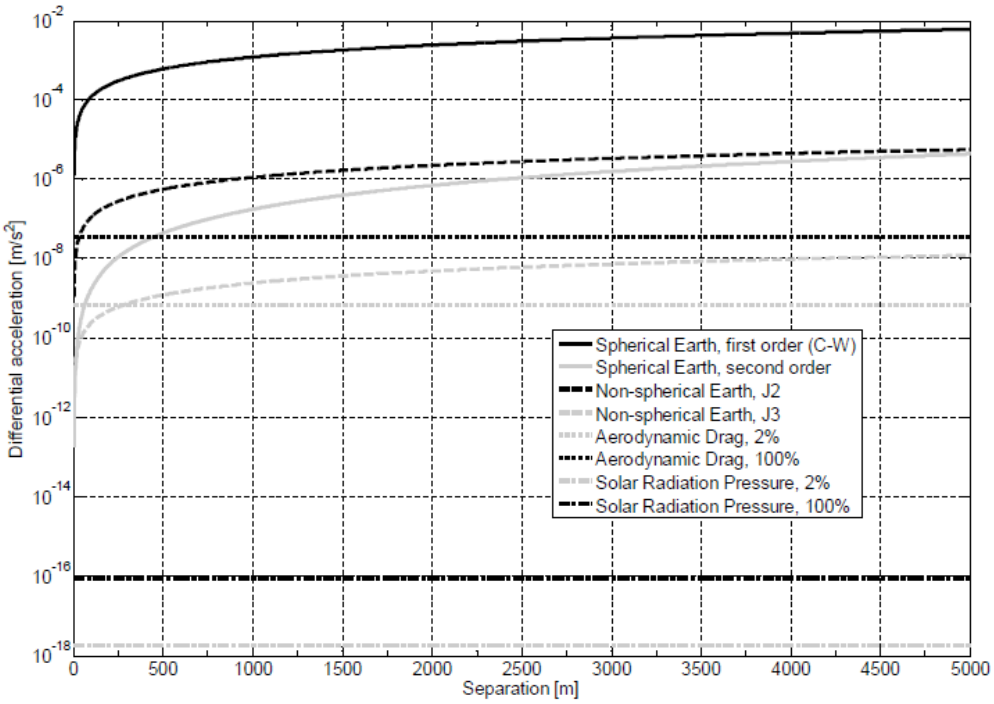

Figure 3.3: Relative accelerations in the LEO environment due to multiple sources, for various inter-satellite distances [14].

by which atmospheric density models are characterised. For the above reasons, no non-linear perturbations are included and only the first order spherical Earth is considered.

3.3. Translational Dynamics

The section provides an overview of the translational dynamics, used to model the satellite motion. First of all the full-force model is discussed, used to integrate the true, non-linear motion of the satellite. Second, two different representations of relative motion, Cartesian and Orbital Elements, are discussed and their specific uses highlighted. Lastly a short review is given of relative dynamics, using the Clohessy-Wiltshire equations.

3.3.1. High Precision Model

The guidance and navigation system both employ linear models to approximate the dynamics. A high precision simulation of the true satellite dynamics is therefore required for validation of these models. Use is made of an existing MATLAB high precision integrator by Mahooti [49] which uses an implicit Runge-Kutte (Radau IIa) integration method [93] with variable order. This architecture solves the equation of motion

$$\ddot{\boldsymbol{r}} = m \cdot \boldsymbol{a} \tag{3.10}$$

$$= m \cdot \left(\boldsymbol{a_{sh}} + \boldsymbol{a_{sun}} + \boldsymbol{a_{moon}} + \boldsymbol{a_{planets}} + \boldsymbol{a_{solrad}} + \boldsymbol{a_{drag}} + \boldsymbol{a_{rel}} \right) \tag{3.11}$$

where m represents the mass of the satellite and the total acceleration vector a is comprised of the following set of accelerations

a_{sh}	Spherical harmonic acceleration for an elastic Earth up to degree and order 70 (m = n = 70). Including tides for solid Earth and ocean.
a_{sun}	Point mass acceleration of the sun.
a_{moon}	Point mass acceleration of the moon.
$a_{planets}$	Point mass acceleration for all planets in the solar system, including Pluto.
a_{solrad}	Acceleration due to solar radiation pressure.

a_{drag} Acceleration due to atmospheric drag, using the JB2008 atmospheric model.

a_{rel} Acceleration due to the effects of special relativity.

This high precision model was already validated by the author, using true Envisat DORIS Doppler data. Its accuracy was found to be better than $\boldsymbol{\sigma}^{3D}_{RMS}$ = 3m over a period of 24 hours, with cm-level accuracy over a period of several hours. The absolute chaser and target states are integrated in the ECI frame with the high precision model.

3.3.2. Cartesian State Representation

The Cartesian parameterization is a commonly used form of the state vector, describing the position and velocity of the satellite as translational coordinates along three orthogonal axis, usually labelled *X*, *Y* and *Z*. The state vector in this case is written as

$$\bar{\boldsymbol{X}} = \begin{pmatrix} r_x \\ r_y \\ r_z \\ \dot{r}_x = v_x \\ \dot{r}_y = v_y \\ \dot{r}_z = v_z \end{pmatrix} \tag{3.12}$$

where r_x, r_y, r_z represent the position in three dimensional space and v_x, v_y, v_z represent the velocity along the same axis. This state vector is composed of rectilinear elements and can either be used to describe absolute positions in the ECI frame or relative positions in the RTN frame.

The relative motion uses a linearised model to describe the dynamics. Under the assumption of an unperturbed and near-circular reference orbit, a linear model of the relative dynamics is found in the Clohessy-Wiltshire-Hill (CWH) equations [12]. Formulated in the target-centred RTN frame, Equation (3.13) describes the motion of the chaser with respect to the target:

$$\ddot{x} = 3n^2 x + 2n\dot{y} + u_x \tag{3.13a}$$

$$\ddot{y} = -2n\dot{x} + u_y \tag{3.13b}$$

$$\ddot{z} = -n^2 z + u_z \tag{3.13c}$$

with n the mean orbital motion and $\boldsymbol{u} = (u_x, u_y, u_z)^T$ the control vector. The validity of these equations is limited to near-circular orbits, and inter-satellite distances much smaller than the orbital radius. Due to the lack of perturbations in the model, it is only accurate over short time periods. Conveniently, the navigation filter is updated with measurements regularly, meaning that the linear model should be valid over the time span between two measurements. A State Transition Matrix (STM) for these equations can be formulated to achieve a closed-form solution. Without perturbations or control forces this STM can be written as [16]:

$$\bar{\boldsymbol{X}}_t = \boldsymbol{A}(t, t_0)\bar{\boldsymbol{X}}_0 + \boldsymbol{B}\bar{\boldsymbol{u}} \tag{3.14a}$$

$$\boldsymbol{A} = \begin{bmatrix} 4-3\cos nt & 0 & 0 & \frac{1}{n}\sin nt & \frac{2}{n}(1-\cos nt & 0 \\ 6(\sin nt - nt) & 1 & 0 & -\frac{2}{n}(1-\cos nt & \frac{1}{n}(4\sin nt - 3nt) & 0 \\ 0 & 0 & \cos nt & 0 & 0 & \frac{1}{n}\sin nt \\ 3n\sin nt & 0 & 0 & \cos nt & 2\sin nt & 0 \\ -6n(1-\cos nt) & 0 & 0 & -2\sin nt & 4\cos nt - 3 & 0 \\ 0 & 0 & -n\sin nt & 0 & 0 & \cos nt \end{bmatrix} \tag{3.14b}$$

where $\boldsymbol{A}$ is the STM, $\bar{\boldsymbol{X}}_t$ represents the relative state at time t, $\boldsymbol{u}$ are the control forces in the RTN frame and n is the mean orbital motion. For completion:

$$\boldsymbol{B} = \begin{bmatrix} 0 & 0 & 0 \\ 0 & 0 & 0 \\ 0 & 0 & 0 \\ \frac{1}{m} & 0 & 0 \\ 0 & \frac{1}{m} & 0 \\ 0 & 0 & \frac{1}{m} \end{bmatrix} \tag{3.15}$$

3.3.3. Relative Orbital Elements

The orbit may also be parameterized in the form of orbital elements. The absolute state of the satellite in the ECI frame can be described using a set of modified Kepler elements $\boldsymbol{\alpha}$ [14]:

$$\boldsymbol{\alpha} = \begin{pmatrix} a \\ u \\ e_x \\ e_y \\ i_x \\ i_y \end{pmatrix} = \begin{pmatrix} a \\ \omega + M \\ e\cos\omega \\ e\sin\omega \\ i \\ \Omega \end{pmatrix} \tag{3.16}$$

This formulation is a modified version of the classical Kepler elements and introduces the relative eccentricity vector $\boldsymbol{e} = (e_x, e_y)^T$ and mean argument of latitude u, which are helpful in avoiding the singularities in e, ω and M found for near-circular orbits.

Contrary to the Cartesian parameterization, where Equation (3.12) could be used to describe both absolute and relative states, modelling the relative state of the target with respect to the chaser requires a new set of elements called the Relative Orbital Elements (ROE), introduced by D'Amico [20] to model the relative motion of two satellites in low earth orbit. The formulation of the ROE is based on the parameterization in Equation (3.16) and given as:

$$\delta\boldsymbol{\alpha} = \begin{pmatrix} \delta a \\ \delta\lambda \\ \delta e_x \\ \delta e_y \\ \delta i_x \\ \delta i_y \end{pmatrix} = \begin{pmatrix} (a_t - a)/a \\ (u_t - u) + (\Omega_t - \Omega)\cos i \\ e_{x_t} - e_x \\ e_{y_t} - e_y \\ i_t - i \\ (\Omega_t - \Omega)\sin i \end{pmatrix} \tag{3.17}$$

The subscript t is introduced to indicate properties belonging to the target satellite, while the properties without subscript belong to the chaser satellite. The parameters δa and $\delta\lambda$ represent the (dimensionless) relative semi-major axis and relative mean longitude between the target and chaser spacecraft.

The other four elements present the relative eccentricity and inclination vectors, which could alternatively be written in polar representation as [14]:

$$\delta\boldsymbol{e} = \begin{pmatrix} \delta e_x \\ \delta e_y \end{pmatrix} = \delta e \begin{pmatrix} \cos\varphi \\ \sin\varphi \end{pmatrix} \tag{3.18}$$

$$\delta\boldsymbol{i} = \begin{pmatrix} \delta i_x \\ \delta i_y \end{pmatrix} = \delta i \begin{pmatrix} \cos\vartheta \\ \sin\vartheta \end{pmatrix} \tag{3.19}$$

where δe and δi are the magnitude of respectively the relative eccentricity and relative inclination vectors. These properties have no physical meaning and are not the same as the arithmetic differences between eccentricity and inclination. The angles φ and ϑ are called relative perigee and relative ascending node. Although the parameters in Equation (3.17) carry no physical significance, when multiplied with the chaser semi-major axis a, the resulting elements $a\delta\boldsymbol{\alpha}$ describe physical properties of the resulting relative orbit as shown in Figure 3.4.

The angles φ and ϑ deserve a more in-depth examination due to their usefulness in determining the position of the spacecraft on the relative orbit. Making use of the polar representation of $\delta\boldsymbol{e}$ and $\delta\boldsymbol{i}$, Equation (3.20) can be derived [14], expressing the chaser position components in the target RTN frame as function of the angles φ and ϑ:

$$\begin{aligned} \delta r_r/a &= \delta a - \delta e\cos(u-\varphi) \\ \delta r_t/a &= \delta\lambda - \frac{3}{2}\delta a\cdot u + 2\delta e\sin(u-\varphi) \\ \delta r_n/a &= +\delta i\sin(u-\vartheta) \end{aligned} \tag{3.20}$$

where $\delta r_r, \delta r_t$ and δr_n represent the relative separations along the R, T and N axes. For the case where $\delta a = \delta\lambda = 0$, these equations show that whenever the argument of latitude u is equal to the relative perigee φ, the chaser is directly 'below' the target satellite. This is visualised in Figure 3.5, where this moment is highlighted. Similarly, the motion along the N-axis is described by angle $u - \vartheta$. The consequence of this definition is that, when designing relative orbits, it grants the ability to choose an ideal 'starting-point' with respect to u.

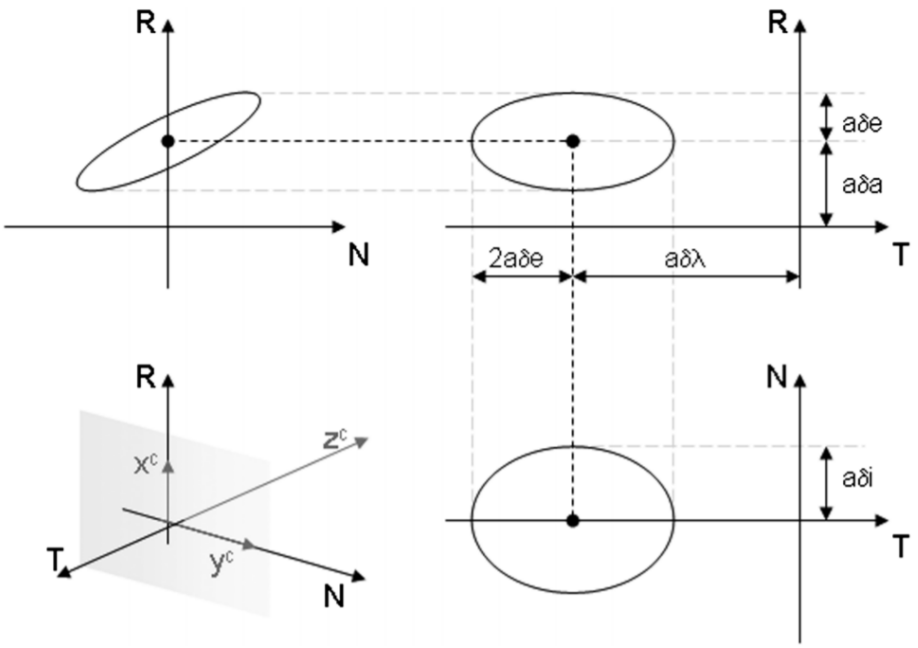

Figure 3.4: Representation of the relative orbit through the use of the ROE (Equation (3.17)) [27].

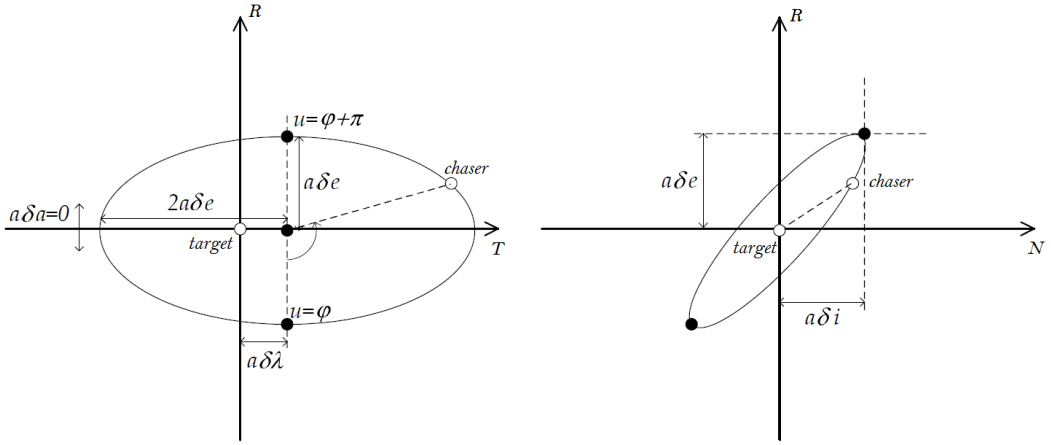

Figure 3.5: Projection of the relative orbit on the *R-T* plane (left) and the *R-N* plane (right) for orbits with $\delta a = 0$ [79].

3.3.4. Passively Safe Relative Orbits

Defining a passively safe relative orbit is useful, as it permits the chaser to safely observed the target, giving the navigation filter time to converge without spending any fuel. Passively safe orbits are defined from the concept of e/i-vector separation, first introduced by Eckstein et al. [23] for safe collocation of satellites in geostationary orbit and applied by D'Amico [14] for satellites in the LEO orbit regime.

This concept is based on the principle that the error in determining the along-track separation of two satellites is usually higher than the error in the other two directions. This is in part due to the coupling between semi-major axis and orbital period [14], and predictions of the relative motion are therefore sensitive to both errors from orbit determination and manoeuvres.

Parallel alignment of $\delta\boldsymbol{e}$ and $\delta\boldsymbol{i}$ implies the equality of the phase angles φ and ϑ [14]. As can be deduced from Equation (3.20) and Figure 3.5, $u = \varphi + k\pi$ (with k an integer) marks the positions of maximum radial separation and $u = \varphi + (k + \frac{1}{2})\pi$ marks the minimum separation in radial direction (= 0m). Setting $\varphi = \vartheta + k\pi$ (parallel or anti-parallel alignment) ensures that when δr_r vanishes, δr_n is at a maximum, while setting $\varphi = \vartheta + (k + \frac{1}{2})\pi$ (orthogonal alignment) causes separations in radial (δr_r) and cross-track (δr_n) directions to jointly vanish. If along-track position uncertainties are large, this can impose serious risk, therefore safety is

achieved from the parallel or anti-parallel alignment of the relative eccentricity and inclination vector [23]. Figure 3.6 shows the relative orbits for parallel and orthogonal e/i-vectors.

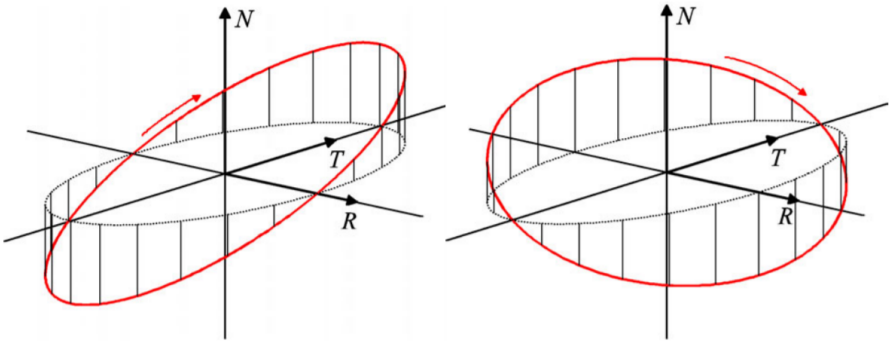

Figure 3.6: The concept of e/i-vector separation. The relative orbits are characterised by parallel (left) and orthogonal (right) e/i-vectors. [53]

3.4. Attitude Dynamics

First, the theory of Euler angles and quaternions is discussed, as they are commonly used representations for attitude, both having advantages and flaws that need to be considered. Next, the conversions between sets of attitude representations are described before moving to the kinematics and dynamics associated with rotations in different reference frames.

3.4.1. Euler Angles

The Euler angle representation is the most intuitive way of representing attitude and rotation. Three axis are chosen (usually pitch, roll and yaw) and the rotations are represented with angles (θ, φ, ψ) around these axes. Usually intrinsic rotation are applied, meaning the next rotation is around the new axis from the previous rotation and not around the original, as shown in Figure 3.7. The kinematics are simply represented as the change of these angles $(\dot{\theta}, \dot{\varphi}, \dot{\psi})$.

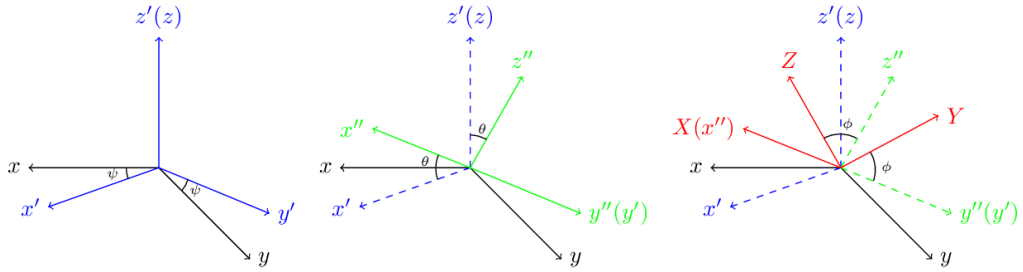

Figure 3.7: Euler angle *x*-*y*'-*x*" sequence of intrinsic rotations.

In the Euler angle representation, dynamics are modelled as subsequent rotations around the three axes. The problem with this is the occurrence of a phenomenon called 'gimbal lock'. The Euler angle system can be represented as a virtual gimbal with three circles. When two of the virtual circles are aligned, a degree of freedom is lost and thus a degree of control is lost. This is highly undesirable in any situation, making the Euler angles unsuitable for adoption in control systems. However, Euler angles are very intuitive and therefore are an excellent way to verify the correct performance of less intuitive attitude representations, such as quaternions.

3.4.2. Quaternions

In order to address the gimbal lock problem with Euler angles, the quaternion system was developed. It follows from Euler's rotational theorem [58] that every representation of 3D space exploiting only 3 variables displays singularities. As such the quaternion system is composed of four variables and a quaternion is defined as:

$$\boldsymbol{q} \equiv \begin{bmatrix} q_0 \\ \boldsymbol{q_{13}} \end{bmatrix} \qquad \boldsymbol{q_{13}} \equiv \begin{bmatrix} q_1 \\ q_2 \\ q_3 \end{bmatrix} = \hat{\boldsymbol{n}} sin\left(\frac{\theta}{2}\right) \qquad q_0 = cos\left(\frac{\theta}{2}\right) \tag{3.21}$$

where $\hat{\boldsymbol{n}}$ is the axis of rotation and θ is the rotation angle around this axis. For quaternions that represent rotations, the norm of the quaternion should always equal 1 [88]:

$$q_0^2 + \boldsymbol{q_{13}^T q_{13}} = 1 \tag{3.22}$$

For unit quaternions the quaternion inverse q^{-1} is equal to the quaternion conjugate $q*$ which is defined as:

$$\boldsymbol{q*} = \begin{bmatrix} q_0 \\ -\boldsymbol{q_{13}} \end{bmatrix} \tag{3.23}$$

Since the quaternion exists of four parameters instead of three, it is free of the 'gimbal lock' problem found in Euler angles, but instead suffers from over-determination [88], meaning that different quaternions can represent the same rotation. A property of quaternions is therefore that when multiplied by a scalar, the same rotation is still represented. By defining attitude quaternions to have a unit norm, this is only a problem in the case of -1/1. This requires an additional check to be built into the algorithm processing the quaternions. This check uses of the following quaternion property

$$\begin{aligned} \boldsymbol{q} \otimes \boldsymbol{q}^{-1} &= [+1, \ \ \boldsymbol{0}] \\ -\boldsymbol{q} \otimes \boldsymbol{q}^{-1} &= [-1, \ \ \boldsymbol{0}] \end{aligned} \tag{3.24}$$

where $\otimes$ represents the quaternion product, also called the Hamilton product. Using Equation (3.24) a check can be performed to see if the quaternion has flipped (i.e. been multiplied with -1). This is done by comparing

$$\begin{aligned} \delta q_1 &= [1 \ \ \boldsymbol{0}] - \left(+\boldsymbol{q} \otimes \boldsymbol{q}^{-1}\right) \quad \text{and} \\ \delta q_2 &= [1 \ \ \boldsymbol{0}] - \left(-\boldsymbol{q} \otimes \boldsymbol{q}^{-1}\right) \end{aligned}$$

If $\delta q_2 < \delta q_1$ the quaternion has 'flipped' and should be manually 'flipped back', by multiplying with -1, to ensure smoothness in the quaternion.

Quaternions are used to describe the attitude of one frame with respect to another and are always labelled accordingly. This following convention is used:

$$\boldsymbol{q}_A^B \otimes \boldsymbol{v}_A \otimes \left(\boldsymbol{q}_A^B\right)^{-1} = \boldsymbol{v}_B \tag{3.25}$$

where $\boldsymbol{q}_A^B$ describes the relative attitude of frame A with respect to frame B, $\boldsymbol{v}_A$ is a vector in frame A and $\boldsymbol{v}_B$ is a vector in frame B. The 'attitude of frame A with respect to frame B' describes the required rotation to go from frame A to frame B. The relative attitude of the target with respect to the chaser is calculated as their quaternion product

$$\boldsymbol{q_{TBF}^{CBF}} = \boldsymbol{q_{TBF}^{RTN}} \otimes \boldsymbol{q_{RTN}^{CBF}} \tag{3.26}$$

where TBF, CBF and RTN are the coordinate frames as discussed in Section 3.1.1. In reality the relative quaternion q_{TBF}^{CBF} is directly computed from the camera pseudo-measurements as in Equations (2.1) and (2.2) and q_{RTN}^{CBF} is retrievable from the attitude determination system of the chaser spacecraft. Using Equation (3.26) it is possible to compute q_{TBF}^{RTN}. This is a useful parameter, as it describes the orientation of the target with respect to the RTN frame. This quaternion is used to convert the target rotation from the body frame to the RTN frame, where it might be used by the guidance system (see Equation (5.9c)). In a simulated environment however, Equation (3.26) may be used to calculate q_{TBF}^{CBF} from the chaser and target separate orientations.

3.4.3. Modified Rodrigues Parameters

The Modified Rodrigues Parameters (MRP) build on the quaternion representation and again use a total of 3 parameters to represent an object in 3D space. Therefore, according to Euler's rotation theorem [58], this method is no longer over-determined at the cost of displaying singularities. The definition can be directly traced back to quaternions and can best be seen as a mapping of quaternions onto a 3D sphere [88]. Using the two parts of the quaternion $q_0, \boldsymbol{q_{13}}$ the definition of the Rodrigues Parameters (Equation (3.27)) and Modified Rodrigues Parameters (Equation (3.28)) follows:

$$\boldsymbol{rp} = \frac{\boldsymbol{q_{13}}}{q_0} = \hat{\boldsymbol{n}} \tan\left(\frac{\theta}{2}\right) \tag{3.27}$$

$$\boldsymbol{\sigma} = \frac{\boldsymbol{q_{13}}}{1+q_0} = \hat{\boldsymbol{n}} \tan\left(\frac{\theta}{4}\right) \tag{3.28}$$

The difference in the two formulations is found in the location of the singularity, existing at angles of $\pm 180^o$ (Equation (3.27), $q_0 = 0$) and $\pm 360^o$ (Equation (3.28), $q_0 = -1$). Due to the location of the singularity MRP allow for turning larger angles without encountering singularities. For this reason the MRP is almost always preferred over the 'normal' Rodriguez Parameters.

3.4.4. Conversions

This section discusses the conversion between quaternions and Euler angles, which aid in intuitive verification of the rotations. The conversion from quaternion to MRP is evident from the definition of the MRP in Equation (3.28). The way in which Euler angles are related to the quaternions depends on the specific sequence of the rotations. From Equation (3.21) it can be observed that the quaternion is related to a rotation angle θ and a spin axis $\hat{\boldsymbol{n}}$. This means that for rotations around the X-, Y- or Z- axis (respectively [1 0 0], [0 1 0], [0 0 1]), the quaternion consists of two numbers $(\cos(\theta/2), \sin(\theta/2))$ and two zeros. Consider that

$$\boldsymbol{q}_{total} = \boldsymbol{q_3} \otimes \boldsymbol{q}_2 \otimes \boldsymbol{q}_1 \tag{3.29}$$

where q_{total} represents the rotation by $\boldsymbol{q}_1$ followed by $\boldsymbol{q}_2$ followed by $\boldsymbol{q}_3$. From this it follows that rotation around X with θ, followed by rotation around Y with φ, followed by rotation around Z with ψ results in the following quaternion

$$\boldsymbol{q}_{\theta,\varphi,\psi} = \begin{bmatrix} \cos\psi/2 \\ 0 \\ 0 \\ \sin\psi/2 \end{bmatrix} \cdot \begin{bmatrix} \cos\varphi/2 \\ 0 \\ \sin\varphi/2 \\ 0 \end{bmatrix} \cdot \begin{bmatrix} \cos\theta/2 \\ \sin\theta/2 \\ 0 \\ 0 \end{bmatrix} \tag{3.30}$$

Similarly, extracting the Euler angles from the quaternion also depends on the particular sequence of rotations. MATLAB offers a complete framework for performing these conversions in the Aerospace Toolbox.

The quaternion rotation as described in Equation (3.25) can also be performed using a direct cosine matrix $\boldsymbol{R}$ as

$$\boldsymbol{R}_A^B \boldsymbol{v}_A = \boldsymbol{v}_B \tag{3.31}$$

where $\boldsymbol{R}_A^B$ is equivalent to q_A^B and can be found from q_A^B as

$$\boldsymbol{R}_A^B = \begin{pmatrix} q_0^2+q_1^2-q_2^2-q_3^2 & 2(q_1q_2-q_0q_3) & 2(q_1q_3+q_0q_2) \\ 2(q_1q_2+q_0q_3) & q_0^2-q_1^2+q_2^2-q_3^2 & 2(q_2q_3-q_0q_1) \\ 2(q_1q_3-q_0q_2) & 2(q_2q_3+q_0q_1) & q_0^2-q_1^2-q_2^2+q_3^2 \end{pmatrix} \tag{3.32}$$

3.4.5. Kinematics and Dynamics

For clarity it is repeated that any quaternion $\boldsymbol{q}$ represents an attitude, or rotation from one frame to another, and is not expressed in either of those frames. Quaternion $\boldsymbol{q}_A^B$ thus represents a rotation from frame A to B, but is expressed in neither frame. For rotations this is quite different, as any rotation $\boldsymbol{\omega}$ is expressed both with respect to a set of axes and within a set of axes. Rotation $\boldsymbol{\omega}_A^{A/B}$ represents the rotation of axis system A with respect to B (superscript) and is expressed in system A (subscript). The following equations apply when considering rotations in multiple systems:

$$\begin{aligned}\boldsymbol{\omega}_A^{A/B} &= -\boldsymbol{\omega}_A^{B/A} \\ \boldsymbol{\omega}_B^{A/B} &= \boldsymbol{q}_A^B \cdot \boldsymbol{\omega}_A^{A/B} \cdot \left(\boldsymbol{q}_A^B\right)^{-1} = \boldsymbol{R}_A^B \cdot \boldsymbol{\omega}_A^{A/B}\end{aligned} \tag{3.33}$$

which are useful when considering the kinematics of quaternions. For the quaternion representation, the kinematics can be modelled as

$$\dot{\mathbf{q}} = \frac{1}{2}\Omega\mathbf{q} \tag{3.34a}$$

$$\Omega = \begin{bmatrix} 0 & -\omega_1 & -\omega_2 & -\omega_3 \\ \omega_1 & 0 & \omega_3 & -\omega_2 \\ \omega_2 & -\omega_3 & 0 & \omega_1 \\ \omega_3 & \omega_2 & -\omega_R & 0 \end{bmatrix} \tag{3.34b}$$

where $\boldsymbol{\omega} = (\omega_1, \omega_2, \omega_3)$ is the corresponding rotation rate of the satellite in the chosen reference frame. The corresponding rotation for $\boldsymbol{q}_A^B$ is $\boldsymbol{\omega}_B^{A/B}$ [78]. For MRP the kinematics are modelled as [13]:

$$\dot{\boldsymbol{\sigma}} = \frac{1}{4}\{(1 - \boldsymbol{\sigma}^{\boldsymbol{T}}\boldsymbol{\sigma})\boldsymbol{I}_{3\times 3} + 2[\boldsymbol{\sigma}\times] + 2\boldsymbol{\sigma}\boldsymbol{\sigma}^T\}\boldsymbol{\omega} \tag{3.35a}$$

$$[\boldsymbol{\sigma}\times] \equiv \begin{bmatrix} 0 & -\sigma_3 & \sigma_2 \\ \sigma_3 & 0 & -\sigma_1 \\ -\sigma_2 & \sigma_1 & 0 \end{bmatrix} \tag{3.35b}$$

The dynamics for both quaternions and MRPs, under the assumption of a rigid body, are described by Euler's equation [88], valid for rotations around the principle axis of the body:

$$\dot{\omega} = \boldsymbol{J}^{-\mathbf{1}} \cdot ((-\boldsymbol{\omega} \times \boldsymbol{J}\boldsymbol{\omega}) + \boldsymbol{T}_d + \boldsymbol{T}_c) \tag{3.36}$$

where $\boldsymbol{J}$ is the satellite inertia matrix, $\boldsymbol{T}_d$ represent the disturbance torques and $\boldsymbol{T}_{\boldsymbol{c}}$ the control torques. Three significant causes of disturbance torques include gravity, solar pressure and drag. The influence of solar radiation was found to be very small due to the orientation of the Envisat solar panel [64]. Furthermore, drag is highly dependent on instantaneous conditions, and including it is as likely to make the model worse as opposed to making it better [35]. Therefore only the gravity gradient torque is modelled and Euler's equation becomes:

$$\dot{\omega} = \boldsymbol{J}^{-\mathbf{1}} \cdot \left((-\boldsymbol{\omega} \times \boldsymbol{J}\boldsymbol{\omega}) + \left(3n_{Orbit}^2 \cdot \boldsymbol{r} \times \boldsymbol{J}\boldsymbol{r}\right) + \boldsymbol{T}_{\boldsymbol{c}}\right) \tag{3.37}$$

where $3n^2 \cdot \boldsymbol{r} \times \boldsymbol{J}\boldsymbol{r}$ represents the gravity gradient term, in which n is the orbital mean motion ($=\sqrt{\mu/a^3}$) and r represents the vector pointing towards Earth in the body frame. This vector can be calculated at any instant using

$$\boldsymbol{r} = \boldsymbol{q}_{\boldsymbol{RTN}}^{\boldsymbol{TBF}} \cdot \begin{bmatrix} -1 \\ 0 \\ 0 \end{bmatrix} \cdot \left(\boldsymbol{q}_{\boldsymbol{RTN}}^{\boldsymbol{TBF}}\right)^{-1} \tag{3.38}$$

since $[-1 \;\; 0 \;\; 0]$ in the RTN plane points in negative radial direction (towards Earth) by definition.

4

Methodology

This chapter is concerned with the methodology of the research. Section 4.1 shortly discusses the assumptions that were adopted in this research, followed by an examination of the expected rendezvous scenario and intended reference trajectory in Section 4.2. Section 4.3 outlines several of the expected scenarios that are likely encountered by the chaser spacecraft camera. Finally, the chapter is concluded in Section 4.4 with a list of metrics, used to evaluate the performance of the GNC system in this research.

4.1. General Assumptions

The analysis in this thesis requires a number of assumptions, which may be divided into three categories, 'Guidance and Navigation', 'Initial conditions' and 'Final conditions'.

4.1.1. Guidance and Navigation

In this first category fall assumptions about inputs to the guidance and navigation algorithm. These mainly concern time and covariance parameters. The assumptions for guidance can be summarised as

- Trajectories shall always be safe. Trajectories that include collisions are not considered in this analysis unless for a specific reason which is explicitly stated.
- Guidance shall be updated at intervals of length t_{up}. At this update new information from the navigation system is received and the OCP is re-evaluated (see Section 2.4).

The assumptions on navigation mainly concern the setup of the measurements, along with the filter covariances used to estimate the current chaser state. These assumptions can be summarised as

- The measurements shall have a noise that is characterised by a normal distribution $N(\mu, \sigma^2)$ with zero mean ($\mu = 0$) and a standard deviation as in Table 4.1. Since no elaborate research on the real-world performance of pose estimation systems is available, the values are loosely based on research by Sharma and D'Amico [22, 70, 72] and a survey by Cassinis et al. [10].
- Measurements shall be taken at an interval of $\Delta t_{\text{meas}} = 1$ seconds. This time interval is identified as a crucial parameter by Volpe et al. [91], who conclude that setting the interval too low prevents a good observability of the relative motion, as the displacement of features on the image plane between two frames is not large enough. Setting it too high would instead impact the tracking of features, and reduce the number of guaranteed matches with the model. Volpe et al. [91] select a value of $\Delta t_{\text{meas}} = 2$ s, however, their main rotation is assumed to have a magnitude of 0.721 deg/s, which is much lower than the expected main rotation of Envisat (= 3.5 deg/s) adopted in this research (see Section 2.2). Therefore a value of 1 s is assumed more realistic for the faster spin rate.

Table 4.1: Levels of measurement accuracy. Provided numbers are 1-σ values used, to generate the measurements from a standard deviation $N(\mu,\sigma)$ with $\mu = 0$. Standard deviations σ_r and σ_q represent position and attitude respectively.

Level of Accuracy	Abbreviation	σ_r (m)	σ_q (deg)
High 1	High_1	0.05	0.50
High 2	High_2	0.10	1.00
Moderate 1	Mod_1	0.50	3.00
Moderate 2	Mod_2	1.00	4.00
Moderate 3	Mod_3	1.50	5.00
Low / Fail	Low	5.00	15.00

- Measurements taken during a period decreased performance of the pose estimation system are assumed to have a standard deviation of

$$\sigma_{\text{pos}} = 5 \quad \text{m}$$
$$\sigma_{\text{att}} = 15 \quad \text{deg}$$

  These values are considered large enough to prevent any useful information for the navigation filter, which is the intended effect of the period of decreased pose estimation performance.

- Measurement feedback, under nominal operation conditions, is provided in the form of measurement covariance. The value of this covariance is equal to σ^2. Exceptions to this are presented in Section 4.3, as scenarios may arise where the feedback is not statistically accurate.

4.1.2. Initial Conditions

The initial conditions for all scenarios are as summarised in Table 4.2, unless specifically stated otherwise.

Table 4.2: Initial conditions. r and v describe the relative state of target and chaser, while q and ω describe the target initial attitude and rotation.

Parameter	Value	Unit
$\boldsymbol{r}_0$	(-34.454, 82.729, 46.329)	m
$\boldsymbol{v}_0$	(0.045, 0.072, 0.039)	m/s
$\boldsymbol{q}_0$	(0.911; -0.244; -0.086, -0.322)	-
$\boldsymbol{w}_0$	(0.5, 0.5, 3.5)	deg/s

This is consistent with a position on a closed relative orbit defined by the ROE: $a\delta a = a\delta\lambda = 0$, $a\delta\boldsymbol{e} = 50$, $a\delta\boldsymbol{i} = 60$ with phase angles $\varphi, \vartheta = 0^o$ (see Section 3.3.3) and argument of longitude $u = 42$ degrees. Furthermore, $\boldsymbol{q}_0$ is consistent with a tilt angle between spin-axis and orbit normal of 30 degrees (see Section 2.2).

4.1.3. Final Conditions

The final position of the optimal manoeuvre in phase 2 of the rendezvous process (see Section 4.2) shall be at the intersection of the target spin-axis with its KOS. As such, an estimate of the location of the spin-axis at t_f is required, where t_f is the final time at the end of the optimal manoeuvre. This estimate shall be made using Equation (3.37), assuming uncertainties of the inertia matrix $\boldsymbol{J}$ as inTable 2.1. The current navigation estimate of $\boldsymbol{\omega}_{TBF}^{TBF/RTN}$ and $\boldsymbol{q}_{TBF}^{RTN}$ shall be used as initial conditions for the intrgration of Equation (3.37).

4.2. Reference Trajectory

The intended reference trajectory was already shortly highlighted in Section 2.1 and is further elaborated upon in this section to clarify some assumptions, definitions and constraints. Section 2.1 described the trajectory, consisting of three parts. For each part a short description is provided, stating the guidance methods that are expected to be used during the respective phases.

- **PHASE 1: Passive Observation, no translational guidance, pointing only.** The first phase consists of observing the target from a passively safe orbit, such as discussed in Section 3.3.4. This phase allows the

navigation filter to converge, such that it can supply more accurate data about the attitude dynamics of the target in the RTN frame. One full orbit is assigned for this phase, to accommodate filter convergence and the target dynamics.

During this manoeuvre the camera on the chaser satellite should be continuously pointed at the target satellite, requiring a form of forced attitude guidance. No translational guidance is applied in this phase, as the orbit is passively safe and closed.

- **PHASE 2: Alignment with spin-axis, optimal guidance, pointing only.** The second phase consists of aligning the position of the chaser satellite with the spin-axis of the target satellite. The starting point of this phase is the position of the satellite on the closed orbit from phase 1 and the final point is the expected intersection of the spin-axis with the target KOS at t_f, the end of the optimal manoeuvre.

  This phase starts with a short period of observation of 150 seconds, to provide time for the navigation filter to converge after the eclipse period during which no measurements were possible. Subsequently, the optimal guidance algorithm, discussed in Section 5.1, is used to calculate a fuel efficient trajectory for aligning the chaser with the target spin-axis at a distance determined by the KOS. This trajectory is updated with new information every t_{up} seconds. Similar to phase 1, the camera should be continuously pointed at the target satellite. As discussed in Section 2.1 this phase ends on the KOS of Envisat. The KOS radius will be discussed in Section 5.1.2 and Section 5.1.6, and its value is set to 25 m.

  The total time for the optimal manoeuvre is restricted to the illuminated time in a single orbit which, in the case of the Envisat, is approximately 4000 seconds, approximately two thirds of the orbital period. According to Volpe [89] the optimal manoeuvre time for a similar scenario lies around $0.22T$ - $0.25T$, where T represents the orbital period. With T at 6030 seconds, a total manoeuvre time of 1300-1500 seconds is calculated, and a value of 1500 s is selected for the total manoeuvre time in phase 2.

- **PHASE 3: Approach along spin-axis, forced guidance, pointing and synchronisation.** In this final phase the chaser approaches the Envisat along the spin-axis, as determined by ESA [5]. During this phase the chaser satellite is guided by forced guidance, where the path of the satellite is determined from the rotation of the target, as will be shown in Section 5.1.7. To minimise the risk of collision the approach velocity is constrained to a constant value of 5 cm/s during this phase.

  This phase shall end at a distance of 5 meters from the CoM of the target. At this point the chaser satellite is at a distance of 3.7 meters of the target. The final approach requires a different approach to navigation (feature tracking instead of pose estimation) and likely incorporates different guidance and control algorithms that can safely control the spacecraft when the robotic arm [5] is deployed. As the chaser shall cover a distance of 20 meters towards the target with a relative imposed velocity of 5 cm/s, the forced manoeuvre is expected to last approximately 400 seconds.

The entire approach is thus expected to last less than 2000 seconds, as the optimal manoeuvre lasts 1500 seconds and the forced approach is expected to last 400 seconds, together occupying 1900 seconds. The reference trajectory described above is visualised in Figure 4.1.

4.3. Typical Error

In a real scenario the measurement errors are influenced by the inter-satellite distance, position of the camera with respect to the sun and the background of images [10]. This means that trajectories that exhibit a constant measurement accuracy are not likely, but nevertheless they are useful as means of analysis. Using a constant measurement accuracy allows to clarify the effects of error magnitude on the navigation and guidance systems. Unless specified otherwise, the measurement standard deviation, σ_r/σ_q, is constant, both during the nominal part of the trajectory as well as during the periods of failure (see Table 4.1). This section discusses the magnitude of typical errors. The words 'failure' and 'decreased performance' are used interchangeably and both refer to a decrease of the accuracy in the pose measurements.

4.3.1. Short periods of high error

The first subset of scenarios that is likely to be encountered is a set where the measurement error is very high over a short period of time. This could be caused by particular situations in which the reflection of sunlight on the target is such that it creates a lot of noise in the images. Other examples are found in difficult or ambiguous orientations of the target spacecraft with respect to the camera, or partial visibility of the target,

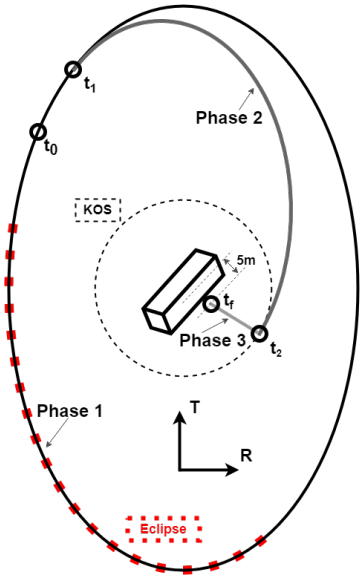

Figure 4.1: Reference trajectory with three phases. Time difference between t_0 and t_1 exceeds one orbital period.

both creating difficulties for the pose estimation system. All these situations are linked to specific orientations of the target with respect to the camera. This means that, considering the relatively fast rotation of 3.5 deg/s, these situations are expected to only last for a short amount of time, as the rotation would cause these undesirable orientations to disappear rapidly.

Sharma and D'Amico [73] show that, although pose estimation architectures provide an excellent mean error value and achieve sub-meter and sub-degree accuracy, scenarios can be found where no pose estimate is available or where the pose estimate fails to converge. In such special cases the measurement errors easily exceed 5m in position and 30 degrees in attitude. Kisantal et al. [34] report similar findings from a competition with 50 teams, where excellent mean values are achieved, however, errors are easily increased for special scenarios.

The subset of scenarios with high errors shall therefore be applied over short periods of 30-120 seconds. Furthermore these periods shall be introduced at different instants at the beginning, middle and end of the manoeuvre to evaluate the robustness of the guidance algorithm with respect to these periods of decreased performance. As specified in Table 4.1, σ_r/σ_q in these periods of failure have a value of 5 m and 15° respectively.

Measurement feedback

The measurements of a real pose estimation system are supplied with a feedback metric, the measurement covariance. The measurement covariance, in a nominal case, takes the value of the square of the standard deviation, however, the pose estimation will not always provide an accurate measure of the covariance. Therefore, three types of feedback are considered, which are named 'true', 'optimistic' and 'pessimistic' feedback. As no quantitative data about this feedback measure was found, the numbers presented for optimistic and pessimistic feedback are based on assumptions.

True feedback

The first type of feedback is called 'true feedback' and represents the statistically perfect feedback. This means that when the artificial measurement is generated with a standard deviation of σ = 1.5 m, the measurement covariance that is returned by the pose estimation system has a value of σ^2 = 2.25m.

Pessimistic feedback

In addition to the true feedback, cases might arise where the measurement covariance is either too high or too low. In the first case the measurements are undervalued and the navigation thinks that the measurement is less accurate than it is in reality. This will be called 'pessimistic feedback'. Using the same example as before, when an artificial measurement is generated from a statistical distribution with standard deviation σ = 1.5 m,

the pessimistic measurement covariance that is returned by the pose estimation system has a value of (5~15 $\sigma)^2 > \sigma^2$.

Optimistic feedback

In some scenarios the opposite happens, and measurements are overvalued. This means that the measurement is thought to be accurate while, in reality, the measurement is not accurate at all. This will be called 'optimistic feedback'. Again using the same example of an artificial measurement with σ = 1.5m, the optimistic measurement covariance that is returned by the pose estimation system has a value of (0.1~0.5 $\sigma)^2 < \sigma^2$.

This overvaluation of measurements is not expected to happen for more than 1 or 2 images at a time. For this reason the previously determined period of 30-120 s is reduced to a very short period of 1-3 s for the optimistic feedback case.

How the optimistic and pessimistic type of feedback may be caused in a real-world scenario is demonstrated by Sharma and D'Amico [70, 74], shown in Figures 4.2 and 4.3. These figures show that probabilities are assigned to possible poses. In specific cases, there is a possibility for the pose estimation to be considered high confidence while, in reality, the agreement between the model and the target is bad, demonstrated in Figure 4.2. In other cases the pose estimation is considered low confidence while, in reality, the agreement between the model and the actual orientation is very good, demonstrated in Figure 4.3.

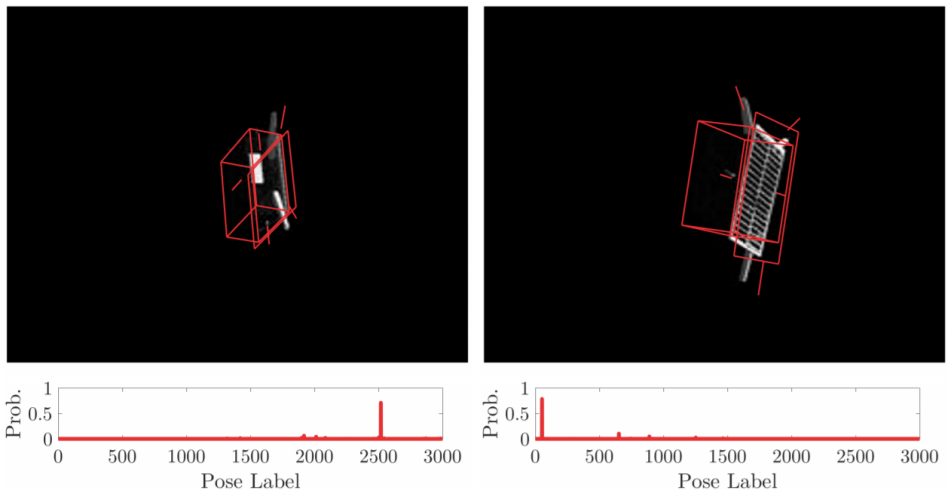

Figure 4.2: A montage of a few images with high confidence pose solutions [74]. From the images it becomes clear that the fitted model (red) does not always match the satellite orientation well. However, in both cases the pose estimation system has assigned a high confidence pose estimate, as a single orientation is identified as the most probable orientation (pose label) with a high probability. This might lead to the system overvaluing the measurements, resulting in optimistic feedback.

4.3.2. Long periods of moderate error

The second subset of scenarios is composed, including those scenarios where the measurement error is consistently at a moderate level over a longer period of time. This could be caused by situations where a specific undesirable orientation of the target and chaser spacecraft is maintained for an extended period of time. Examples of such situations may be found when Earth is in the background of the image for a long time, or when the sun is in front of the camera, rather than behind it. These situations, even though they should be avoided whenever possible, are sometimes imposed through the geometry of the mission and should therefore be carefully analysed to evaluate their effects on the guidance algorithm. An example of a situation that is imposed by the mission geometry is when the spin-axis would be aligned with the +r-direction of the RTN frame. This alignment would cause Earth to be in the background of the images for a relatively long period of time in phase 3, as the orientation of the spin-axis can not be influenced.

Sharma et al. [75] show that in many of these cases a high confidence pose estimate is not available and a low confidence estimate is the best that can be achieved. The authors report error values with a norm of approximately 1 m for position and 5 to 10 deg for attitude. These errors were reported for cases where Earth was in the background or cases in which the camera experienced sub-optimal lighting conditions.

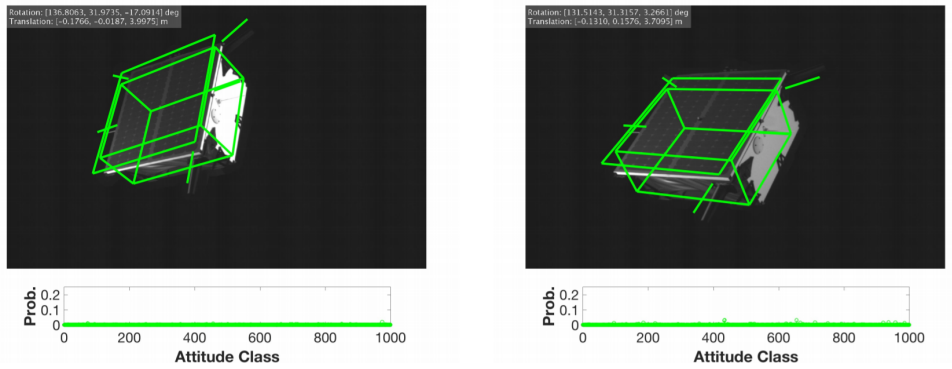

Figure 4.3: A montage of a few images with low confidence pose solutions [70]. The images show that the fitted model (green) is in relatively good agreement with the satellite orientation. However, in both cases the pose estimation system fails to identify a single orientation (attitude class) that matches the model and low probability is assigned to the full range of possible orientations. This results in the system undervaluing the measurements, resulting in pessimistic feedback.

The errors in this subset of scenarios are characterised by a zero mean and standard deviation as described by the moderate cases in Table 4.1. These errors shall be applied over the length of the entire manoeuvre to evaluate the robustness of the guidance algorithm with respect to these errors.

4.4. Performance Metrics

This section shortly discusses the metrics used to measure the performance of the guidance system as well as that of the GNC system as a whole.

4.4.1. Delta V

The ΔV is separated into open-loop and closed-loop ΔV, where the open-loop ΔV represents the estimate made by the guidance system, while the closed-loop ΔV resembles the total control effort in the simulated real-world environment. Open-loop ΔV is representative of the performance of the guidance system, while closed-loop ΔV measures the overall performance of the entire GNC architecture, being more dependent on navigation and control than on guidance.

Open-loop ΔV is computed using an integral. This integral can be evaluated for $t_0 \rightarrow t_f$, which represents the estimate total ΔV for the trajectory, and is the classical definition of open-loop ΔV. However, the integral can also be evaluated over a shorter interval $t \rightarrow (t + t_{up})$. In this context, t_{up} is the time interval at which the guidance algorithm re-evaluates the near-optimal trajectory to make a new estimate. This evaluation over a period of length t_{up} is named piece-wise ΔV, as it is evaluated over a small piece of the optimal trajectory.

Closed-loop ΔV does not have this distinction. The control effort is calculated at every step based on the current difference between the estimated navigation state and the desired guidance state. The closed-loop ΔV can be summed over any time interval to obtain an estimate of the total. The most important difference between the closed-loop and open-loop ΔV values is that the open-loop value presents a prediction, while the closed-loop value reports a result.

4.4.2. Errors

Three types of errors are identified as useful metrics for analysing the performance of the GNC system. These are schematically represented in Figure 4.4.

Guidance Error

The guidance error is defined as the vector norm of the 3D difference between the true chaser state and the desired, guided, spacecraft state. This metric shows the ability of the control system to follow the reference trajectory plotted by the guidance system, as well as the reference attitude. The lower the guidance error, the closer the chaser follows the intended trajectory and the closer it is to a truly optimal trajectory. The guidance error is a direct result of the navigation error and the ability of the controller.

Navigation Error

The navigation error is defined as the vector norm of the 3D difference between the true spacecraft state and the estimated spacecraft state provided by navigation. Although this error is part of the navigation system

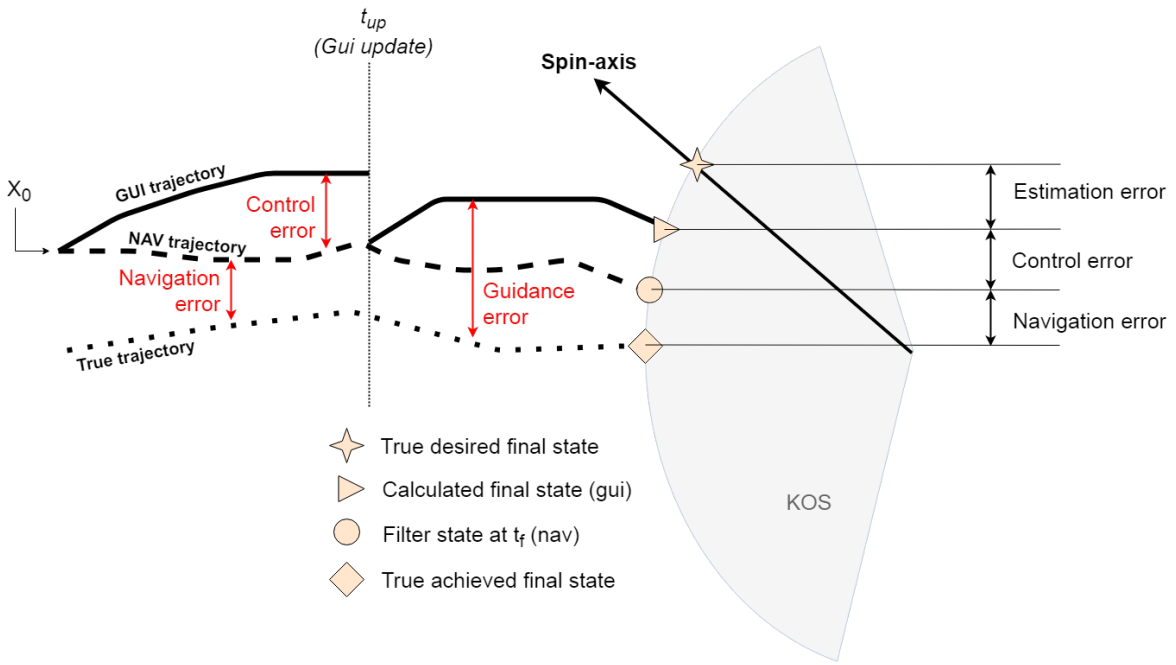

Figure 4.4: Types of error to be analysed. The total final position is built of three components: the navigation error, the control error and the estimation error. The estimation error is a measure of how accurately the guidance system estimates the final desired state using Equation (5.9) and is caused by errors in the estimation of target rotation and inertia.

only, which is not the focus of this work, this metric is very useful for visualising the source of specific errors. As the navigation is the only system receiving input from the real-world, the accuracy of the state estimate can often be directly linked to the performance of the complete GNC system.

Control Error

The control error defines how well the controller is able to align the navigation state with the guidance state. If the control error is zero, this means that the difference between the satellite on-board, estimated, navigation state and the desired guidance state is zero. This is the case when the guidance trajectory is updated at $t = t_{up}$. At this update, the current navigation state is used as a set of initial state constraints, from which a near-optimal trajectory is calculated.

Final position error

The final position error is defined as the norm of the 3D difference between the intended final state and the true final state. As can be seen in Figure 4.4, this error is the sum of the guidance error and an estimation error. The guidance system tries to make an estimate of the intended final state using integration of the currently estimated target attitude dynamics over the remaining manoeuvre time, a process that necessarily introduces some error due to uncertainties in $\boldsymbol{\omega}$ and $\boldsymbol{J}$. The final position error can thus be visualised as the sum of two components. First, the error that the guidance system makes in estimating the correct final state and, second, the guidance error at t_f. These two components could theoretically be in the same or opposite direction, either reinforcing or counteracting each other.

The estimation error on the final state, as in Figure 4.4, is also used as a performance metric. This metric is a good indicator of expected guidance performance, although its complexity requires a more elaborate examination, which is provided in Chapter 7.

5

The GNC Framework

5.1. Guidance

The guidance laws applied in this work are of the type 'Model Predictive Control' [81], as introduced in Section 2.4. This type of guidance law is based on the repeated evaluation of the Optimal Control Problem (OCP), with the current state as initial conditions for the OCP. In this type of guidance a cost function is minimised and the chaser is controlled to follow a resulting optimal trajectory. Once the control effort has been established and a new position is reached, the optimal trajectory is re-evaluated and the OCP is solved again, repeating the process. This approach lends itself very well to pose estimation, as the navigation state is continuously refined through the processing of new images, allowing more optimal trajectories. The OCP approach can be mathematically exploited through either a linear or a non-linear method.

5.1.1. Algorithm Selection

This section discusses the selection and working principles of the guidance algorithm. The choice for a non-linear model is discussed, presenting a short comparison between linear and nonlinear models along with a short analysis of how both models work, what the benefits and drawbacks are and why a nonlinear method was selected as most viable option.

Linear guidance: Theory

Linear methods usually contain a degree of simplicity which allows these methods to be used for a wide range of problem to produce general solutions. Despite the fact that linear mathematics produces simpler computations than non-linear mathematics, and the theory of linear mathematics is richer, there are computationally efficient solutions for both linear and non-linear problems. The choice for linear optimization is usually made due to its simple formulation and analysis and not because of the computational effort [47].

A linear guidance method, suitable for optimal rendezvous, is demonstrated by Breger et al. [9]. It defines the final state as a linear combination of all earlier states and control inputs. Mathematically this means that motion is defined by a linear system written as

$$\boldsymbol{x_{k+1}} = \boldsymbol{A}^{k}_{k+1}\boldsymbol{x}_k + \boldsymbol{B}_k\boldsymbol{u}_k \tag{5.1}$$

where k represents the instant in time, $\boldsymbol{x}$ represents the state, $\boldsymbol{A}^{k}_{k+1}$ is the STM from Equation (3.14), $\boldsymbol{B}_k$ is the system response to inputs (Equation (3.15)) and $\boldsymbol{u}_k$ is the control/perturbing input. This way any future state $\boldsymbol{x}_k$ is simply a linear combination of the $\boldsymbol{A}$, $\boldsymbol{B}$ and $\boldsymbol{u}$ matrices and can be written as [9]

$$\boldsymbol{x}_k = \boldsymbol{A}^0_k + \boldsymbol{\Gamma}_k \begin{bmatrix} \boldsymbol{u}_0 \\ \vdots \\ \boldsymbol{u}_{k-1} \end{bmatrix} \tag{5.2}$$

where $\boldsymbol{\Gamma}_k$ is a convolution matrix, defined as

$$\boldsymbol{\Gamma}_k = \begin{bmatrix} \boldsymbol{A}^0_{k-1}\boldsymbol{B}_k & \boldsymbol{A}^0_{k-2}\boldsymbol{B}_k & \cdots & \boldsymbol{A}^0_1\boldsymbol{B}_k & \boldsymbol{B}_k \end{bmatrix} \tag{5.3}$$

An example cost function J can be formulated as

$$J = \sum_{i=0}^{N-1} ||\boldsymbol{u}_i||_1 \tag{5.4}$$

If the aim is to minimise the fuel consumption, which is proportional to the control effort ΔV, this cost function can be minimised and the optimal control is given by the set of values for $\boldsymbol{u_i}$ that minimise this cost function

$$J^* = \underset{\boldsymbol{u}_0 \cdots \boldsymbol{u}_{N-1}}{min} \sum_{i=0}^{N-1} ||\boldsymbol{u}_i||_1 \tag{5.5}$$

Nonlinear guidance: Theory
The demonstration of a non-linear method, suitable for the intended optimal rendezvous, is performed by Ventura et al. [86], using the CWH equations Equation (3.13) as a basis. These equations are reorganised to define the control effort as

$$u_x = \ddot{x} - 3n^2 x - 2n\dot{y} \tag{5.6a}$$

$$u_y = \ddot{y} + 2n\dot{x} \tag{5.6b}$$

$$u_z = \ddot{z} + n^2 z \tag{5.6c}$$

The trajectory components x, y, z are parameterized as polynomials which, according to Ventura et al. [86], are both light in terms of computational effort and approach the shape of optimal trajectories very well compared to other parameterization such as B-splines, Hermite polynomials or Bezier curves. The parameterization should have at least 5 free coefficients, to allow constraining the trajectory with the initial and final position and velocity and retaining one free parameter for optimization [86]. This sets the minimal polynomial degree $N = 4$. On the other hand, to avoid oscillations at the edges of the time interval, typical of high-order polynomials, the order should be limited to $N \leq 8$ [45]. The trajectory components are defined as

$$x(t) = \sum_{j=0}^{N} \alpha_{x,j} t^j \tag{5.7a}$$

$$y(t) = \sum_{j=0}^{N} \alpha_{y,j} t^j \tag{5.7b}$$

$$z(t) = \sum_{j=0}^{N} \alpha_{z,j} t^j \tag{5.7c}$$

where t represents the time, α represents the parameters of the trajectory and $4 \leq N \leq 8$. Derivatives of these functions are easily obtained to find $\dot{x}, \dot{y}, \dot{z}$ and $\ddot{x}, \ddot{y}, \ddot{z}$. All these can then be substituted into Equation (5.6) to express the control effort in each direction as a function of the coefficients α.

The cost function is defined as an integral over the total manoeuvre time to find the total control effort. The cost function J is defined as:

$$J = \min \int_{t_0}^{t_f} \sqrt{u_x^2 + u_y^2 + u_z^2} \tag{5.8}$$

Choice for Non-linear Guidance
Linear methods usually offer a simplicity in the definition of the problem [47], along with possible computational benefits. However, multiple formulations of objectives and constraints in 3D space are such that the linear problem might not be simply defined at all.

When the cost function in Equation (5.5) is examined, it can be observed that the absolute value or 1-norm of the control effort is analysed. This is, however, not a linear property and requires a re-formulation of the problem. The introduction of a set of modified parameters and additional constraints is required, which allows the optimization problem to be rewritten in the following way [92]:

Linear:	*Non-linear:*
$\min \lvert u \rvert \rightarrow \min u'$	$min \lvert u \rvert$
$u < u'$	
$-u < u'$	

where u' is a newly introduced shadow parameter which is substituted for the real control effort in the optimization process. Every step of the optimization process thus requires twice the amount of variables and produces six (two in every thrust direction) inequality constraints. This tends to slow the linear optimization algorithm significantly when the size of the problem is increased [50]. Non-linear methods do not suffer from this problem as both the 1-norm, as well as the 2-norm, can be directly incorporated into the algorithm as non-linear properties.

Another drawback of the linear method is in the formulation of the safety constraint. This constraint is defined by a spherical region around the target, which is nonlinear. This again requires a re-formulation of the constraint in the linear case. The equivalent of the sphere in a linear setting is a cube, which can be defined around the target as a series of planes. Breger et al. [9] apply the so-called 'Big M' method to constrain the state to lie outside a region through the use of binary variables [66]

Linear:	*Non-linear:*
$\vec{\boldsymbol{x}}_t \leq \bar{b}_t + M\boldsymbol{y}_t$	$\lvert\lvert \vec{\boldsymbol{x}}_t \rvert\rvert \leq \bar{b}_t$
$\lVert \boldsymbol{y}_t \rVert_1 \leq m-1$	

where m is the length of $\boldsymbol{y}_t$, $\vec{\boldsymbol{x}}_t$ is the chaser state at instant t, b_t is the constraint value, $\boldsymbol{y}_t$ is a vector whose elements are either 0 or 1 and M is a large number on the scale of $\boldsymbol{x}$. This method works by relaxing, at most, all but 1 of the avoidance constraints. This effectively means that the algorithm checks that at least one of variables x, y or z is larger than a reference value (e.g. r_{KOS}), ensuring collision avoidance.

The consequence of this method is that it requires the additional optimization of binary vector $\boldsymbol{y}_t$, adding three additional parameters to the optimization at each time step. Another consideration to be made is that the linear method is more restrictive than its nonlinear equivalent, as a cube rules out a larger amount of the 3D space compared to a sphere. As linear optimization algorithms usually approach their constraint boundaries and find solutions that lie on these boundaries [39] this is considered a degradation of the optimality of the algorithm.

A minor drawback of the non-linear method is that the optimization of the trajectory is aimed at optimising the $3 \cdot (N+1)$ scalar parameters that define the shape of the trajectory and is thus decoupled from the physical parameters x, y, z. Also the constraints are not automatically evaluated at each time step, but rather the time steps at which the constraints shall be evaluated must be determined prior to the optimization process. The choice of this time step influences the computational efficiency of the optimization process, as it determines the total amount of constraint evaluations that are performed.

Considering the drawbacks of the linear method listed above and the small differences in computational efficiency between linear and nonlinear methods [47], the choice was made to employ a nonlinear guidance algorithm, based on the algorithm presented by Ventura et al. [86].

5.1.2. Constraints

The manoeuvre in phase 2 is limited by a number of constraints, which need to be considered in the optimization. Three types of constraints can be listed, from different sources:

Initial and final state

The first set of constraints stems from the initial (measured) and final (desired/calculated) state of the chaser spacecraft. The need for these constraints is obvious, as the trajectory has to start from the initial position of the chaser, with the corresponding velocity, both which are fully determined by the position on the closed orbit or phase 1. The trajectory also has to end at a specific position relative to the target, aligned with the target spin-axis, again with a corresponding velocity, both which are defined by the rotational motion of the target. These constraints can be written in general form as

$$\boldsymbol{r}(t_0) = \boldsymbol{r}_0 \tag{5.9a}$$
$$\dot{\boldsymbol{r}}(t_0) = \dot{\boldsymbol{r}}_0 \tag{5.9b}$$
$$\boldsymbol{r}(t_f) = \boldsymbol{r}_f = r_{\text{KOS}} \cdot \frac{\boldsymbol{\omega}_f}{|\boldsymbol{\omega}_f|} \tag{5.9c}$$
$$\dot{\boldsymbol{r}}(t_f) = \dot{\boldsymbol{r}}_f = \boldsymbol{r}_f \times \boldsymbol{\omega}_f \tag{5.9d}$$

where $\boldsymbol{r}(t)$ is the relative position vector at time t, t_0 and t_f represent the initial and final time of the optimal manoeuvre, r_{KOS} is the radius of the Keep-Out-Sphere and $\boldsymbol{\omega}_f$ is the rotation $\boldsymbol{\omega}_{RTN}^{TBF/RTN}(t_f)$. The third sub-equation from Equation (5.9) imposes that the final position is located along the target spin-axis. This results in a total of 12 constraints, which need to be adapted to fit the formulation of the optimization. The formulation of these constraints immediately raises the need for an accurate estimation of the final rotational motion of the target spacecraft.

As already shortly discussed in Section 5.1.1, these constraints are imposed by fixing the values of four coefficients, $\alpha_{\ldots,0}, \alpha_{\ldots,1}, \alpha_{\ldots,N-1}, \alpha_{\ldots,N}$ in each of the three sub-equations of Equation (5.7). For the coefficients in x this results in [86]:

$$\alpha_{x,0} = x_0 \tag{5.10a}$$
$$\alpha_{x,1} = \dot{x}_0 \tag{5.10b}$$
$$\alpha_{x,N} = \frac{x_f - \sum_{j=0}^{N-1} \alpha_{x,j} t_f^j}{t_f^N} \tag{5.10c}$$
$$\alpha_{x,N-1} = \frac{\dot{x}_f - \sum_{j=0}^{N-2} j\alpha_{x,j} t_f^{j-1} - N\alpha_{x,N} t_f^{N-1}}{(N-1)\, t_f^{N-2}} \tag{5.10d}$$

where N is the degree of parameterization and the subscript $\ldots_f$ references to the value at the end of the optimal manoeuvre. Similarly the coefficients for y and z can be calculated.

Thrust

The thrust constraint is the result of the physical limitations of the thrusters on board of the chaser spacecraft. For obvious reasons these can only deliver a finite amount of thrust, which is limited by the specifications of the selected thruster. The constraint can be expressed simply as

$$-\boldsymbol{u}_{max} \leq \boldsymbol{u} \leq \boldsymbol{u}_{max} \quad \rightarrow \quad \sqrt{\boldsymbol{u}^2} \leq \sqrt{\boldsymbol{u}_{max}^2} \tag{5.11}$$

where $\boldsymbol{u}$ represents the control thrust. This assumes symmetric thruster configuration and an equal amount of thrust possible in all directions, both positive and negative. Based on the ESA baseline for the Clean Space Initiative the chaser spacecraft will receive 12 (+12 redundant) 22N thrusters, meaning a total of 44N of thrust in each direction nominally [4].

Safety

The third subset of constraints can be obtained from the need for safety during the rendezvous operation. Safety during the optimization can be achieved in two ways. The first is by defining a classical Keep Out Sphere (KOS), which defines a single region (sphere) around the target. Second, a Keep Out Coat (KOC) around the target vehicle might be used, which defines multiple regions around the target body that should be avoided. Both have clear advantages and disadvantages:

Keep Out Coat

Following the approach by Volpe et al. [90] the KOC can defined mathematically as a superellipsoid

$$h(\boldsymbol{x}) = \left(\frac{x - x_c}{a}\right)^{n_1} + \left(\frac{y - y_c}{b}\right)^{n_2} + \left(\frac{z - z_c}{c}\right)^{n_3} - 1 \tag{5.12}$$

where x_c, y_c and z_c are the coordinates of the ellipsoid centre, a, b and c are the semi-lengths of the ellipsoid axes and n_1, n_2 and n_3 describe a degree of curvature along that axes. This function returns zero if evaluated

on the surface of the ellipsoid and a negative or positive number if evaluated respectively inside or outside the solid. The safety zone can be completely adapted to the target's shape and multiple ellipsoids can be defined to cover different parts of the target body. A single function $l(\boldsymbol{x})$ can be obtained by multiplying the functions of all different hyper-ellipsoids. By imposing that for every point on the trajectory this functions returns a positive value, it is ensured that the chaser never enters the KOC and thus safety is ensured.

Keep Out Sphere

The Keep Out Sphere is more easily defined and is simply a sphere with radius r_{KOS} centred in the target CoM. This sphere is mathematically formulated as

$$x^2 + y^2 + z^2 = r_{KOS}^2 \tag{5.13}$$

and by imposing that the chaser position $\boldsymbol{r} = (x, y, z)$ is always outside of this sphere, safety is assured. This sphere shall have a radius >19 meters, since the tip of the solar panel is approximately 19m from the CoM. A visualisation of the KOS and KOC is presented in Figure 5.1.

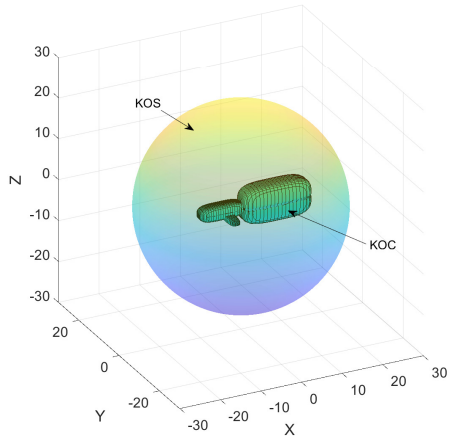

Figure 5.1: KOS with radius 25m versus KOC with $n_1 = n_2 = n_3 = 4$ (see Equation (5.12)). The KOC parameters a,b,c and x_c,y_c,z_c were chosen such that the KOC is at a distance of 0.5 m around the Envisat body.

Trade-off KOS and KOC

Whereas the KOS assumes a fixed final distance from the target (equal to the radius of the sphere) the KOC allows the shape to be completely adapted to the target body, which allows the safety surface to be defined at as little as 1~3 meter from the target body. The choice for KOC or KOS is therefore particularly relevant in the phase of the approach when the optimal guidance is used. If the spacecraft is delivered to a location closer to the target in the second phase, a lesser amount of forced motion is required in the subsequent final phase. Since forced motion is not optimal, considering that it completely ignores natural orbital dynamics, any reduction of the final distance to the target at the end of the optimal trajectory thus reduces the total ΔV, as will be shown in Section 5.1.6.

There is however a drawback in the choice for KOC. Since the ellipsoid is tailored to the target body it needs to be defined in the target body frame. The constraint is formulated as

$$h\left(\boldsymbol{R}_{RTN}^{TBF}\vec{\boldsymbol{x}}(t)\right) > 0 \tag{5.14}$$

with the function $h()$ as in Equation (5.12). $\boldsymbol{R}_{RTN}^{TBF}$ is the rotation matrix from the RTN frame to the target body-fixed frame and $\boldsymbol{x}(t)$ is the chaser state at time t. As becomes immediately clear from Equation (5.14), accurate knowledge of the target attitude is required for all future times up to the final time t_f. Considering the accuracy of the attitude estimation discussed in Section 2.4.1, uncertainties in estimated rotations and uncertainties in the estimate of the target inertia, it is highly unrealistic to assume an accurate attitude estimate over an extended period of time.

Since Envisat extends approximately 19 meters from its CoM to the tip of its solar panel, attitude uncertainties of merely 10 degrees would already cause the estimated location of the tip of the solar panel to contain an error of 3 meters. Considering that expected attitude uncertainties could easily exceed 10 degrees, the KOC is considered unsafe and would introduce significant risk of collision. In space, usually safe missions are preferred over optimal missions, and for this reason the KOC is discarded as a safety constraint, considering the current capabilities of pose estimation systems. Instead, a KOS is selected with a radius of 25 meters, allowing a 5m uncertainty in the position error, which is not expected to occur at this distance. It also allows for some tolerance in the final position estimate of the guidance algorithm. The KOS only requires an estimate of the CoM of the target, which is usually of high accuracy, as explained in Section 2.4.1.

5.1.3. Dependence on initial conditions

In order to demonstrate the volatility of the optimization with respect to the initial conditions, Figure 5.2 shows the result of 100 optimisations for the initial conditions described by Table 4.2, to a final Cartesian state $\boldsymbol{X}_f$ = [0.5 24.98 0.5 0 0 0]. For each run a small amount of uniformly distributed random noise with a magnitude of 1 or 10 cm (position) and 1 or 10 mm/s (velocity) was added to the initial conditions.

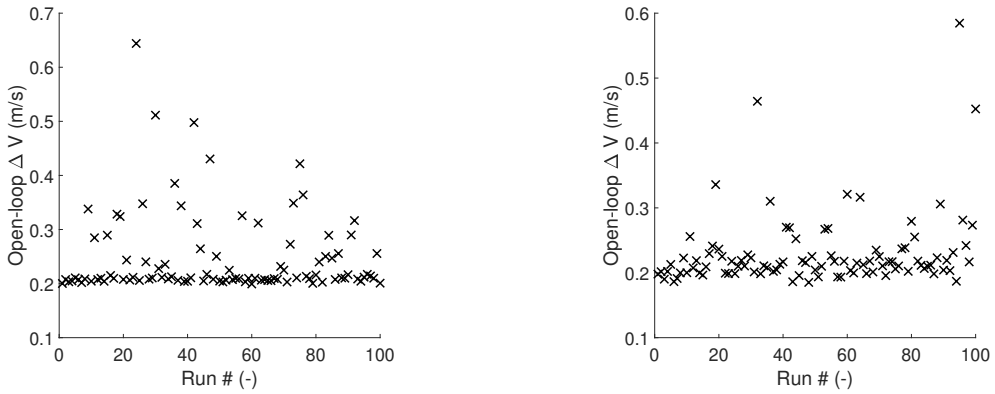

(a) Magnitude of random noise: 1 cm, 1 mm/s.

(b) Magnitude of random noise: 10cm, 1 cm/s

Figure 5.2: Open-loop ΔV values for 100 runs of an optimization process. The initial and final conditions for all runs are the same, but have a small amount of random noise.

Figure 5.2 shows that the vast majority of the runs obtains a satisfactory value for the open-loop ΔV and, therefore, a near-optimal trajectory. However, a small portion of runs fails to converge correctly, for the specific combination of initial and final conditions. The magnitude of the noise makes little difference, except that Figure 5.2 suggests that there is better agreement on the optimal value for smaller magnitude. This failure to converge results in an unacceptable ΔV value, sometimes more than 300% of the optimal value. In order to prevent the satellite from following this trajectory, a mitigation strategy must be implemented.

In order to prevent such a failure to converge from happening, the trajectory shall be evaluated at least 3-5 times shortly before the approach, when situated in the passively safe observation orbit. This process will provide a baseline value for the expected open-loop ΔV and prevent the satellite from following a non-optimal trajectory. When starting the manoeuvre, the ΔV of the current trajectory should be compared to the baseline and if the value is within ±10% of the baseline, the approach may be initiated. This margin ensures the rejection of truly non-optimal trajectories, while allowing some margin for the near-optimality of the optimization process and navigation errors.

Ventura et al. [86] show that the optimisation procedure is a computationally expensive process and therefore it is undesirable to evaluate the trajectory 3-5 times at every trajectory update. Instead, the expected open-loop ΔV for the current estimate shall be compared to the previous estimate. Theoretically, as the spacecraft gradually gets closer to the target, the expected remaining open-loop ΔV should always decrease. If the expected ΔV therefore increases by more than 10% after the update, compared to before the update, the new estimate shall be rejected and the satellite shall continue to follow the previously estimated reference trajectory. Again this margin will ensure rejection of truly non-optimal trajectories, while allowing some margin for near-optimality and navigation errors.

5.1.4. Degree of Parameterization

As discussed in Section 5.1.1, the degree of parameterization, N, should be between 4 and 8. The performance of the algorithm in terms of optimality (ΔV) and computing time is assessed for different degrees of parameterization N = 4, 5, 6 and 7. The performance was evaluated for a total of 13 different runs with initial points on a reference orbit with ROE (Section 3.3.3) $a\delta\alpha$ = [0 0 -40 0 -50 0], equally spaced over intervals of 500 seconds. The final conditions were fixed in a point along the target spin-axis at 25m from the target and the same for all trajectories. The results are presented in Figure 5.3.

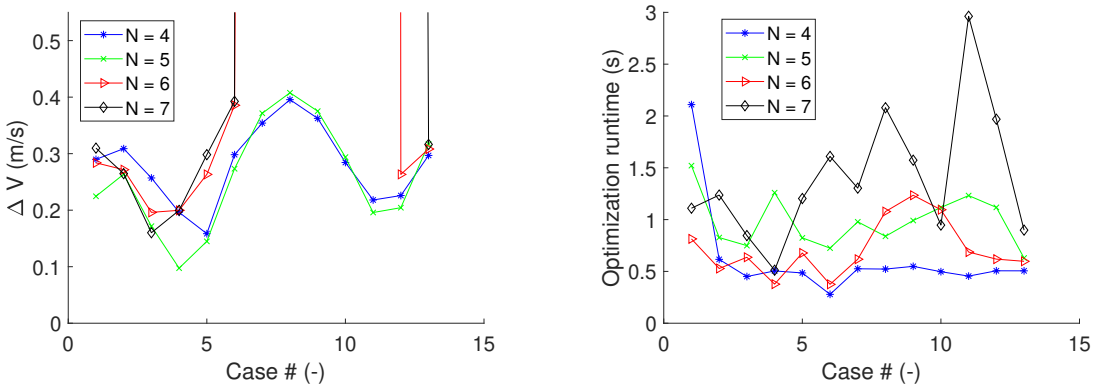

(a) Open-loop ΔV

(b) Runtime of the optimization

Figure 5.3: Performance for 13 different scenarios for 4 degrees of parameterization N = 4,5,6,7. t_f = 1000s.

First of all, Figure 5.3 shows that the optimal ΔV is correlated with the initial position. Second, more relevant to this analysis, the results show that the degree of parameterization, together with the total manoeuvre time, plays a large role in the ability of the guidance to converge. When examining Figure 5.3b it can be seen that there are no clear differences between the curves for N = 4, 5, 6 and 7, which hints at a failure to converge for the higher values of N. Only the curves of N = 4 and N = 5 show a clear distinction, where the run time for N = 5 is slightly larger than for N = 4. This lack of convergence for the cases where N = 6,7 is most likely related to MATLAB's floating-point accuracy (eps), which is fixed at $eps = 2^{-52}$ or $eps = 2.2204e^{-16}$.

It was shown in Section 5.1.2 that the parameters $\alpha_{...,N}, \alpha_{...,N-1}$ are fixed by the final conditions. The restricting elements for the convergence are then the coefficients $\alpha_{...,N-2}$, which are multiplied with t_f^{N-2}. If the value of t_f^{N-2} is too large, the algorithm is unable to take sufficiently small steps of $\alpha_{...,N-2}$ to provide convergence. It is easy to make an estimate of the required floating point accuracy for $\alpha_{...,N-2}$ by looking at the values of t_f^{N-2}. Table 5.1 shows the value of t_f^{N-2} for N = 4, 5, 6 and 7, from which it can be observed that especially for N = 6,7 the value for t_f^{N-2} is so large that it is almost the same magnitude as $1/eps \approx 4.5e^{15}$. At this point the step size for optimization becomes an issue for the algorithm and it often fails to converge as could be observed in Figure 5.3.

Table 5.1: t_f^{N-2} for t_f = 200, 500, 1000, 1500 and $4 \leq N \leq 7$.

N-2	t_f			
	200	500	1000	1500
2	$4.0e^4$	$2.5e^5$	$1.0e^6$	$2.3e^6$
3	$8.0e^6$	$1.3e^8$	$1.0e^9$	$3.4e^9$
4	$1.6e^9$	$6.3e^{10}$	$1.0e^{12}$	$5.1e^{12}$
5	$3.2e^{11}$	$3.1e^{13}$	$1.0e^{15}$	$7.5e^{15}$

If the step size is indeed the problem, the algorithm should be able to converge better for smaller manoeuvre times t_f, which was also assessed. The results are presented in Figure 5.4.

From Figure 5.4 it can be observed that for lower t_f indeed the higher degrees of parameterization are better able to converge. A clear distinction is present in the run times of the curves with N = 4, 5 and 6, with Figure 5.4b showing a clear increase in the run time from N = 4 to N = 5 to N = 6. The case with N = 7 still shows a run time that hints at a lack of convergence, which is further supported by the ΔV values in the case

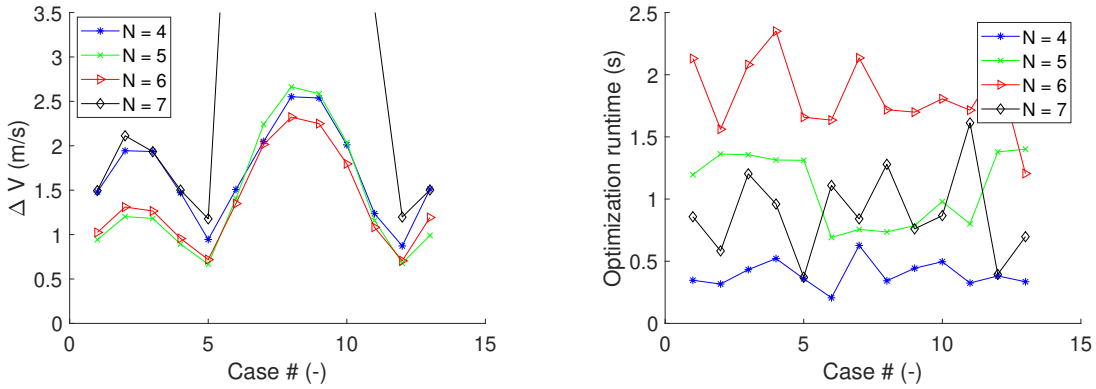

(a) Open-loop ΔV

(b) Runtime of the optimization

Figure 5.4: ΔV and runtime for 13 scenarios and 4 degrees of parameterization N = 4,5,6,7. t_f = 150s.

of $N = 7$, which are worse than for $N = 4$.

The conclusions that can be drawn from Figures 5.3 and 5.4 are twofold. The first is that the algorithm performance in terms of ΔV can improve significantly when moving from $N = 4$ to $N = 5$. The increase in efficient from $N = 4$ to $N = 5$ can be witnessed both in Figure 5.3a as well as Figure 5.4a, especially for specific ranges of the initial conditions (Cases # 1 - 5).

The second conclusion is that for very low values of t_f the parameterization with $N = 6$ does not offer clear benefits over $N = 5$, while the parameterization with $N = 7$ still fails to converge in the first place. From Figure 5.4a it becomes clear that increasing N to 6 does not further improve the ΔV by much, despite that Figure 5.4b indicates that the runs have converged properly. The computational effort required for the evaluation however still increases when moving to $N = 6$, also visible in Figure 5.4. The lack of convergence for the case where $N = 7$ might be partially caused by the tendency of higher order polynomials to exhibit large oscillations near the constraint boundaries, which was listed by Liu et al. [45] as the main reason to keep $N < 8$.

Considering both these conclusions it is decided to employ a parameterization of degree $N = 5$ in this thesis work, similar to Ventura et al. [86] and Volpe and Circi [90]. This also allows to keep using the manoeuvre time of 1500 seconds established in Section 4.2.

5.1.5. Update interval

The parameter t_{up} was introduced in Figure 2.7 and represents the interval at which guidance uses the information from navigation to recompute the OCP described by Equation (5.8). This interval, at which the guidance estimate is updated and the trajectory is re-evaluated, has already been analysed by Volpe et al. [90], whose findings are summarised in Table 5.2. The parameter t_{up} represents the time between two guidance updates.

Table 5.2: Final, mean and maximum guidance errors and ΔV for different trajectory update times [90]. The case where $t_{up} = 0$ implies that the trajectory is only calculated once, at the beginning of the manoeuvre.

t_{up} (s)	Final error (m)	Mean error (m)	Maximum error (m)	ΔV
0	0.250	0.748	1.061	0.261
20	0.088	0.170	0.302	0.356
40	0.092	0.170	0.380	0.338
60	0.077	0.200	0.437	0.337
80	0.205	0.235	0.547	0.328
100	0.281	0.276	0.664	0.328

Table 5.2 shows that decreasing the time between updates yields a higher accuracy (lower error) and slightly increases ΔV. It can also be noticed that the accuracy does not increase anymore for update times smaller than 60 seconds. Although the actual error values highly depend on the accuracy achieved by the navigation system, a clear trend can be derived. Opposed to Volpe et al. [90], the optimal manoeuvre of phase 2 is not the

end of the total approach. Because of this, position errors can still be corrected in the subsequent phase and therefore the efficiency (ΔV) is valued higher than the final error. Because of this it is decided to employ an update time t_{up} of 100 seconds. This allows the guidance to be efficient and safe whilst relieving the chaser of some computational effort.

5.1.6. Distance to Target

A final consideration for the guidance algorithm is the final distance to the target. In ESA's original mission design a KOS with 50m radius was considered [17]. This would require the chaser to synchronise with the target spin-axis at a distance of 50m and approach the target from there. This is however far from an optimal solution in terms of efficiency. Figure 5.5 shows the optimal, forced-motion and total ΔV plotted against the final distance of the optimal manoeuvre.

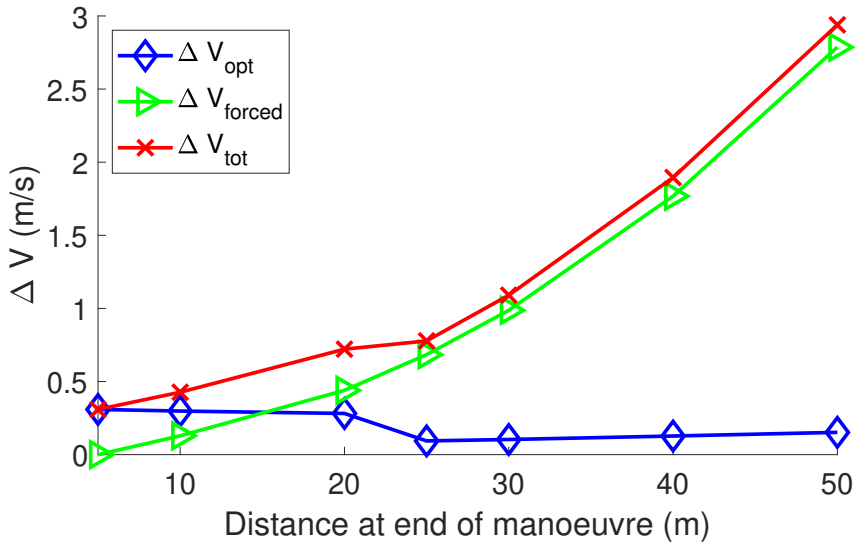

Figure 5.5: Total approach ΔV for various final distances at the end of the optimal manoeuvre.

It becomes very clear from Figure 5.5 that a final position as close to the target is desired. The ΔV of the final forced-motion approach along the spin-axis seems to increase steadily when the distance of this approach increases. This causes the total ΔV to be almost completely determined by ΔV_{forced} for values of $R_{KOS} >$ 20m.

From the viewpoint of efficiency the KOC would thus be valued over the KOS, as discussed in Section 5.1.2 and confirmed by Figure 5.5, provided that the accuracy of the target attitude estimation for future time steps is high enough. Since this is not the case, the KOS is selected and the radius of the KOS is a driving factor in the efficiency of the manoeuvre. As discussed previously in Section 5.1.2 a value > 19m is required at all times. Considering the accuracy of the pose estimation and a margin for safety, a value of 25m is selected for the KOS and the guidance shall aim at a point 25 meters from the Envisat CoM.

5.1.7. Phase 3 Forced Guidance

The final part of the rendezvous trajectory, outlined in Section 4.2, is the third phase which requires the chaser to approach the target along the spin-axis. The rotational velocity of the target $\boldsymbol{\omega}_{RTN}^{TBF/RTN}$ is estimated by the navigation filter and can be used by the guidance to calculate the desired position, similar to the third sub-equation of Equation (5.9), using current distance $r(t)$ in the equation instead of r_{KOS}.

In this phase the distance towards the target is evaluated at every step. Next a desired relative velocity is selected, in the case of this thesis V_{rel} = 0.05m/s or 5 cm/s. This is deemed a safe velocity for approach, small enough to avoid collision. Also it is sufficiently larger than the magnitude of the error on the navigation velocity estimate, enabling the navigation filter to provide a good estimate of the difference between the current en desired velocities. The desired state at any time t, where the start of phase 3 is t = 0, is calculated using

$$\begin{cases} \boldsymbol{r}_t &= \left(||\boldsymbol{r}_0|| - V_{rel} \cdot \delta t_{p3}\right) \cdot \frac{\boldsymbol{\omega}_{tar}}{||\boldsymbol{\omega}_{tar}||} \\ \boldsymbol{v}_t &= (\boldsymbol{\omega}_{tar} \times \boldsymbol{r}_t) - V_{rel} \cdot \frac{\boldsymbol{\omega}_{tar}}{||\boldsymbol{\omega}_{tar}||} \end{cases} \tag{5.15}$$

where $\boldsymbol{\omega}_{\text{tar}}$ is $\boldsymbol{\omega}_{RTN}^{TBF/RTN}$ and δt_{p3} is the time that has passed since the start of the third phase

5.1.8. Attitude Guidance

Finally, the attitude of the spacecraft needs to be properly guided throughout the entire manoeuvre. In the first two phases the attitude guidance is limited to pointing the camera towards the target CoM, while the third phase also requires the rotational motion to be synchronised with the target. The following two sections outline the calculation of the reference attitude, made by the guidance system, for both cases, while the control laws to follow these reference orientations are presented in Section 5.3.

Camera pointing

During the first two phases the pointing of the chaser camera towards the target CoM should be ensured at all times, to allow the camera to take images, required for generating the pose estimate. This can be achieved simply by using the information about the relative position. If $\boldsymbol{r} = (x, y, z)$ is the relative position between the chaser and target in the target RTN-frame, then the required rotation matrix to point the camera (aligned with the +z axis of the chaser body frame) towards the target CoM, while pointing the +y-axis of the CBF frame 'down' in the image frame, can be written as

$$\boldsymbol{R}_{\text{Cam}} = \boldsymbol{R}_{RTN}^{CBF} = \boldsymbol{R}_{RTN}^{CBF} = \boldsymbol{R}_2(\psi)\boldsymbol{R}_1(\varphi) \tag{5.16a}$$

$$\boldsymbol{R}_2 = \begin{bmatrix} cos(\psi) & -sin(\psi) & 0 \\ sin(\psi) & cos(\psi) & 0 \\ 0 & 0 & 1 \end{bmatrix} \tag{5.16b}$$

$$\boldsymbol{R}_1 = \begin{bmatrix} 1 & 0 & 0 \\ 0 & cos(\varphi) & -sin(\varphi) \\ 0 & sin(\varphi) & cos(\varphi) \end{bmatrix} \tag{5.16c}$$

with φ and ψ the relative azimuth and elevation angles of $\boldsymbol{\rho}$. Those are computed as

$$\varphi = \arcsin\left(\frac{z}{||\boldsymbol{r}||}\right) - 90^o \tag{5.17a}$$

$$\psi = \arctan\left(\frac{y}{x}\right) - 90^o \tag{5.17b}$$

$\boldsymbol{R}_{\text{Cam}}$, which functions as $\boldsymbol{R}_{RTN}^{CBF}$, can then be used to define $\boldsymbol{q}_{RTN}^{CBF}$, which is in turn to be controlled by the attitude controller presented in Section 5.3. In order to mitigate the singularity present in this control law, the desired rotations of the chaser body can additionally defined as [90]:

$$\boldsymbol{\omega}_{CBF}^{CBF/RTN} = \boldsymbol{R}_{RTN}^{CBF} \cdot \begin{bmatrix} 0 \\ 0 \\ \dot{\psi} \end{bmatrix} + \boldsymbol{R}_1(\varphi) \begin{bmatrix} \dot{\varphi} \\ 0 \\ 0 \end{bmatrix} \tag{5.18}$$

where $\dot{\varphi}$ and $\dot{\psi}$ are computed as derivatives of Equation (5.17)

$$\dot{\varphi} = \frac{\dot{z}\rho - z\dot{\rho}}{\sqrt{\rho^4 - \rho^2 z^2}} \tag{5.19a}$$

$$\dot{\psi} = \frac{\dot{y}x - y\dot{x}}{x^2 + y^2} \tag{5.19b}$$

Near the singularity of the control law, $\boldsymbol{\omega}_{CBF}^{CBF/RTN}$ can be used instead of $\boldsymbol{q}_{RTN}^{CBF}$ by using Equation (3.36) to compute the torque from the difference between the current and desired value of $\boldsymbol{\omega}_{CBF}^{CBF/RTN}$. This is sufficiently accurate for the short time interval over which the singularity is expected to occur.

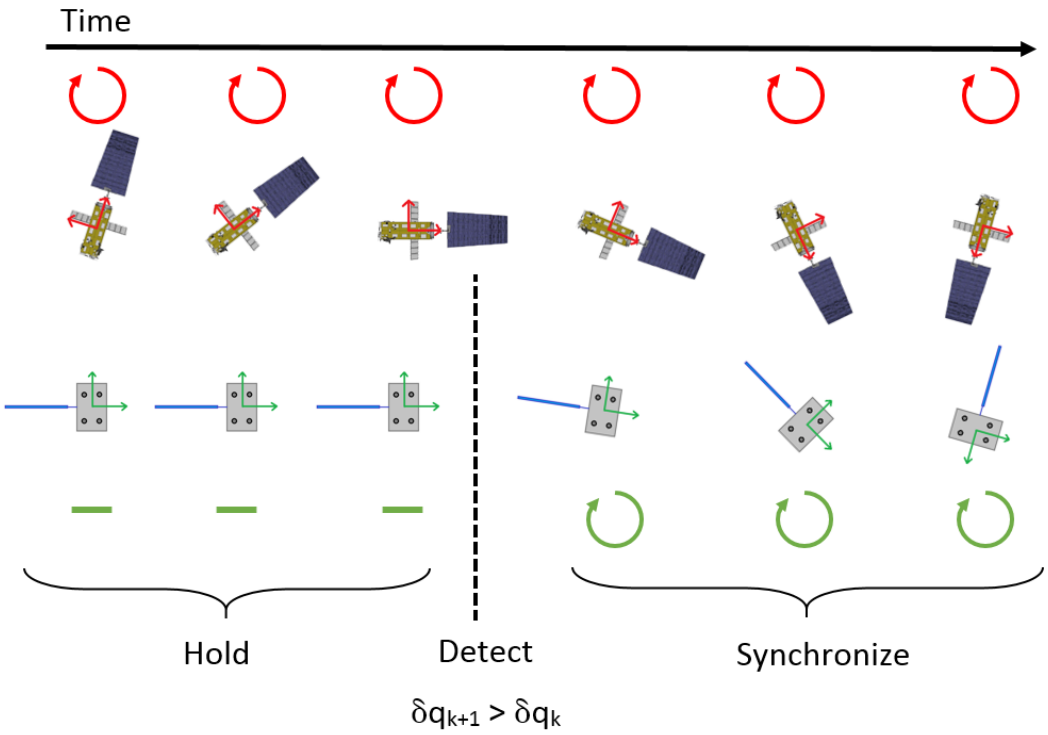

Figure 5.6: The rotation synchronisation process, showing the target rotation (top,red) and chaser rotation (bottom, green). The chaser holds a non-rotating state until the target reference axes are aligned with the chaser's. When this point is detected, the chaser increases its rotation to match that of the target.

Synchronising rotation

During the third phase the rotational motion of the chaser should be aligned with the spinning of the target. The synchronisation consists of two separate phases. First a 'hold phase', in which the chaser waits for the target to reach a specific reference state before initiating the 'synchronisation phase' in which the chaser increases its own rotation to match the target rotation. This process is visually demonstrated in Figure 5.6.

As explained in Section 2.3, the synchronisation means a parallel alignment of the x-axes and anti-parallel alignment of the y- and z-axes of the CBF and TBF system. This means a change of variables with respect to the control law in phase 2, where only the camera was pointed. Rather than using $\boldsymbol{q}_{RTN}^{CBF}$ as a reference, a change of variables is implemented and instead $\boldsymbol{q}_{CBF}^{TBF}$ is used as a reference.

This results in a required relative quaternion $\boldsymbol{q}_{CBF}^{TBF}$ = [0 0 1 0], which is the unit quaternion representing a y-axis rotation with a 180^o angle. As will be shown in Section 5.3 the selected attitude controller contains a singularity at $q_0 = 0$ and therefore a new coordinate system, CCBF, is introduced. This CCBF system is simply the result of a rotation of the CBF coordinate system around its own y-axis with an angle of 180^o. By using this simple convention, the desired relative quaternion becomes $\boldsymbol{q}_{CCBF}^{TBF}$ = [1 0 0 0], the identity quaternion, staying far away from the control law singularity. The current value of $\boldsymbol{q}_{CCBF}^{TBF}$ can be calculated from $\boldsymbol{q}_{RTN}^{CBF}$, estimated by the ADCS system on the chaser, $\boldsymbol{q}_{TBF}^{RTN}$, estimated by the navigation filter, and $\boldsymbol{q}_{CBF}^{CCBF}$ = [0 0 1 0]. The detection point in Figure 5.6 is detected by evaluating $\delta\boldsymbol{q}$, which is the multiplication of the current $\boldsymbol{q}_{CCBF}^{TBF}$ with the inverse of the desired value ([1 0 0 0]). When $\delta\boldsymbol{q}$ has reached a minimum and starts to increase, the chaser immediately takes action and the synchronisation process is set in motion.

The benefit of this approach is that it allows for a specific final relative orientation, which is convenient in the case of robotic capture. Any value for $\boldsymbol{q}_{CCBF}^{TBF}$ can be selected, as long as camera pointing is considered and $q_0 \neq 0$. The main downside of this method is that the camera is not pointed perfectly at the target as the spin-axis is not perfectly aligned with the Envisat z-axis, while the camera is aligned with the CBF z-axis. As long as the main rotation is much larger than the wobbling amplitude, which is predicted for Envisat (see Section 2.2), this is not expected to be a problem.

5.2. Navigation

5.2.1. Artificial Measurements

In a pose estimation framework the relative position and attitude are directly obtained from the images or via pseudo-measurements, obtained from the images, as outlined in Section 2.4.1. Relative velocity and rotation are estimated from position and attitude over time. Due to the lack of availability of a pose estimation system, no real pose estimation is used in this work, and instead the measurements are artificially generated. Therefore, an attempt shall be made to resemble a real-world scenario as closely as possible. When considering a nominally operating pose estimation system, measurement noise is mainly dependent on three aspects:

- Distance to the target
- Camera orientation
- Lighting/viewing conditions

each of which is discussed separately. Measurement errors will be referred to by ε_r for position and ε_q for rotation.

Distance to target

The distance to the target is an important parameter when considering vision-based pose estimation systems. For an object with a fixed size, the distance fully defines how large the object is in the image frame. If the object is too small the pose estimation process will yield unsatisfactory results, as shapes are not clearly distinguishable. Similarly the accuracy of the pose estimate decreases if the object is too large, and only partially visible. At this point the edges and corners cannot be fully detected anymore and fall outside of the image.

The most reliable estimate of the relationship between target size, distance to target and error magnitude was created by Sharma and D'Amico [22], obtained through validation with images from the PRISMA mission. Their estimate of this relationship is visualised in Figure 5.7, which expresses the expected error as a function of the ratio of inter-satellite distance and target size.

In Figure 5.7, three methods were presented by the authors, respectively Newton-Raphson (N-R), POSIT and ePnP. The N-R method was found to be slow, the POSIT method less robust to Gaussian noise and the ePnP method unreliable at large inter-satellite distances [71]. All three methods thus have their own deficiencies, and the choice is made to select the least accurate method as a reference. When the expected error of the ePnP is approximated by a linear model, a slope of approximately 3/45 can be extracted, as shown by the lines that were drawn in Figure 5.7. This means a 3%, or 3^o, error for a distance/size ratio of 45. In this respect, the size of the Envisat satellite is a clear advantage. Since the orientation of the solar panel is unknown, the size of Envisat without the solar panel (10 m) is used in the calculation of measurement error. A quick calculation then provides the expected error for selected inter-satellite distances, summarised in Table 5.3.

Table 5.3: Initial guess of expected pose estimation error, based on Envisat body size (10m) and Figure 5.7.

Distance (m)	1σ (m)	1σ (^{o})
10	0.01	0.07
25	0.04	0.17
50	0.17	0.33
100	0.67	0.67
150	1.50	1.00
250	4.18	1.67
500	16.65	3.33

The estimation in Table 5.3 follows a somewhat parabolic distribution for position. The estimated error for attitude, however, is rather optimistic. Considering a camera field-of-view of 25~30 degrees, the maximum virtual width of the image plane is calculated by

$$w_v = d_{is} \cdot \tan(30^o)$$

where w_v is the virtual width of the image and d_{is} is the inter-satellite distance. At a distance of 100 meters, the image plane would represent a width of 60m, of which the Envisat would only fill a relatively small part

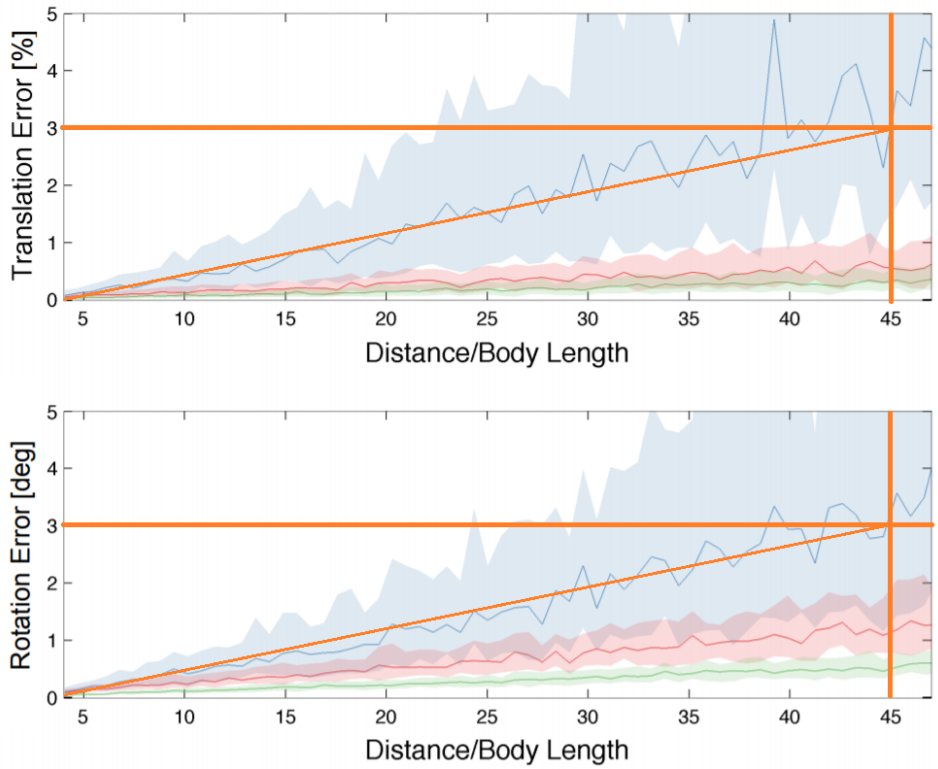

Figure 5.7: Expected accuracy for three different image processing algorithms, respectively Newton-Raphson (green), POSIT (red) and ePnP (blue) [71]. The orange diagonal line represents a line with slope 3/45 and serves as a linear estimate of the performance of the worst performing method, ePnP (blue).

considering its dimensions (see Section 2.2). At a distance of 500m the image width would represent 290 meters and Envisat would be only be several pixels on the image. The possibility to perform a highly accurate attitude estimation (in the order of 3^o, as suggested by Table 5.3) would be highly unlikely. This is confirmed by attitude errors found in studies by Sharma et al. [70, 72], which show that when the spacecraft fills a considerable part of the image, it would still be optimistic to assume only 3.33 degrees of error.

Using the same reasoning, and considering the same field-of-view of 25~30 degrees, features of the Envisat body would start disappearing from the image as soon as the inter-satellite distance decreases beyond approximately 20 meters. This leads to the formulation of a quadratic formula to describe the expected error. For position

$$\begin{cases} r > 20m & \sigma_r = \frac{16.65}{500^2} \cdot r^2 \\ r \leq 20m & \sigma_r = \frac{0.5}{15^2} \cdot (r-20)^2 + \frac{16.65}{500^2} \cdot 20^2 \end{cases} \tag{5.20}$$

and for attitude

$$\begin{cases} r > 20m & \sigma_q = \frac{30}{250^2} \cdot r^2 \\ r \leq 20m & \sigma_q = \frac{5}{15^2} \cdot (r-20)^2 + \frac{30}{250^2} \cdot 20^2 \end{cases} \tag{5.21}$$

The resulting expected errors, modelled using Equations (5.20) and (5.21), are presented in Table 5.4. These errors are considered more representative for real-world scenarios under nominal viewing conditions.

Lighting conditions

Second, the noise level in the camera can be modelled according to the lighting conditions, which are almost fully determined by the sun. As there have been no clear results published on this topic, several assumptions are required for modelling the behaviour of noise under various sun condition. The following assumptions are made:

- *The angle of the sun-vector with the camera boresight vector (sun-camera angle) is the largest indicator of the noise.* For small values of this angle the light source is positioned directly behind the camera.

Table 5.4: Modelled pose estimation error based on Envisat size and Figure 5.7.

Distance (m)	1σ (m)	1σ (^{o})
5	0.53	5.19
10	0.25	2.41
25	0.04	0.30
50	0.17	1.20
100	0.67	4.80
150	1.49	10.80
250	4.16	30.00
500	16.65	120.00

When this angle increases, the probability increases that one or more surfaces on the target spacecraft are completely shaded and not (completely) visible to the camera. This is expected to increase the overall noise level since it could easily lead to ambiguities in the pose estimation process as discussed in [22]. The greater the sun-camera angle, the larger the probability of the spacecraft being partially or completely shaded, decreasing the expected accuracy of the pose estimation. The sun-camera angle is mathematically defined as the following dot product

$$\chi_{\text{cam}} = \hat{\boldsymbol{r}}_{\text{Sun}} \cdot \hat{\boldsymbol{r}}_{\text{Rel}} \tag{5.22}$$

where χ_{cam} is the sun-camera angle, defined by the dot product of $\hat{\boldsymbol{r}}_{\text{Sun}}$, the sun unit vector in the orbital frame, with $\hat{\boldsymbol{r}}_{\text{Rel}}$, the unit vector describing the position of the chaser with respect to the target in the orbital frame.

- *The behaviour of the error level follows a sinusoidal curve.* The magnitude of the error is expected to follow a sinusoidal pattern. The error is expected to only slowly develop for small sun-camera angles, and increase more rapidly when angles are around 90^o. At 90^o, the sun orientation changes from 'behind' the camera to 'in front of' the camera, which is expected to cause significant additional shadowing on the target. When the sun-camera angle is already large, additional growth is not expected to introduce more error. This behaviour is consistent with the development of a standard sine wave from -90 to +90°.
- *No additional noise is expected when the sun-camera angle < 1/2 FoV angle.* When the sun-camera angle is smaller than half of the camera Field-of-View (FoV) angle, the sun is in an ideal position and no additional noise is expected. Therefore, noise is modelled with a standard deviation of zero in this range.
- *The camera is unable to provide images when sun-angle > (180-FoV angle).* At this point the sun could enter directly into the camera field of view. This is highly undesirable as the intensity of direct sunlight could potentially damage hardware in the camera. Therefore, the camera shall enter a protective mode in which it is unable to provide any measurements. Such situations should be avoided, since all ability for relative navigation is lost.

These assumptions lead to the following algebraic formulation of the normalised sun-noise magnitude

$$\begin{cases} \chi < \frac{FoV}{2} & \sigma_{sun} = 0 \\ \frac{FoV}{2} \leq \chi \leq 180 - FoV & \sigma_{sun}(\chi) = 0.5 \cdot \sin\left(\frac{2\pi}{c_1} \cdot \chi + c_2\right) + 0.5 \\ \chi > 180 - FoV & \sigma_{sun} = 1 \end{cases} \tag{5.23}$$

where χ again represents the sun-camera angle and c_1, c_2 are two coefficients that ensure

$$\sigma_{sun}(\frac{FoV}{2}) = 0$$
$$\sigma_{sun}(180 - FoV) = 1$$

Figure 5.8 shows the expected, normalised, standard deviation (1σ) of the noise, with respect to the sun-camera angle, based on the assumptions. Several sun-camera angles are highlighted, such as the 90^o, which

has a normalised 1σ value of ~0.6, meaning that at an angle of 90^o, 60% of the total sun-noise is added to the measurements.

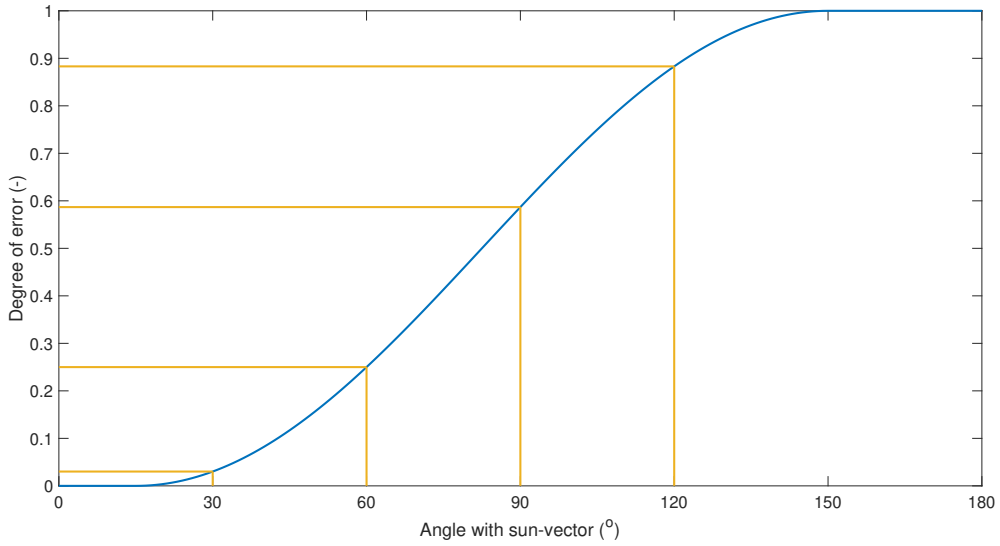

Figure 5.8: Expected normalised magnitude of the error introduced by the sun-camera angle. FoV is assumed to be 30°.

This only leaves the modelling of the total sun noise. The total position sun-noise is assumed 3 meters (1σ). This is enough to theoretically place an object at the other side of Envisat. This assumption is slightly conservative, since position errors would usually be expected at sub-meter level, especially close to the target, however, it is consistent with currently expected worst-case errors from pose estimation systems [21, 22, 72]. The attitude noise is decided to be 20 degrees (1σ), which similarly is consistent with the expected errors.

Camera orientation

Finally, it is a property of monocular cameras that noise in the boresight direction is always larger than the noise perpendicular to this direction, due to the depth ambiguity that arises when using a single monocular camera [56]. A realistic error model has to consider this ambiguity, and appropriately scale the noise that is introduced onto the measurements.

It is necessary to first define the direction of the camera axis. The guidance law requires the camera to point at the target, determining the orientation of the chaser in the RTN frame, $\boldsymbol{q}_{RTN}^{CBF}$. Since the camera boresight axis is assumed to be aligned with the CBF z-axis (see Section 2.3), the noise can be modelled in the CBF frame using the z-axis as boresight axis. The errors can be translated to the RTN-frame using $\boldsymbol{q}_{RTN}^{CBF}$.

There is no clear data available about the noise ratio between boresight axis and the other two axes. Therefore, the assumption is made that error along/around the boresight axis is three times larger than along/around the other two axes. Based on research by Sharma and D'Amico [70, 72] this ratio of 3/1 is a conservative estimate, as ratios as small as 10/1 are reported in some cases, while a ration of 3/1 preserves larger errors in the directions perpendicular to the boresight axis.

The boresight factor is included as a final step. To preserve the magnitude of σ_t, a boresight model is used that multiplies σ_t with vector

$$b_c = \begin{bmatrix} 0.3 \\ 0.3 \\ 0.9 \end{bmatrix} \rightarrow \qquad |b_c| = 0.995. \tag{5.24}$$

Since $|b_c| \approx 1$, the total noise around the three axes of the *CBF*-frame, $\boldsymbol{\sigma}_{CBF}$, defined by

$$\boldsymbol{\sigma}_{\text{CBF}} = \sigma_t \cdot b_c \tag{5.25}$$

has the same magnitude as the original σ_t. The total noise level σ_t is determined from the distance to the target and the lighting conditions.

This depth ambiguity is not expected to affect the noise on the attitude measurements. During the pose estimation process a 3D model is used to fit points on the image, which is expected to cancel any orientation bias. This is confirmed by Sharma and D'Amico [72], who report attitude errors of similar magnitude around all axes.

Total noise

The total noise is calculated from a Gaussian distribution, $N(\mu,\sigma)$, with zero mean ($\mu = 0$). The total standard deviation of the noise σ_t is computed using

$$\sigma_{\mathrm{t,CBF}} = \left(\sqrt{\sigma^2_{\mathrm{distance}} + \sigma^2_{\mathrm{sun}}}\right) \cdot b_c \tag{5.26}$$

where $\sigma_{\mathrm{distance}}$ is calculated from Equation (5.20) (position) or Equation (5.21) (attitude), σ_{sun} is calculated from Equation (5.23) multiplied with a factor 3 (position) or 20 (attitude), as previously discussed, and b_c as in Equation (5.24). Figure 5.9 shows the total obtained 1σ values of the artificial measurements for both position and attitude. The total sigma value, σ_t is referred to as σ_r when position measurements are concerned and σ_q when attitude is concerned.

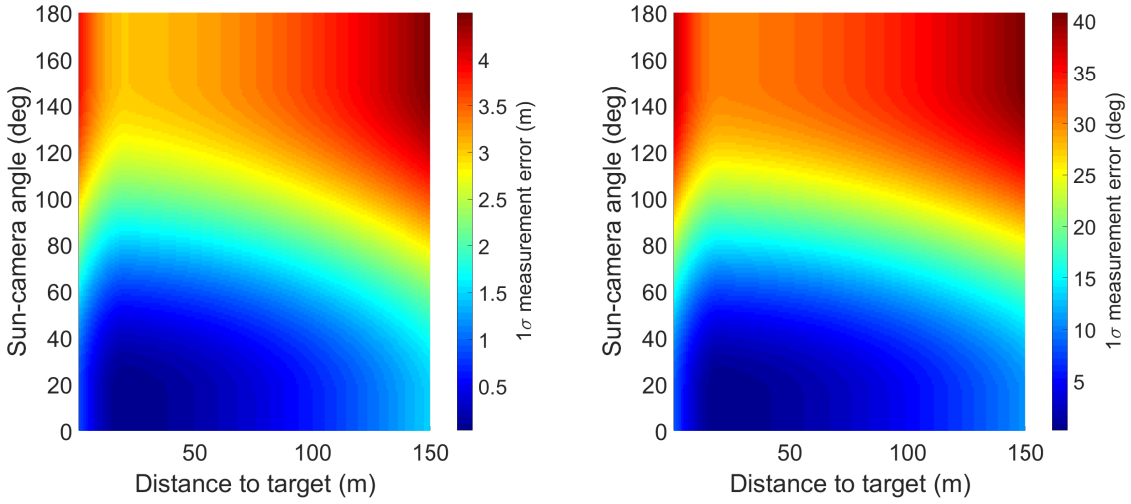

Figure 5.9: Color plot of total 1σ measurement noise σ_t for combined influences of inter-satellite distance and sun-camera angle for position (left) and attitude (right).

Position

The standard deviation around the three axes of the *CBF*-frame is calculated by applying Equation (5.25). The elements of the measurement error vector $\boldsymbol{\eta}_{\mathrm{CBF}}$ are found from a Gaussian distribution

$$\boldsymbol{\eta}_{\mathrm{CBF},i} \in N(0, \boldsymbol{\sigma}_{\mathrm{CBF},i}) \qquad i = 1,2,3$$

Finally, the vector containing the measurement errors in the *RTN*-frame, $\boldsymbol{\eta}_{\mathrm{RTN}}$, is found as in Equation (3.25)

$$\boldsymbol{\eta}_{\mathrm{RTN}} = \boldsymbol{q}^{\mathrm{RTN}}_{\mathrm{CBF}} \otimes \boldsymbol{\eta}_{\mathrm{CBF}} \otimes \left(\boldsymbol{q}^{\mathrm{RTN}}_{\mathrm{CBF}}\right)^{-1} \tag{5.27}$$

Attitude

Using the total noise and a random axis of rotation $\hat{\boldsymbol{n}}$, an error quaternion can be defined from Equation (3.21). The axis $\hat{\boldsymbol{n}}$ is a unit vector, defined using uniformly distributed random values on the interval [-1 1]. The angle of rotation θ is found from a Gaussian distribution:

$$\theta \in N(0, \sigma_\mathrm{t})$$

The error quaternion is calculated by inserting $\theta, \hat{\boldsymbol{n}}$ in Equation (3.21), and the resulting error quaternion is called $\boldsymbol{q}_\eta$.

The measurement
The measurements Z_k are computed as:

$$Z_k = \begin{bmatrix} \boldsymbol{r}_{\text{true}} + \boldsymbol{\eta}_{\text{RTN}} \\ \boldsymbol{q}_{\text{true}} \otimes \boldsymbol{q}_{\eta}. \end{bmatrix} \tag{5.28}$$

5.2.2. Navigation Filter

The navigation filter used in this work is based upon the work of Tweddle and Saenz-Otero [85] and uses the CWH equations (Equation (3.13)) and a linearized form of Euler's rotational equation (Equation (3.36)), making use of the Modified Rodriguez Parameters (MRP) (Section 3.4.3) to find a suitable linearization point. The CWH equations are inserted into a Multiplicative Extended Kalman Filter (MEKF) to estimate the state from measurements and internal propagation.

The MEKF uses two sets of variables, both the quaternions discussed in Section 3.4.2 and the MRP's from Section 3.4.3. The MRP representation is used in the filter since quaternions are overdetermined and causes a divergence of the Kalman Filter [85]. The quaternion is therefore kept as reference, while the MRP's are used as a three-element "error" parameterization, used in the propagation and update step. A final reset step is introduced where the quaternion is update with the "error" MRP's and the MRP's are reset to [0 0 0] [85], avoiding the singularity at 360^o (see Section 3.4.3). The filter relies on the general Kalman filter equations, which are given by the following equations:

A priori state estimate:

$$\hat{\boldsymbol{x}}_{k|k-1} = \boldsymbol{\Phi}_k \hat{\boldsymbol{x}}_{k-1|k-1} + \boldsymbol{B}_k \boldsymbol{u}_k + \boldsymbol{W}_s \tag{5.29}$$

$$\boldsymbol{P}_{k|k-1} = \boldsymbol{\Phi}_k \boldsymbol{P}_{k-1|k-1} \boldsymbol{\Phi}_k^T + \boldsymbol{\Gamma} \boldsymbol{Q} \boldsymbol{\Gamma}^T \tag{5.30}$$

Measurement:

$$\tilde{\boldsymbol{y}}_k = \boldsymbol{z}_k - \boldsymbol{H}_k \hat{\boldsymbol{x}}_{k|k-1} \tag{5.31}$$

Kalman Gain:

$$\boldsymbol{K}_k = \boldsymbol{P}_{k|k-1} \boldsymbol{H}_k^T \left(\boldsymbol{H}_k \boldsymbol{P}_{k|k-1} \boldsymbol{H}_k^T + \boldsymbol{R}_k \right)^{-1} \tag{5.32}$$

A posteriori state estimate:

$$\hat{\boldsymbol{x}}_{k|k} = \hat{\boldsymbol{x}}_{k|k-1} + \boldsymbol{K}_k \tilde{\boldsymbol{y}}_k \tag{5.33}$$

$$\boldsymbol{P}_{k|k} = (\boldsymbol{I} - \boldsymbol{K}_k \boldsymbol{H}_k) \boldsymbol{P}_{k|k-1} \tag{5.34}$$

where $\boldsymbol{x}$ represents the state, $\boldsymbol{P}$ the state covariance, $\boldsymbol{W}_s$ is a noise vector, the diagonal elements of $\boldsymbol{Q}$ represent the standard deviation of the noise in $\boldsymbol{W}_s$, $\boldsymbol{\Gamma}$ is a STM associated with $\boldsymbol{W}_s$, $\boldsymbol{u}$ is the control effort and $\boldsymbol{H}$ is the Jacobian of the measurement $\boldsymbol{z}$. The matrix $\boldsymbol{R}_k$ represents the measurement covariance. This measurement is constructed of six elements, three position parameters and three MRP's indicating the relative pose of target with respect to the chaser. Additionally the relative quaternion is measured and inserted to the filter separately. The filter calculates an error quaternion δq from the measured and expected quaternions, transforms this error quaternion into MRP's and uses the MRP's in the measurement equation to update the filter. The filter then uses the following equation:

$$\dot{\boldsymbol{x_k}} = \boldsymbol{\Phi}(k) \boldsymbol{x_{k-1}} + \boldsymbol{\Gamma}(k) \boldsymbol{W}(k) \tag{5.35}$$

where the continuous time dynamics are propagated linearly for a discrete time step Δt, assuming a piecewise constant process noise during the time step [85], and with:

$$\boldsymbol{x}_k = \begin{bmatrix} \boldsymbol{r}_k \\ \boldsymbol{v}_k \\ \boldsymbol{a}_{p,k} \\ \boldsymbol{\omega}_k \end{bmatrix} \tag{5.36}$$

$$\mathbf{\Phi} = \begin{bmatrix} \mathbf{\Phi}_{CWH,1:3|1:3} & \mathbf{\Phi}_{CWH,1:3|4:6} & 0_{3\times3} & 0_{3\times3} \\ \mathbf{\Phi}_{CWH,4:6|1:3} & \mathbf{\Phi}_{CWH,4:6|4:6} & 0_{3\times3} & 0_{3\times3} \\ 0_{3\times3} & 0_{3\times3} & \boldsymbol{e}^{-\frac{1}{2}[\omega\times]\Delta t} & \int_0^{\Delta t} \boldsymbol{e}^{-\frac{1}{2}[\omega\times]\tau} d\tau \\ 0_{3\times3} & 0_{3\times3} & 0_{3\times3} & I_{3\times3} \end{bmatrix} \tag{5.37}$$

$$\mathbf{\Gamma} = \begin{bmatrix} \frac{1}{2m}\boldsymbol{I}_{3\times3}\Delta t^2 & 0_{3\times3} \\ \frac{1}{m}\boldsymbol{I}_{3\times3}\Delta t & 0_{3\times3} \\ 0_{3\times3} & \Delta t \int_0^{\Delta t} \boldsymbol{e}^{-\frac{1}{2}[\omega\times]\tau} \boldsymbol{J}^{-1} d\tau \\ 0_{3\times3} & \boldsymbol{J}^{-1}\Delta t \end{bmatrix} \begin{bmatrix} \boldsymbol{W_v} \\ \boldsymbol{W_\omega} \end{bmatrix} \tag{5.38}$$

where $\mathbf{\Phi}_{CWH}$ is the STM described by Equation (3.14), $\boldsymbol{a}_p$ represents the MRP and $\boldsymbol{W_v}$ and $\boldsymbol{W_\omega}$ represent the process noise which is thus assumed piecewise constant over Δt. The state transition matrix $\mathbf{\Phi}$ is solved numerically at each time step.

5.2.3. Filter tuning

In order to achieve satisfactory results in the estimation of all state variables a proper tuning of process noises $\boldsymbol{W_v}$ and $\boldsymbol{W_\omega}$ is required. The process noises $\boldsymbol{W_v}$ and $\boldsymbol{W_\omega}$ are included in the model to incorporate disturbance forces applied to both spacecraft [85] and allow the $\boldsymbol{v}$ and $\boldsymbol{\omega}$ of the model to be updated correctly. These parameters can be considered tuning parameters as they strongly affect the convergence and overall accuracy of the navigation solution. Too much noise means that the filter cannot reliably update $\boldsymbol{\omega}$, $\boldsymbol{v}$ and estimates of these parameters will be noisy. Not enough process noise results in the filter being constrained and the values for $\boldsymbol{\omega}$, $\boldsymbol{v}$ being too 'stiff' which eventually results in the filter diverging.

The proper tuning of the process noises $\boldsymbol{W_v}$ and $\boldsymbol{W_\omega}$ is thus of high importance to allow for accurate estimation of both $\boldsymbol{\omega}$ and $\boldsymbol{v}$. Usually, a filter is tuned with process noise to account for accelerations that are neglected in the linearisation process of dynamic models [80]. As can be seen in Equation (5.38), the process noises $\boldsymbol{W_v}$ and $\boldsymbol{W_\omega}$ are scaled with respectively $\frac{1}{m}$ and $\boldsymbol{J}^{-1}$ before being added to the state. As a starting point the following assumptions are made (see also Chapter 2)

$$\begin{aligned} \Delta t &= 1 \text{ s} \\ m &= 8000 \text{ kg} \\ J &= \text{diag}(17000, 125000, 129000) \end{aligned}$$

where m is the Envisat mass and J the Envisat inertia. The vectors $\boldsymbol{W_v}$ and $\boldsymbol{W_\omega}$ consist of three numbers taken from a normal distribution $N(\mu,\sigma)$ with zero mean ($\mu = 0$) and standard deviation $\sigma = Q_v/Q_\omega$. The value of Q_v/Q_ω is determined experimentally, however, an initial guess can be deduced through reasoning.

The expected translational accelerations are caused by orbital perturbations and the optimal value of Q_v should be determined accordingly. While phase 1 only contains orbital disturbances, phases 2 & 3 also contain some control uncertainties, caused by using a linear controller and actuator uncertainties. To determine a baseline value of Q_v, the dominant neglected translational accelerations must be identified. Likewise, to determine a baseline value for Q_ω, the rotational accelerations should be considered, which are derived from the target attitude dynamics.

Translational noise Q_v

The dominant accelerations are determined by disturbances. D'Amico [14] reports that, for near-circular orbits in the LEO regime, the J_2 effect is the dominant relative acceleration for small spacecraft separations. For inter-satellite distances of 100 to 200 m, this relative acceleration has a magnitude of $\sim 10^{-7}$ m/s^2 [14]. Scaled with Envisat mass m, this requires Q_v to have a magnitude of ~ 0.001 or 10^{-3}. In order to investigate the optimal value of Q_v for phase 1, a range of 10 values around this expected value are evaluated.

$$Q_v = 10^{-4}, \quad 5\cdot10^{-4}, \quad 10^{-3}, \quad 5\cdot10^{-3}, \quad 10^{-2}, \quad 5\cdot10^{-2}, \quad 0.1, \quad 0.5, \quad 1, \quad 2$$

Furthermore, measurements were generated using a constant standard deviation of 0.1 m over the entire orbital period. The results are presented in Figure 5.10 and Table 5.5. This shows that when the value of Q_v is too small, the navigation is unable to update and a diverging behaviour can be experienced in the position error, as shown in Figure 5.10a. If the value of Q_v is too large the error at the end of the eclipse period grows rapidly, as shown in Table 5.5.

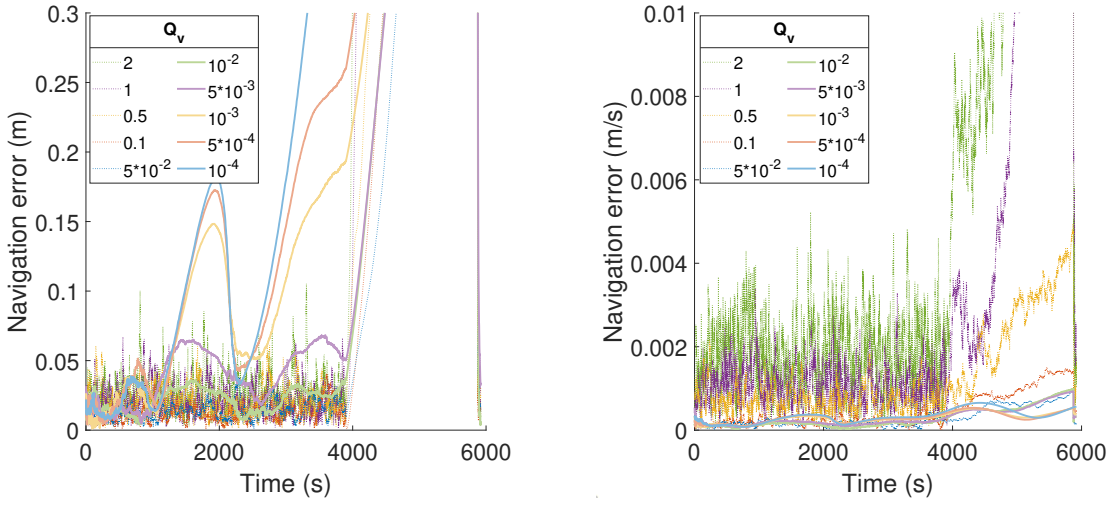

(a) Position

(b) Velocity

Figure 5.10: Phase 1 navigation position and velocity errors for 10 different tuning values of Q_v

Table 5.5: Mean and maximum navigation error for a range of Q_v values. The mean navigation error is evaluated during the illuminated part of the trajectory, while the maximum error is found at the end of the eclipse period.

Q_v	Mean error		Max error	
(-)	r (m)	v (mm/s)	r (m)	v (mm/s)
10^{-4}	0.1273	0.245	0.713	0.566
5* 10^{-4}	0.1012	0.237	0.719	0.538
10^{-3}	0.0823	0.225	0.703	0.525
5* 10^{-3}	0.0385	0.169	0.787	0.929
0.01	0.0213	0.130	0.819	0.991
0.05	0.0137	0.155	0.936	0.958
0.1	0.0120	0.197	1.366	1.487
0.5	0.0207	0.712	4.461	4.950
1	0.0214	1.090	16.454	21.780
2	0.0261	1.825	18.751	30.979

Furthermore, Table 5.5 shows that the mean error follows a parabolic curve with respect to Q_v, with its minimum around $Q_v = 10^{-2}$, while the maximum error only increases. This shows that a high level of noise is undesirable when no measurements are available.

Based on Figure 5.10 and Table 5.5, the optimal values of Q_v are found to be 0.01 and 0.05, which is slightly higher than the expected value of 10^{-3}. When increasing the measurement noise, to a standard deviation of 1.5 m, these two values still emerge as the optimum. The larger value is selected due to its lower mean error for r, and the value of 0.05 is used for Q_v.

The additional accelerations from thrust uncertainties are found to make a small difference in the tuning process. Analysis of multiple runs of phases 2 and 3, for a constant measurement standard deviation of 1.5 m, show that the optimal value of Q_v is found between 0.05 and 0.1, only slightly larger than the previous optimum of Q_v between 0.01 and 0.05. The selected value of Q_v for phases 2 and 3 is 0.1. Furthermore, analysis of phase 2 has shown that the convergence of the filter in the 150 s observation period (see Section 4.2) is slow. This period was introduced to allow convergence of the navigation filter, following the eclipse period. The value of Q_v in this period was set to $Q_v = 0.05$, equal to the optimal value found for phase 1 which, however, has proven too small to provide a full convergence of the filter. This can be solved by temporarily increasing the value of Q_v in this period or by extending the length of this period. Due to the limited illuminated time in a single orbit, an increase of Q_v is preferred over an extension of this period of observation. Setting $Q_v = 0.5$ temporarily ensures rapid convergence in this period.

Rotational noise Q_ω

When integrating the rotational dynamics with Equation (3.37) an estimate can be made of the expected rotational acceleration. The maximum $\dot{\omega}$ is found to be caused by the 'wobbling' and has a value of $5.6{\cdot}10^{-4}$ rad/s^2. Scaled with the Envisat inertia J, assumed 125000, the value of $\boldsymbol{W_\omega}$ is required to have a magnitude of ~ 69.91. In order to investigate the optimal value of $\boldsymbol{W_\omega}$, again a range of 10 values around this expected value are evaluated.

$$Q_\omega = 1, \quad 10, \quad 50, \quad 75, \quad 100, \quad 200, \quad 350, \quad 500, \quad 1000, \quad 2000$$

This analysis was performed using a constant measurement standard deviation of 5 degrees. Care should be taken not to select a too large or too small value of $\boldsymbol{Q_\omega}$ as too small values easily lead to filter divergence while too large values introduce a lot of noise. This is confirmed by the results of the tuning, shown in Figure 5.11 and Table 5.6, as it becomes clear that the filter diverges for $Q_\omega = 1$ and unacceptable levels of noise are introduced on $\boldsymbol{\omega}$ when $Q_\omega = 2000$.

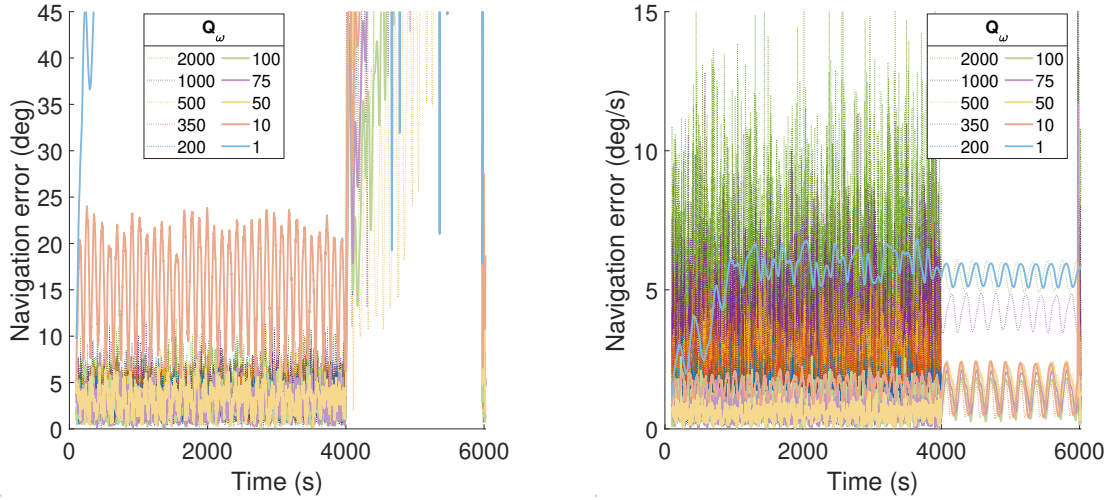

(a) Attitude

(b) Rotation

Figure 5.11: Phase 1 navigation attitude and rotation errors for 10 different tuning values of Q_ω.

Table 5.6: Mean and maximum navigation error for a range of Q_ω values. The mean navigation error is evaluated during the illuminated part of the trajectory, while the maximum error is found during the eclipse period.

Q_ω	Mean error		Max error	
(-)	q (deg)	ω (deg/s)	q (deg)	ω (deg/s)
1	107.9982	5.362724	327.4041	5.946357
10	15.51347	1.527722	289.7892	5.974087
50	3.122699	0.538501	124.4299	2.42978
75	2.707552	0.575727	241.0057	11.68573
100	2.619702	0.672417	161.6784	3.401487
200	2.663958	0.988386	237.137	18.66381
350	2.754959	1.411169	211.7378	47.88906
500	2.933641	1.845283	126.7429	6.650801
1000	3.264312	2.850042	294.3508	23.01274
2000	3.489709	4.510862	264.7546	21.1263

Based on Figure 5.11 and Table 5.6 the optimal value for Q_ω is found at 50 or 75. Whereas a further increase in Q_ω does not affect the attitude error much, it causes the rotation error to increase to unacceptable magnitudes. Since an increase from 50 to 75 still seems to improve the mean error on attitude, the value of 75 is selected for Q_ω.

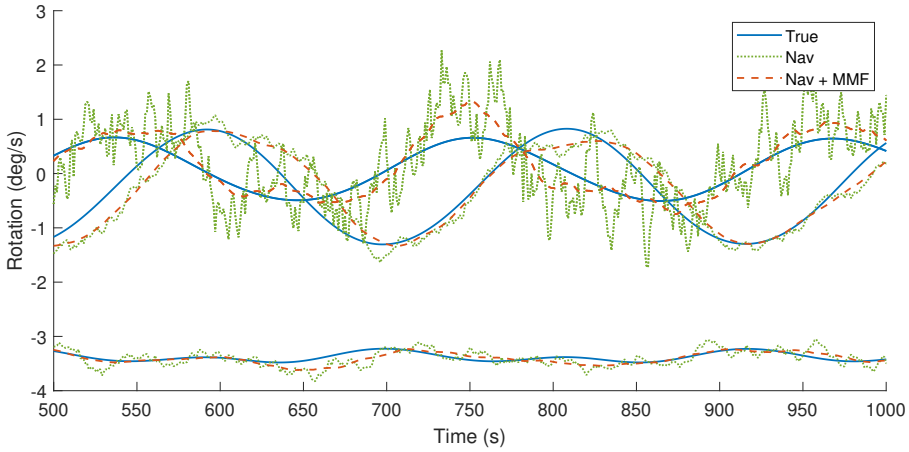

Figure 5.12: True, estimated (navigation) and averaged (navigation + MMF) estimated values of rotation $\boldsymbol{\omega}_{TBF}^{RTN/TBF}$ between $t = 500$ and $t = 1000$. Navigation estimate provided by the filter using $Q_\omega = 75$.

Furthermore, Figure 5.11 shows that the filter, regardless of tuning, has great difficulty estimating the relative rotation. The best achievable accuracy is around 0.5 deg/s, which is the magnitude of the secondary rotations imposed around the x- and y-axes of Envisat (see Section 2.2). Therefore, the relative attitude estimate should not be used during periods when no measurements are available. Also, this provides a challenge for the guidance system in estimating the final conditions as in Section 5.1.2, since these are fully dependent on the target rotational properties. Contrary to the position error, the attitude estimate quickly regains a high accuracy after the eclipse period and no additional tuning of Q_ω is required in this period.

In an attempt to improve the accuracy of the estimate of $\boldsymbol{\omega}$, a moving mean filter (MMF) is employed. This filter averages takes the mean over a sliding window of specified length. This is an excellent addition to the MEKF, as the MEKF continuously readjusts $\boldsymbol{\omega}$ to fit the measurements of $\boldsymbol{q}$. This naturally causes $\boldsymbol{\omega}$ to move around the true value, sometimes preceding it and sometimes lagging behind it. A MMF filter smoothens this behaviour and should result in a better estimate of $\boldsymbol{\omega}$ over time. By applying a MMF that uses 20 elements backward and forward of the current value, the mean error can be reduced from 0.576 deg/s to 0.347 deg/s, which is a significant reduction. Figure 5.12 illustrates how the rotation estimate is refined by the MMF. Unfortunately, these settings cannot be used in real-time, as there are no 20 forward elements, however, it can be very useful for on-board analysis and characterisation of the target dynamics. Also the MMF estimate is used to smoothen the real-time estimate of $\boldsymbol{\omega}$ in phase 3. Using a MMF with only backward elements, the mean error could be reduced from 0.576 deg/s to 0.537 deg/s.

Final tuning parameters

The optimal values achieved from the tuning process are summarised in Table 5.7.

Table 5.7: Tuned navigation filter process noises.

Parameter	Phase	Value
Q_v	1	0.05
	after eclipse	0.5
	2,3	0.1
Q_ω	all	75

5.3. Control

5.3.1. Actuators

The chaser spacecraft translational motion is assumed to be controlled through a set of 24 AOCS thrusters, capable of delivering 22N of thrust each (see Section 2.3). The thrusters are positioned in pairs, aligned in all 6 directions (12 thrusters) plus a redundant set of 12 thrusters. This is according to the ESA baseline design [6].

The chaser spacecraft attitude motion is assumed to be controlled through a set of 4 control wheels (3 nominal + 1 redundant), aligned in a pyramid configuration tilted 53.736 degrees from the z-axis (angle β = 35.264 degrees), positioned between the positive and negative x- and y- axes (angle θ = 45 degrees), as shown in Figure 5.13. The control wheels are assumed to be capable of delivering a maximum of 40 Nm torques around all axis.

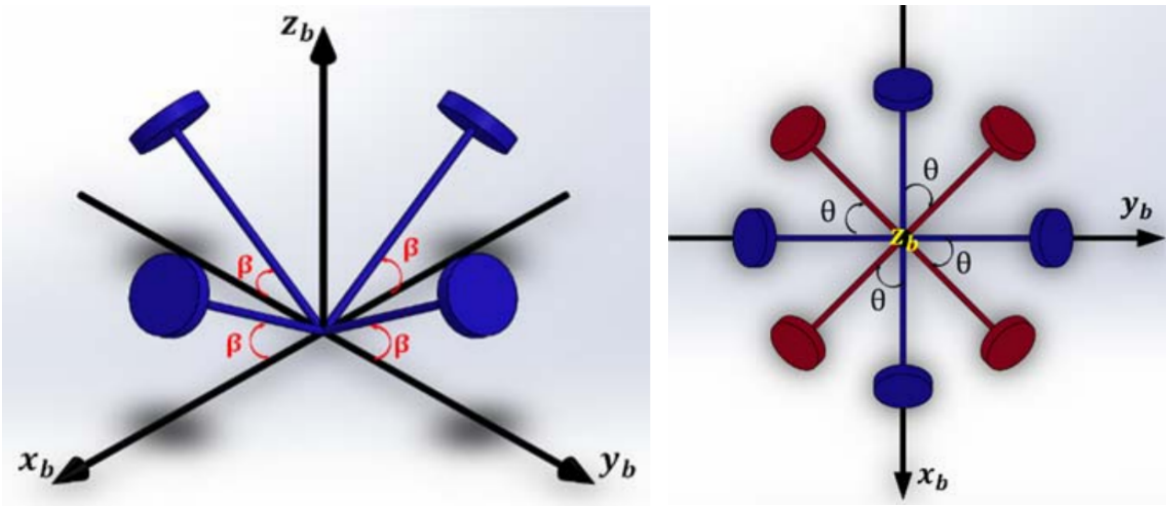

Figure 5.13: Reaction wheel pyramid configuration. [55]

Actuator uncertainties
Some uncertainty can be expected in the performance of the actuators in a real-world scenario. Therefore a small level of uncertainty is introduced into the simulation, both on the magnitude and the direction of the forces and torques. The following uncertainties are introduced [83]

- *Magnitude:* $\pm 5\%$
- *Direction:* $\pm 1^o$

Both are introduced as 3σ values in a Gaussian distribution, $N(\mu,\sigma)$.

5.3.2. Linear Quadratic Regulator

Both translational control and attitude control are based on the Linear Quadratic Regulator (LQR). The LQR is a well defined control model within the control community but has seen no application in space missions as of this day [32] although its use has been proposed in the design of new missions [62]. According to Jankovic et al. [32] the LQR has a computational load that is similar to that of a PID controller. The LQR controller, however, is much better equipped to deal with the optimisation process. The LQR uses a linear system model

$$\boldsymbol{x}_{k+1} = \boldsymbol{A}_k \boldsymbol{x}_k + \boldsymbol{B}_k \boldsymbol{u}_k \tag{5.39}$$

where $\boldsymbol{x}_k$ is the state at time t_k, $\boldsymbol{A}_k$ is the STM, $\boldsymbol{B}_k$ is the control matrix and $\boldsymbol{u}_k$ is the control input. The optimisation associated with the LQR then consists of finding the optimal gain matrix $\boldsymbol{K}_k$ such that a cost function J is minimised [62]

$$J = \int_k^{k+1} \left(\boldsymbol{x}_i^T \boldsymbol{Q} \boldsymbol{x}_i + \boldsymbol{u}_i^T \boldsymbol{R} \boldsymbol{u}_i \right) \tag{5.40}$$

where $\boldsymbol{Q}$ and $\boldsymbol{R}$ are gain matrices containing only diagonal elements and control effort $\boldsymbol{u}_k$ is defined as

$$\boldsymbol{u}_k = \boldsymbol{K}_k \boldsymbol{x}_k \tag{5.41}$$

The optimal gain matrix $\boldsymbol{K}_k$ is then calculated as [32]:

$$\boldsymbol{K}_k = -(\boldsymbol{R} + \boldsymbol{B}_k^T \boldsymbol{P}_{k+1} \boldsymbol{B}_k)^{-1} \boldsymbol{B}_k^T \boldsymbol{P}_{k+1} \boldsymbol{A}_k \tag{5.42}$$

with $\boldsymbol{P}$ that satisfies the so-called Riccati equation

$$\boldsymbol{P}_{k-1} = \boldsymbol{Q} + \boldsymbol{A}_k^T \boldsymbol{P}_k \boldsymbol{A}_k - \boldsymbol{A}_k^T \boldsymbol{P}_k \boldsymbol{B}_k (\boldsymbol{R} + \boldsymbol{B}_k^T \boldsymbol{P}_k \boldsymbol{B}_k)^{-1} \boldsymbol{B}_k^T \boldsymbol{P}_k \boldsymbol{A}_k \tag{5.43}$$

This process is available in MATLAB through the 'lqr' command, which takes the $\boldsymbol{A}$, $\boldsymbol{B}$, $\boldsymbol{Q}$ and $\boldsymbol{R}$ matrices as inputs. The matrices $\boldsymbol{Q}$ and $\boldsymbol{R}$ are to be tuned manually. Increasing the value of $\boldsymbol{R}$ results in the controller becoming more efficient, at the cost of creating higher errors. Contrarily, if the value of $\boldsymbol{Q}$ is increased the controller follows the reference state more accurately, at the cost of higher control effort.

Translational controller - Tuning

Thrust effort required for effective translational control can then be computed using Equation (3.14) (Matrix $\boldsymbol{A}$) and Equation (3.15) (Matrix $\boldsymbol{B}$). The gain matrix $\boldsymbol{R}$ = diagonal($[1e^{11}, 1e^{11}, 1e^{11}]$) as proposed by Volpe and Circi [90], leaving $\boldsymbol{Q}$ to be tuned manually. The gain matrix $\boldsymbol{Q}$ consists of 6 elements

$$\boldsymbol{Q} = \begin{bmatrix} \boldsymbol{I}_{3\times3} \cdot Q_{r,lqr} & \boldsymbol{0}_{3\times3} \\ \boldsymbol{0}_{3\times3} & \boldsymbol{I}_{3\times3} \cdot Q_{v,lqr} \end{bmatrix} \tag{5.44}$$

where the subscript $()_{...,lqr}$ is introduced to avoid confusion with the Q_v of the navigation filter, tuned in Section 5.2.3. The values of $Q_{r,LQR}$ and $Q_{v,LQR}$ are tuned experimentally. These values need to be tuned separately for phases 2 and 3 (see Section 4.2), since the expected accelerations are higher for the forced motion in phase 3, compared to the near-optimal motion in phase 2. The tuning runs were performed using σ_r = 0.5 m, σ_q = 3.0 deg.

Phase 2

The results for the tuning of the LQR parameters $Q_{r,lqr}$ and $Q_{v,lqr}$ are presented in Figure 5.14 and Table 5.8.

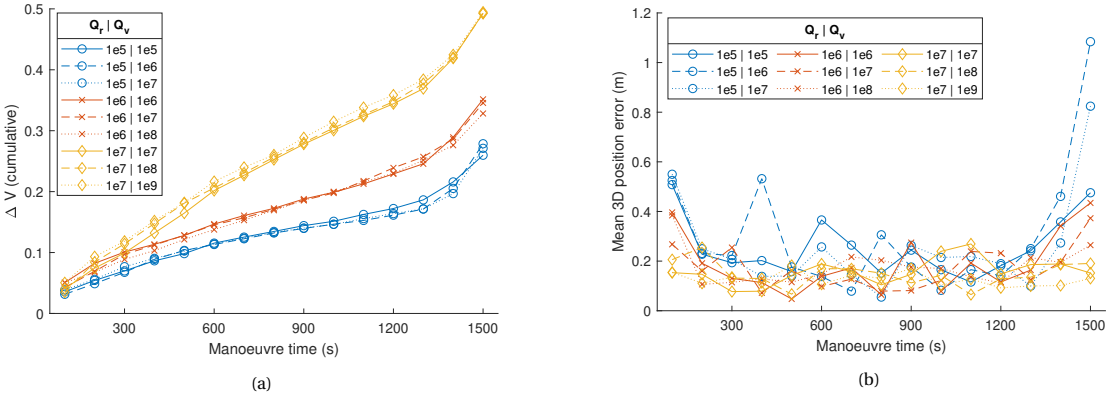

(a) (b)

Figure 5.14: Cumulative closed-loop ΔV (left) and mean 3D position guidance error averaged over increments of 100 seconds (right), for the complete optimal manoeuvre, using different settings for LQR matrix $\mathbf{Q}$ (Equation (5.44)).

Table 5.8: Phase 2 Final position guidance error and closed-loop ΔV, using different settings for LQR matrix $\mathbf{Q}$ (Equation (5.44)).

$Q_r = 10^5$		
Q_v	Final error	ΔV
10^5	1.145	0.260
10^6	1.760	0.276
10^7	1.813	0.271

$Q_r = 10^6$		
Q_v	Final error	ΔV
10^6	0.427	0.351
10^7	0.583	0.346
10^8	0.594	0.328

$Q_r = 10^7$		
Q_v	Final error	ΔV
10^7	0.331	0.493
10^8	0.298	0.492
10^9	0.404	0.495

From the data in Figure 5.14 and Table 5.8 it becomes clear that tuning of the LQR for phase 2 is a choice between ΔV and remaining position error at the end of the manoeuvre. Both show that the effect of Q_r is much larger than Q_v, both in determining the final ΔV as well as the remaining error. When examining Table 5.8 it can be noted that, when moving from $Q_r = 10^5$ to 10^6, the decrease in final position error, more than 65% on average, weights against the increase in ΔV, which is, on average, merely 26%. However, when

moving from $Q_r = 10^6$ to 10^7 the decrease in final position error is much smaller, on average only 35%, while the increase in ΔV becomes 45% on average. This leads to the selection of 10^6 as optimal value for Q_r. As the effect of Q_v is only marginal compared to Q_r its selection is less important and a value of 10^7 is selected, following the example of Volpe et al. [91] and keeping $Q_v > Q_r$.

Furthermore, the right sub-figure of Figure 5.14b shows that the highest guidance errors are found at the beginning and end of the trajectory. The performance of all settings is similar in the middle of the trajectory and decreased performance of the lower Q_r values can be found at the first and especially the last increments of the optimal trajectory. This indicates that a variable tuning of the LQR filter might be more suitable to optimise the total control effort. However, this research is aimed at developing feasible and robust guidance algorithms for vision-based systems, which is unrelated to controller tuning. Therefore the investigation of variable LQR tuning is left as a recommendation for further research.

Phase 3

The phase 3 trajectory is overall difficult to control. It is shaped as a spiral, making it incredibly difficult for the controller to correctly follow the trajectory at large distances from the chaser, as the spiral is wider when the separation between target and chaser is larger. This is demonstrated in Figure 5.15, showing the nominal trajectory in red and several controlled trajectories for different settings of LQR matrix $\boldsymbol{Q}$.

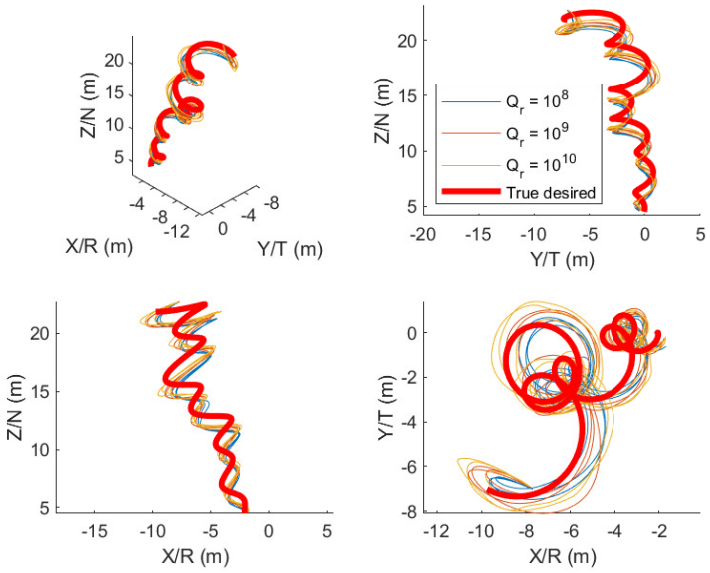

Figure 5.15: The phase 3 trajectory to be followed by the spacecraft (red), along with the trajectories achieved by the LQR controller for different settings of matrix $\boldsymbol{Q}$.

Additionally Figure 5.16 shows that indeed the guidance error decreases as the chaser gets closer to the target. It also becomes clear that the performance does not really improve when $Q_r = 10^8 \rightarrow 10^9 \rightarrow 10^{10}$. The error decreases and increases in fashion that is consistent with the spiral found in Figure 5.15. When further decreasing the value of Q_r it can be observed that the controlled trajectory loses some of its spiral motion and becomes more similar to a line. This results in higher guidance errors, but similar final position errors.
Finally, a significant increase in ΔV is found for the trajectories in phase 3, compared to phase 2, illustrated in Table 5.9. Whereas the ΔV values for phase 2 were all smaller than 1 m/s, the ΔV values for phase 3 easily exceed 4 m/s.
The trajectory of phase 3 might thus require some further consideration when planning the real mission to remove Envisat from orbit. Approach along the spin-axis is especially costly when the secondary rotations increase with respect to the main rotation, increasing the 'wobbling' of the satellite due to its inertia. As the satellite is expected to gradually slow down, which was explained in Section 2.2, this is a very realistic scenario. Since the efficiency of the trajectory from a control aspect is unrelated to the vision-based focus of this research it will not be further discussed. Instead a recommendation is made to re-asses this trajectory when the Envisat attitude dynamics have been established with a higher reliability.

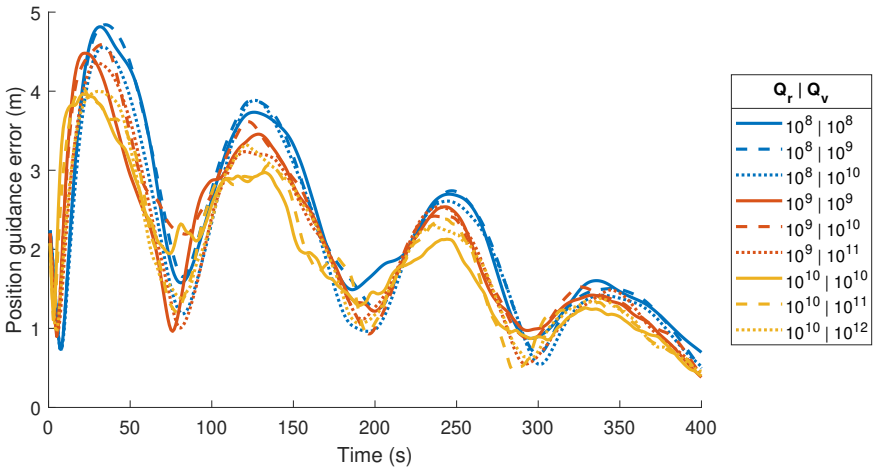

Figure 5.16: Position guidance error for the phase 3 trajectories achieved by the LQR controller for different settings of matrix $\boldsymbol{Q}$.

Table 5.9: Phase 3 final position guidance error and closed-loop ΔV, using different settings for LQR matrix $\boldsymbol{Q}$.

$Q_r = 10^8$		
Q_v	Final error	ΔV
10^8	0.697	4.212
10^9	0.495	4.179
10^{10}	0.516	3.308

$Q_r = 10^9$		
Q_v	Final error	ΔV
10^9	0.381	5.705
10^{10}	0.416	5.905
10^{11}	0.418	4.270

$Q_r = 10^{10}$		
Q_v	Final error	ΔV
10^{10}	0.397	8.616
10^{11}	0.437	8.822
10^{12}	0.454	11.413

5.3.3. Attitude Controller

The attitude controller in this section is based on the quaternion-based control method presented by Navabi and Hosseini [55]. This method uses a configuration of reaction wheels as presented in Figure 5.13. The individual torques of the wheels are linked to the torques along the x-, y-, z-axis as

$$\begin{bmatrix} T_{cx} \\ T_{cy} \\ T_{cz} \end{bmatrix} = \begin{bmatrix} \frac{\sqrt{3}}{3} & -\frac{\sqrt{3}}{3} & -\frac{\sqrt{3}}{3} & \frac{\sqrt{3}}{3} \\ \frac{\sqrt{3}}{3} & \frac{\sqrt{3}}{3} & -\frac{\sqrt{3}}{3} & -\frac{\sqrt{3}}{3} \\ \frac{\sqrt{3}}{3} & \frac{\sqrt{3}}{3} & \frac{\sqrt{3}}{3} & \frac{\sqrt{3}}{3} \end{bmatrix} \begin{bmatrix} T_{w1} \\ T_{w2} \\ T_{w3} \\ T_{w4} \end{bmatrix} = \boldsymbol{L}_c \begin{bmatrix} T_{w1} \\ T_{w2} \\ T_{w3} \\ T_{w4} \end{bmatrix} \tag{5.45}$$

where T_{cx}, T_{cy}, T_{cz} are the control torques and T_{w1} up to T_{w4} represent the torques generated by the reaction wheels around their own spin axis. The attitude kinematics and dynamics are defined by Equation (3.34) and Equation (3.36), creating the following non-linear system

$$\begin{aligned} \dot{x} &= f(x) + g(x) \cdot u \\ y &= h(x) \end{aligned} \tag{5.46}$$

with the state variable x defined as $[q_0\ q_1\ q_2\ q_3\ \omega_x\ \omega_y\ \omega_z]^T$. When using this definition $f(x)$ and $g(x)$ can be written as

$$f(x) = \begin{bmatrix} \frac{1}{2}\Omega q \\ J^{-1}[-\omega \times (J\omega + h_w) + T_e] \end{bmatrix} \tag{5.47}$$

$$g(x) = \begin{bmatrix} \mathbf{0}_{4\times 3} \\ J^{-1} \end{bmatrix} \tag{5.48}$$

where h_w is the angular momentum of the wheels and T_e is a vector of external torques such as the gravity gradient. The output y of the system is $[q_1\ q_2\ q_3]$, using Equation (3.22) to find q_0. Angular momentum h_w is related to control torque as

$$\dot{h_w} = -T_c \tag{5.49}$$

According to control theory a non-linear system can be converted to a linear one using Lie-derivatives in a process called input-output linearization [31]. The current system can be converted to a linear system

$$\begin{aligned} \dot{\xi} &= A_l \xi + B_l \nu \\ y &= C_l \xi \end{aligned} \tag{5.50}$$

with state variable $\xi = [q_1\ q_2\ q_3\ \dot{q}_1\ \dot{q}_2\ \dot{q}_3]$ and

$$A_l = \begin{bmatrix} 0_{3\times3} & I_{3\times3} \\ 0_{3\times3} & 0_{3\times3} \end{bmatrix} \qquad B_l = \begin{bmatrix} 0_{3\times3} \\ I_{3\times3} \end{bmatrix} \qquad C_l = \begin{bmatrix} I_{3\times3} & 0_{3\times3} \end{bmatrix}. \tag{5.51}$$

Then for the linear system described in Equation (5.50) the linear control vector ν can be calculated from

$$\nu = -K \begin{bmatrix} \boldsymbol{q} - \boldsymbol{q}_d \\ \dot{\boldsymbol{q}} \end{bmatrix} \tag{5.52}$$

where the gain matrix K is computed using the LQR method discussed in Section 5.3.2 and $\boldsymbol{q}_d$ is the desired reference quaternion, $\boldsymbol{q}_d = [q_{d1}\ q_{d2}\ q_{d3}]$. Finally the linear control effort ν can be related to the non-linear control effort u through

$$u = E^{-1}(x)\,(\nu - D(x)) \tag{5.53}$$

with

$$E(x) = \begin{bmatrix} \frac{q_0}{J_{xx}} & \frac{-q_3}{J_{yy}} & \frac{q_2}{J_{zz}} \\ \frac{q_3}{J_{xx}} & \frac{q_0}{J_{yy}} & \frac{-q_1}{J_{zz}} \\ \frac{-q_2}{J_{xx}} & \frac{q_1}{J_{yy}} & \frac{q_0}{J_{zz}} \end{bmatrix} \tag{5.54}$$

$$D(x) = \frac{1}{2} \begin{bmatrix} 0 & \omega_z & -\omega_y & \omega_x & q_0 & -q_3 & q_2 \\ -\omega_z & 0 & \omega_x & \omega_y & q_3 & q_0 & -q_1 \\ \omega_y & -\omega_x & 0 & \omega_z & -q_2 & q_1 & q_0 \end{bmatrix} f(x) \tag{5.55}$$

For the complete theory and an evaluation of the performance of this method the reader is referred to Navabi and Hosseini [55]. Using the theory stated in this section the LQR controller can be employed to control the attitude of the chaser spacecraft under all conditions. This linearization is only possible if the matrix $E(x)$ is non-singular, which means that $q_0 \neq 0$ [55]. The singularity at $q_0 = 0$ is avoided by a change of variables, which in the case of phase 2 is a switch from $\boldsymbol{q}_{RTN}^{CBF}$ to $\boldsymbol{\omega}_{CBF}^{CBF/RTN}$. In the third phase a change is made from $\boldsymbol{q}_{RTN}^{CBF}$ to $\boldsymbol{q}_{CCBF}^{TBF}$, using a new coordinate system *CCBF*. Both changes of variables were explained in Section 5.1.8.

Tuning

The controller is tuned separately for the pointing mode in phase 2 and the synchronisation mode in phase 3, outlined in Section 5.1.8. Since the attitude control law also uses a LQR controller, the tuning process is similar to that of the translational controller. The diagonal values of the $\boldsymbol{R}$ matrix are set to 1000, same as Navabi and Hosseini [55]. For the pointing law in phase 2 and the hold period of phase 3 the diagonal values of the $\boldsymbol{Q}$ matrix, Q_q and Q_ω (Q_r / Q_v in Equation (5.44)) are set to 5. This setting achieves sub-degree control accuracy for the chaser pointing attitude.

For the synchronisation period of phase 3 the tuning of the controller is more difficult. The $\boldsymbol{R}$ matrix is left untouched, and for the values in the $\boldsymbol{Q}$ matrix a number of candidates was selected. The results are presented in Figure 5.17.

Figure 5.17 demonstrates the working of the attitude guidance outlined in Section 5.1.8. During the hold phase the chaser is non-rotating and the attitude error is fully determined by the rotation of the target. The error can be seen to be first increasing, then decreasing and reaching a minimum value at $t \approx 115$. At this point the control law is activated and the chaser slowly increases its rotation to match the target, which results in a very small peak around $t \approx 130$ before settling on a constant error around $t \approx 140$.

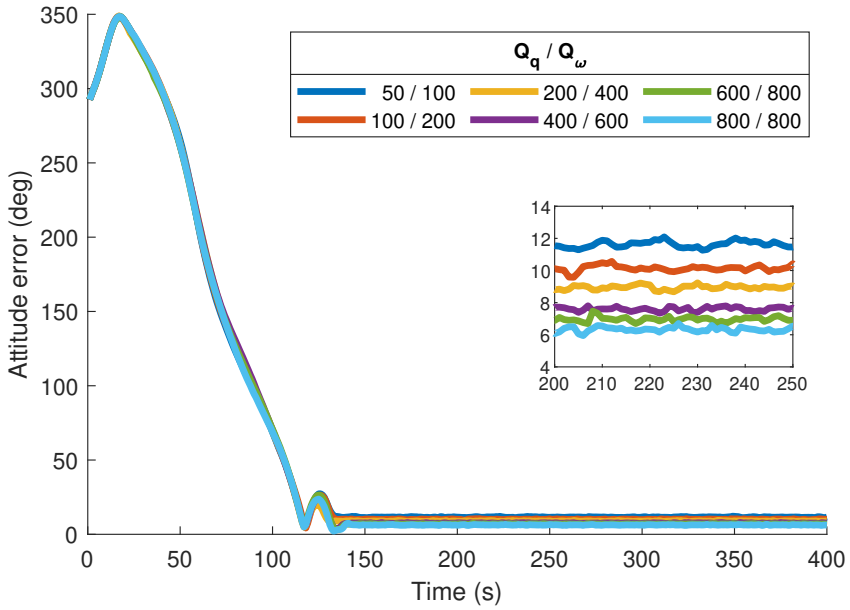

Figure 5.17: Attitude control error, achieved during tuning of Q_q/Q_ω. The hold phase is present up to $t \approx 110$, after which the control mode is engaged and the rotation is synchronised, resulting in a low and constant attitude error.

Furthermore, Figure 5.17 shows that for relatively large values of Q_q and Q_ω, almost the same magnitude as $\boldsymbol{R}$, the attitude control error still exceeds 5 degrees, while a value smaller than 5 degrees is considered desirable to achieve successful docking according to Ventura et al. [86]. As measurement accuracy is around 2-3 degrees, the control error must be very small, however, even when $\boldsymbol{Q}$ is almost the same magnitude as $\boldsymbol{R}$ this is very difficult to achieve with this controller. This raises the question if this control strategy is suitable for this purpose.

Since the main concern of this research is to evaluate the influence of vision-based aspects, it is decided to keep using the linear controller and use Q_q = 600 and Q_ω = 800 in this research. The 7 degree control error, achieved in this configuration, still allows influences of vision-based aspects on the control law to be evaluated. However, for an actual mission a more suitable control strategy should be implemented, preferably one that is better equipped to deal with the wobbling caused by inertia, as this is one of the main causes of error. This could mean switching to a non-linear controller, or designing a controller that also accounts for ω as a reference, such as the controller presented by Biggs and Horri [7]. Or it could mean a complete revision of the reference attitude and rotation, where the wobbling motion is mitigated through a form of approximation of linearization. Designing such a control strategy will be crucial to the success of an ADR mission to remove Envisat.

6

GNC Sensitivity Analysis

The effect of the performance of pose estimation systems on the efficiency of a GNC architecture and its ability to safely guide the satellite to its final desired position has not been previously investigated. Previous studies usually build on a specific pose estimation system, designed by the authors, and simply report the guidance system performance based on the performance of this specific pose estimation system [26, 91]. Other studies design a guidance system and assume a nominal and good performance of the pose estimation system to verify the working of the guidance system [86, 90]. Earlier studies thus assume a specific pose estimation system, under nominal performance. This chapters reverses this process, starting with a specific guidance system and varying the performance of the pose estimation system to assess the sensitivity of the guidance system with respect to these changes.

The chapter aims to analyse the effect of several specific scenarios, outlined in Chapter 4, on the performance of the GNC architecture. First, Section 6.1 will analyse scenarios with long periods of moderate error, exploring the impact of position and attitude errors separately and discussing their individual influences on the guidance algorithm. Subsequently, Section 6.2 provides an extensive analysis on a range of plausible scenarios, during which the pose estimation system fails to provide accurate measurements. Based on this analysis, Section 6.3 presents some conclusions, which serve as an introduction to the strategies for improvement discussed in Chapter 7.

The measurement accuracy, represented by a 1σ value (see Table 4.1), is kept constant over the course of the entire trajectory. This creates a less realistic simulation, however, it allows to distinguish the effects of measurement accuracy on the performance of the system, which is the main goal of this chapter. As the performance of the guidance system is not directly dependent on the measurements, multiple performance metrics (see Section 4.4) are required to provide a complete impression of the GNC performance. The navigation error is an indication of how the measurements influence the performance of the navigation system. The guidance error is a measure of the overall performance of the GNC system, as it measures how well the spacecraft follows the intended trajectory in reality.

6.1. Long periods of moderate error

An overview of possibly failure scenarios was provided in Chapter 4, which separated error scenarios into 'long periods of moderate error' and 'short periods of high error'. The definition of 'moderate accuracy' was provided in Table 4.1, where three levels of moderate accuracy, Mod_1, Mod_2 and Mod_3, were introduced. This section analyses the performance of the guidance system for these three levels of moderate accuracy, together with the two levels of high accuracy High_1 and High_2, also presented in Table 4.1. The length of the period is set to the total manoeuvre time, which is 1500 seconds, as decided in Section 4.2. The analysis is performed for both phase 2 and phase 3 (see Section 4.2) separately. Furthermore, a distinction is made between the effects of position and attitude errors.

6.1.1. Phase 2

The current position (and velocity) of the chaser, relative to the target, appear in two facets of the guidance algorithm (see Section 5.1), respectively the initial conditions for the reference trajectory (Equation (5.9), lines

1 and 2) and the attitude pointing law (Equations (5.17) and (5.19)). The attitude (and rotation) of the target appear in the estimation of the final state (Equation (5.9), lines 3 and 4).

Position Error

The reference trajectory during phase 2 is influenced by the position error through the initial conditions, and consequently at all guidance updates every t_{up} (see Section 5.1.5). All error in the initial conditions is directly transferred to the reference trajectory. The mean navigation error for position and attitude, as well as the guidance error for position, are listed in Table 6.1, showing a slight increase in all these metrics.

Table 6.1: Navigation position and attitude error and guidance position error for five different levels of measurement accuracy. A slight increase in all performance metrics may be noted. See Table 4.1 for the definitions of the level of measurement accuracy.

	High_1	High_2	Mod_1	Mod_2	Mod_3
Position					
σ_p (m)	0.05	0.1	0.5	1.0	1.5
Nav pos error (m)	0.008	0.014	0.043	0.084	0.112
Gui pos error (m)	0.114	0.111	0.135	0.161	0.180
Attitude					
σ_q (deg)	0.5	1.0	3.0	4.0	5.0
Nav att error (deg)	0.345	0.650	1.722	2.157	2.744

In the case of navigation errors, and without any failure periods, the mean value presented in Table 6.1 provides a good representation of the navigation error behaviour. In the case of guidance error however, the mean values are a poor representation of the true behaviour of the guidance error, visualised in Figure 6.1. This shows that the mean value is only achieved in the middle sections of the trajectory (t = 300-1200 s) and thus only a good representation of this time frame. The final guidance error is consistently much larger than the mean, reaching a magnitude of around 1 m, almost 500% larger than the mean errors reported in Table 6.1.

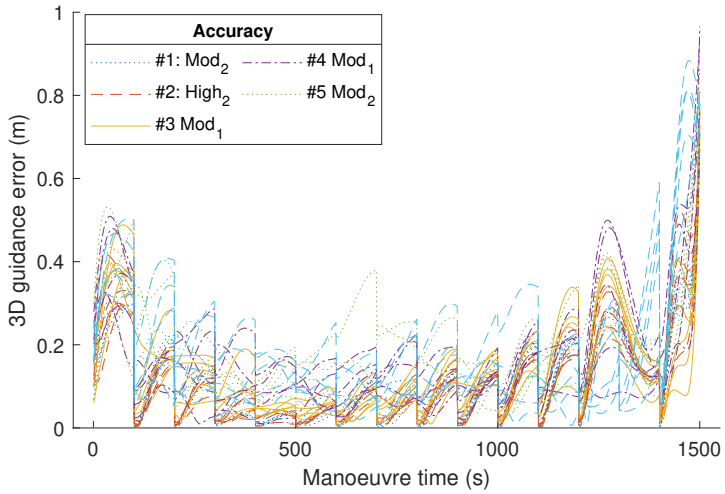

Figure 6.1: Guidance position errors for five levels of measurement accuracy. First of all, it may be noted that the behaviour of the guidance error is similar for all levels of accuracy. Second, it can be seen that summarising this behaviour using the mean values in Table 6.1 fails to accurately represent the situation, as mean values are around 0.1-0.2 m while the final guidance error is nearly 1 m in magnitude.

Examining the ΔV values for the runs with five different levels of accuracy, presented in Figure 6.2, learns that despite the differences in navigation and guidance error in Table 6.1, no significant differences in ΔV can be observed. Furthermore, it can be seen from Figure 6.2 that the influence of individual cases on the total ΔV is larger than the overall effect of measurement accuracy, which is an indication that the guidance algorithm is not very sensitive to measurement accuracy, but rather robust.

Furthermore, Figure 6.2 shows a clear tendency towards higher ΔV expenditure near the beginning and end of the trajectory. This is a likely aspect of optimal trajectories, since two-impulse transfers are frequently

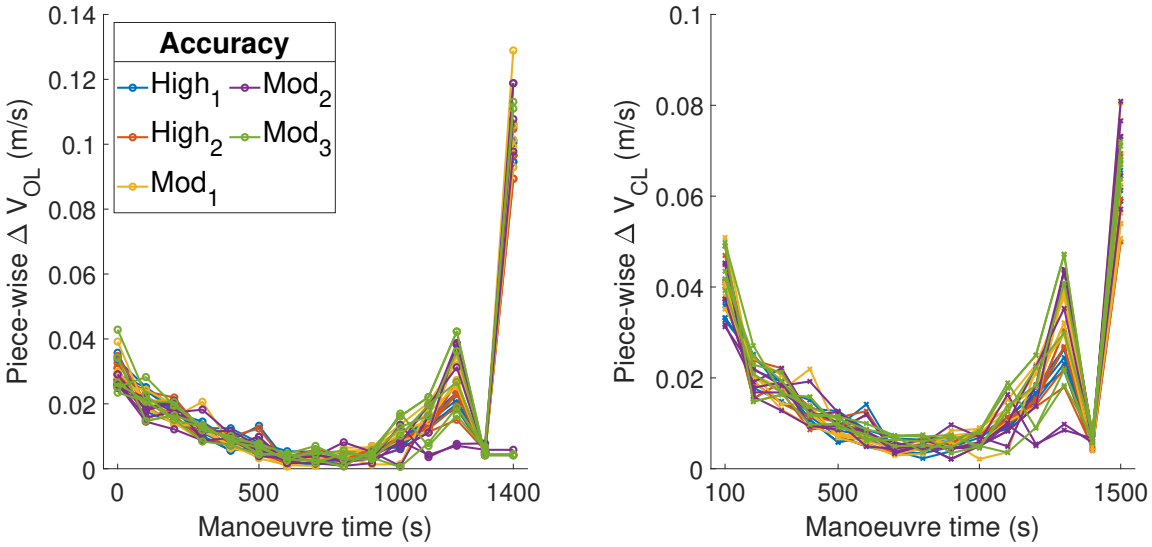

(a) Open-loop (piece-wise).

(b) Closed-loop (piece-wise).

Figure 6.2: Comparison of open-loop and closed-loop ΔV magnitudes for different levels of measurement accuracy. It can be seen that the accuracy of the measurements does not affect the efficiency of the trajectory, which means the guidance algorithm is robust with respect to measurement accuracy. Also the differences between individual cases of the same measurement accuracy are larger than the differences between the five levels of measurement accuracy.

found to be the most optimal in space. This behaviour also indicates that the controller is trying to correct the increased guidance error near the beginning and end of the trajectory, shown in Figure 6.1.

The total open-loop and closed-loop ΔV values, averaged over all runs of the same accuracy, are provided in Table 6.2, together with the averaged final position error.

Table 6.2: Final position error and total ΔV. Averaged over all runs. See Table 4.1 for the definitions of the level of measurement accuracy.

	High_1	High_2	Mod_1	Mod_2	Mod_3
Final position error (m)	2.787	2.994	3.775	4.071	4.856
ΔV_{OL} (m/s)	0.261	0.260	0.275	0.218	0.218
ΔV_{CL} (m/s)	0.245	0.249	0.260	0.254	0.277

In a nominal situation, the closed-loop ΔV should not be allowed to be smaller than its open-loop counterpart, as the closed-loop value necessarily contains the effects of unmodeled and non-optimal perturbations. This is only possible if the final position is not accurately reached, exchanging control effort for an increase in position error. This is related to the tendency of optimal trajectories towards highest ΔV at the beginning and end of the trajectory. When this ΔV is not sufficiently accurately enforced, higher position errors are inevitably created. This is an indication that the controller, or the tuning of the controller, might be improved for future applications. Since this type of mitigation is unrelated to any vision-based aspects, it is left as a recommendation.

In order to observe the differences between the levels of measurement accuracy, the difference between open-loop and closed-loop ΔV of the individual runs should be considered. If this difference between prediction and realisation is calculated and averaged over all runs, a small difference may be observed, as shown in Figure 6.3, where a clear trend can be observed.
As could be expected, Figure 6.3 shows that the runs with higher standard deviations use more ΔV compared to the runs with lower standard deviations. This behaviour is easily explained by examining the control strategy, which compares the current state estimate, made by navigation, to the guided reference state. When the measurement error increases, the navigation error inevitably increases and the difference between the navigated state and guided reference state becomes larger, as this difference has a lower limit at the value of the navigation error. As a consequence the control effort, which is based on this difference, increases.

The position errors thus mainly decrease the optimality of the solutions, as higher measurement errors result in high navigation errors, which results in the chaser being farther away from the calculated optimal

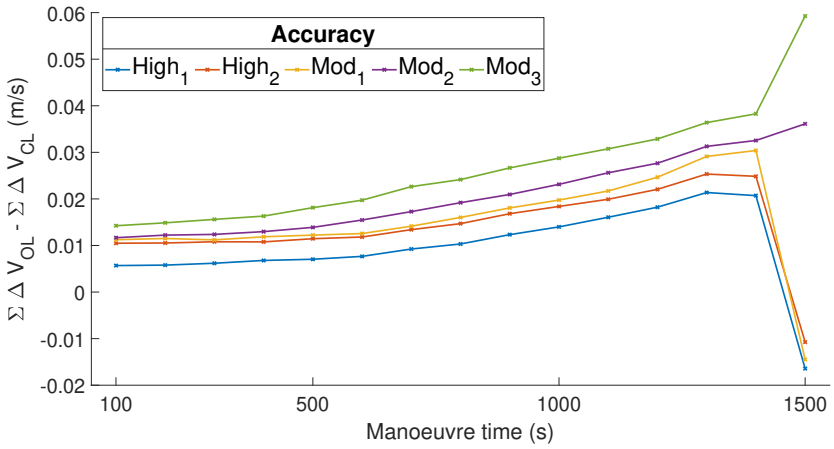

Figure 6.3: Averaged differences between closed-loop and open-loop ΔV.

trajectory, ultimately resulting in an increase of the required control effort in following the calculated trajectory, as shown in Figure 6.3.

Attitude error

When re-examining Figures 6.2 and 6.3 it must be noted that both figures show strange behaviour near the end of the trajectory. The piece-wise ΔV shows a steep increase, while the difference between closed-loop and open-loop ΔV even becomes negative. Also Table 6.2 shows that final $\Delta V_{CL} < \Delta V_{OL}$. This behaviour, and resulting final position error, can be attributed to the volatility of the estimation of the final desired state, stemming from uncertainties in the estimate target rotation.

The target rotational velocity vector at the end of the optimal manoeuvre in the orbital frame, $\left(\boldsymbol{\omega}_{RTN}^{TBF/RTN}\right)_{\text{final}}$ (or simply $\boldsymbol{\omega}_{final}$), is estimated by taking its current value, $\left(\boldsymbol{\omega}_{RTN}^{TBF/RTN}\right)_t$, and integrating this value, together with the current target attitude, $\left(\boldsymbol{q}_{TBF}^{RTN}\right)_t$, over the remaining manoeuvre time $t_{\text{int}} = t_{\text{final}} - t$. This integration is performed assuming perfect knowledge of the target inertia, however, still introduces significant error due to uncertainties in the target attitude and rotation $\boldsymbol{q}$ and $\boldsymbol{\omega}$, which are provided by the navigation filter.

The guidance algorithm is updated every $t_{up} = 100$s, at which instant a new value for $\boldsymbol{\omega}_{final}$ is computed, and thus a new value for $\boldsymbol{r}_{final}$. To demonstrate the magnitude of the integration error, the 3D position error of the final position estimate, for all consecutive estimates during the 1500 second manoeuvre, is presented in Figure 6.4.

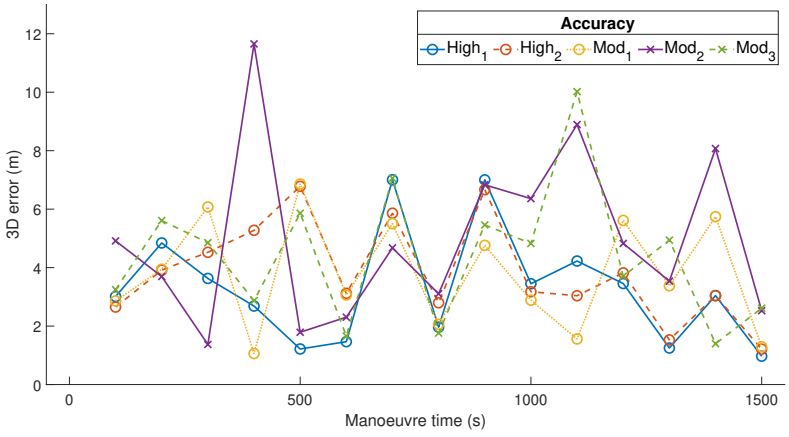

Figure 6.4: 3D position error for the estimate of $\boldsymbol{r}_{final}$ at all consecutive guidance updates during a 1500 second manoeuvre. It can be seen that the error is large compared to the guidance error in Figure 6.1 and no trends can be observed in the magnitude of this error.

Examining the behaviour of this estimate it becomes apparent that the final position error, obtained from the estimate of $\boldsymbol{\omega}_{final}$, is much larger than the final guidance error (see Figure 6.1) and highly sensitive to

small uncertainties in $\boldsymbol{\omega}_{RTN}^{TBF/RTN}$. This sensitivity is likely caused by the relatively fast dynamics (3.5 deg/s), combined with long integration times (100-1500 s). No trend in the magnitude of this error is found either. If the estimated final position were plotted on a sphere with radius r_{KOS}, it would likewise not show any directional trend, but be randomly scattered around its true desired location.

The estimation error of the final position can, according to Figure 6.4, easily exceed 5 meters, and the estimation of $\boldsymbol{\omega}_{final}$ can thus be identified as the single greatest source of error introduced into the guidance process. Not only does it vary in degree of error, it also varies in direction. Despite the fact that this is not reflected in the ΔV, its impact on the final position is disproportional compared to the guidance error.

To further demonstrate the impact of this error, a comparison can be made using the true value of $\boldsymbol{\omega}_{final}$, rather than an integrated value. Table 6.3 shows the final position error when using the true value of $\boldsymbol{\omega}_{final}$ versus using the integration process. The difference between the two is large, as the final position error achieves sub-meter accuracy when the true value is used, while producing 4 to 5 meters of error when the integration is used.

Table 6.3: Final position error when using true final state versus estimate obtained from integration. See Table 4.1 for the definitions of the level of measurement accuracy.

	Mod_2	Mod_3	Mod_2
Final state estimation	Integrated	Integrated	True
Final position error	4.071	4.856	0.713

Two very important conclusions must be drawn from the analysis of attitude error. First, due to uncertainties in attitude and rotation, the magnitude of the final position error grows large. Whereas imposing the true final position allows the position error to remain at sub-meter level, this error exceeds 4 meters when using the method of integration. Second, and perhaps more importantly, the error is spread over a wide range, which means the error is not predictable. Unpredictability is always undesirable and thus a degree of mitigation is desirable in this scenario. Achieving a more robust estimate for $\boldsymbol{\omega}_{final}$ is therefore elaborately discussed in Chapter 7.

6.1.2. Phase 3

Both the position (and velocity) of the chaser relative to the target, as well as the target rotation, appear in the expression of the desired state for phase 3 (Equation (5.15)). Furthermore, the target attitude is required in the execution of the attitude control law for synchronisation in phase 3 (in the calculation of $\boldsymbol{q}_{TBF}^{RTN}$, see Section 5.1.8).

Position error

To investigate the effect of position errors in phase 3 the true target rotation is used to calculate the desired position using Equation (5.15). This discards the influences of the attitude measurement errors and allows to isolate the position error influences. Initial separation is set to 25m (KOS radius), final separation is set to 5m and the desired relative velocity is set to 5 cm/s, making the nominal time span 400 seconds. The results are summarised in Table 6.4.

Table 6.4: Final error, ΔV and duration for the forced motion of phase 3, averaged over 10 runs with outliers excluded. See Table 4.1 for the definitions of the level of measurement accuracy.

	High 1	High 2	Mod 1	Mod 2	Mod 3
Final error (m)	0.222	0.219	0.603	0.785	1.043
ΔV (m/s)	4.394	4.381	4.743	5.154	5.461
Duration (s)	397	397	395	398	397

As expected, an increase in ΔV is found when the accuracy of the measurements decreases. The duration of the phase does not show significant differences. The most significant result is the average magnitude of the final error, which exceeds 1m for the Mod_2 and Mod_3 cases. Although the errors are found to be almost completely parallel to the Envisat surface (i.e. the error component towards Envisat CoM is small) the magnitude of this error is considered undesirable at a distance of 5 meters. These errors can be completely attributed to the controller, since navigation errors are consistently smaller ($\approx$ 0.2 m) than the position errors reported in Table 6.4. Further increasing the values in $\boldsymbol{Q}$ would not be useful, as Section 5.3.2 has shown that

further increasing $Q_{r,lqr}$ and $Q_{v,lqr}$ leads only to a moderate decrease of the final error, while significantly increasing the total ΔV. The trajectory of phase 3 likely requires either a different control method capable of better following the spiralling reference trajectory, or a different reference trajectory, which was also already concluded in Section 5.3.2. Such methods are however unrelated to any vision-based aspects and not further considered.

Attitude error

The error in estimating $\boldsymbol{\omega}_{RTN}^{TBF/RTN}$ plays a crucial part in this phase of the manoeuvre. As became clear in Section 5.2.3, the estimation of $\boldsymbol{\omega}_{RTN}^{TBF/RTN}$ is the most difficult task of the navigation system, including a high level of uncertainty. When directly using the $\boldsymbol{\omega}_{RTN}^{TBF/RTN}$ estimated by the filter, the noise in $\boldsymbol{\omega}$ raises the required control effort by a very large amount, which is why the choice was made to pass $\boldsymbol{\omega}_{RTN}^{TBF/RTN}$ through a moving mean filter (MMF) (see Section 5.2.3,Figure 5.12). Employing the $\boldsymbol{\omega}$ after passing through the MMF yields convergence but, as Table 6.5 shows, the cost of fuel is still high.

Table 6.5: Final position error, ΔV and duration for the forced motion manoeuvre in phase 3 when using $\boldsymbol{\omega}_{RTN}^{TBF/RTN}$ from the moving mean filter. See Table 4.1 for the definitions of the level of measurement accuracy.

	High 1	High 2	Mod 1	Mod 2	Mod 3
Final error (m)	0.534	0.505	0.799	1.192	1.783
ΔV (m/s)	6.482	9.163	15.559	20.256	22.672
Duration (s)	397	397	394	399	396

Examining the values in Table 6.5 immediately results in the conclusion that these ΔV values cannot be acceptable for this manoeuvre. The reason for this increase in ΔV can be understood from Figure 6.5, showing the reference trajectories available in phase 3, together with the true desired trajectory.

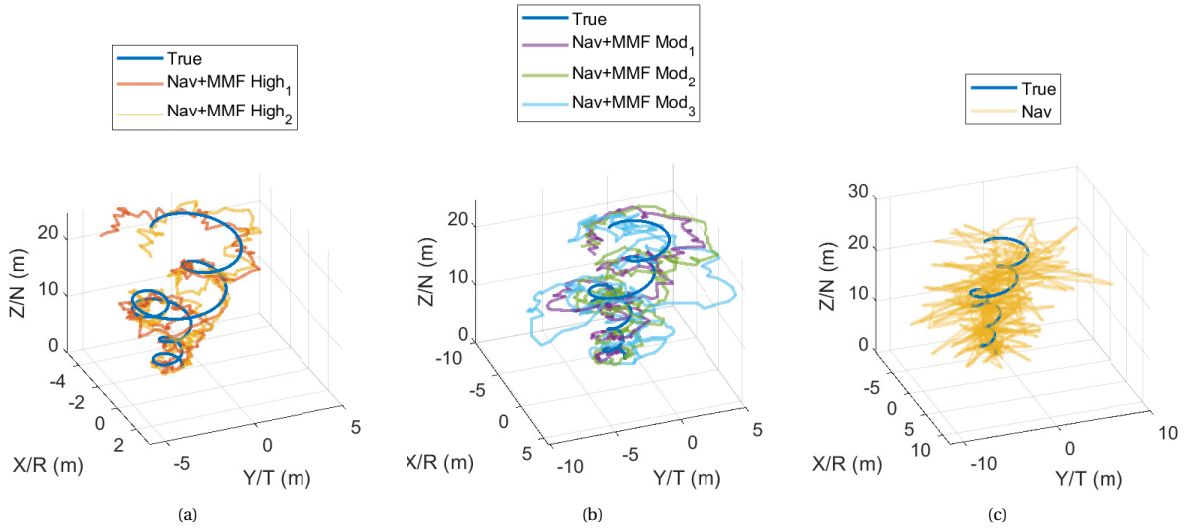

Figure 6.5: Reference trajectories used in phase 3, computed using the true rotation, only navigation (right) and navigation with additional moving mean filter for the high (right) and moderate (middle) levels of accuracy from Table 4.1. It may be observed that the quality of the approximation of the true desired trajectory decreases when measurement accuracy decreases.

It can be seen in Figure 6.5 that the on-board reference trajectory, calculated from Equation (5.15) using the Nav+MMF estimate of $\boldsymbol{\omega}_{RTN}^{TBF/RTN}$, becomes an increasingly worse approximation of the true desired trajectory. This leads to a large increase in ΔV as was shown in Table 6.5, and it is clear that mitigation is desirable to decrease the error on $\boldsymbol{\omega}_{RTN}^{TBF/RTN}$. This mitigation should aim at providing a smoother estimate of $\boldsymbol{\omega}_{RTN}^{TBF/RTN}$.

Furthermore, influence of the attitude error is found in the computation of the reference attitude, $\boldsymbol{q}_{TBF}^{CCBF}$, for the synchronisation of rotational motion in phase 3. However, as outlined in Section 5.1.8, the computation of this reference attitude is based on the target attitude and not its rotation. The attitude estimation error is found to be similar to the value of σ_q in all cases. Tuning of the attitude controller has shown that it is very

difficult to reach the same level of accuracy on the controlled attitude (see Section 5.3.3), and the achieved control error stays of the same magnitude (≈ 7 deg), despite the changing level of measurement accuracy.

6.2. Short periods of high error

Scenarios of high error were outlined in Chapter 4. These scenarios are characterised by a severe decrease in measurement accuracy over a short period of time, due to unforeseen circumstances such as bad relative orientations, reflections, etc. When looking at these scenarios two factors are considered, respectively the length of the error period and the occurrence of the error period at a specific time in the manoeuvre.

The length, or time-span, of the period is expected to be short. It is difficult to define with high certainty what the length of such a period will be, as concluded in Chapter 4, and thus a small range is examined. The choice is made to examine three different period lengths of 30, 60, 120 seconds respectively. The starting times of the periods are determined randomly. The measurements during the nominal part of the trajectory are generated with the Mod_2 level of accuracy, σ_r = 1.0 m / σ_q = 4.0 deg, as presented in Table 4.1. During the short periods of error the measurements from the camera are generated with the Low level of accuracy, σ_r = 5.0 m / σ_q = 15.0 deg, also described in Table 4.1.

6.2.1. Type of Feedback

Feedback, from the pose estimation system to the navigation system, might not always be accurate. Therefore, an analysis is performed with failures occurring throughout the optimal trajectory, changing the type of feedback provided by the pose estimation system. Three types of feedback were described in Chapter 4, which are employed in the analysis of this section. First, true feedback, which means a statistically perfect measurement feedback. Second, optimistic feedback, where the pose estimation system thinks the measurements more accurate than they are in reality and, finally, pessimistic feedback, the opposite of optimistic feedback, where the pose estimation system thinks the measurements less accurate than they are in reality.

True feedback

The resulting open-loop and closed-loop ΔV values, obtained from this scenario, are presented in Figure 6.6, together with the position guidance error and the attitude navigation error. It can be seen that the period of failure hardly influences the total ΔV. When compared to the nominal cases without failure, in Figure 6.2, similar behaviour and ΔV magnitude is found.

It can be concluded that when the feedback is true, the navigation position error is not influenced. Figure 6.6d shows that the navigation position error remains constant, with a magnitude that is consistent with that reported in Table 6.1 for the Mod_2 level. This is an indication that the estimated velocity is sufficiently accurate for the Kalman Filter to accurately update the satellite state, allowing the chaser to remain completely safe, despite the lack of accurate measurements. As a result, also the guidance error (Figure 6.6c) shows no significant differences with respect to the case where no degraded performance of the pose estimation system was present Figure 6.1.

Furthermore, Figures 6.6e and 6.6f shows that both the navigation attitude and rotation error are affected by this failure. In the previous section the estimation errors on the final conditions were discussed, caused by forward integration with small errors in $\boldsymbol{\omega}$. If then this error is significantly increased, which is the case for both attitude and rotation, the guidance system cannot make a reliable estimate of the final desired state during these periods of decreased performance of the pose estimation system, and shall therefore not perform trajectory updates within such a period.

The mean final position error for all runs is presented in Table 6.6. This shows that the final position error is not affected by the length of the period, however, its magnitude is slightly increased when compared to the average final position error achieved by the Mod_2 runs in Table 6.1. The control effort, reflected in the ΔV values is of the same magnitude as in the runs where no periods of decreased performance of the pose estimation system were introduced (Table 6.1).

Table 6.6: Final position error and ΔV for the true feedback scenario.

Period (s)	30	60	180
Final position error (m)	5.352	4.787	4.604
ΔV_{OL} (m/s)	0.252	0.267	0.234
ΔV_{CL} (m/s)	0.261	0.273	0.258

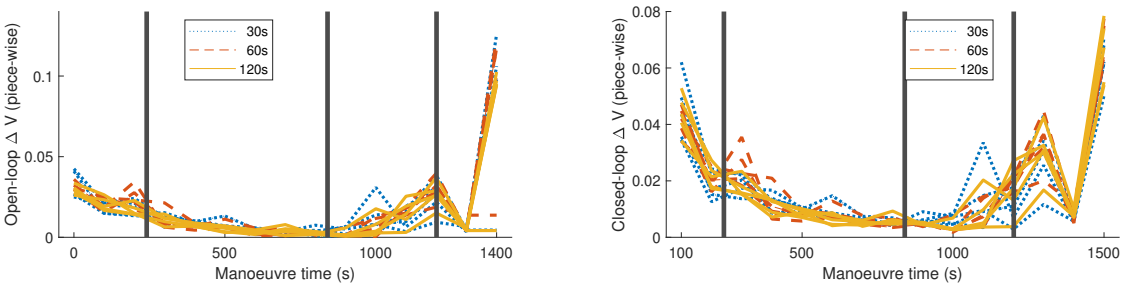

(a) Open-loop, piece-wise ΔV

(b) Closed-loop, piece-wise ΔV

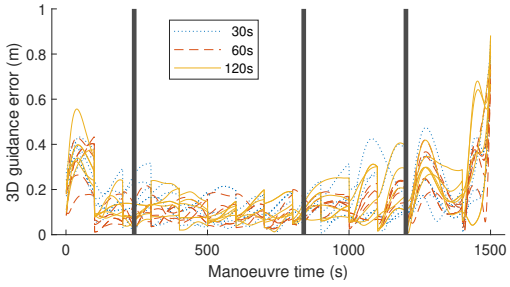

(c) Guidance position error (3D-norm)

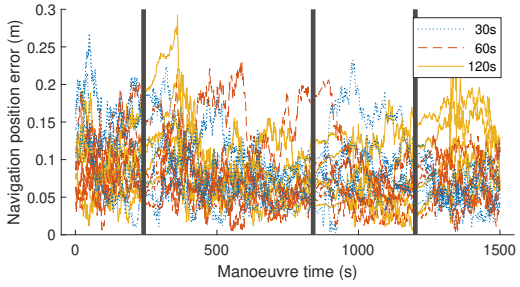

(d) Navigation position error (3D-norm)

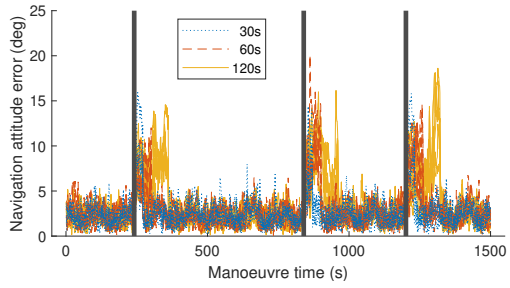

(e) Navigation attitude error (3D-norm)

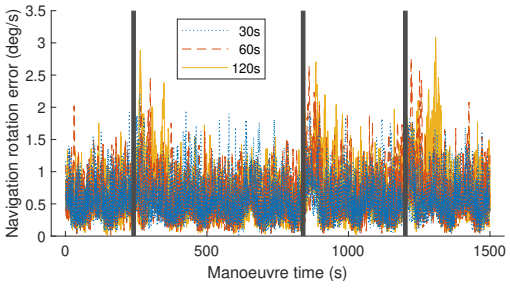

(f) Navigation rotation error (3D-norm)

Figure 6.6: True covariance feedback comparison of open-loop and closed-loop ΔV magnitudes and navigation and guidance error for three different lengths of high error periods. Black lines indicate the start of the error period. When compared to Figures 6.1 and 6.2 it can be noted that ΔV and guidance errors are very similar. This is due to the navigation position error (d) hardly being affected, showing no peaks and being of the same order as the values presented in Table 6.1. The navigation attitude (e) and rotation (f) error show a clear increase in magnitude during the periods of failure.

Optimistic feedback

The resulting open-loop and closed-loop ΔV values for this scenario are presented in Figure 6.7, together with the guidance position error and the navigation position, attitude and rotation error. This shows a completely different behaviour from the scenario with good feedback. Additionally, the final position error and total ΔV for all optimistic feedback runs is provided in Table 6.7.

It can be seen in Figure 6.7 that the open-loop ΔV has only slightly increased, compared to the nominal runs in Figure 6.2, while the closed-loop ΔV shows a significant increase in magnitude, showing multiple peaks extending to values as large as 0.15 m/s (Figure 6.7b) whereas previously these were confined to 0.04-0.08 m/s (Figure 6.6b). From Table 6.7 it becomes clear that the total open-loop ΔV is indeed similar to the nominal cases (i.e. no periods of decreased performance of the pose estimation system) from Figure 6.2, while the closed-loop ΔV shows an increase of approximately 100% compared to the same nominal cases. Furthermore, Table 6.7 suggests that increasing the length of the periods where optimistic feedback is provided, results in a further increase of closed-loop ΔV.

The behaviour of the guidance and navigation position error may be explained by examining the feedback process. Remember that the state covariance is the internal measure of accuracy in the Kalman Filter (see Section 5.2.2). The behaviour of the state covariance for several randomly selected optimistic feedback runs is

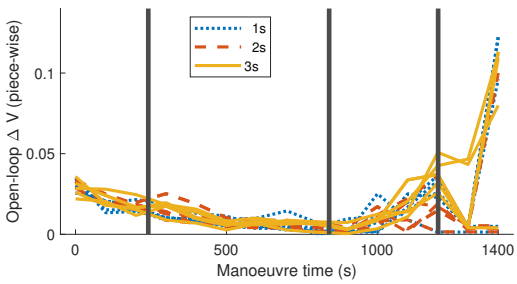

(a) Open-loop, piece-wise ΔV

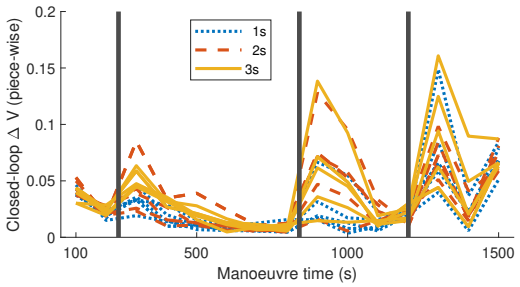

(b) Closed-loop, piece-wise ΔV

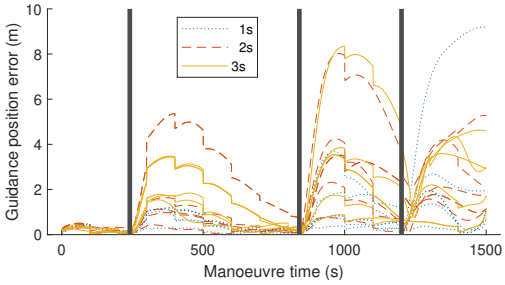

(c) Guidance position error (3D-norm)

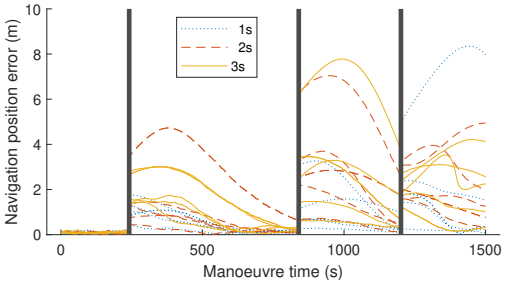

(d) Navigation position error (3D-norm)

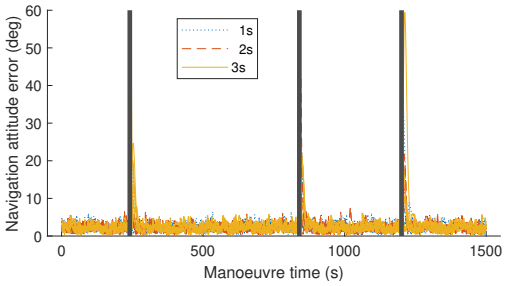

(e) Navigation attitude error (3D-norm)

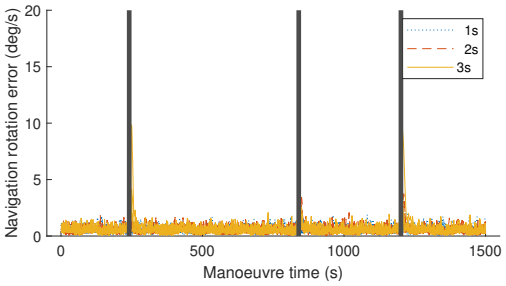

(f) Navigation rotation error (3D-norm)

Figure 6.7: Optimistic covariance feedback comparison of open-loop and closed-loop ΔV magnitudes and navigation and guidance error for three different lengths of high error periods. Black lines indicate the start of the error period. When compared to Figure 6.6 it can be noted that ΔV_{OL} (a) is similar, but ΔV_{CL} (b) is increased and shows higher peaks. Guidance position errors (c) are also increased, which can be attributed to an increase in the navigation position error (d) being increased to a magnitude of multiple meters. The navigation attitude (e) and rotation (f) error show a different behaviour compared to Figure 6.6, as errors are larger, but remain present only for short periods of time.

presented in Figure 6.8, where it can be seen that it is reduced during this period, resulting in the filter thinking it has become more accurate, rather than less accurate. The optimistic feedback has caused the navigation filter to think that it is performing more accurately than before, while in reality a failure is occurring.

This behaviour is caused rather by the valuation of the measurement in the filter. Because the measurements are thought to be accurate, the filter adapts the velocity and rotation to accommodate the position and attitude obtained from the measurement. Accordingly it adapts the state covariance to be consistent with the measurement that was thought to be accurate. However, as the measurement was not accurate in reality, this leads to the creation of velocity error, and consequently position error, as well as a wrongful update of the state covariance.

Especially the wrongful update of the state covariance presents an issue for the navigation filter, as it fails to value the subsequent measurements correctly. At this point the state covariance, used to value the internal propagation, overrules the measurement covariance, used to value the measurements, and the navigation errors persist at a large magnitude, as can be observed in Figure 6.7d. Consequently the guidance error (Figure 6.7c), which is an accumulation of navigation and control errors (see Section 4.4), persists at a large magnitude.

Table 6.7: Final position error and ΔV for the optimistic feedback scenario.

Period (s)	1	2	3
Final position error (m)	5.949	4.531	5.571
ΔV_{OL} (m/s)	0.211	0.209	0.293
ΔV_{CL} (m/s)	0.398	0.499	0.544

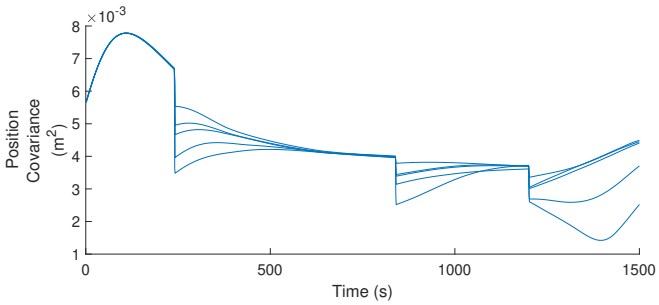

Figure 6.8: Position state covariance, as evaluated withing the navigation filter, based on optimistic feedback. The instants at which the period of decreased performance is imposed on the pose estimation system can be recognised by the sudden decreases in state covariance.

This slow recovery of the navigation error can, however, not be completely attributed to the state covariance, as it must be partially assigned to the tuning of the filter. The state noise Q_v seems to be too tightly tuned, such that it does not allow for enough noise to be introduced to change the velocity rapidly, such that the position error may also be reduced rapidly. This theory is supported by the behaviour of the navigation attitude error (Figure 6.7e), which does not experience this problem and is returned to its nominal value rather rapidly, despite suffering from a similar decrease in attitude state covariance upon the introduction of the optimistic feedback.

It is clear that mitigation strategies against this scenario, should be put into place. These strategies should focus on recognising periods where the measurement feedback is too optimistic, such that measurements might be discarded despite the feedback telling the system that the measurement is of high quality.

These results function as an unmistakable warning, both for guidance as well as pose estimation systems. If even a single measurement is valued too optimistically, without any possibility to discard this measurement, the consequences for the total ΔV can be severe.

Pessimistic feedback

Finally, the resulting open-loop and closed-loop ΔV values for the pessimistic feedback scenario are presented in Figure 6.9, together with the guidance position error and the navigation position, attitude and rotation error, showing many similarities with the true feedback scenario. Furthermore, the mean final position error and average total ΔV for all cases are presented in Table 6.8.

Table 6.8: Final position error and ΔV for the pessimistic feedback scenario.

Period	30s	60s	120s
Final position error	4.038	4.770	4.630
ΔV_{OL}	0.271	0.261	0.265
ΔV_{CL}	0.284	0.252	0.270

By comparing Table 6.8 with Table 6.6 it can be concluded that providing true or pessimistic feedback does not influence the final position error or total control effort. Similar to what was found for the true feedback case, final position error is not influenced by the length of the period of decrease pose estimation performance, neither is the ΔV.

Comparing the resulting ΔV and error from the optimistic feedback case (Figure 6.7) with those presented in Figure 6.9 for the pessimistic feedback case, it might be concluded that a pessimistic feedback representation results in lower ΔV_{CL} as well as lower navigation and guidance errors. This is an indication that, when estimating the measurement accuracy, pose estimation systems should prefer a conservative (pessimistic)

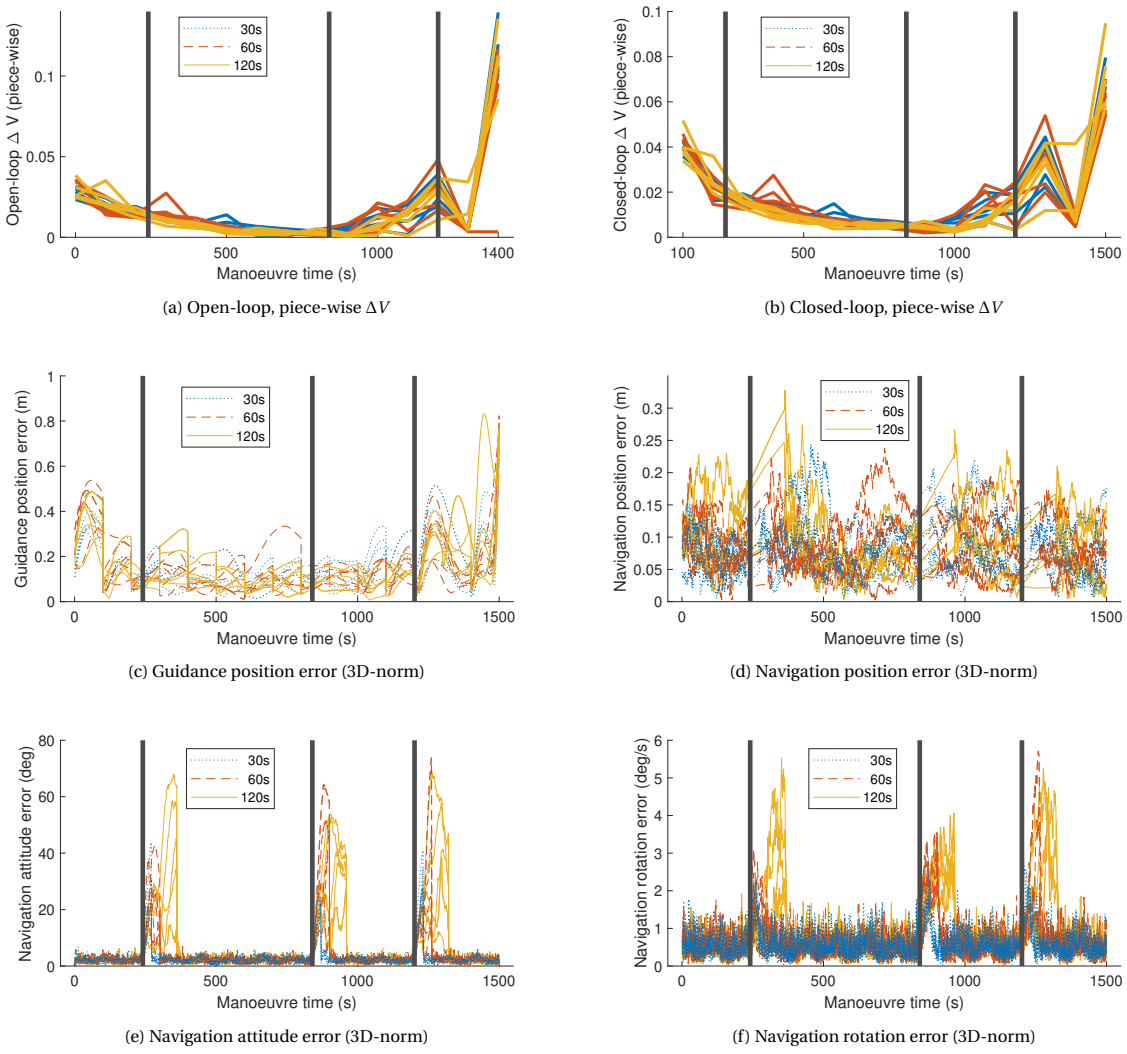

(a) Open-loop, piece-wise ΔV

(b) Closed-loop, piece-wise ΔV

(c) Guidance position error (3D-norm)

(d) Navigation position error (3D-norm)

(e) Navigation attitude error (3D-norm)

(f) Navigation rotation error (3D-norm)

Figure 6.9: Pessimistic covariance feedback comparison of open-loop and closed-loop ΔV magnitudes and navigation and guidance error for three different lengths of high error periods. Black lines indicate the start of the error period. It can be noted that both ΔV_{OL} (a) and ΔV_{CL} (b) are very similar to the true feedback case (Figures 6.6a and 6.6b). Guidance position errors (c) are also similar and the same can be said about the navigation position error (d). The navigation attitude (e) and rotation (f) error also show similar behaviour compared to Figure 6.6, however, the magnitude of the errors during the periods of decreased pose estimation performance is increased.

estimation of the measurement accuracy, and assign a measurement covariance that presents the measurement as less accurate than it is in reality, rather than more accurate.

Furthermore, Figure 6.9e shows that the attitude estimate is severely affected by this failure, as was found also in the case of true feedback (Figure 6.6e). Due to the estimation error in the final conditions, caused by forward integration with uncertainties in $\boldsymbol{\omega}$, the advice was issued not to perform trajectory updates during these periods of decreased performance of the pose estimation system. Considering the severity of the navigation attitude and rotation errors, respectively exceeding 60 deg (Figure 6.9e) and 4 deg/s (Figure 6.9f, which is larger than the Envisat's main rotation, it is likely that the trajectories calculated during this period are characterised by high ΔV_{OL}, and are consequently rejected by the strategy presented in Section 5.1.3. This is indeed observed in the data, however, a mitigation strategy is still desirable.

6.2.2. Placement of the error period

In this section only periods of decreased pose estimation performance are considered using true feedback. The length of the periods is fixed to 60 seconds for all runs and nominal accuracy is set to the Mod_2 level, σ_r = 1.0 m / σ_q = 4.0 deg (see Table 4.1). The periods in this analysis are strategically selected to be at the beginning, middle and end of the trajectory. Additionally these periods are placed such that either a guidance update is

performed in the middle of the period, or that a period is places completely in-between two updates of the guidance trajectory.

More specifically, with t_{up} = 100 s (see Section 5.1.5), failures are introduced during and after guidance updates #3, 8 and 14 (total 15, first at t = 0 s), at t_{f1} = 170, 670, 1270 seconds and t_{f2} = 220, 720 and 1320 seconds. As guidance updates are performed every 100 seconds, the first set, t_{f1}, ensures that guidance is updated in the middle of the 60 second period, while the second set, t_{f2}, ensures that no guidance updates occur during the 60 second period. Five runs are evaluated for each scenario.

The resulting open-loop and closed-loop ΔV values, as well as the navigation guidance error are all found to be very similar to those reported before in Figure 6.6, as might be expected. Therefore these are not presented here to avoid repetition. This is confirmed by the data in Table 6.9, summarising the total final position error and ΔV, the values in this table being very similar to Table 6.6.

Table 6.9: Final position error and ΔV for the scenarios with periods of decreased pose estimation performance occurring both at and in-between guidance trajectory updates.

	Begin	Middle	End
At guidance updates			
Final position error	3.695	4.559	4.267
ΔV_{OL}	0.266	0.239	0.265
ΔV_{CL}	0.262	0.268	0.272
In-between guidance updates			
Final position error	4.130	4.352	4.730
ΔV_{OL}	0.274	0.280	0.222
ΔV_{CL}	0.268	0.272	0.283

Furthermore, it is found that there is no observable correlation between the final ΔV magnitude and failure at or in-between guidance updates. This is slightly curious, as theoretically the end of the trajectory should thus be the worst time to enter a period of decreased performance. Failure at the beginning or middle of the trajectory should allow sufficient time for corrections, arriving with the nominal amount of error. Failure at the end of the trajectory, however, would cause the forward integrated estimate of the final position to be completely wrong, therefore inducing more ΔV or increasing the final position error. When further examined, this expected behaviour is already mitigated by the strategy outlined in Section 5.1.3 for rejecting newly formed guidance trajectories. In fact, all of the trajectories that were calculated at t = 1300 when a period of failure was introduced at this time were rejected by this strategy, preventing a possible excessive growth of ΔV.

It is however observed that navigation attitude error is significantly increased during period of decreased pose estimation performance, shown in Figures 6.6e and 6.9e and also true here. This increase in error on the estimation of attitude, and consequently rotation, has a significant influence on the correct estimation of the trajectory by the guidance system, despite not being visible in the behaviour of the ΔV and guidance error. In order to quantify the effect of the decreased performance of the pose estimation system on the ability of the guidance system to calculate the final conditions correctly, a data analysis was performed, comparing the average final position error obtained during periods of decreased pose estimation performance with the same error obtained when this decrease in performance was not present. This analysis only considers the 3D norm of the position error on the desired final position, calculated using Equation (5.9). The results of this analysis are presented in Table 6.10.

It can be seen in Table 6.10 that, on average, the final position error is nearly doubled due to the influences of decreased performance of the pose estimation system. Despite this behaviour not resulting in an increase of control effort or guidance error, it is still undesirable and mitigation strategies should be put into place to reduce either the occurrence of periods of decreased pose estimation performance, or their impact on the estimation of the desired final conditions, or both. Let it be noted, finally, that this short analysis does not do justice of the subtleties of the error in the estimate of the final desired position, as this error comes from multiple sources in various degrees. As the final position estimation error has been identified as a large source of error on multiple occasions in this chapter, a more detailed analysis of this error is provided in Chapter 7.

Table 6.10: Results of data analysis on the quantification of final position error from decreased pose estimation performance. The largest contribution of error comes from the pessimistic feedback case and, on average, the decreased performance of the pose estimation system causes the final position error to nearly double (196%).

	Begin		Middle		End		
	Average estimation error (m)	(%)	Average estimation error (m)	(%)	Average estimation error (m)	(%)	
No failures (Mod_2)	5.473	100.00	3.196	100.00	5.548	100.00	
True feedback	6.353	116.09	6.586	206.05	9.903	178.52	
Optimistic feedback	6.438	117.63	3.341	104.53	6.018	108.49	
Pessimistic feedback	7.299	133.37	17.579	549.99	13.976	251.94	
Total average	6.697	122.36	9.169	286.86	9.966	179.65	**196.29%**

6.3. Conclusions

The analysis in this chapter has shown the potential difficulties that could be experienced when guiding a spacecraft for scenarios typical for vision-based systems. The conclusions that may be reached from it are listed here.

First, as long as the navigation filter receives proper feedback about the accuracy of the measurements, the GNC algorithm is able to perform correctly. When the measurements become inaccurate, a pessimistic estimation of their accuracy is preferred to an optimistic one, however, both require a form of mitigation. The different scenarios provide completely different challenges, as the forms of feedback result in different responses from the GNC system, which require different methods to recognise and prevent failures.

Second, the most important conclusion of this chapter is the identification of the integration process, used to predict the target attitude dynamics, as the largest source of error in the GNC system. Whereas the guidance error is at a sub-meter level, the estimation error on the final desired position easily exceeds 4 meters due to an inaccurate prediction of the target's rotational dynamics. Furthermore, the estimate is highly sensitive to small uncertainties and is unpredictable when integrated over long time periods.

Third, there is a very low correlation between measurement accuracy and ΔV. Both the open-loop and closed-loop ΔV are surprisingly robust with respect to measurement accuracy. Reasons for this could be found in the optimisation process, which can not succeed in finding the absolute optimal trajectory most of the time. This might be investigated in further research, as it is outside the scope of this research. Furthermore, no correlation is found between time of failure and ΔV either.

Finally, a tendency of the open-loop ΔV to increase near the end of the trajectory could be observed. This behaviour is also found when imposing true (constant) final conditions, implying that it is a property of the most optimal trajectory.

In order to improve the GNC performance, several mitigation strategies should be explored, as well as strategies for a more accurate prediction of the target attitude dynamics. Based on the conclusions found in this chapter, these strategies should allow to

1. Recognise error periods and implement suitable strategies for mitigation of failure in these periods. This will be discussed in Section 7.1.

2. Make a more accurate prediction of the target attitude dynamics, or at least a less sensitive prediction. This will be discussed in Section 7.3.

Two recommendations for further research are made based on this chapter. First, a variable controller tuning could be considered such that the the guidance error at the beginning and end of the trajectory can be decreased. Second, the trajectory for phase 3 might require a redesign, as the controller has great difficulty to correctly follow the spiral, burning a lot of valuable fuel in the process.

7

Strategies for Increased Robustness

This chapter provides a number of methods that aid in the recognition and mitigation of error within the vision-based GNC system. The chapter starts by outlining two strategies for error recognition in Section 7.1. These strategies are based on respectively the state covariance and comparison of the position navigation estimate to a propagated state.

Section 7.2 continues with a quantification of the performance of the forward integration, used to determine the final desired state. The need for a more robust estimate of the target future rotation was established in Chapter 6, but the sensitivity of the current solution should be explored first. This provides a basis for comparison, as Section 7.3 presents a new method for estimation of the final desired state, based on curve fitting, which should be both more robust and more accurate. This new method is compared to the integration method in Section 7.4. Finally, Section 7.4.1 shows the impact of both the new method, as well as the strategies presented in Section 7.1, on the GNC algorithm.

7.1. Recognition and Mitigation

The first step to addressing the failure cases, which were identified in the previous chapter, is being able to recognise moment of failure. Directly after recognition, a strategy must be implemented to mitigate the undesirable behaviour that was recognised. The navigation architecture has the ability to recognise part of these errors itself, using the state covariance matrix P_{state} (see Section 5.2). This is however not sufficient in all cases, as situations might occur where the state covariance is not a reliable metric. Examples of such situations can be found in scenarios where the measurement feedback is inaccurate, as was discussed in Section 6.2.1. For this reason a second method is considered, complementary to the feedback received from P_{state}. A method for error recognition based on the state covariance is outlined first, after which this second method, based on a linearly propagated state, is discussed.

7.1.1. State covariance

An estimate of the state covariance is always present in a Kalman Filter and is updated with the state noise and the measurement covariance, as explained in Section 5.2. The state noise was tuned in Section 5.2.3 and remains constant. The measurement covariance is the feedback metric from the measurements, providing an indication of the accuracy of the measurements. As this feedback is not always accurate, three types of simulated feedback were proposed and outlined in Section 4.3.1, namely true, optimistic and pessimistic feedback, where true feedback represents a statistically perfect representation of the measurement accuracy, optimistic feedback presents the measurements as more accurate than they are in reality and pessimistic feedback presents the measurements as less accurate than they actually are.

Behaviour

The behaviour of the state covariance for position and attitude is presented in Figures 7.1 to 7.3, for the three scenarios analysed in Chapter 6 with true, optimistic and pessimistic measurement feedback respectively. Only position and attitude covariance are shown, as the state covariance of velocity and rotation is a reflection of the state covariance of position and attitude, only with a smaller magnitude.

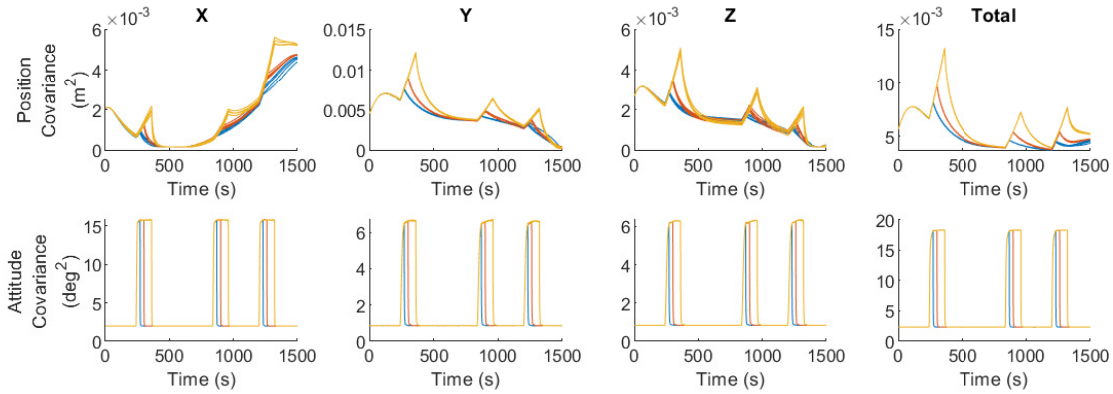

Figure 7.1: Position and attitude covariance for the failure periods with true feedback. The different colours represent the different lengths of the failure periods, respectively 30 (blue), 60 (red) and 120 (yellow) seconds. Three instances of decreased performance of the pose estimation system may be recognised from the triangular peaks (top) or the square peaks (bottom) in the covariance data. Especially the behaviour of the attitude covariance lends itself excellently for detection, as it shows large differences between nominal performance and decreased performance, whereas these differences are smaller for the position covariance.

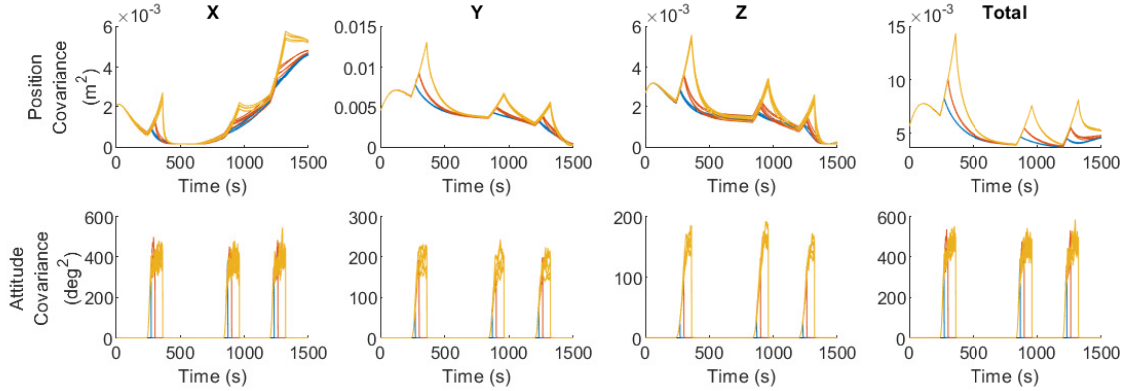

Figure 7.2: Position and attitude covariance for the failure periods with pessimistic feedback. The different colours represent the different lengths of the failure periods, respectively 30 (blue), 60 (red) and 120 (yellow) seconds. Three instances of decreased performance of the pose estimation system may be recognised from the triangular peaks (top) or the square peaks (bottom) in the covariance data. It can be observed that the behaviour of the covariance is similar to that of the true feedback case, however, the magnitude of the peaks, especially in the attitude covariance, is increased.

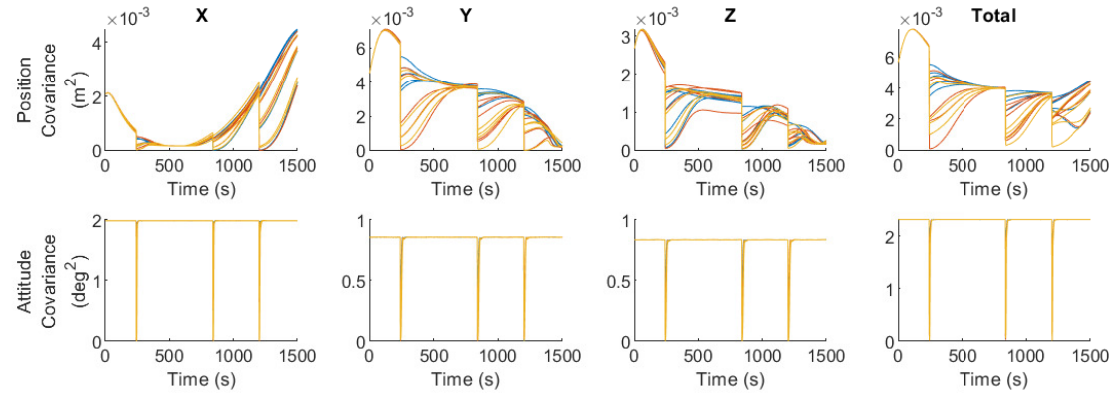

Figure 7.3: Position and attitude covariance for the failure periods with optimistic feedback. The different colours represent the different lengths of the failure periods, respectively 1 (blue), 2 (red) and 3 (yellow) seconds. Three instances of decreased performance of the pose estimation system may be recognised from the steep sudden drops in the covariance data. It can be observed that the covariance behaviour in this particular case is opposite the behaviour observed for the true and pessimistic feedback cases, where the covariance showed peaks rather than drops.

Using the case with true feedback (Figure 7.1) as example, it can be shown that the magnitude of P_{state} correctly reflects the actual navigation error in the case of nominal performance of the pose estimation system. Observing from Figure 7.1, the total position covariance, P_{pos}, is approximately between 0.001 and 0.01 m^2. Similarly, the total attitude covariance P_{att} has a value of approximately 3 deg^2. This indicates a standard deviation, σ, between 0.01 and 0.1 m for position and 1.7 deg for attitude. The mean accuracy in these cases was reported in Table 6.1 (Mod_2 level) and found to be 0.084 m for position and 2.157 degrees, of which P_{state} is thus a good reflection. Furthermore, navigation position error was found to be smaller than 0.3 m at all times (see Figure 6.6d) and navigation attitude error was found to be mainly smaller than 5 deg (see Figure 6.6e), both of which are within a 3σ interval.

The estimate of the state covariance is only a good reflection of the true accuracy as long as the feedback is consistent with the real accuracy of the measurements, however, a truly accurate feedback of the measurement is not always possible. This can be observed for the cases of pessimistic and optimistic feedback, in respectively Figures 7.2 and 7.3, which show that when the measurement covariance is not accurate, neither is the state covariance. In the case of pessimistic feedback, navigation attitude errors were found in the order of 40-60 deg (see Figure 6.9e) whereas the state covariance indicates errors of approximately 20 deg (400 deg^2, see Figure 7.2). In the optimistic feedback scenario navigation position errors grow to several meters (see Figure 6.7d), whereas the state covariance indicates that the measurement has become more accurate, which was also highlighted in Section 6.2.1.

Recognition Strategy

Now that it is understood how the state covariance reflects the true system behaviour, recognition strategies can be planned. Most importantly, the periods of failure can be recognised in Figures 7.1 to 7.3, which means that the state covariance might be used as an indicator to track situations where mitigation is desirable. As the behaviour of the state covariance in the true and pessimistic feedback cases is similar, a similar strategy for recognition may be implemented. In these cases the state covariance experiences an increase, and a threshold might be determined above which mitigation should be performed.

In the case of optimistic feedback, however, the state covariance shows opposite behaviour and decreases rather than increases, requiring a different strategy. Setting a threshold value is not desirable in this case, as it would of necessity, due to the behaviour of the state covariance, be an upper threshold, below which values of the state covariance should be discarded. When values of the state covariance should, however, rightfully move below this threshold, they should definitely not be rejected, which would require the formulation of many exceptions. As such, a different method is formulated for the scenarios with optimistic feedback, which is reported in Section 7.1.2. Below continues the description of a method for recognition of error based on the state covariance metric, to be used in the cases of true and pessimistic feedback. The strategies presented below are only suitable when state covariance increases, as they depend on a lower threshold.

It could be observed in Figures 7.1 and 7.2 that the attitude covariance is a more suitable metric, compared to the position covariance, as its behaviour shows larger differences between nominal and decreased performance. It was determined that the absolute magnitude of the attitude state covariance is not always a reliable indicator, and therefore working with a threshold value on the magnitude is not always desirable. Rather, the change in magnitude

$$\Delta|P_{\text{att}}| = |P_{\text{att}}|_t - |P_{\text{att}}|_{t-\Delta t} \tag{7.1}$$

is first considered, where $|P_{\text{att}}|_t$ represents the norm of the attitude covariance (right-bottom in Figure 7.1) at time t. $|P_{\text{att}}|$ is chosen as a metric since it can be observed from Figures 7.1 and 7.2 that P_{att} shows only little variations during nominal performance, while rapidly increasing when performance of the pose estimation system is decreased. Therefore evaluating $\Delta|P_{\text{att}}|$ over small intervals of time Δt should yield ≈ 0 during nominal performance, being able to recognise periods of failure, as these would result in much larger values of $\Delta|P_{\text{att}}|$.

Approach 1: Threshold ΔP

One option is to select a suitable threshold value for $\Delta|P_{\text{att}}|$, and employ a mitigation strategy whenever this value is higher than the threshold. The first step in the selection of a suitable threshold value for $\Delta|P_{\text{att}}|$ would be the selection of a suitable interval Δt over which $\Delta|P_{\text{att}}|$ shall be evaluated. In order to evaluate this strategy, the value of $\Delta|P_{\text{att}}|$ was computed for the attitude covariance presented in Figure 7.1, for a range of Δt from 10 to 300, the results of which are presented in Figure 7.4.

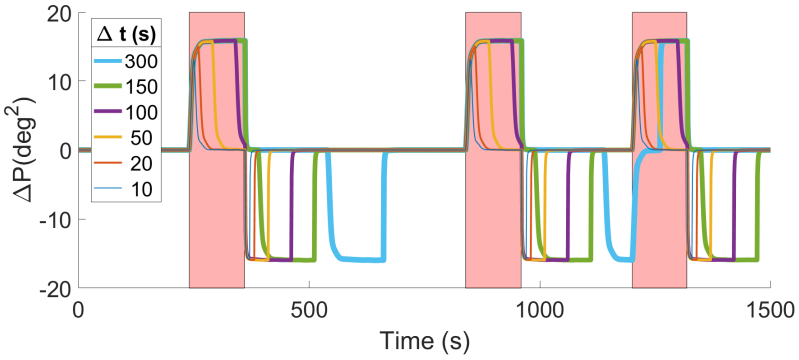

Figure 7.4: Computed values of $\Delta|P_{att}|$, using Equation (7.1), over different time intervals Δt between 10 and 300 s. The true periods of decreased performance have been marked in red. It can be observed that when Δt is too small the period is not entirely detected, however, when Δt is too large, subsequent periods might not be properly detected, as happens with the third period for Δt = 300 s.

From Figure 7.4, two important issues arise when using this strategy. First, when the value of Δt is chosen too small, the strategy is unable to detect the entire period. Second, when the value of Δt is too large, this strategy is unable to identify two periods of decreased performance when following each other closely. This is demonstrated by the case with Δt = 300 s in Figure 7.4. This strategy would thus require Δt to be a good reflection of the duration of the period of decreased performance of the pose estimation system. As this duration is unknown and cannot be predicted beforehand, this is considered a large weakness of this method, and this method should not be used.

Approach 2: Threshold ΔP + Logical

An alternative approach can be based on setting two threshold values, one positive and one negative. As can be seen in Figure 7.4, the behaviour of $\Delta|P_{att}|$ is such that is is positive at the beginning of the period of decreased performance and negative at the end of it, both in equal degree, which is a result of its calculation using Equation (7.1). This property can however be used to advantage, exploiting it to define a beginning and end of the trajectory. Rather than employing a mitigation strategy whenever $\Delta|P_{att}|$ is above a defined threshold value, a logical value L_P is introduced, assuming the value of 1 as soon as $\Delta|P_{att}|$ passes the threshold value, and remaining at a value of 1 until $\Delta|P_{att}|$ passes the negative threshold value, only then returning to 0. In this case the mitigation strategy shall be executed whenever $L_P = 1$.

In this case a low value of Δt should be selected, as the value of Δt determines the minimum allowable time between two periods of decreased performance for them both to be correctly detected. From this perspective Δt should be as small as possible, however, from the perspective of a suitable threshold value this is not the case. Figure 7.5 shows the computed value of $\Delta|P_{att}|$, using Equation (7.1), for small values of Δt.

It can be observed from Figure 7.5 that choosing a very small Δt requires a low value for the threshold on $\Delta|P_{att}|$, which could lead to erroneous detection of error periods. For this reason Δt should not be chosen too small. A suitable threshold value must be experimentally determined, based on which the minimal required Δt can be identified. Furthermore, it can be observed from Figure 7.5 that the left side of the 'waves' is continuous, indicating that detection time is only related the the threshold value and that an equal detection time is achieved from any value of Δt high enough to allow detection of the threshold.

A threshold value for $\Delta|P_{att}|$ of 5 deg^2 is experimentally selected, resulting in a minimum value of Δt = 3 s to allow detection. Since during a nominal scenario the state covariance difference $\Delta|P_{att}|$ is expected to be much smaller, 5 deg^2 is considered a value with enough margin to not falsely identify a nominal situation as a period of decreased performance. This value results in a proper and robust detection of the error periods, as shown in Figure 7.6.

The detection of periods of decreased pose estimation performance with this method, for this particular threshold, is possible with a small delay of approximately 3 s (see Figure 7.6). The calculated delay of 3 s must be noted to be consistent with the simulation and its assumptions. The value of this parameter is reality must be determined through experimentation. The correct detection that was shown in Figure 7.6 for a single example run was reproduced over for all runs that have been analysed in Section 6.2.1 with true and pessimistic feedback. Detection rate in the simulation was determined at 100%, but detection rate in a real-world scenario will have to be established in future experiments.

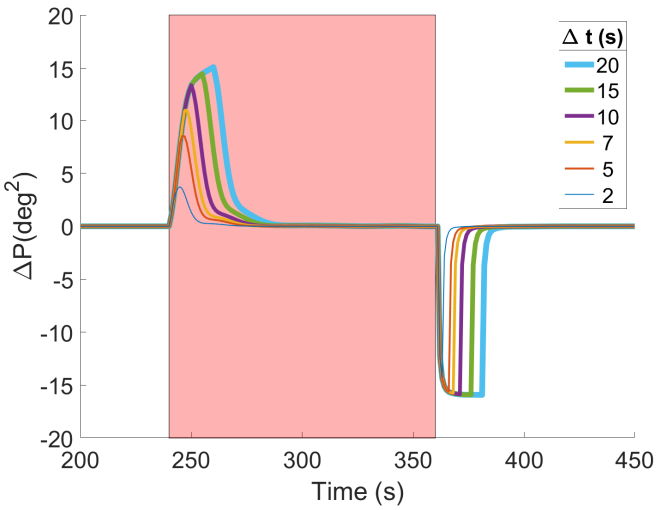

Figure 7.5: Computed values of $\Delta|P_{\text{att}}|$, using Equation (7.1), over different time intervals Δt between 2 and 20 s for t = 200-450. The true period of decreased performance has been marked in red, and is consistent with the first red period in Figure 7.4. It can be observed that when Δt is too small a very small threshold would be required for detection.

Approach 3: Threshold P

A third method can be formulated considering the reason for the desired mitigation. It was established in Chapter 6 that, in the cases of true and pessimistic feedback, the error in the estimation of the final desired position was significantly increased during the periods of decreased performance. A method can then be formulated that detects periods of decreased performance based on the rotation covariance, and the desire to mitigate situations where the rotational error is too large.

It is, however, inconvenient to use the rotation state covariance $|P_{\text{rot}}|$, as the differences in this parameter are small. As an example, it is found that, during the same trajectory represented in Figure 7.1, $|P_{\text{rot}}|$ has a magnitude of approximately 0.25 deg/s in the nominal part of the trajectory and 0.5 deg/s during the periods of decreased performance. Instead of using $|P_{\text{rot}}|$, $|P_{\text{att}}|$ can be used to set a threshold value, as the two show very similar behaviour, $|P_{\text{rot}}|$ being estimated from consecutive measurements of the attitude.

Finding a suitable threshold is difficult, since the value of $|P_{\text{att}}|$ during nominal performance is dependent on the measurement standard deviation σ_q. The estimation of the desired final conditions is dependent on the navigation estimate of ω, the accuracy of which decreases when σ_t is increased. It was experimentally determined that when $\sigma_q > 10$ deg, the mean error on ω exceeds 1 deg/s, which is considered unacceptable in relation to the main rotation of 3.5 deg/s. Furthermore it was found that the value of $|P_{\text{att}}|$ is a good reflection of σ_q. This can be observed in Figure 7.1, right-bottom plot, where the value of $|P_{\text{att}}|$ under nominal pose estimation performance can be seen to have a value of approximately 3-4 degrees, while the measurements were characterised by $\sigma_q = 4$ deg, being a good reflection of $|P_{\text{att}}|$. This was found to be true for a wide range of scenario's and σ_q. Since $\sigma_q > 10$ deg was determined as a limiting case, a threshold value of $|P_{\text{att}}| = 10$ deg^2 is selected. The detection that was achieved with this method is presented in Figure 7.7.

Similar to 'Approach 2', presented above, this method also achieves a 100% detection rate, and the results from Figure 7.7 can be duplicated for all runs with true or pessimistic feedback. This third method has a detection delay at the beginning of the period equal to 6 s, which is slightly larger than that of the second method, however, the delay of detection at the end of the period is only 1 s, which is smaller than that of the second methods.

This approach has the additional characteristic of always executing mitigation whenever expected accuracy is too low. Whereas the previous method using ΔP could theoretically still reach high values of P as long as this would happen slowly ($\Delta P <$ threshold), this method, using a threshold on P, always performs mitigation when $|P_{\text{att}}|$ exceeds the set threshold. This means that, depending on the measurement accuracy, mitigation may be executed over extended periods of time, potentially also during periods of nominal performance. Whether this is beneficial or unfavourable will need to be determined in future experiments with real pose estimation systems.

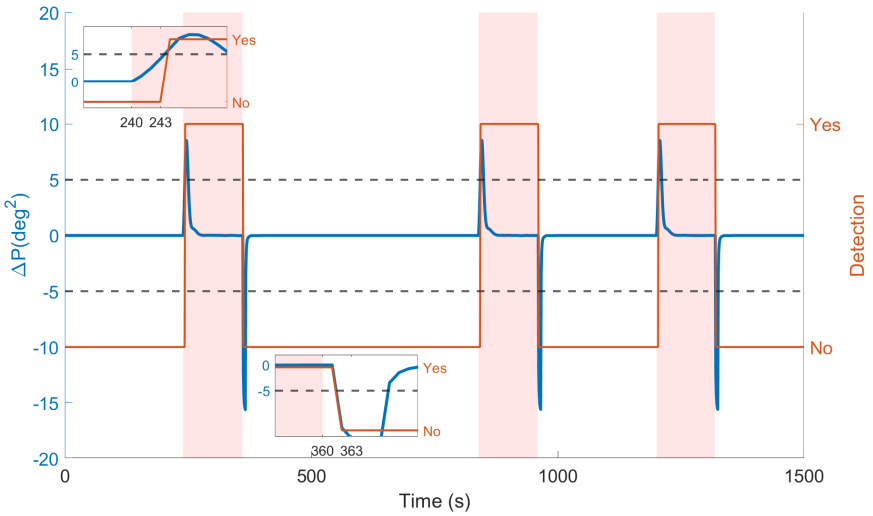

Figure 7.6: Detection of error periods using a threshold value $|P_{att}| = 5$ deg^2. It may be observed that succesful detection is achieved for all periods, marked in red. The behaviour of the detection at the beginning and end of the first period is highlighted, such that it can be better observed that detection of both beginning and end are delayed by 3 seconds.

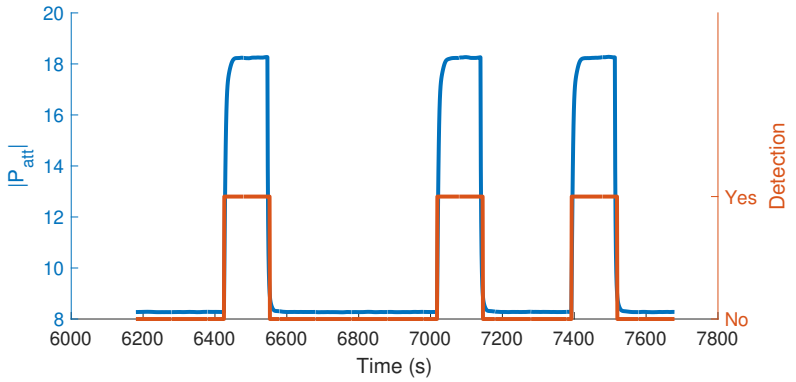

Figure 7.7: Detection of error periods using $|P_{att}| = 10$ deg^2 as threshold value. All periods are again correctly identified. With this method, their beginning time is detected with a delay of 6 seconds, while the end time only eperiences a delay of 1 second in detection.

Conclusion

The first method, using a threshold on ΔP, rejecting the estimate whenever $\Delta P >$ threshold, was discarded directly, as it required the estimate of Δt, the period over which $\Delta P = P_{t+\Delta t} - P_t$ was evaluated, to be a good reflection of the length of the period of decreased performance, as this length cannot be known beforehand. The second method, using a threshold on ΔP in combination with a logical L_P, as well as the third method, using a threshold on P directly, both proved to work properly and both showed a detection rate of 100% in the simulated trajectories.

The differences in these methods lie in the delay of detection, of both the beginning and end of periods of decreased performance of the pose estimation system. It was found that the second method provided delays of 3 s for both beginning and end, while the third method provided delays of 6 s and 1 s for beginning and end respectively. Furthermore the third method might also perform mitigation during nominal performance of the pose estimation system, when the measurement accuracy is too low to achieve a satisfactory accuracy on the estimate of target rotation. Which method is preferable in a real situation needs to be investigated in future experiments. In the analysis of the impact of the proposed mitigation strategies at the end of this chapter (see Section 7.4.1), the third method for recognition is implemented, but similar results may be obtained using the second method.

Intended Mitigation

Finally, the type of mitigation for the recognition strategies presented in this section must be discussed. As these strategies depended on the increase of state covariance, a strong indicator for a loss of accuracy in the estimate of target dynamics, the desired mitigation is the rejection of the estimates of the navigation filter for attitude and rotation. Since the state covariance is increased, no adequate measurements are available and guidance shall be prevented from updating the trajectory based on estimations of the target attitude dynamics made during this period. Preventing this update is especially relevant, as the optimal trajectory uses an estimate of the current rotation to integrate the target attitude and calculate the final desired position of the manoeuvre (see Section 5.1.2), which was shown in Section 6.1 to introduce most (>80%) of the total error on the achieved final position.

When the periods of decreased performance of the pose estimation system exist for prolonged periods of time, or if the measurement accuracy is not adequate for achieving a reliable estimate of the target attitude dynamics, the manoeuvre should possibly be abandoned or a passively safe orbit should be adopted based on the relative position and velocity measurements. Such situations should be further investigated with a real pose estimation system in the GNC loop.

7.1.2. Linear Reference State:

The results from the previous section are not applicable in the case of optimistic feedback. In that case the covariance behaviour is such that the magnitude of the state covariance decreases rather than increases, while the navigation error increases and the guidance is unable to recover properly, as shown in Figure 6.7. Therefore another method is required in addition to the two successful methods that were presented in the previous section.

The Reference State

The proposed additional method compares the state vector that is estimated by the navigation system to a reference state vector, which is propagated linearly from a past navigation state. This approach is suggested as the navigation filter uses both a prediction step (state propagation) and an update step (measurements), see Figure 2.7, and diverges because of the influence of the measurements during the update step. The reason for this divergence was discussed in the section on optimistic feedback in Section 6.2.1. To remove this source of error, a comparison can be made between the current state vector, estimated by the navigation system, $\boldsymbol{X}_{\text{nav},t}$, and a linearly propagated state, $\boldsymbol{X}_{\text{prop},t}$, that does not include the update step nor any process noise. The linearly propagated state is calculated from a past value of the navigation state, $\boldsymbol{X}_{\text{Nav},(t-\Delta t)}$, analogous to Equation (5.2):

$$\boldsymbol{X}_{\text{prop},t} = \boldsymbol{X}_{\text{Nav},(t-\Delta t)} + \boldsymbol{\Gamma}_{t-\Delta t} \begin{bmatrix} \boldsymbol{u}_{t-\Delta t} \\ \vdots \\ \boldsymbol{u}_{t-1} \end{bmatrix} \tag{7.2}$$

where $\boldsymbol{\Gamma}_{t-\Delta t}$ is a convolution matrix, defined as in Equation (5.3), with $\boldsymbol{A}$ and $\boldsymbol{B}$ the linear CWH matrices presented in Equation (3.14) and $\boldsymbol{u}_{t-i}$ the control effort at time $t-i$. This propagation is only performed for position, as attitude is less reliable when considering the larger uncertainties in the estimated target rotation that were highlighted multiple times in Section 5.2.3 and Chapter 6.

Recognition Strategy

Whenever the difference between $\boldsymbol{X}_{\text{nav},t}$ and $\boldsymbol{X}_{\text{prop},t}$ becomes larger than a selected threshold value, a mitigation strategy should be adopted. This process is visually represented in Figure 7.8.

The process represented in Figure 7.8 is valid for the cases with optimistic feedback, described in Section 6.2.1, and builds on the assumption that the linearly propagated state is a very good approximation of the chaser's actual position. A discussion about the validity of such approximation was already provided in Section 3.2, and was found to be valid over short intervals Δt.

Two parameters must be assessed in this analysis. First, a suitable value of Δt can be selected. Second, the threshold value placed on

$$\Delta X = |\boldsymbol{X}_{\text{nav},t} - \boldsymbol{X}_{\text{prop},t}| \tag{7.3}$$

must be determined, where $\boldsymbol{X}$ represents a position vector, $|\ldots|$ is the vector norm and ΔX is a single number, expressed in the unit of meters. The main difficulty lies in choosing a suitable time period Δt over

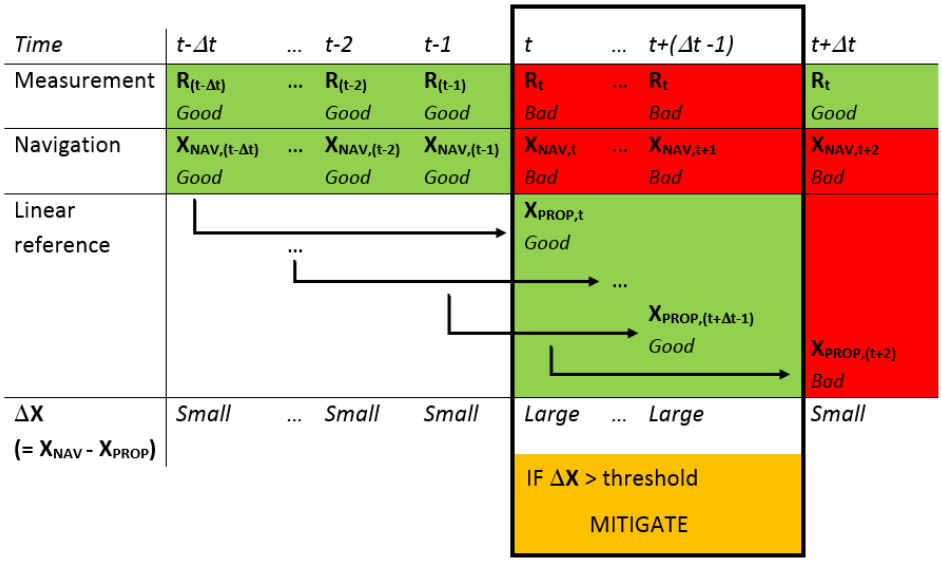

Figure 7.8: Visual overview of the process comparing the estimated state from navigation with a linearly propagated reference state. Because the linearly propagated state is not updated with measurements it is not instantly affected by them, because, due to its definition from $\boldsymbol{X}_{\text{Nav},(t-\Delta t)}$, it 'lags behind' the navigation estimate and is only affected by all measurements up to $t-\Delta t$. Therefore it continues to provide a more robust estimate of the chaser position for an interval Δt after the failure. This overview is only valid for the cases with optimistic feedback (see Section 6.2.1).

which the reference trajectory is to be propagated. If the value of Δt is too large, a significant amount of linearization error may be introduced and the propagated state loses its value as an accurate reference. However, if the value of Δt is too small, the difference between $\boldsymbol{X}_{\text{Prop},t}$ and $\boldsymbol{X}_{\text{Nav},t}$ may be too small to be observed, in the case when the navigation filter diverges slowly. A good value for Δt may be determined experimentally and a number of candidates have been selected

$$\Delta t = 5, 10, 20, 50, 100$$

The threshold should be selected sufficiently larger than the expected differences between the navigated and linearly propagated state. The results of preliminary analysis of ΔX are presented in Figure 7.9a. As it is clear from Figure 7.9a that this parameter can be noisy in periods when no decreased performance of the pose estimation system is found, the differentiated parameter $d\Delta X/dt$ is also analysed, and the results of this analysis are presented in Figure 7.9b.
From Figure 7.9 it can be observed that, when Δt is too large, the error between the propagated state and navigation estimate can easily exceed 1 meter even when no failure is present, which can be accounted to linearization errors and control uncertainties (see Section 5.3). This is an undesirable property and given an impression of a 'noisy' propagated state. Therefore the analysis is adjusted to include the time derivative of ΔX, rather than ΔX itself, as this time derivative shows a less noisy behaviour during periods of nominal performance, remaining ≈ 0.

The magnitude of the peaks in Figure 7.9b can be observed to be unrelated to the value of Δt, such that error can be identified from all values of Δt equally well. This is likely related to the nature of the error, which is caused by the optimistic feedback (see Section 4.3.1). Due to this feedback the measurements are valued too highly, causing a high error over a very short period of time. This behaviour is outlined in more detail in Section 6.2.1. This means that a low value for Δt is an excellent choice, also considering that propagation over short periods of time naturally results in smaller errors when compared to the navigation estimate, as linearization errors compound over time. As could be observed in Figure 7.9b, errors in a nominal situation are very small, and the threshold value for recognition can also be relatively low. When selecting $\Delta t = 5$ s, the value of $d|X_{\text{prop}} - X_{\text{nav}}|/dt$ for nominal performance of the pose estimation system is in the order of 1 cm. A threshold value of 10 cm is selected, as this is considered sufficient margin (1000%) compared to the nominal performance. This combination of threshold and Δt is sufficient for a 100% success rate in the recognition of periods of decreased performance, with optimistic feedback, in all simulated runs. On some cases the detection of the periods is found to be lagging 1 or 2 seconds behind the actual occurrence of the period.

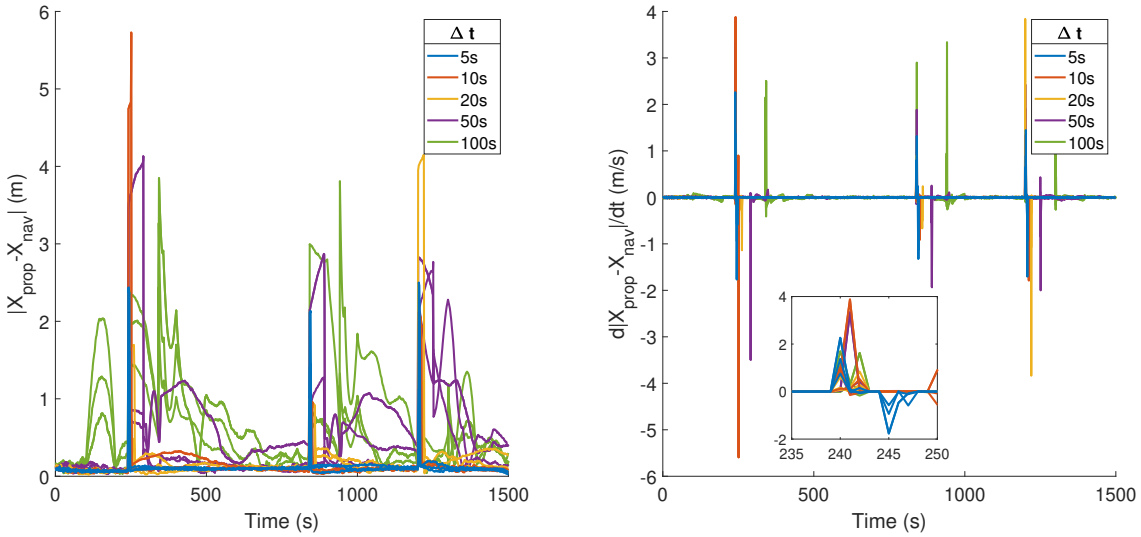

(a) 3D vector norm of error.

(b) Time derivative of 3D vector norm of error.

Figure 7.9: Position difference between the estimate of the navigation system and a linearly propagated reference, for a selection of propagation times Δt (see Equation (7.2)). Periods of decreased pose estimation performance are found at t = 241, 840 and 1201 s. The left shows ΔX (Equation (7.3)) and the right its time difference $d(\Delta X)/dt$. It can be seen that the time difference is less noisy and therefore a better candidate for introducing a threshold.

The validity of this combination of threshold and Δt shall be verified in future experiments with real pose estimation systems under realistic operating conditions.

Intended Mitigation

Contrary to the scenarios with true and pessimistic, where the decreased performance of the pose estimation system is assumed over an extended period of time (60-120 s), scenarios with optimistic feedback are expected to last only 1-3 s (see Section 4.3.1), therefore a different method of mitigation is required. If a period of decreased performance is recognised using this method, it indicates a failure of the navigation system. The filter state $\boldsymbol{X}_{\text{nav},t}$ shall thus be reset, by overriding it with a state that is not updated with the measurements at time t. Both position and attitude shall be propagated from the previous estimate ($X_{\text{nav},t-1}$) and the relative velocity and rotation shall be copied directly from this previous step, which should provide a reasonably accurate estimation. Furthermore, the state covariance shall be replaced with the value that was identified at the previous step (t-1). Performing this reset step also prevents the occurrence of the negative peaks that could be observed in Figure 7.9b.

As explained previously, an optimistic feedback scenario is expected to occur only for a very short period of time, as it would be caused by a single image or a short series of images providing a wrong pose estimate. If, therefore, this filter reset is performed for periods longer than 30 seconds, there is likely some other problem with the pose estimation system and the manoeuvre should be abandoned to ensure the safety of the chaser spacecraft. Such situations, however, should be more closely studied with a real pose estimation system in the GNC loop.

Finally, the accuracy of the propagated state could potentially be improved by including the J_2 perturbation in the CWH STM to decrease the linearization errors. The effects of this correction are, however, marginal over the periods of length Δt suggested here. It is found that the capacity of the above method to recognise the periods of decreased performance is not increased by including the J_2 perturbation.

7.1.3. Impact on Guidance

Two different methods of recognition were discussed. The first strategy was based on the state covariance, and could be used with the true and pessimistic feedback cases. The second strategy used a linearly propagated reference state and could be used in cases with optimistic feedback.

State covariance method

A comparison of the control effort for the cases of true and pessimistic feedback with or without the implementation of the recognition strategy resulted in no significant differences. As could be seen previously in Figure 7.7, the error periods are correctly recognised, however, the rejection of guidance updates in these periods does not significantly influence the total open- or closed-loop ΔV. This is most likely due to the fact that less efficient trajectory estimates are already rejected based on their ΔV value, as described in Section 5.1.3.

This conclusion is consistent with the analysis conducted in Section 6.1.1 concerning the attitude error, where it was shown that using the true final state severely decreased the final guidance error, however, the ΔV was unaffected. It is still believed that keeping the recognition strategy and subsequently rejecting these trajectories is the best choice, since the large final position error resulting from these periods of decreased pose estimation performance, is under no circumstances desirable.

Reference state method

The resulting navigation error and state covariance from an evaluation of several runs with short periods of decreased performance of the pose estimation system, with optimistic feedback, are presented in Figures 7.10 and 7.11. The only difference between these runs and those from Section 6.2.1 with optimistic feedback is the active mitigation strategy.

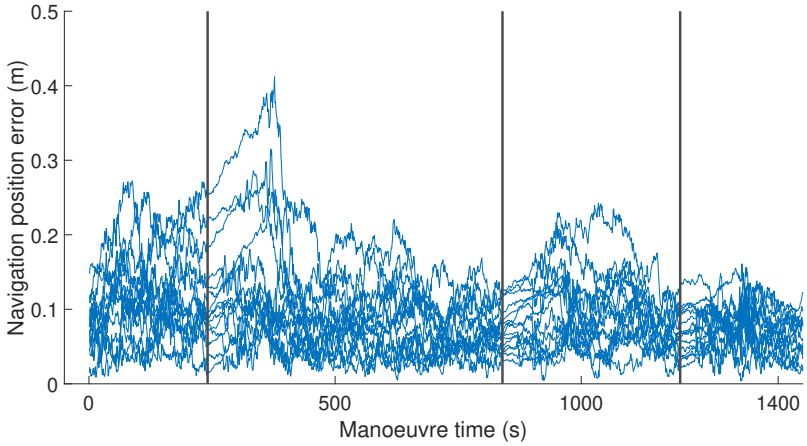

Figure 7.10: Navigation errors for 15 randomly selected runs with optimistic feedback periods and active mitigation. Black lines indicate instances where periods of 3 s of decreased pose estimation performance with optimistic feedback are occurring. It may be observed that none of the undesirable behaviour that was observed in Figure 6.7 remains and the navigation error is relatively constant despite the occurring failures.

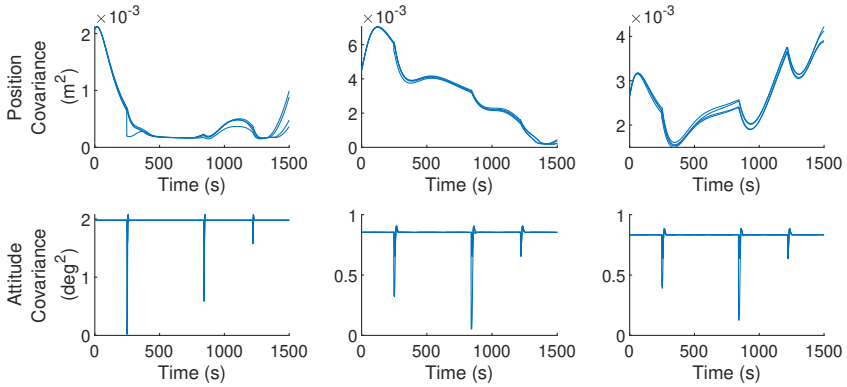

Figure 7.11: Position and attitude state covariance for 15 randomly selected runs with mitigated failure periods and optimistic feedback.

When comparing Figure 7.10 with the navigation error that was presented in Figure 6.7, large differences may be observed. Whereas previously the navigation position error grew to several meters after the occurrence of a period of optimistic feedback, the navigation position error remains stable after the implementation of

the recognition and mitigation strategy. The influence of the periods of optimistic feedback is not completely negated, as still a slight increase in navigation error may be witnessed in some cases, however, despite this increase the position navigation error stays well below 1 m.

Furthermore, as was outlined in Section 7.1, the state covariance of the filter is reset when the mitigation takes place. This should result in a smoother state covariance, without the drops that could be observed in Figure 7.3. Indeed Figure 7.11 shows that the state covariance is smoother than in the case without mitigation. Still some small jumps occur and the covariance is not completely smooth, but the mitigation is nevertheless successful, as the navigation error is not increased due to the periods of decreased pose estimation performance, and shows no signs of failure.

7.2. Estimating Future Rotation: Integration

As discussed in Section 5.1.2, the guidance algorithm requires an estimate of the target rotation at time t_f to make an estimate of the desired final position of the manoeuvre (see Equation (5.9)). More specifically, this required the rotation of the target body with respect to the RTN frame, represented in the RTN frame at time t_f, $\boldsymbol{\omega}_{RTN}^{TBF/RTN}(t_f)$ (see Section 3.4.5).

Up to this point, the target rotation at time t_f is estimated by integrating the current target rotation between t and t_f using Euler's equation, Equation (3.37). This integration has, up to this point, assumed perfect knowledge of target inertia $\boldsymbol{J}_{\text{tar}}$, which is not available in a real-world scenario. Despite the perfect knowledge of $\boldsymbol{J}_{\text{tar}}$, this integration process was identified as the main source of error in the guidance process in Chapter 6, both in nominal situations as well as during periods of decreased performance of the pose estimation system, during which its effect was increased (see Section 6.2.1).

A very limited analysis of the effects of this integration process was already provided in Section 6.2.2, however, this did not provide a complete nor satisfactory analysis of the behaviour of this error. This section shows the limitations of this method of integration in detail and explores its sensitivity to uncertainties found in the target inertia $\boldsymbol{J}_{\text{tar}}$, rotation $\boldsymbol{\omega}_{TBF}^{TBF/RTN}(t)$ and attitude $\boldsymbol{q}_{TBF}^{RTN}(t)$. In order to ease reading, $\boldsymbol{\omega}_{TBF}^{TBF/RTN}(t_f)$ is expressed as $\boldsymbol{\omega}_f$ and $\boldsymbol{\omega}_{TBF}^{TBF/RTN}(t)$ is expressed as $\boldsymbol{\omega}_0$.

All sensitivity analyses in this section have been performed using an initial attitude that places the spin-axis in the R-T plane, at a 90^o angle with the orbit normal. This was done to improve the presentation of the results, which

7.2.1. Theory:

The theory of this method is well-known. The calculation of $\boldsymbol{\omega}_{\text{final}}$ is performed by integrating Euler's equation, Equation (3.37), over the remaining time until the end of the manoeuvre. As Euler's equation is valid for rotations expressed in the body frame and with respect to an inertial frame, this equation can be used to make an estimate of $\boldsymbol{\omega}_{TBF}^{TBF/ECI}$ for all times between $t_0 = t_{\text{current}}$ and $t_f = t_{\text{final}}$.

As becomes clear from Equation (3.37), the initiation of this integration process requires three parameters. First and foremost it requires an estimate of the current rotation of the target with respect to an inertial frame, represented around the principle axis of the target body ($\boldsymbol{\omega}_{TBF}^{TBF/ECI}$). Second, it requires the target inertia matrix ($\boldsymbol{J}_{\text{tar}}$), which in reality is not fully known and can only be estimated up to a certain degree of accuracy. Third, it requires an estimate of the current attitude of the target spacecraft with respect to the RTN frame $\boldsymbol{q}_{RTN}^{TBF}$, to be able to correctly evaluate the gravity gradient torques.

The navigation system does not provide these estimates directly, instead it only measures the relative attitude of the target with respect to the camera, $\boldsymbol{q}_{TBF}^{CBF}$, and from this it estimates the corresponding rotation, $\boldsymbol{\omega}_{TBF}^{CBF/TBF}$, represented in the target body frame. The required rotation, $\boldsymbol{\omega}_{TBF}^{TBF/ECI}$, can be found from the estimation of $\boldsymbol{\omega}_{TBF}^{CBF/TBF}$. Similarly $\boldsymbol{q}_{RTN}^{TBF}$ can be found from $\boldsymbol{q}_{TBF}^{CBF}$. The process through which the desired parameters may be extracted from the measured/estimated parameters is described by the following series of equations, using Equation (3.33):

$$\boldsymbol{q}_{TBF}^{RTN} = \boldsymbol{q}_{TBF}^{CBF} \otimes \left(\boldsymbol{q}_{RTN}^{CBF}\right)^{-1} \tag{7.4a}$$

$$\boldsymbol{\omega}_{RTN}^{TBF/CBF} = \boldsymbol{q}_{TBF}^{RTN} \otimes \boldsymbol{\omega}_{TBF}^{CBF/TBF} \otimes \left(\boldsymbol{q}_{TBF}^{RTN}\right)^{-1} \tag{7.4b}$$

$$\boldsymbol{\omega}_{RTN}^{TBF/RTN} = \boldsymbol{\omega}_{RTN}^{TBF/CBF} - \boldsymbol{\omega}_{RTN}^{RTN/CBF} \tag{7.4c}$$

$$\boldsymbol{\omega}_{TBF}^{TBF/RTN} = \left(\boldsymbol{q}_{TBF}^{RTN}\right)^{-1} \otimes \boldsymbol{\omega}_{RTN}^{TBF/RTN} \otimes \boldsymbol{q}_{TBF}^{RTN} \tag{7.4d}$$

$$\boldsymbol{\omega}_{TBF}^{TBF/ECI} = \boldsymbol{\omega}_{TBF}^{TBF/RTN} + \left(\boldsymbol{q}_{TBF}^{RTN}\right)^{-1} \otimes [0, 0, n_{Orbit}] \otimes \boldsymbol{q}_{TBF}^{RTN} \tag{7.4e}$$

where $\boldsymbol{q}_{RTN}^{CBF}$ and $\boldsymbol{\omega}_{RTN}^{RTN/CBF}$ are obtained from the ADCS system on board of the chaser and are assumed to be known with high accuracy. Having found both $\boldsymbol{\omega}_{TBF}^{TBF/ECI}$ and $\boldsymbol{q}_{RTN}^{TBF}$ Euler's equation (Equation (3.37)) can be evaluated and a value for $\boldsymbol{\omega}_f$ can be obtained.

7.2.2. Sensitivity to Rotation

When attempting this integration process, uncertainties are present in the initial rotation at time t_0, $\boldsymbol{\omega}_0$. In order to analyse the sensitivity of the integration process to this uncertainty, random noise was added to the true value of $\boldsymbol{\omega}_0$. The 'noise level' represents the maximum magnitude of the noise, which is uniformly distributed between -ϵ_ω and +ϵ_ω, for six different noise levels

$$\epsilon_\omega = 0.1,\ 0.2,\ 0.4,\ 0.6,\ 0.8 \text{ and } 1.0 \text{ deg/s}$$

As discussed previously in Section 5.1.2, the estimate of $\boldsymbol{\omega}_f$ is used to evaluated the desired final position of the rendezvous trajectory, $\boldsymbol{r}_f$, according to Equation (5.9c). Equation (5.9c) can be used to calculate the intersection of the spin-axis and the KOS at any specific point in time, allowing this analysis to consider multiple integration times, respectively

$$t_{\text{int}} = 100,\ 500,\ 1000 \text{ and } 1500 \text{ s}$$

The analysis in this section compares the state estimate of the 500 noisy runs, at the above integration times, to the true desired state, that is obtained from Equation (5.9c) using the true rotation. A KOS radius of 25 m is used (see Section 4.2).

Figure 7.12 show the true spin-axis location (red) and the estimated spin-axis from the 500 noisy runs for short (100, 500 s) and long (1000, 1500 s) integration times respectively. Only a selection of three noise levels is shown to provide an idea of the behaviour when uncertainties increase.
It can be observed from Figure 7.12 that both the level of noise on $\boldsymbol{\omega}_0$ and the integration time significantly influence the accuracy of the estimate. For short integration times and low level of noise on $\boldsymbol{\omega}_0$, the estimate of the spin-axis is accurate and might even achieve sub-meter accuracy, however, when either uncertainty or integration time is increased the error on the final desired position rapidly increases.

Table 7.1 shows the mean error and standard deviation of the position estimate average over all 500 runs. Both the mean and the standard deviation of the error increase when increasing ϵ_ω, as well as when increasing time period of integration. This shows that whenever the estimate of $\boldsymbol{\omega}$, made in the navigation filter, contains uncertainties as small as 0.1 deg/s, the estimation of the final conditions for the guidance algorithm exceeds 4 m when the integration time is long.

Table 7.1: Mean (μ) and standard deviation (σ) of position error obtained through integration with uncertainties in $\boldsymbol{\omega}_0$, for all integration times and noise levels. It may be observed that higher errors are created both by increasing ϵ_ω and by increasing integration time, although the former has a larger impact.

ϵ_ω (m)	t = 100		t = 200		t = 500		t = 1000		t = 1500	
	μ (m)	σ (m)	μ (m)	σ (m)	μ (m)	σ (m)	μ (m)	σ (m)	μ (m)	σ (m)
0.1	0.635	0.340	1.282	0.756	1.665	1.006	1.810	0.832	3.997	1.888
0.2	1.271	0.673	2.499	1.421	2.932	1.555	2.729	1.436	4.746	2.011
0.4	2.518	1.296	4.476	2.445	3.734	2.053	3.595	1.789	5.387	2.517
0.6	3.757	1.899	5.722	2.682	4.155	2.295	3.922	2.219	6.098	3.104
0.8	4.796	2.452	6.412	3.117	4.655	2.738	4.770	2.673	6.692	3.576
1.0	5.954	3.100	6.813	3.572	5.510	3.272	5.217	3.181	7.002	4.101

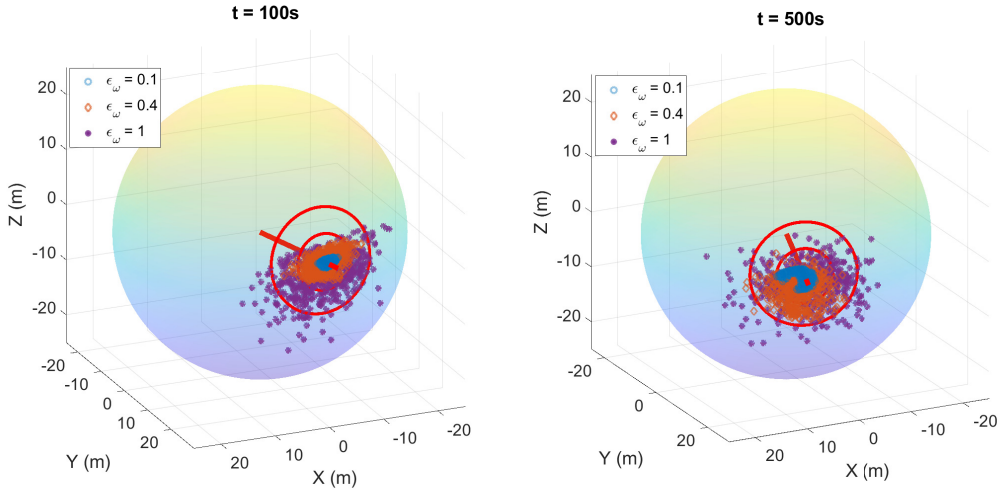

(a) Short integration times, 100 s (left) and 500 s (right).

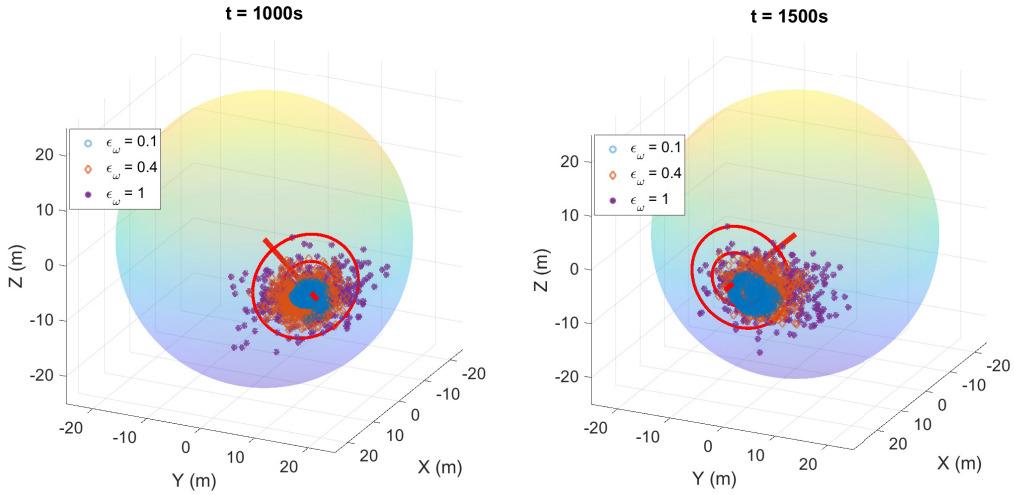

(b) Long integration times, 1000 s (left) and 1500 s (right).

Figure 7.12: Position estimation error for short (top) and long (bottom) integration times, and three different noise levels ϵ_ω. The red line indicates the true orientation of the spin-axis and the red circles have a radius of 5m and 10m respectively, and serve as an indication of the error magnitude. It may be observed that errors grow significantly when the uncertainty in $\boldsymbol{\omega}_0$ is increased.

Another observation that can be made from Figure 7.12 is that the estimations of the spin-axis location from the 500 noisy runs are, in most cases, not centred around the true spin-axis, but seem to display a bias. As the spin-axis orientation is constant in the inertial frame, it 'moves' in the RTN frame, or rather the RTN frame rotates with respect to the inertial. This can be observed in Figure 7.12, where the direction of motion of the spin-axis may be observed from being pointed at +y/-x at t = 100, 'moving' gradually to +x/-y.

The estimates at t = 500 s show a clear bias towards negative values of Z, whereas all estimates at t = 1500 s seem to 'lag behind' the true spin-axis and show a clear bias towards positive values of Y. The direction of this bias is continuously changing, while at some instants it disappears, which may be observed for t = 1000 s, as there seems to be no such bias at all.

This bias can most likely be attributed to the instantaneous direction of the wobbling motion of the spin-axis, which the integration process fails to identify accurately. The bias is therefore unpredictable and de-

pends on the combination of specific values of initial rotation $\boldsymbol{\omega}_0$, initial attitude $\boldsymbol{q}_0$ and inertia matrix $\boldsymbol{J}$. Specific combinations of these parameters likely cause the estimate to diverge in a specific direction, however, as the uncertainties in these parameters cannot be known, this bias is remains unpredictable. As is clear from Figure 7.12, the estimation error at an integration time of 1500 s, which represents the end of the optimal manoeuvre, easily exceeds 5 m even for small ϵ_ω, and could potentially increase to as much as 10 m for larger values of ϵ_ω.

These are unfavourable conclusions, as they mean that the magnitude of error on the estimate of the final position, which is required for efficient guidance, is likely to be several meters from the true value. In particular, since an accuracy of $0.5°/s$ is expected for $\boldsymbol{\omega}_0$ (see Section 5.2.3), the error on the final position likely exceeds 5 m, and could potentially exceed 10 m, which was already observed in the results of Section 6.1.1. It can therefore be concluded that uncertainties in $\boldsymbol{\omega}_0$ account for all present error, however, in a real scenario, $\boldsymbol{\omega}_0$ is merely one of three uncertain parameters used in this integration process.

7.2.3. Sensitivity to inertia errors

Up to this point a perfect knowledge of the target inertia was assumed, which is not attainable in a real-world situation. Similar to the previous section, studying the sensitivity of the integration process to $\boldsymbol{\omega}_0$, this section explores the sensitivity to uncertainties in the target inertia $\boldsymbol{J}_{\text{tar}}$. An analysis of 500 noisy runs is performed, where the noise is uniformly distributed and added to the true value of $\boldsymbol{J}$ prior to the integration. The true value of $\boldsymbol{J}_{\text{tar}}$ was presented in Table 2.1. Integration is performed over the same integration times as before, respectively

$$t_{\text{int}} = 100,\ 500,\ 1000 \text{ and } 1500\text{s}$$

Adding a realistic level of noise on the inertia matrix is not straightforward. When considering the inertia matrix in an uncontrolled setting, the absolute values are not relevant, but rather the ratios of inertia should be considered. This is easily demonstrated through the examination of Equation (3.36), after which it may be concluded that all components in the equation, except disturbance torques (which were assumed negligible over the course of a single orbit, see Section 3.2), are multiplied with $\boldsymbol{J}$. Thus, dividing all elements by $|\boldsymbol{J}|$ has no effect on the equation, showing that the absolute values are not relevant.

Therefore, when introducing noise, the inertia ratios have to be considered rather than the absolute values. Introducing -2% error on J_{yy} while introducing +2% error on J_{zz} results in the ratio of the two changing 4% (for elements of similar magnitude), which is not considered an accurate representation of a 2% inertia error. Multiple better approaches are found, for example: Pesce et al. [60] use ratios of inertia $k_1 = J_{xx}/J_{yy}$, $k_2 = J_{yy}/J_{zz}$ as metric, using a diagonal form of the inertia matrix. Furthermore, Benninghoff and Boge [2] use a normalised inertia matrix $\boldsymbol{J}/|\boldsymbol{J}|$, including also products of inertia. Both papers investigate the accuracy that can be achieved in estimating $\boldsymbol{J}$ of an unknown satellite, and report errors on the (dominant) diagonal terms in the order of 0.01 - 0.06, or 1 to 6%. This is consistent with the reported uncertainty in the diagonal elements of $\boldsymbol{J}_{\text{Envisat}}$, reported by ESA and presented in Table 2.1. The off-diagonal products of inertia are likely prone to larger uncertainties, considering that Envisat is presumably damaged due to years of uncontrolled orbiting. For simplicity the magnitude of the error on all elements is considered equally large.

For introducing the uncertainties in $\boldsymbol{J}_{\text{tar}}$ the following approach is taken. First, one of the diagonal elements is randomly selected, to be used as reference. Second, the ratio with the other two diagonal elements is calculated. Third, a uniformly distributed random noise with magnitude ϵ_J (in %) is added to this ratio of inertia. Fourth, the new, noisy, ratios of inertia are multiplied with the randomly selected reference element of the first step to find the remaining two noisy values of inertia. An example of this procedure is provided below:

1. J_{yy} is randomly selected from the set (J_{xx}, J_{yy}, J_{zz}).
2. Ratios of inertia $k_1 = J_{xx}/J_{yy}$ and $k_2 = J_{zz}/J_{yy}$ are calculated.
3. Noise on k_1 and k_2 is introduced using $-\epsilon_J < \delta k_i < +\epsilon_J$, where $k_{i,\text{new}} = k_i + \delta k_i$.
4. New inertia components are calculated $J_{xx,\text{new}} = k_{1,\text{new}} J_{yy}$, $J_{zz,\text{new}} = k_{2,\text{new}} J_{yy}$.

A similar approach is taken for the off-diagonal elements, where instead one is randomly selected from the set (J_{xy}, J_{xz}, J_{yz}) and the procedure is repeated. This method ensures that the inertia ratios stay within the correct boundaries. Six different values for ϵ_J were selected:

$$\epsilon_J = 0.005\ (0.5\%),\ 0.01\ (1\%),\ 0.02\ (2\%),\ 0.04\ (4\%),\ 0.06\ (6\%)\ \text{and}\ 0.1\ (10\%)$$

The results of the analysis are presented in Figure 7.13, which shows the true location of the spin axis, together with the estimates of the desired location on the KOS for the different noise levels on $\boldsymbol{J}$ for the four selected integration times, similar to the previous section.

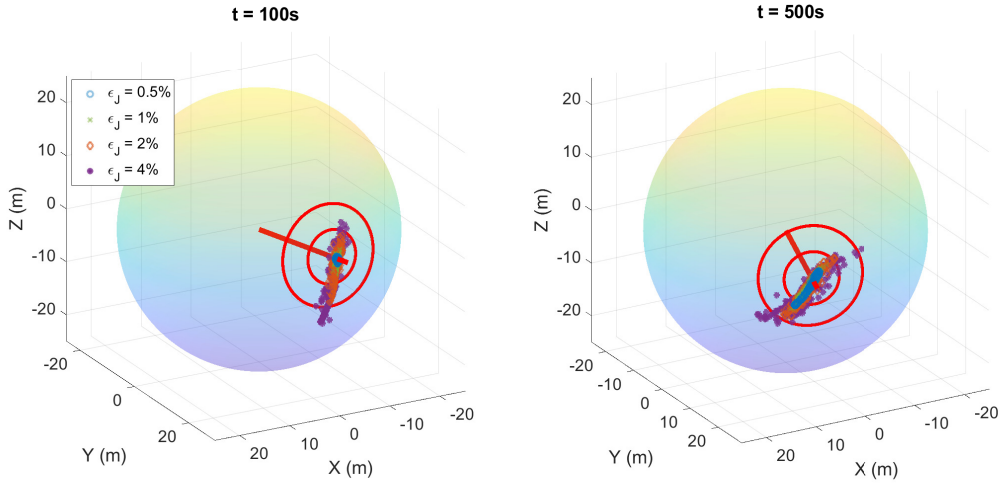

(a) Short integration times, 100 s (left) and 500 s (right).

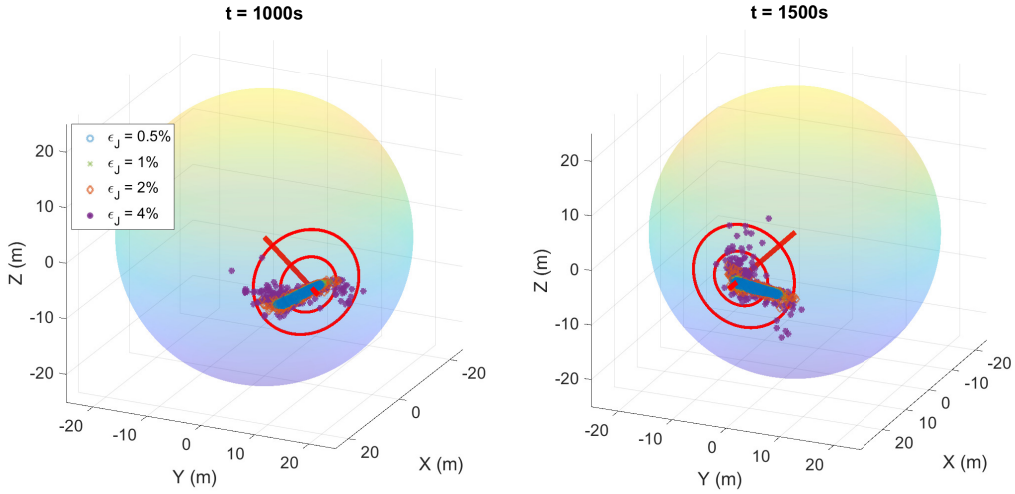

(b) Long integration times, 1000 s (left) and 1500 s (right).

Figure 7.13: Position estimation error for short (top) and long (bottom) integration times, and three different noise levels ϵ_J. The red line indicates the true orientation of the spin-axis and the red circles have a radius of 5m and 10m respectively, and serve as an indication of the error magnitude. It may be observed that a strong directional bias is present in the results and that the area over which the estimated positions are spread remains similar when integration time is increased.

It can be observed from Figure 7.13 that already for small integration times the estimation error can potentially exceed 10 m, and the 'stretch' of the 500 noisy runs is similar for t = 100 s and t = 1500 s. This indicates that the magnitude of ϵ_J is the main contributor to the final error, whereas integration time has a much smaller effect on the final error.

Additionally, a numerical overview of the achieved estimation errors is presented in Table 7.2. This shows

that when both integration time and ϵ_J are small, the estimate of the spin-axis is very accurate and sub-meter accuracy can be achieved. The role of ϵ_J, compared to integration time, becomes increasingly clear for larger values of ϵ_J, as it can be observed in Table 7.2 that for ϵ_J = 4% or 6%, the mean and standard deviation of the error stay at a rather constant level when the integration time is increased.

Table 7.2: Mean (μ) and Standard Deviation (σ) of error for estimating ω through integration with initial error in J, for different lengths of time and different error magnitudes.

ϵ_J %	t = 100		t = 200		t = 500		t = 1000		t = 1500	
	μ (m)	σ (m)	μ (m)	σ (m)	μ (m)	σ (m)	μ (m)	σ (m)	μ (m)	σ (m)
0.5	0.689	0.172	0.437	0.268	1.852	1.593	2.700	2.037	3.635	2.096
1	1.017	0.543	1.141	1.255	2.384	1.839	2.759	2.034	3.715	2.085
2	2.028	1.796	2.320	2.061	2.842	1.971	2.971	2.074	3.630	2.077
4	4.466	3.637	2.945	2.417	3.384	2.664	3.641	2.619	3.307	2.159
6	5.672	3.971	2.786	2.366	3.900	2.766	4.214	3.062	3.769	2.770
10	6.641	3.829	3.378	3.779	4.524	3.327	5.056	3.766	4.509	3.441

Furthermore, it can be observed from Figure 7.13 that the error, caused by the inertia uncertainties, is strongly biased in a specific direction. This direction is approximately along the *Z*/*N*-axis for t = 100 s it seems to 'rotate' towards the *X*/*Y*- (or *R*/*T*-) plane. When extending the integration time beyond 1500 s, this 'rotation' of the bias continues in the expected direction and rotates away from the R/T-plane again.

The direction of this bias is most likely dependant on the current direction of motion of the spin-axis, which is completely dependant on target wobbling, which, in turn, is completely dependant on the $\boldsymbol{\omega}_t$. As $\boldsymbol{\omega}_t$ cannot be accurately known, or else there would be no need for this analysis, the bias cannot be compensated for and presents some challenges regarding the accuracy of the integration.

Contrary to the data in Table 7.1, Table 7.2 shows that, when the uncertainties in $\boldsymbol{J}$ exceed a certain threshold, in this case approximately 4%, the error does not grow with integration time. This results in position errors exceeding 10 m in several cases for integration times as short as 100 s, with ϵ_J only 4%. This is highly undesirable, as 4% error is a very realistic level of uncertainty for the target inertia [2, 60]. As a consequence, accurate estimation of the desired position would not be possible even for short integration times, unless a highly accurate estimate of the target inertia is available, which is doubtful. The results of the analysis of uncertainties in $\boldsymbol{J}$ thus provide further motive to find different methods for estimating the target future rotation.

7.2.4. Sensitivity to attitude errors

The third, and final, parameter, required in the integration of the target dynamics through Equation (3.37), is the initial attitude $\boldsymbol{q}_{TBF}^{RTN}(t_0)$, or simply $\boldsymbol{q}_0$. Similar to the previous sections, the results of 500 noisy runs are analysed, comparing the estimated intersection-point of the spin-axis and the KOS with its true value. The noise is uniformly distributed and added to $\boldsymbol{q}_0$ prior to the integration.

Attitude uncertainty is expressed in degrees and is added to $\boldsymbol{q}_0$ by multiplying $\boldsymbol{q}_0$ with an error quaternion $\delta\boldsymbol{q}_\epsilon$. The error quaternion $\boldsymbol{q}_\epsilon$ is constructed by taking a random unit vector $\hat{\boldsymbol{n}}$ and angle α, after which Equation (3.21) is used to construct the error quaternion $\delta\boldsymbol{q}_\epsilon$. The noise level is thus determined by the magnitude of α, distributed uniformly between -ϵ_α and +ϵ_α, for which the following values are selected:

$$\epsilon_\alpha = 0.1,\ 0.5,\ 1,\ 2,\ 5,\ \text{and}\ 10\ \text{deg}$$

In this analysis it is assumed that perfect information is available about $\boldsymbol{\omega}_0$ and $\boldsymbol{J}_{\text{tar}}$. The results of this analysis, only for the long integration times, are presented in Figure 7.14, from which it may be observed that the error caused by uncertainties in $\boldsymbol{q}_0$ is small, compared to the errors observed in the previous sections due to uncertainties in $\boldsymbol{\omega}_0$ and $\boldsymbol{J}$. Additionally, the numerical data from this analysis is available in Table 7.3.
The magnitude of the error from uncertainties in $\boldsymbol{q}_0$ does not change when integration time is increased, as can be observed in Figure 7.14 and is confirmed through the data in Table 7.3. Furthermore, the error is a good reflection of true error in the initial attitude $\boldsymbol{q}_0$, which may be demonstrated by further examining some values from Table 7.3. The mean and standard deviation of the error for ϵ_α = 2 deg, respectively $\mu \approx 0.37$ m and $\sigma \approx 0.24$ m, result in a 99.7% confidence interval of 1.09 m (μ+3σ). A calculation shows that an error arc of 2° on a sphere with radius 25m results in an error of $25 \cdot \sin(2°) \approx 0.87$ m, which is an accurate representation of the error that was found. The error caused by uncertainties in $\boldsymbol{q}_0$ thus shows predictable behaviour, contrary to the errors caused by uncertainties in $\boldsymbol{\omega}_0$ and $\boldsymbol{J}$.

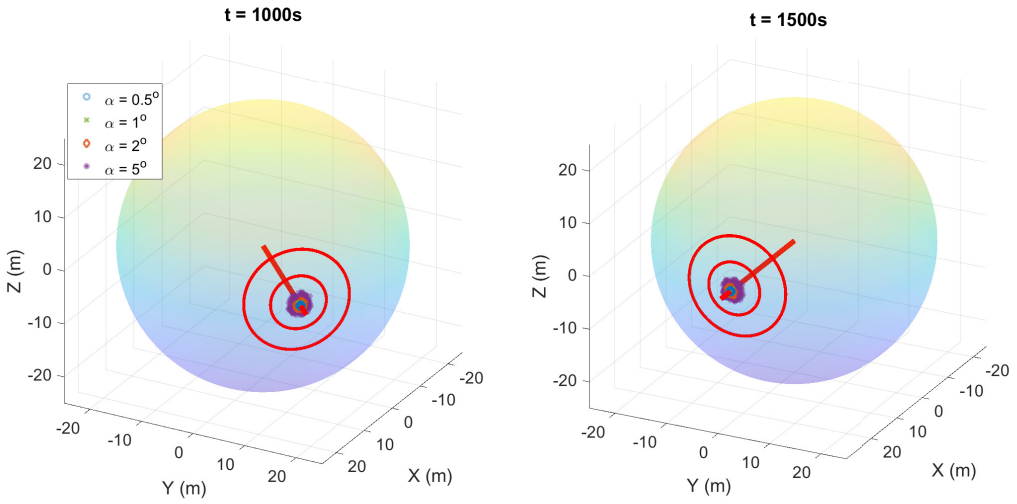

Figure 7.14: Position estimation error for noise in the initial attitude, at 1000 seconds (left) and 1500 seconds (right) into the future.

Table 7.3: Mean (μ) and Standard Deviation (σ) of error for estimating ω through integration with initial error in $\boldsymbol{q}$, for different lengths of time and different error magnitudes.

α	t = 100		t = 200		t = 500		t = 1000		t = 1500	
(deg)	μ (m)	σ (m)	μ (m)	σ (m)	μ (m)	σ (m)	μ (m)	σ (m)	μ (m)	σ (m)
0.1	0.035	0.023	0.035	0.023	0.035	0.023	0.035	0.023	0.035	0.023
0.5	0.086	0.057	0.085	0.057	0.086	0.057	0.085	0.057	0.085	0.057
1	0.161	0.108	0.162	0.108	0.162	0.108	0.161	0.108	0.161	0.107
2	0.367	0.238	0.363	0.234	0.365	0.236	0.363	0.235	0.367	0.235
5	0.833	0.561	0.824	0.557	0.832	0.559	0.830	0.558	0.826	0.555
10	1.820	1.152	1.776	1.129	1.808	1.145	1.803	1.145	1.800	1.136

7.2.5. Sensitivity to combined errors

Finally, as both uncertainties in $\boldsymbol{\omega}_0$ and $\boldsymbol{J}$ are expected to arise simultaneously, an analysis is made of the combined error of noise in $\boldsymbol{J}_{\text{tar}}$ and $\boldsymbol{\omega}_0$. Uncertainties in $\boldsymbol{q}_0$ are not considered in this analysis due to their limited magnitude and predictable behaviour, demonstrated in the previous section.

The uncertainties are modelled as in Section 7.2.2 for $\boldsymbol{\omega}_0$ and Section 7.2.3 for $\boldsymbol{J}$. Similar to the previous sections, an analysis is made of 500 noisy runs, comparing the estimates from these runs with the true values, for the same five integration times as previously. The noise is included in $\boldsymbol{J}$ and $\boldsymbol{\omega}_0$ prior to the integration. Five different levels of uncertainty were used for $\boldsymbol{J}$:

$$\epsilon_J = 0.5,\ 1,\ 2,\ 4 \text{ and } 6 \text{ deg}$$

consistent with the expected magnitude of inertia uncertainties presented in Section 7.2.3 ([60],[2]). Furthermore, three different levels of uncertainty were used for $\boldsymbol{\omega}_0$:

$$\epsilon_\omega = 0.1,\ 0.5 \text{ and } 1 \text{ deg/s}$$

ranging from optimistic (0.1 deg/s) to expected (0.5 deg/s) to conservative (1.0 deg/s) uncertainty, as demonstrated during the tuning of the navigation filter in Section 5.2.3.

The results of this combined uncertainty analysis are presented in Figure 7.15, showing only the cases with low uncertainties, and Table 7.4, showing numerical results for all examined cases. These show the influences of both $\boldsymbol{J}$ and $\boldsymbol{\omega}$, as well as the effect of time. It becomes clear that for low errors over short integration times, the integration method delivers reasonable results, with an error of approximately 1 m, however, when either the level of error or the integration time increases, the accuracy of the estimated desired position is strongly

deteriorated with mean (μ) and standard deviation (σ) of the estimation error exceeding respectively 5 m and 3 m in many cases.

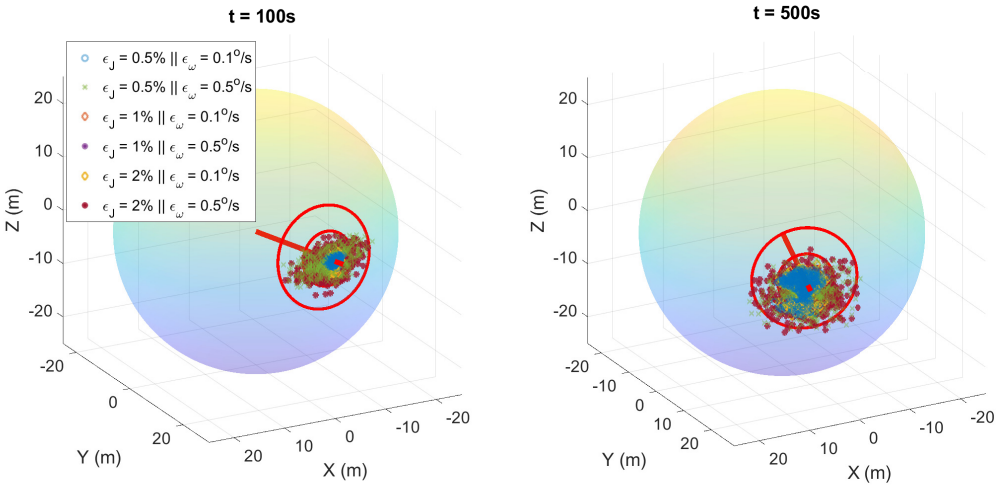

(a) Position estimation error at 100 seconds (left) and 500 seconds (right) into the future. Combined noise on ω_0 and J.

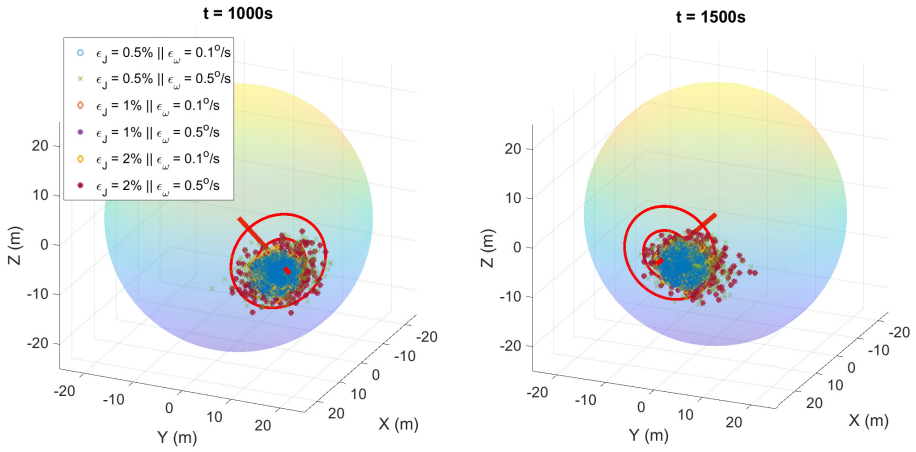

(b) Position estimation error at 1000 seconds (left) and 1500 seconds (right) into the future. Combined noise on ω_0 and J.

Figure 7.15: Position estimation error for combined noise om ω_0 and J of low magnitude.

From Figure 7.15 it can be observed that, for low integration time (t = 100 s), the narrow stretch of data that was observed in Section 7.2.3 for uncertainties in $\boldsymbol{J}$ can be identified, however, in all other cases the distribution of error is more similar to the one found in Section 7.2.2 for uncertainties in $\boldsymbol{\omega}_0$. The strong directional biases observed for ϵ_J in Section 7.2.3 thus seem to mostly disappear in this combined analysis. The biases that were found when further increasing the uncertainties are also similar to those observed in Section 7.2.2 for uncertainties in $\boldsymbol{\omega}_0$.

The effects of uncertainties in $\boldsymbol{J}$ are visible only for short integration times and low values of ϵ_ω, as may be observed from the first five rows in Table 7.4 (ϵ_ω = 0.1). Increasing ϵ_J from 0.5% to 6% results in an increase of μ and σ from 0.802 and 0.406 to 6.314 and 3.960 in the case of t = 100, and from 4.167 and 1.848 to 4.788 and 2.703 in the case of t = 1500. However, this strong effect disappears for t = 100 when ϵ_ω is increased to 1 deg/s.

In terms of magnitude, ϵ_ω and ϵ_J are found to have a similar influence, as errors for ϵ_J = 6% combined with any ϵ_ω are found to be of similar magnitude when compared to errors for ϵ_ω = 1 deg/s combined with

Table 7.4: Mean (μ) and Standard Deviation (σ) of error for estimating ω through integration with initial error in both J and $\boldsymbol{\omega}_0$, for different lengths of time and different error magnitudes.

$\boldsymbol{\epsilon_\omega}$ (°/s)	$\boldsymbol{\epsilon_J}$ (%)	t = 100		t = 200		t = 500		t = 1000		t = 1500	
		μ (m)	σ (m)	μ (m)	σ (m)	μ (m)	σ (m)	μ (m)	σ (m)	μ (m)	σ (m)
0.1	0.5	0.802	0.406	1.400	0.663	2.429	1.276	3.081	1.428	4.167	1.848
	1	1.042	0.642	1.780	1.165	2.738	1.482	3.176	1.452	4.262	1.728
	2	2.108	1.949	2.806	1.864	3.155	1.559	3.240	1.468	4.069	1.766
	4	4.655	3.727	3.343	2.142	3.927	2.306	3.826	2.189	4.406	2.224
	6	6.314	3.960	3.413	2.599	4.746	3.002	4.396	2.724	4.788	2.703
0.5	0.5	3.126	1.645	4.629	2.477	4.025	2.184	3.830	2.052	5.775	2.960
	1	3.202	1.536	4.636	2.335	3.973	2.084	4.021	2.150	5.700	2.855
	2	3.951	2.185	4.679	2.299	4.079	2.064	4.131	2.187	5.781	2.929
	4	6.040	3.271	5.184	2.554	4.549	2.589	4.536	2.549	6.261	3.101
	6	6.858	3.496	5.570	2.990	5.068	2.789	4.763	2.798	6.294	3.283
1	0.5	6.007	3.369	6.558	3.416	5.651	3.474	5.391	3.312	7.245	4.303
	1	5.989	2.945	6.445	3.534	5.595	3.190	5.271	2.996	7.056	3.959
	2	6.434	3.492	6.111	3.468	5.507	3.142	5.395	3.174	7.156	4.219
	4	7.480	3.797	6.791	3.618	6.269	3.748	6.365	3.527	7.690	4.577
	6	7.401	3.917	7.199	3.874	6.082	3.579	6.217	3.649	7.639	4.413

any ϵ_J, as may be observed in Table 7.4, the errors from high $\epsilon_o mega$ only very slightly exceeding those from high ϵ_J.

Furthermore, the influence of the uncertainties is higher than the influence of integration time, as errors found for t = 100 with large values of ϵ_ω,ϵ_J are higher than those found for t = 1500 for low values of ϵ_ω,ϵ_J. Especially increasing the uncertainty in $\boldsymbol{\omega}_0$ for higher values of integration time results in a relatively large increase in error, as may be observed from the final column of Table 7.4.

Finally, two main conclusions can be drawn from this analysis

- Errors increase significantly over longer periods of time, reaching an error. In the best case scenario, μ ≈ 4 m and σ ≈ 2 m for very small uncertainties in $\boldsymbol{\omega}_0$ and $\boldsymbol{J}$.
- Considering realistic uncertainties in $\boldsymbol{J}$ (≈ 4%, see [2, 60]) and $\boldsymbol{\omega}$ (≈ 0.5 deg/s, see Section 5.2.3), the expected mean and standard deviation μ/σ of the error in the estimation of the intersection-point of the spin-axis with the KOS is 6.04 m/3.27 m for t = 100 s and 6.261 m/3.10 m for t = 1500 s.

These conclusions imply that, in a real-world scenario, estimation errors could potentially reach 15m (μ+3σ) in magnitude, even for short integration times, which would mean that the final position estimate of the trajectory contains an error of 15m. This is highly undesirable and results in a need to explore different methods that can provide a more accurate estimate of $\boldsymbol{\omega}_f$.

7.3. Estimating Future Rotation: Curve fitting

The sensitivity analysis of the integration method has shown that the method is inadequate for accurately estimating the desired chaser position in the presence of uncertainties. Therefore, a new method for estimating ω_{final} is formulated. This method requires the acquisition of a large number of measurements prior to the approach, which is possible from a passively safe relative orbit around the target (see Section 4.2). These measurements allow the characterisation of the target attitude dynamics and can be fitted by means of a least squares regression analysis, which allows to formulate a function to estimate the future location of the spin-axis in the RTN-frame. This method has its limitations, which are mainly related to the relative magnitude of the rotations around the target principal axes, however, also has the potential to outperform the integration method in terms of accuracy and robustness, as is shown below.

The fitting process occurs prior to the approach and one full orbital period is assigned for the acquisition of measurements. The orbital period, T_{orbit}, is approximately 6025 seconds, and, considering an eclipse period of ≈ 1900 s [52], this leaves a period of approximately 4000 seconds for acquiring measurements upon which the least squares regression may be performed. This analysis uses a spin-axis orientation that is aligned with the orbital plane, which, however inconsistent with the expected orientation identified in Section 2.2,

was chosen for the purpose of visualisation and in no way decreases the general applicability of the results reported in this chapter, as is additionally demonstrated in Section 7.3.2.

7.3.1. Theory:

This method uses the theory of least squares as a method of regression to find a best fit for $\boldsymbol{\omega}$ over the period of one orbit. In essence the least-squares theory comes down to the following simple minimisation problem:

$$\min_{t_1 \cdots t_n} \sum_{i=1}^{n} r_i^2 \tag{7.5}$$

where r_i is a so-called residual, which is defined as

$$r_i = y_i - f(t_i, \boldsymbol{\beta}) \tag{7.6}$$

with y_i a data point at time t_i and $f(t_i, \boldsymbol{\beta})$ the function value of the fitting function, used to make an estimate of the data points. Least-squares problems can either be linear or non-linear, depending on the fitting function $f(t_i, \boldsymbol{\beta})$ which has to be carefully selected to match the expected system behaviour.

In the case of $\boldsymbol{\omega}$, or rotations in general, sinusoidal functions are an excellent choice due to their periodic nature which excellently describes the movement of points undergoing a rotational motion. The general sinusoidal function is described by

$$f(t, \boldsymbol{\beta}) = \sum_{k=1}^{N} \beta_{k,1} \cdot \sin\left(\frac{2\pi}{\beta_{k,2}} \cdot t + \beta_{k,3}\right) + \beta_0 \tag{7.7}$$

where parameters $\beta_{k,1}, \beta_{k,2}, \beta_{k,3}$ represent respectively the amplitude, frequency and phase shift and β_0 represents the mean (or vertical shift) of the function. Due to the non-linearity of sinusoidal functions and their many local minima, such functions are difficult to use in least-squares regressions [69] and are unlikely to yield good results without a good estimate of the initial conditions [40], with the frequency usually being the most difficult parameter. The importance of a good estimate for the frequency of noisy signals is highlighted by Tretter et al. [84].

These conclusions create the need for a discussion on the estimation of the initial parameters for the least squares regression employing sinusoidal functions. At this point two fitting options can be separated and should be treated separately. The first option, 'Option A', is concerned with finding a fit for $\boldsymbol{\omega}_{RTN}^{TBF/RTN}$ to directly find an estimate of the spin axis location. The second option, 'Option B', is concerned with finding a fit for $\boldsymbol{\omega}_{TBF}^{TBF/RTN}$. Option B allows to find $\boldsymbol{\omega}_{RTN}^{TBF/RTN}$ by multiplying with $\boldsymbol{q}_{TBF}^{RTN}$ (estimated from navigation), or it can serve as an improvement over the moving mean filter estimate presented in Section 5.2.3. All fits were computed using the *'cfit'* function from the MATLAB Curve Fitting toolbox.

Option A

In this analysis the non-periodic orbital disturbances, such as drag, are ignored, as they cause changes over extended periods of times and are negligible over the course of a single orbit (see Section 3.2). The target is considered in a state of uncontrolled motion, only influenced by the gravity-gradient torque. According to Equation (3.37), the consequence of this assumption is that, for any combination of $\boldsymbol{\omega}_0, \boldsymbol{J}$, the orientation of the rotational motion is periodically constant with respect to the inertial frame. It must be stressed that this assumption is valid for the relatively short intervals (1-2 orbital periods, or ≈ 3h) discussed in this analysis, but becomes invalid as longer intervals of time are considered.

Frequency and Period

This assumption can be exploited to define the periodicity of $\boldsymbol{\omega}$ in the RTN frame. By definition the orbital plane (R-T plane) is at constant inclination i with respect to the ECI frame, fixing the angle between the Z-axis of the ECI frame and the N-axis of the RTN frame. This creates a periodic motion of the other two axes with respect to each other, with a frequency equal to the orbital mean motion. This principle is illustrated in Figure 7.16, which shows the spin-axis of the target spacecraft at a constant orientation with respect to the inertial frame, aligned with the negative Y-axis. With respect to the RTN frame, the spin-axis is aligned with the -R-axis when the target is on the left side of the image, and then over the course of the orbit, the target travelling in counter-clockwise direction, the spin-axis is aligned with the -T, +R and +T directions respectively, before again being aligned with the -R axis after one full orbital period.

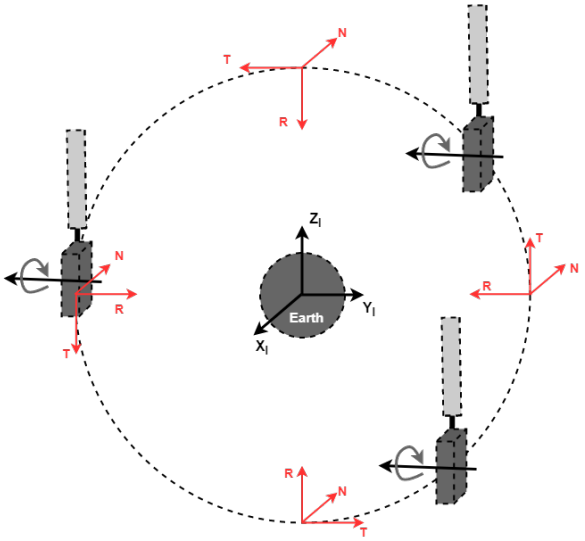

Figure 7.16: Rotation of the spacecraft in the ECI frame and the RTN frame. Direction of motion of the target in the orbit is counter-clockwise. It may be observed that the spin-axis is continuously aligned with the -*Y* direction of the inertial frame *I*, while the RTN-frame is rotating, causing the spin-axis to be aligned subsequently with -*R*/-*T*/+*R*/+*T*.

A sinusoidal function to estimate $\boldsymbol{\omega}_{RTN}^{TBF/RTN}$ can then be found from Equation (7.7) by setting degree N to 1 or 2. The main period, $\beta_{1,2}$, should be set to T_{Orbit}, whereas the secondary period, $\beta_{2,2}$, is equal to the period of the wobbling motion due to inertia. According to Wertz [94], the wobbling frequency W_n is calculated as

$$W_n = \sqrt{\frac{(J_{11} - J_{33})(J_{22} - J_{33})}{(J_{11} J_{22})}} \omega_{ECI,3} \tag{7.8}$$

where $\omega_{ECI,3} > \omega_{ECI,1}, \omega_{ECI,2}$. This frequency thus depends on the magnitude of the rotations around the principal axes, as estimated by the navigation algorithm. The corresponding period is found using

$$T_n = \frac{2\pi}{W_n} \tag{7.9}$$

with W_n in rad/s. The value of T_n in seconds may be used as an initial estimate for $\beta_{2,2}$ in Equation (7.7).

Amplitude

The main amplitude, $\beta_{1,1}$, is determined from the amplitude of the largest rotation around the principal axes of the target body, while the secondary amplitude, $\beta_{2,1}$, is determined from the second largest rotation. As rotations around the three axes of the target are estimated by the navigation algorithm, an estimate of the amplitude can be made using

$$\beta_{i,1} = \frac{\max(\omega_{pi,\text{nav}}) - \min(\omega_{pi,\text{nav}})}{2} \tag{7.10}$$

where it is assumed that $\omega_{p1} \gg \omega_{p2}, \omega_{p3}$ (with $p1, p2, p3$ the principal axes). This is considered a valid assumption in the case of Envisat (see Section 2.2).

Vertical shift and phase shift

The vertical shift (β_0) can simply be estimated from the mean of the set of measurements. The estimate for phase shift $\beta_{k,3}$ is completely dependent on the attitude of the target with respect to the inertial frame and the time at which measurements are initiated and can be estimated by finding the first zero-crossing with positive derivative $\frac{\Delta f(t,\boldsymbol{\beta})}{\Delta t}$ from the set of measurements. These estimates form the starting point for regression.

Results

The results are presented in Figure 7.17 and Figure 7.18. An analysis is made using both order N=1 and N=2 (see Equation (7.7)) and the method is evaluated for its performance in estimating $\boldsymbol{\omega}_{RTN}^{TBF/RTN}$ which

defines the location of the spin-axis in the RTN-frame. Figure 7.17 shows the achieved fit of $\boldsymbol{\omega}_{RTN}^{TBF/RTN}$, using measurements of high accuracy ($\sigma_q = 10^{-6}$ deg, see Section 5.2.1). Figure 7.18 shows the 3D position error that is obtained from this method, when the fitted rotation is used to predict the intersection of the spin-axis with the KOS to calculate the desired chaser state according to Equation (5.9c). Furthermore, a short numerical summary of the results in provided in Table 7.5.

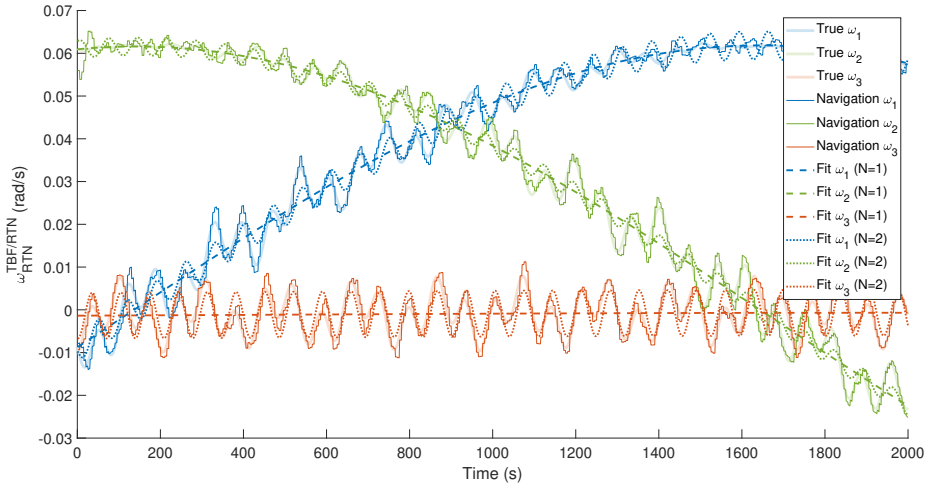

Figure 7.17: Achieved fit of $\omega_{RTN}^{TBF/RTN}$ with method A, using sinusoids of order $N = 1$ and $N = 2$. It may be observed that a good fit is achieved, especially when $N = 2$, accounting for the period of the wobbling very well, however, not fully capturing the amplitude of the wobbling. The method with $N = 1$ does not account for the wobbling motion, however, still achieves a satisfactory fit and is a good representation of the general trend of $\omega_{RTN}^{TBF/RTN}$.

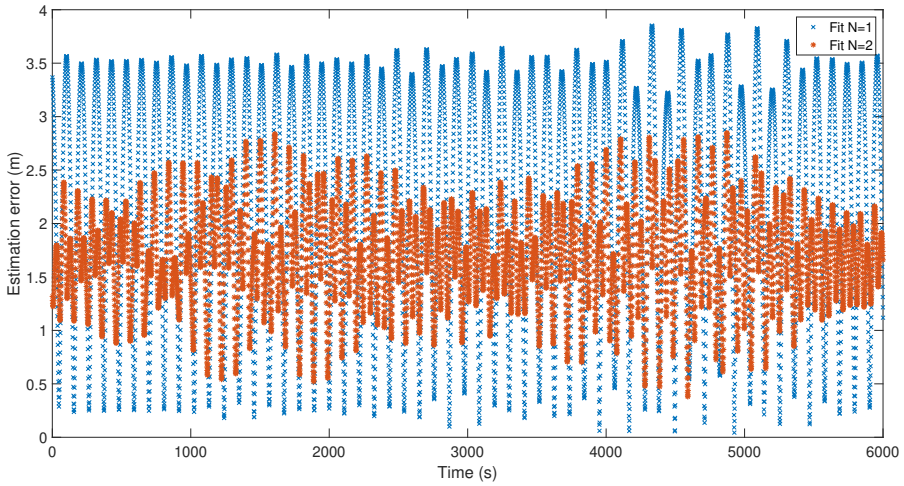

Figure 7.18: Estimation error in meters for the estimation of spin axis location over time using method A, for sinusoids of order $N = 1$ and $N = 2$. It can be seen that the error does not increase over time, contrary to the results from the integration method. The mean values of the error achieved in the cases with $N = 1$ and $N = 2$ is similar, however, the maximum error as well as the spread of the error is larger for $N = 1$.

When comparing the estimation error from Figure 7.18 with the errors obtained in the integration method in Section 7.2, it becomes clear that this method has a lot of potential. Previously, integration errors for combinations of realistic error in $\boldsymbol{J}$ and $\boldsymbol{\omega}$ could easily exceed 10 meters (see Table 7.4), whereas Figure 7.18 shows a potential for error in the order of 2-4 meters. More importantly, contrary to the results presented in Section 7.2, the error from this method does not grow over time.

Despite this method showing much potential, its robustness with respect to different scenarios must be confirmed. Furthermore, the results in this section assumed highly accurate measurements ($\sigma_q = 10^{-6}$ deg)

Table 7.5: Summary of estimation error using method A, for sinusoids of order $N = 1$ and $N = 2$. It is clear that mean value of the error is similar, but standard deviation becomes much smaller in the case of $N = 2$.

	N = 1	N = 2
Min. Error (m)	0.043	0.379
Mean. Error (m)	1.846	1.621
Max. Error (m)	3.836	2.845
Error Std. (m)	1.341	0.631

in order to prove the feasibility of this method. Therefore the accuracy of this method for a more realistic level of measurement noise must also be analysed.

Option B

Option B is concerned with fitting the value of $\boldsymbol{\omega}_{TBF}^{TBF/RTN}$ in the target body frame. In the case where $\omega_{p1} \gg \omega_{p2}, \omega_{p3}$ the main rotation is estimates using order $N = 2$, while the two rotations around principal axes $p2, p3$ of the body frame are estimated by a sinusoidal function or order $N = 1$ (see Equation (7.7)).

Frequency and Period

In this case the period $\beta_{1,2}$ can be estimated by, first, finding local minima or maxima of the ω_{p2}, ω_{p3}, estimated by the navigation filter, and, second, determining the time in-between their occurrences.

For the main rotation ω_{a1}, a more accurate estimate can be made by using a sinusoidal function with order $N = 2$. The secondary period $\beta_{2,2}$ is n_{Orbit}, as this is the period of the disturbance caused by the gravity gradient torque in Equation (3.37).

Amplitude, Vertical Shift and Phase Shift

Amplitude $\beta_{1,1}$ can also be found from local minima and maxima according to Equation (7.10). No reliable estimate for $\beta_{2,1}$ can be found, and the only restriction for this parameter is $\beta_{2,1} < \beta_{1,1}$.

The vertical shift β_0 can again be estimated from the mean of the data set and phase shift $\beta_{1,3}$ is dependent on the target attitude and time of measurement, and can be estimated by finding the first zero-crossing with positive derivative $\frac{\Delta f(t,\boldsymbol{\beta})}{\Delta t}$, similar to 'Option A'. For $\beta_{2,3}$ no reliable estimate is available and it can be set to a random value to be changed by the regression process.

Results

Similar to option A, highly accurate measurements are employed ($\sigma_t = 10^{-6}$ deg) to prove the feasibility of this method. The results are presented in Figure 7.19 which shows the true and fitted $\boldsymbol{\omega}_{TBF}^{CBF/TBF}$.
Next, the capability of method B for estimating $\boldsymbol{\omega}_{RTN}^{TBF/RTN}$ is investigated. This requires the fitted values to be converted to the RTN-frame. This conversion requires an estimate of $\boldsymbol{q}_{TBF}^{RTN}$ at every future step, which is obtained by evaluating Equation (3.34). Whereas the fitted model from Figure 7.19 is accurate, the estimate of $\boldsymbol{\omega}_{RTN}^{TBF/RTN}$ that results from it is not. In fact, this method completely fails to correctly identify $\boldsymbol{\omega}_{RTN}^{TBF/RTN}$ after a short period of time.

This failure is likely due to the fact that errors in the estimation of $\boldsymbol{\omega}_{RTN}^{TBF/RTN}$ compound from two sources. Errors in the fitted value of $\boldsymbol{\omega}_{TBF}^{TBF/RTN}$ stack on each other, as was experienced with the integration method. This yields an increasingly worse estimate of $\boldsymbol{q}_{TBF}^{RTN}$ over time. Since an accurate value of $\boldsymbol{q}_{TBF}^{RTN}$ is required to transform $\boldsymbol{\omega}_{TBF}^{TBF/RTN}$ to $\boldsymbol{\omega}_{RTN}^{TBF/RTN}$, this conversion quickly produces useless results. Since this method fails even with highly accurate measurements, and it is decided to abandon method B for estimation of $\boldsymbol{\omega}_{RTN}^{TBF/RTN}$.
In all subsequent sections only an analysis of method A is provided. Method B can however be employed to improve the estimate of the instantaneous $\boldsymbol{\omega}_{TBF}^{TBF/RTN}$, required in phase 3. This is further discussed in Section 7.4.1.

7.3.2. Proof of general applicability

Since several scenarios are possible for the orientation of the spin-axis with respect to the orbital momentum vector, as outlined in Table 2.4, the fitting method needs to be tested against all scenarios. In order to verify the applicability of this method over a wide range of scenarios, tilt angles between the spin-axis and orbit normal of 0, 45 and 90 degrees are considered. In the scenario where the spin-axis is aligned with the orbital

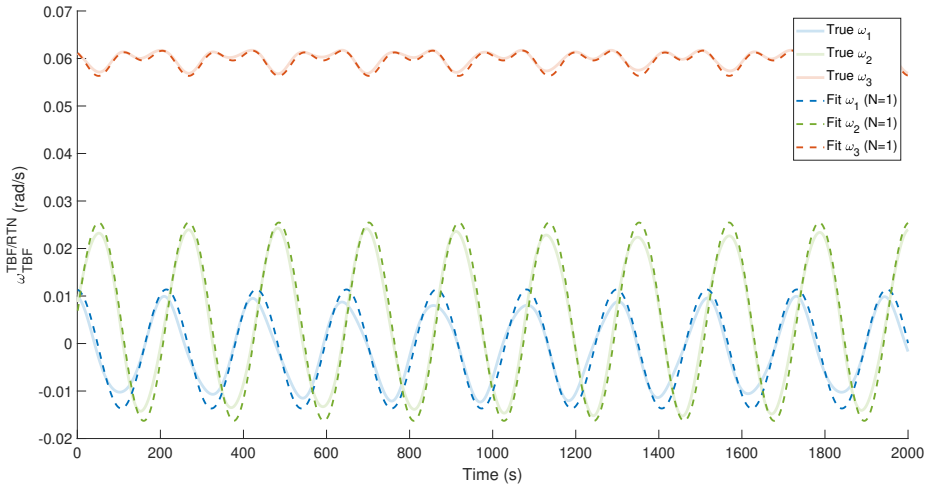

Figure 7.19: Fitting $\omega^{TBF/RTN}_{TBF}$ with method B, using sinusoids of order $N = 2$ for the main rotation and order $N = 1$ for the secondary rotations. It may be observed that a highly accurate fit of $\omega^{TBF/RTN}_{TBF}$ can be produced.

momentum vector (tilt angle 0^o) the main rotation is around the Z-axis and stay there continuously. In a scenario where the spin-axis is at a 45° tilt angle with the orbital momentum vector, the main rotation is distributed between the Z-axis and the X- or Y-axis. The scenario with 90^o tilt angle is used as reference in this entire chapter and indicates the spin-axis being in the orbital plane. Verifying this method for these three values proves its general applicability, as all other tilt angles are variations of the 45^o case.

The results are presented in Figures 7.20 and 7.21, still using highly accurate measurements ($\sigma_q = 10^{-6}$ deg). Furthermore, a numerical summary of the errors obtained from both scenarios is provided in Table 7.6.

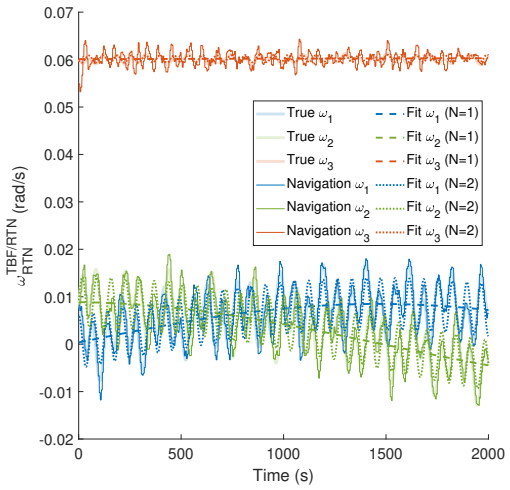

(a) Fitting $\omega^{TBF/RTN}_{RTN}$ for spin-axis aligned with orbital momentum.

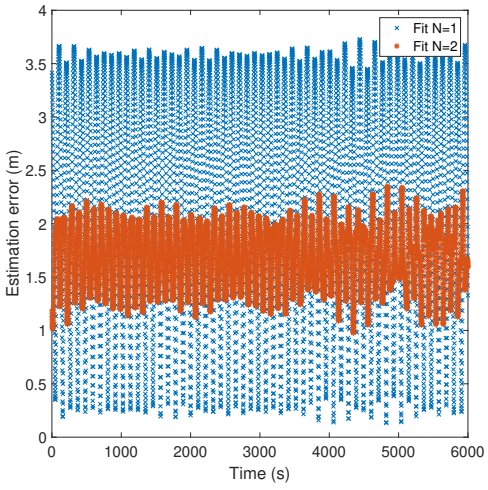

(b) Estimation error in meters for the estimation of spin axis location over time for spin-axis aligned with orbital momentum.

Figure 7.20: Curve fit and corresponing estimation error for $\omega^{TBF/RTN}_{RTN}$ aligned with orbital momentum.

It may be observed that similar results are found from Figures 7.20 and 7.21, compared to Figure 7.18. Furthermore, very similar numerical values may be noticed between Table 7.5 and Table 7.6. This is a strong indication that the fitting method can be considered robust for a range of scenarios that is encountered during the mission.

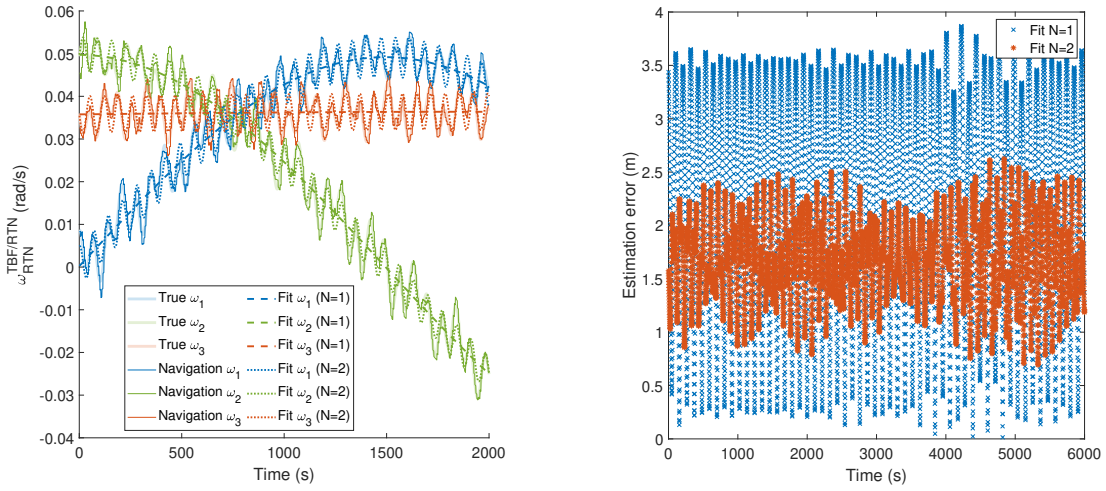

(a) Fitting $\omega_{RTN}^{TBF/RTN}$ for spin-axis at 45 degrees with respect to orbital momentum.

(b) Estimation error in meters for the estimation of spin axis location over time for spin-axis at 45 degrees with respect to orbital momentum.

Figure 7.21: Curve fit and corresponing estimation error for $\omega_{RTN}^{TBF/RTN}$ at 45 degrees with orbital momentum.

Table 7.6: Position errors obtained from fitting $\boldsymbol{\omega}_{RTN}^{TBF/RTN}$, using a spin-axis with tilt-angles 0° and 45°. The standard deviation for the case of N=1 is high due to the error not being normally distributed. Therefore a relatively large interval is required to capture 68.27% of all data.

	Tilt angle 0^o		Tilt angle 45^o	
	N = 1	N = 2	N = 1	N = 2
Min. Error (m)	0.134	0.984	0.013	0.690
Mean. Error (m)	1.938	1.686	1.905	1.630
Max. Error (m)	3.725	2.353	3.869	2.627
Error Std. (m)	1.294	0.431	1.386	0.648

7.3.3. Sensitivity Analysis

The robustness of the fitting process must be analysed by evaluating its sensitivity with respect to several important parameters. First, the robustness is assessed with respect to the initiation time of the curve fitting, as the fitting process requires a minimal number of data points to be initiated. Second, the robustness of the fitting process with respect to measurement errors must be assessed.

Initiation Time

The regression process described by Equation (7.5) computes all fitting parameters $\beta_{k,i}$ in Equation (7.7) during an observation period prior to the actual approach, respectively magnitude, period, phase shift and mean amplitude. This period of observation was determined to have the length of a full orbital period, ≈ 6029 s. In order to avoid errors due to small uncertainties in the orbital period, the fitting process is 're-initiated' after the eclipse. This means that rather than calculating the values of $\boldsymbol{\omega}$ using the current fit at $t > 6029$ s, e.g. $f(6030, \boldsymbol{\beta})$, it is decided to calculate a new value for phase shift $\beta_{k,3}$. This new value is calculated such that the first measurement after the eclipse period is labelled $t = 1$. The other parameters β are simply copied from the fit that was achieved during the period of observation.

Therefore, a satisfactory value of $\beta_{k,3}$ must be determined prior to attempting the manoeuvre, such as to be able to provide the best possible estimate of the future spin-axis orientation. Since the total illuminated time on the orbit is ≈ 4000 seconds and the manoeuvre is 1500 seconds, the maximum allowable time for convergence of the new fit is set to 2000 seconds, assuming a safety margin of 500 seconds for the manoeuvre. However, taking the full 2000 seconds to converge is undesirable, as there would be little room for aborting the manoeuvre near the end of it. Lower converge times would thus be desirable. The initiation time is the time over which measurements are acquired after the eclipse period, before attempting the re-initiation of the fit using those measurements.

An analysis is performed, testing the converge of the re-initiated fit for $\beta_{k,3}$ over different initiation times.

In this analysis the spin-axis of Envisat is aligned with the $+y$-/T-axis of the RTN-frame at $t = 0$. The orbit is initiated such that the period of darkness is at the 'end' of a simulated orbit, which has an orbital period of $T_{orbit} = 6029$s. Table 7.7 presents the achieved mean and maximum error of the fitting process, obtained over a period of 2000 seconds, initiating the fit using different initiation times, starting at $t = 0$, directly after the eclipse period.

Table 7.7: Overview of mean and maximum errors for fitting $\omega_{RTN}^{TBF/RTN}$ for different initiation times, using sinusoids of order 1 and 2 over a period of 2000 seconds. For t = 0 up to t = 2000.

Initiation Time (s)	Mean Error (m)		Max Error (m)	
	N=1	N=2	N=1	N=2
50	3.007	3.044	6.589	8.268
100	2.912	2.437	6.191	6.696
250	2.655	2.293	5.840	6.497
500	2.281	1.970	4.151	4.967
1000	2.240	1.766	3.686	3.348
1500	2.238	1.743	3.627	3.262
2000	2.238	1.717	3.639	3.033

It may be noticed that relatively long convergence times are required, as the mean error in Table 7.7 can be observed to decrease until reaching a stable value after 1000 seconds. This is however highly dependant on the attitude of the target at the time of the initiation, which can be shown by using the same set of initiation times but changing the starting point of the initiation, allowing a different attitude of the target. If the fit would have been initiated at $t = 1000$ s after the eclipse period, instead of directly after the eclipse period, the required time for convergence would be much lower, as demonstrated in Table 7.8

Table 7.8: Overview of mean and maximum errors for fitting $\omega_{RTN}^{TBF/RTN}$ for different initiation times, using sinusoids of order 1 and 2 over a period of 2000 seconds. For t = 1000 up to t = 3000.

Initiation Time (s)	Mean Error (m)		Max Error (m)	
	N=1	N=2	N=1	N=2
50	2.327	25.894	4.242	49.923
100	2.252	1.840	3.817	4.013
250	2.243	1.784	3.694	3.684
500	2.241	1.770	3.657	3.484
1000	2.241	1.703	3.641	2.926
1500	2.242	1.723	3.669	3.101
2000	2.241	1.723	3.639	3.047

This results in an undesirable situation, as the attitude of the target is not a controllable value and a risk is presented when the initiation time is too long. It is therefore decided to abandon the 're-initiation' of the fit and instead calculate the expected rotation using the originally computed set of parameters, $\boldsymbol{\beta}$, using $f(T_{\text{Orbit}} + t, \boldsymbol{\beta})$.

Measurement error

Lastly, it is important to confirm robustness of this process with respect to realistic measurement errors. For this purpose the fits from the previous sections have been recomputed using a measurement standard deviation of respectively

$$\sigma_q = 0.5,\ 1,\ 2 \text{ and } 5 \text{ deg}$$

and a mean of $\mu_q = 0$ degrees. The results have been summarised in Table 7.9.

The most interesting conclusion that can be drawn from this test is the fact that the method with $N = 2$ loses its advantage over the method where $N = 1$ when measurement uncertainties grow. Whereas the higher order method outperformed the lower order method in the earlier scenarios with high accuracy, it performs

Table 7.9: Overview of mean and maximum fitting errors for different levels of measurement accuracy.

σ_q (deg)	N = 1		N = 2	
	Mean Error (m)	Max Error (m)	Mean Error (m)	Max Error (m)
0.5	2.251	3.764	2.154	4.101
1	2.252	3.767	2.223	4.288
2	2.255	3.879	2.445	4.688
5	2.267	4.077	4.130	7.404

worse when the level of measurement noise is increased. It may be observed from Table 7.9 that for accurate measurements ($\sigma_q = 0.5$ deg) the orders $N = 1$ and $N = 2$ exhibit similar performance, and, while the method of order $N = 1$ keeps performing at the same level of error, the method with $N = 2$ shows decreased performance when measurement uncertainties are increased.

The reason for this is that when additional noise is added, the wobbling is harder to observe in the data and therefore harder to accurately estimate. It becomes clear that under these conditions the method with $N = 2$ loses its value. Since under realistic conditions the lower order method ($N = 1$) is more accurate or as accurate as the higher order method ($N = 2$), the lower order method is identified as most promising solution for reaching more accurate estimates of the final position. Table 7.9 also shows that the method with order $N = 1$ is robust to measurement errors, as the error remains stable, despite an increasing measurement accuracy.

This robustness is likely a characteristic of the least squares method, combined with how the navigation filter estimates the target rotation. It was explained in Section 5.2.2 that the filter receives measurements of the attitude, and is required to estimate rotation from these measurements over time. This leads to higher errors in the instantaneous estimate of rotation $\boldsymbol{\omega}$, but should yield a relatively accurate representation of the target rotation over the long term, being near to the true value on average. The least squares method is a perfect tool for estimating this average behaviour, which should thus be a good representation of the true behaviour, as is indeed observed in the good results obtained from this section.

7.4. Comparing Integration and Fitting

Two methods for estimating the desired chaser state, at the intersection of the spin-axis with the KOS, were presented in Sections 7.2 and 7.3, a method of integration and a method of fitting. The integration method is widely used ([86, 90]) and is the current standard method for this type of estimation. It was however shown that in the presence of uncertainties, this method of integration is inadequate in achieving accurate results. For this reason the fitting method was introduced and examined, and the results showed that the method has a potential for delivering a more robust estimate with a higher accuracy.

7.4.1. Impact on guidance

This section evaluates the impact of using both methods on guidance. Focus is on the evaluation of the total efficiency of the manoeuvre and both the estimated as well as the attained final location.

Phase 2: Final position estimation

First, an assessment is made the stability of both methods, meaning the estimation error behaviour and predictability in the magnitude of the error. Several simulations were performed to illustrate this point, the results of which are displayed in Figure 7.22.

Figure 7.22 shows that the estimation error in is rather unpredictable for the integration method, showing large peaks at random moments, while also showing an inconsistent error magnitude over time. Furthermore the error that is achieved in a specific run is unpredictable as the error behaviour achieved over all the runs is very different for each run. For the fitting method, however, it may be observed that the expected error does not grow or decrease over time, only oscillate. This results in its maximum and minimum accuracy being predictable.

The introduction of the fitted final state thus results in a more stable final state, as expected. The resulting individual components of the estimated final state, obtained through both integration and fitting, are shown in Figure 7.23. This shows that the estimate obtained from fitting is more robust than the estimate obtained from integration. In fact, the final position error is nearly constant for all runs when using the fitting method,

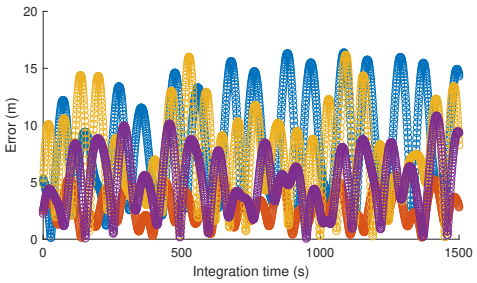

(a) Integration method, 4 simulations.

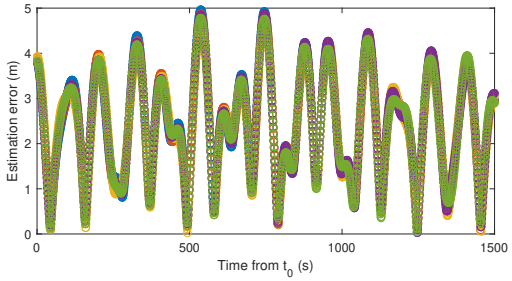

(b) Fitting method, 5 simulations.

Figure 7.22: Error behaviour over time for randomly selected simulations. The error in the case of the integration method is unpredictable and varies strongly per individual simulation. The error of the fitting method oscillates steadily and does not grow over time, making its limits predictable.

and the position error has a value of 3.9 meters. This is an improvement over the final position error for the runs using forward-integration, as those obtain a final state estimate between 2.8 and 13.2 meters.

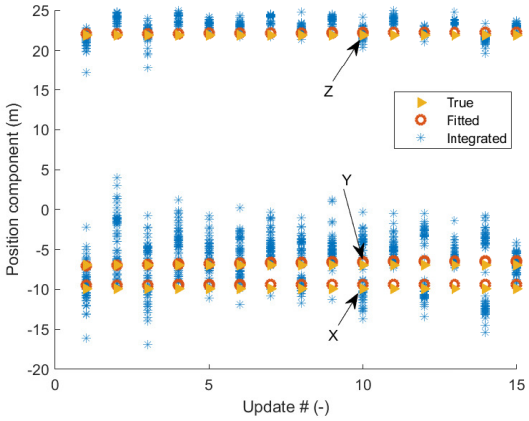

(a) Individual components of the final state.

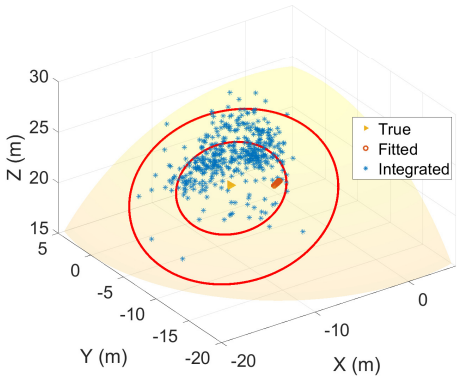

(b) Final state projected on the KOS.

Figure 7.23: True and estimated final position from 30 random simulations using both integration and fitting method. The red circles have a radius of 5m and 10m respectively and are centred around the true value. It may be observed that while the estimated state of the integration method is spread widely, the estimated state of the fitting method is grouped closely together.

One step remains in this comparison, which is the use of both the fitting and integration method in a number of optimal trajectories. An analysis was performed with a total of 45 separate runs. In 15 of these runs the fitting method was used to determined the final position, in the other 30 runs the integration method was used for the same purpose. These 30 runs consisted of 2 sets of 15 runs, each set with a different level of uncertainty. The achieved final position error of the chaser is computed for all runs and the results are summarised in Table 7.10.

This table demonstrates that the choice between the integration and fitting method is not always straightforward. If the measurements and the available information about the target inertia are accurate enough, the integration method may well outperform the fitting method, as demonstrated by Table 7.10. Even for the integration runs with higher uncertainties, there is a 50/50 chance of being more accurate than the fitting method. This is however not considered very desirable, as the odds of doubling the error are as likely, if not more likely, as to halve it.

Furthermore, the table demonstrates the robustness of the fitting estimate. The difference between the maximum and minimum value for 15 runs of the fitting method is only 0.28 m, while this difference is 4.13 m for the high accuracy integration runs and an astounding 13.63 m for the integration runs with lower accuracy. This repeatedly demonstrates that the fitting method is more stable and the error resulting from it more predictable, despite the fact that the integration might outperform this method is some cases. The integration method should be avoided if possible, especially over long time-spans.

Table 7.10: Achieved final position from simulation with the complete GNC architecture, fitted and integrated. The uncertainties on attitude measurements (σ_q, see Section 5.2.1) and target inertia (ϵ_J, see Section 7.2.3) are included. It may be observed that the performance of the fitting method is robust and predictable, while the performance of the integration method is highly sensitive to uncertainties.

	Integrated $\sigma_q = 3$ deg $\epsilon_J = 2\%$	Integrated $\sigma_q = 5$ deg $\epsilon_J = 4\%$	Fitted $\sigma_q = 5$ deg $\epsilon_J = 4\%$
Final Position Error (m)	0.96	0.53	4.80
	1.54	2.94	4.82
	1.60	3.63	4.88
	1.72	3.64	4.91
	1.73	3.84	4.93
	1.73	4.13	4.93
	1.82	4.41	4.94
	1.96	5.03	4.94
	2.03	8.12	4.94
	2.04	8.59	4.96
	2.17	9.23	4.98
	2.31	9.33	4.99
	2.38	9.44	5.01
	5.07	13.95	5.02
	5.17	14.10	5.08

Phase 2: Delta V

Figure 7.24 shows the resulting open-loop ΔV values for several runs using the fitted final state estimate, compared to similar runs from Chapter 6 using the integrated final state estimate. There is no direct link between the magnitude of the final open-loop (or closed-loop) ΔV and the use of the fitted final state estimate. However, Figure 7.24 shows that the integrated cases display a 'bulge' near the end of the trajectory, as well as showing large differences in the final piece-wise ΔV value, which can either increase steeply, or remain close to zero. The fitted cases, on the contrary, shows a great coherence regarding their final piece-wise ΔV values. This robustness is the most significant gain of the fitting strategy. The accuracy of the fitting strategy might be improved in future experiments by using the integration method over a short period of time at the end of the manoeuvre.

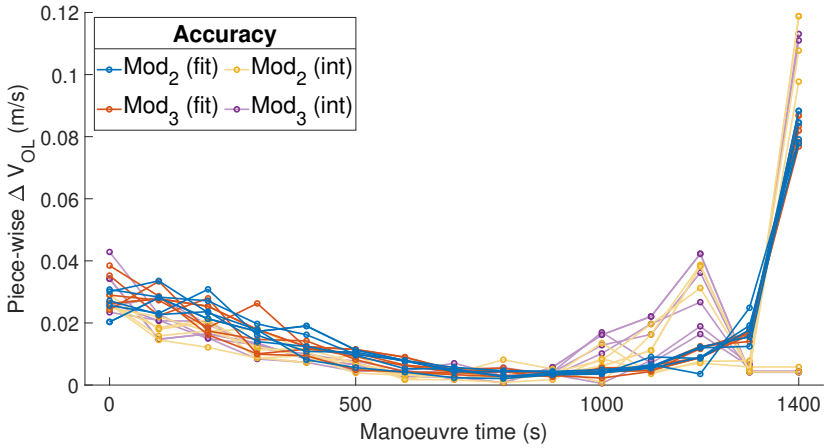

Figure 7.24: Open-loop ΔV values for nominal runs with accuracy level Mod_2 and Mod_3, comparison of runs with integrated and fitted final state.

Phase 3 rotation

The rotation $\boldsymbol{\omega}_{TBF}^{TBF/RTN}$ is the most important parameter of phase 3, as it also fully determines the desired state, according to Equation (5.15). The estimate of this parameter can be retrieved from navigation, or

through fitting method B (see Section 7.3.1). The accuracy of the estimate of $\boldsymbol{\omega}_{TBF}^{TBF/RTN}$ is analysed for a realistic measurement standard deviation of $\sigma_t = 5$ deg, for which the results are presented in Figure 7.25.

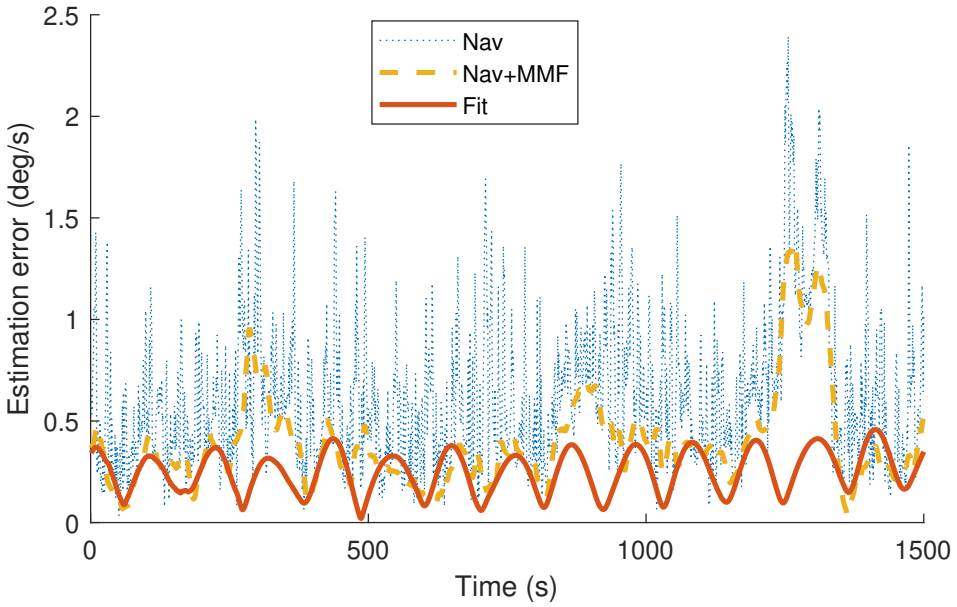

Figure 7.25: Phase 3 $\omega_{TBF}^{TBF/RTN}$ errors achieved from navigation, a moving mean filter and fitting.

The estimate achieved through fitting method B is both smoother and more accurate than the estimates obtained from navigation, even with the moving mean filter. However, when this fitted value is transformed to $\boldsymbol{\omega}_{TBF}^{TBF/RTN}$ using $\boldsymbol{q}_{TBF}^{RTN}$, this smoothness is lost, as is shown in Figure 7.26. With this it also loses its advantage over the estimate made by the navigation filter + MMF, and experimental results show that the ΔV and guidance errors are not improved with respect to the case with navigation and moving mean filter.

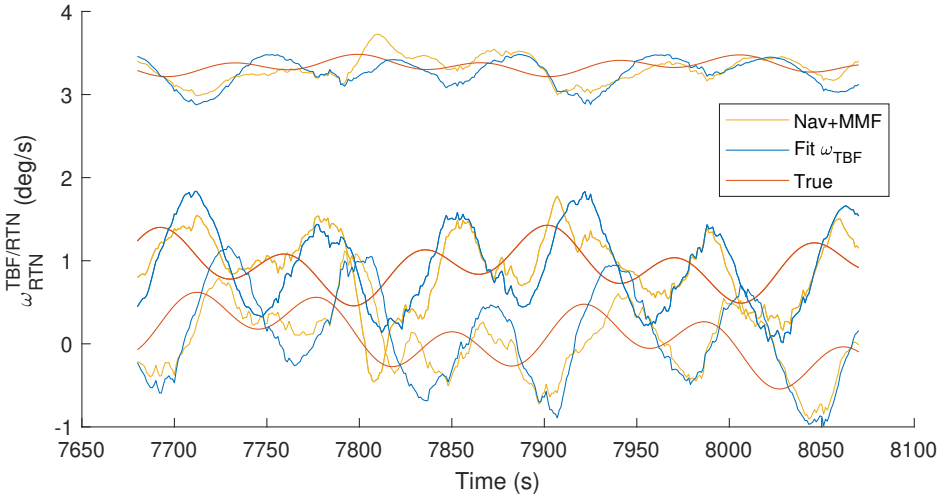

Figure 7.26: Estimating $\boldsymbol{\omega}_{RTN}^{TBF/RTN}$ through navigation and fitting.

7.4.2. Accuracy

The accuracy of both methods has been discussed at length in the previous sections, therefore a short summary is sufficient. Section 7.2 showed that the accuracy of the integration method is dependent on a number of parameters, respectively $\boldsymbol{J}_{\text{tar}}$, $\boldsymbol{\omega}_0$ and $\boldsymbol{q}_0$, where the effect of $\boldsymbol{q}_0$ is negligible compared to the other two. From Table 7.4 it was established that an accurate estimate of the spin-axis location can only be found from

the combination of very accurate initial conditions, low inertia uncertainties and a short integration time. When considering the total manoeuvre time of 1500 seconds and reasonable uncertainties in $\boldsymbol{\omega}$, $\boldsymbol{J}$ of 0.5 deg/s and 4%, the expected accuracy is 5-8 meters with a standard deviation of approximately 2 m (see Table 7.10).

The fitting method was discussed in Section 7.3 and is almost completely uncoupled from initial parameters and the estimate of inertia $\boldsymbol{J}$, as these only influence the prior estimate of the fitting parameters $\boldsymbol{\beta}$ in Equation (7.7), but do not cause problems for the fitting process. The results for this method under realistic measurement conditions were presented in Table 7.9 and the expected accuracy was established to be 4-5 meters with a standard deviation of 10-20cm (see Table 7.10). This is still the largest contributor of final position error, however, more accurate than the integration method and, more importantly, less sensitive to uncertainties.

7.4.3. Advantages and Drawbacks

In conclusion to this chapter, all advantages and disadvantages that were identified for both methods are listed in a single overview.

Integration Method

A lot of disadvantages of this method were identified in the previous sections, along with several advantages of this method. To summarise:

Advantages:

- Always works when an estimate of $\boldsymbol{\omega}_{TBF}^{TBF/ECI}$, $\boldsymbol{q}_{RTN}^{TBF}$ is available. No initiation time is required, allowing to use this method without the need for a dedicated time for measurements prior to the approach.
- This method is a good reflection of the true dynamics and if the estimation of both these parameters would be perfect, the integration would result in a perfect representation of the truth.

Drawbacks:

- Requires very high accuracy of $\boldsymbol{\omega}_{TBF}^{TBF/ECI}$, $\boldsymbol{q}_{RTN}^{TBF}$ to yield accurate results. Estimates of $\boldsymbol{\omega}_{TBF}^{TBF/RTN}$ and $\boldsymbol{q}_{RTN}^{TBF}$ are certain to contain uncertainties.
- Suffers from high errors especially over large integration times, as uncertainties compound over time.
- Highly sensitive to uncertainties in $\boldsymbol{J}$. The inertia matrix $\boldsymbol{J}$ also contains uncertainties (see Table 2.1) and has an large influence on the accuracy of the integrated dynamics, as was shown in Section 7.2.3.
- There is little correlation between error from uncertainties $\boldsymbol{J}$ and $\boldsymbol{\omega}$.
- The behaviour of the error is unpredictable and its magnitude is completely dependant on the accidental conditions and accuracy of the available measurements.

Fitting Method

The fitting method was presented as an alternative for the integration, which is current standard. Also for this method several advantages and drawbacks were identified. To summarise:

Advantages:

- This method is independent from $\boldsymbol{J}$, which is a large advantage when working with uncooperative targets, as those usually exhibit large inertia uncertainties.
- The fitting method does not require an instantaneous estimate of the current dynamics in the form of $\boldsymbol{\omega}_{TBF}^{TBF/RTN}$. This means that the method is not sensitive to any instantaneous errors present in the measurements of $\boldsymbol{\omega}$. Therefore, if the expected rotation of Envisat is assessed prior to the real mission, a good estimate of the expected amount of final position error can be made.
- Predictable error behaviour. The estimate of the final spin axis has a predictable amount of error, which is constant over time. Furthermore, subsequent estimates of the final position are very close together, always guiding the satellite to the same point and saving some ΔV.

Drawbacks:

- Requires (long) period for initiation prior to the approach to allow convergence of the fit. This period is recommended to be one full orbit, as this provides more than enough data, allowing for a more reliable fit.
- Uncoupled from and thus not a good reflection of the true dynamics. Even if the measurements would be perfect, some error would still be retained when using this method. This is inherent to this method, as it does not consider the target dynamics in any way. Furthermore, a sinusoid is not a completely accurate representation of rotations with the triaxial symmetry, obtained when all three diagonal components of $\boldsymbol{J}$ are different in magnitude [51].
- Contrary to the integration method, where accuracy increased when the integration time was decreased, the accuracy of the fitting method is not improved as the remaining time becomes smaller.

8

Trajectory design

This chapter is concerned with the design of an optimal trajectory for the spacecraft to follow. Optimality, in this context, concerns the optimality of lighting conditions and mission geometry, such that optimal performance of the vision-based pose estimation system may be achieved. Lighting conditions, or illumination conditions, are defined from the angle between the camera boresight axis and the incoming solar rays. When then sun is positioned directly behind the camera, these two vectors are aligned and the angle between them is zero. This scenario is considered the most desirable, as all the visible surfaces of the target spacecraft are illuminated in the camera images. Therefore, whenever lighting conditions or illumination conditions are discussed, the angle between the camera boresight vector and the outgoing vector from the sun to the camera is considered. This angle is represented by χ_{cam}. An important parameter in the design of these orbits is the sun-angle β, which is defined as the angle between the vector pointing from the sun to earth and the target orbit normal.

Section 8.1 presents some tools that can be leveraged in the design of such an optimal trajectory. Section 8.2 discusses how the expected orientation and rotation of the target influence the optimal design. Subsequently, Section 8.3 shows how to evaluate the lighting conditions during the three parts of the reference trajectory (see Section 2.1), and how to use those conditions in the design of an optimal orbit. Finally, the performance of the GNC system for an optimally designed trajectory is evaluated in Section 8.4, demonstrating the benefits of such a trajectory.

8.1. Design Tools

This section continues to build on the ROE parameterization presented in Section 3.3.3, and shows how this representation of the 3D motion can be used to design relative orbits with particular beneficial geometries relatively easily. These beneficial geometries may then be employed in the design of optimal trajectories.

8.1.1. Angle with target orbital plane

The first property to discuss is the angle of the relative orbit with respect to the orbital plane. This property is particularly useful when designing the passively safe, closed observation orbit for the first phase of the mission (see Section 4.2). In this phase the satellite is uncontrolled, meaning that the selected relative orbit fully determines the viewing conditions in this phase.

The angle between the relative orbital plane is represented by ρ, and is visualised in Figure 8.1. Figure 8.1b shows that for passively safe relative orbits, where $\delta\boldsymbol{e} \parallel \delta\boldsymbol{i}$ and $\delta a = \delta\lambda = 0$ (see Section 3.3.3), the angle ρ, between the planes of the target orbit and the relative orbit, can be defined as

$$\tan(\rho) = \left|\frac{\delta i}{2\delta e}\right| \quad \rightarrow \quad \rho = \arctan\left(\left|\frac{\delta i}{2\delta e}\right|\right) \tag{8.1}$$

which also represents the angle between the target orbit normal vector and the relative orbit normal vector.

As the camera travels the relative orbit, always pointing at the target, the camera boresight axis has an angle with the target orbital plane that varies between $+\rho$ and $-\rho$. This can be confirmed by investigation the angle

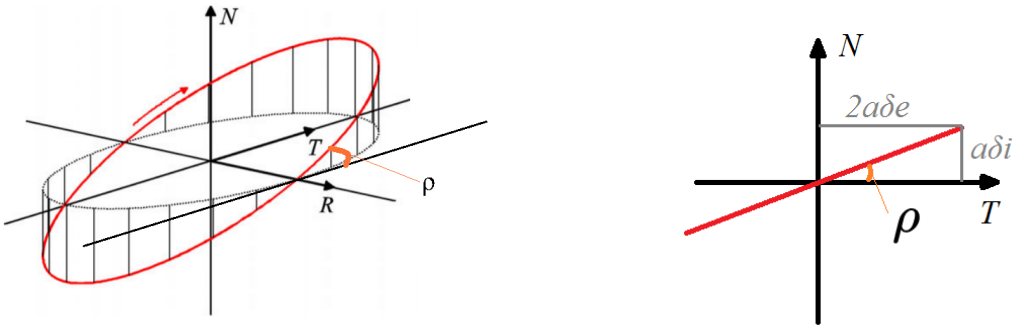

(a) 3D view.

(b) Side-view of the N-T plane.

Figure 8.1: Angle ρ, between the orbital plane and the relative orbital plane. The side-view is obtained by letting $\delta a = \delta\lambda = 0$ in Figure 3.5.

of the camera with respect to the target orbital plane, plotted in Figure 8.2 over the course of a single orbit for fixed $a\delta e$ and varying $a\delta i$. The corresponding values of ρ are presented in Table 8.1.

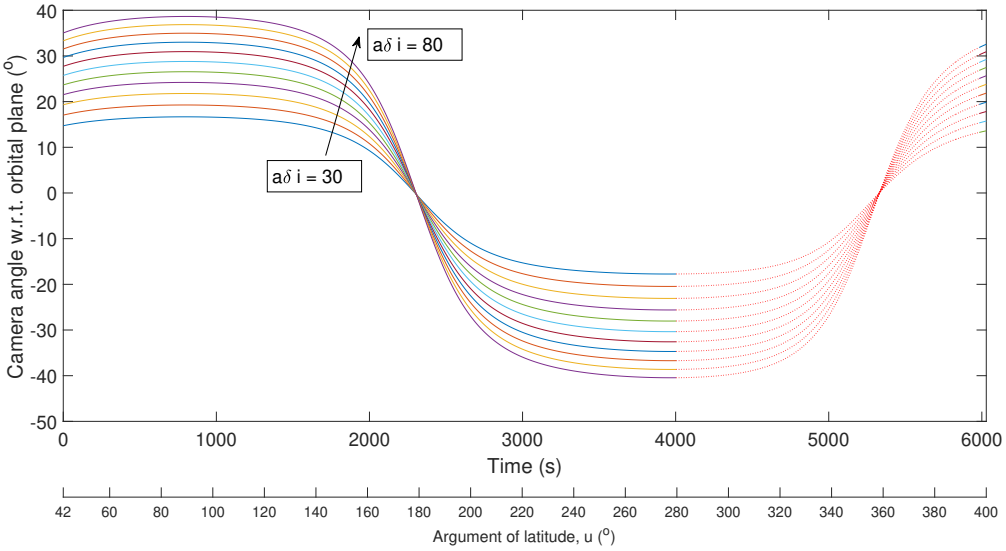

Figure 8.2: Angle of the camera with respect to the target orbital plane during one full orbital period. $a\delta e = 50$ and $\varphi, \vartheta = 0°$ (see Equation (3.20)). The coloured lines represent orbits with $a\delta i$ between 30 and 80, increasing with steps of 5 in the direction of the arrow. The red-dotted lines indicate the eclipse period.

Table 8.1: Angle ρ for the camera angles presented in Figure 8.2. aδe = 50.

aδi (m)	30	35	40	45	50	55	60	65	70	75	80
ρ (deg)	16.7	19.3	21.8	24.2	26.6	28.8	31.0	33.0	35.0	36.9	38.7

Comparing Table 8.1 to Figure 8.2, it can be observed that the angle between the camera and the orbital plane is stable at a value of $+\rho$ for approximately 1800 s, then changes sign over the course of approximately 1000 s and continues to be stable at $-\rho$ for another 1800 s. Since the angle between the boresight axis and the target orbital plane is relatively constant at either $+\rho$ or $-\rho$ over extended periods of time, the angle ρ presents an important design value for influencing the lighting conditions on the relative orbit. The angle ρ can be used as a design parameter to enable alignment of the relative orbital plane with the incoming solar rays. This can be achieved by matching ρ with the sun-angle, β, which is constant for a sun-synchronous orbit.

8.1.2. Phase angles

The position of the chaser spacecraft in the relative orbit is determined by phase angles φ and ϑ, as defined in Equation (3.20). Equation (3.20) shows that when δa and $\delta\lambda$ are equal to zero the relative position is completely defined by both phase angles and the argument of longitude u, which describes the position of the target in its absolute orbit (see Equation (3.16)). In order to meet the condition for passive safety defined in Section 3.3.4, the relation between the two angles is defined as $\varphi = \vartheta + k\pi$, with k an integer. This means that the two angles are necessarily combined and serve as a single design variable together. The phase angles can be used to influence the lighting conditions during the first phase of the rendezvous and to define the starting position of the optimal manoeuvre in the second phase of the rendezvous process (see Section 4.2 for definitions of the phases).

The phase angles, φ and ϑ, can be used to define the optimal position of the chaser. Which position on the orbit is optimal depends on the chosen reference, two of which are available. First, the sun and, second, the target orientation, which will both be discussed later. The exact trajectory and viewing conditions depend strongly on the choice of φ/ϑ, which is visualised in Figure 8.3.

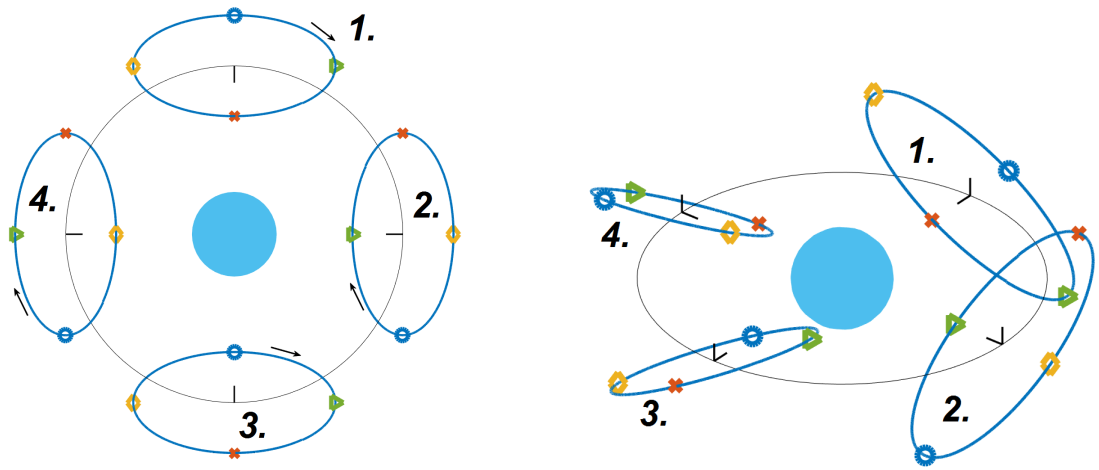

(a) Projection on target orbital plane.

(b) 3D view

Figure 8.3: Reference orbit geometry with respect to target absolute orbit around earth (blue). The four markers show the location of a spacecraft for four different values of φ, ϑ, separated 90° from each other. The R- and N- axes of the RTN frame are visualised in black. Considering that the sun and the target both have a constant position/orientation in the inertial frame, the four markers create very different lighting conditions for the camera and view the target from different perspectives during the illuminated time on the orbit.

Figure 8.3 shows how the reference orbit is oriented with respect to the absolute orbit and how the spacecraft moves in the reference orbit. This shows how the orientation of the reference orbit is fixed to the R-axis, its shortest axis always aligned with R. It can be imagined that by choosing the phase angles φ, ϑ, various lighting conditions and viewing geometries can be achieved, as the target and the sun are at a fixed orientation/position in the inertial frame while the RTN frame, and subsequently the reference orbit, rotate in the inertial frame.

Sun phase angle

Similar to how the phase angles between the target and chaser satellites were defined in Equation (3.20), a phase angle between the target and the sun can be defined. Considering that the relative orbit is not a 'real' motion, but rather a representation of the relative motion of target and chaser in their absolute orbits from the perspective of the target, a similar representation may be constructed of the relative motion between the sun and the target from the perspective of the target. The component of distance is left out of this definition, and only a relative angular position of the sun with respect to the target is defined in the form of a single phase angles φ_{sun} similar to φ, defined by Equation (3.20). As the sun is continuously on the same side of the target orbital plane, defining ϑ_{sun} would be similar to defining a constant elevation angle. Defining this angle would be useless, as it is independent from u and already completely defined from sun-angle β.

The definition of the phase angle φ in Equation (3.20) assumes that the chaser position is aligned with the negative R-axis of the target RTN frame when $\varphi = u$, as shown in Figure 3.5. Similarly, the sun phase angle φ_s can be defined such that $\varphi_{\text{sun}} = u$ when the component of the inverse sun vector in the target orbital

plane, pointing from the target to the sun, is aligned with the negative R-axis of the target RTN frame. This is visualised in Figure 8.4.

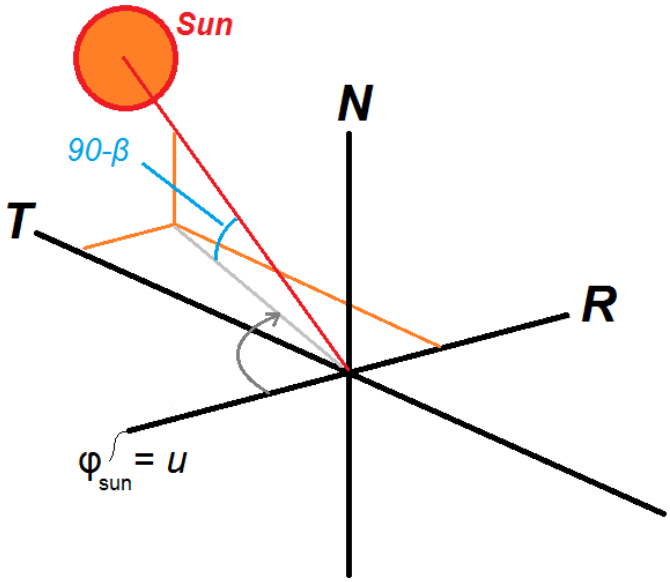

Figure 8.4: Visualisation of the definition of sun phase angle φ_{sun}. Due to the continuous and constant rotation of the RTN frame, the vector pointing from the target to the sun is subsequently aligned with $+T$ when $u = \varphi_{\text{sun}} + \pi/2$, with $+R$ when $u = \varphi_{\text{sun}} + \pi$ and with $-T$ when $u = \varphi_{\text{sun}}$ $-\pi/2$.

If the components of the unit vector pointing from the target towards the sun, are examined, it can be deduced that the inverse sun vector is aligned with $-R$ when $u \approx 340$, shown in Figure 8.5. This means that the sun can be said to have a phase angle of $\varphi_{\text{sun}} = 340$, or -20, degrees.

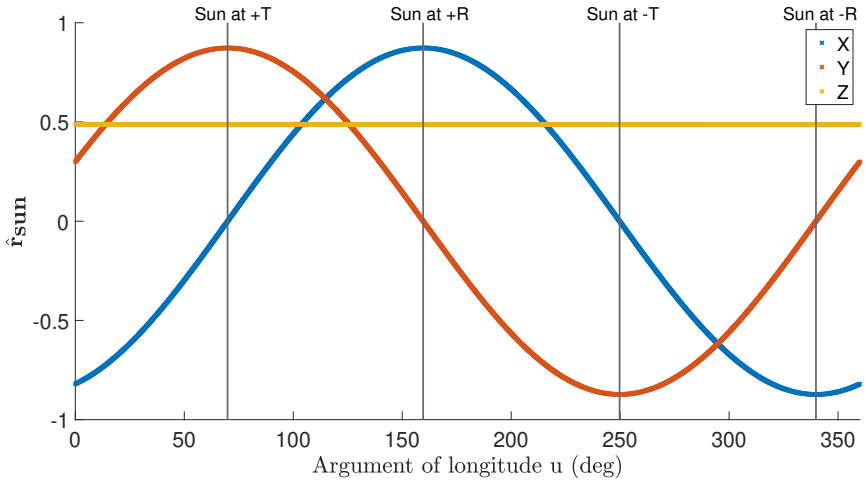

Figure 8.5: Components of the unit vector pointing towards the sun, in the RTN-frame.

Spin-axis phase angle.
The same way that φ and ϑ represent the chaser position on the relative orbit, and φ_{sun} represents the orientation of the sun, a single phase angle φ_{spin} can be used to represent the direction of the target spin-axis in the context of the relative orbit. Let

$$\hat{\boldsymbol{r}}_{\text{spin}} = \begin{bmatrix} \delta r_{R,\text{spin}} \\ \delta r_{T,\text{spin}} \\ \delta r_{N,\text{spin}} \end{bmatrix} \tag{8.2}$$

represent unit the vector that defines the pointing direction of the target spin-axis in the RTN-frame. Then the phase angle φ_{spin} can be defined (similar to φ in Equation (3.20)) from

$$\begin{aligned} \delta r_{r,\text{spin}} &= -\cos(u-\phi) \\ \delta r_{t,\text{spin}} &= \sin(u-\phi) \end{aligned} \tag{8.3}$$

$$\tan(u-\phi) = \frac{\sin(u-\phi)}{\cos(u-\phi)} = \frac{r_{t,\text{spin}}}{-r_{r,\text{spin}}} \quad \rightarrow \quad \phi = u - \text{atan2}(r_{t,\text{spin}}, -r_{r,\text{spin}}) \tag{8.4}$$

where u is the mean argument of latitude of the target orbit. The definition is visualised with respect to the reference orbit in Figure 8.6, which shows that the definition is parallel to the definition of φ as shown in Figure 3.5.

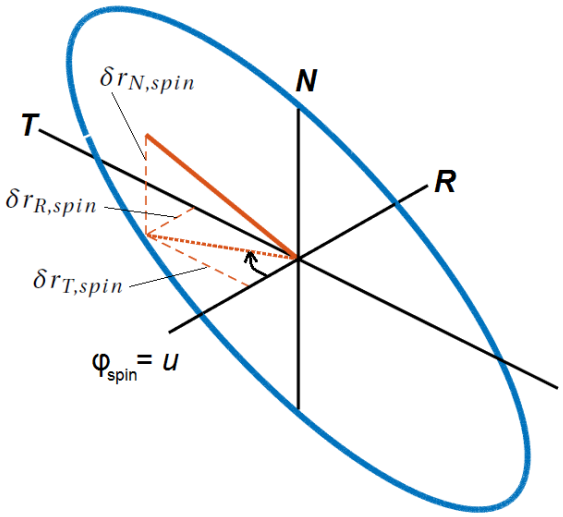

Figure 8.6: Definition of the spin-axis phase angle ϕ. The spin-axis vector pointing from the target is subsequently aligned with $+T$ when $u \approx \varphi_{\text{sun}} + \pi/2$, with $+R$ when $u \approx \varphi_{\text{sun}} + \pi$ and with $-T$ when $u \approx \varphi_{\text{sun}} - \pi/2$. Contrary to the sun vector in Figure 8.4 this alignment is not perfect due to the wobbling motion of the spin-axis in the inertial frame, resulting in the use of ≈ rather than =.

8.2. Spin-axis geometry

The movement of target spin-axis, following from its attitude dynamics, presents an opportunity to optimise the trajectory from a point of mission geometry. Positions on the relative observation orbit in phase 1 might be identified that naturally provide more, or less, favourable initial conditions for the optimal manoeuvre to start, considering that the end point of the manoeuvre is fully determined by the spin-axis movement. The definition of a spin-axis phase angle φ_{spin} in the previous section allows the use of phase angles φ and ϑ to define a suitable initial position on the relative orbit of phase 1 to begin the optimal manoeuvre of phase 2, as φ_{spin} allows a metric for comparison. The following hypothesis is constructed:

> *The most optimal manoeuvre is expected when the phase angle of the spin-axis (φ_{spin}) is equal, or similar, to the phase angle of the satellite in the relative orbit (φ).*

This hypothesis is based on the following line of reasoning.

- First, the spin-axis is assumed to have a constant orientation in the inertial frame. As the RTN frame is rotating with respect to the inertial frame (see Figure 7.16) the projection of the spin-axis travels a virtual circle in the R-T plane as visualised in Figure 8.6. This creates a virtual mean motion in the RTN frame, from the perspective of the target. The magnitude of this motion is the same as the rotation of the RTN frame with respect to the inertial frame, 360 degrees per full orbit.

- Second, the chaser completes one full revolution on the relative orbit for one full orbital period of the target in its absolute orbit. If the relative position of the chaser were projected on the R-T plane, it would similarly complete a virtual circle in the R-T plane over the course of one orbital period. In this case the same virtual mean motion is found, as was found for the spin-axis projected on the R-T plane.

  The validity of this reasoning may be proven by observing the (x,y) components of the spin-axis and chaser position vectors over the course of one orbital period. Figure 8.7 presents the value of $x/\sqrt{x^2+y^2}$ and $y/\sqrt{x^2+y^2}$ for both the spin-axis and the chaser position, where (x, y, z) are the components of the vector describing the position of the chaser and the orientation of the spin-axis in the target RTN frame. It may be observed that these lines do not resemble perfect sine waves, which would be the case if the mean motion were constant, however, approximate alignment of the X/R and Y/T components of spin-axis and chaser position may be observed throughout one orbit, if alignment at $t = 0$ is assured.

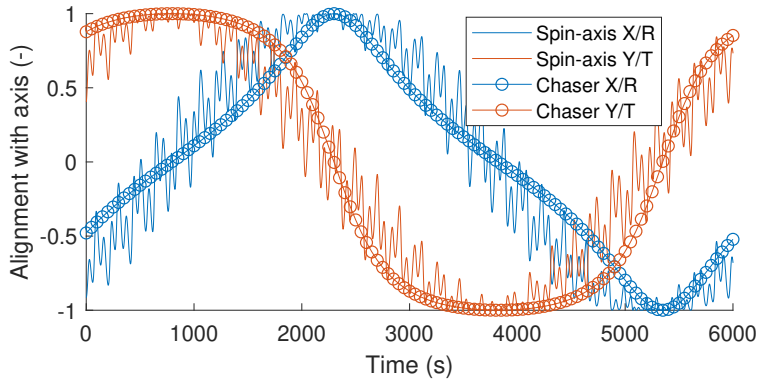

Figure 8.7: Value of $x/\sqrt{x^2+y^2}$ and $y/\sqrt{x^2+y^2}$, with (x, y, z) the components of the vector describing the position of the chaser and the direction of the spin-axis in the target RTN frame. These are not physical quantities and are merely intended to represent alignment of the projection of the vector on the R-T plane with a specific axis. A value of +1 means perfect alignment with the positive axis and -1 perfect alignment with the negative axis. For example, the X-component of both chaser position vector and spin-axis orientation vector are aligned with the $+R$ axis around 2300 s.

- Third, the optimal manoeuvre, due to its definition (see Equation (5.6)), should follow the natural orbital motion as much as possible. Therefore it is likely to resemble a closed relative elliptical orbit [90].
- Fourth, if both the observation orbit in phase 1 and the optimal manoeuvre from phase 2 resemble a closed elliptical orbit around the target, a minimal ΔV is logically achieved through a minimal alteration of the ROE, as all changes in ROE have a cost [26].
- Fifth, the manoeuvre lasts 1500 seconds, as discussed in Section 4.2. The manoeuvre starts from a point on the phase 1 observation orbit at $t = 0$. If no control were applied, the chaser would simply remain in this observation orbit and reach state $\boldsymbol{X}_{1500,\text{free}}$ after 1500 seconds. If the goal is a minimal change in ROE, the final state of the controlled optimal manoeuvre $\boldsymbol{X}_{1500,\text{opt}}$ should, logically, be as close to $\boldsymbol{X}_{1500,\text{free}}$ as possible.
- Sixth, the final position of the manoeuvre is fully defined by the location of the spin-axis (see Equation (5.9)) and the radius of the KOS. This intersection of the spin-axis vector with the KOS should thus be as close to $\boldsymbol{X}_{1500,\text{free}}$ as possible at the end of the optimal manoeuvre. It is assumed that this minimal separation is achieved when the projections on the R-T plane of $\boldsymbol{r}_{1500,\text{free}}$ and $\hat{\boldsymbol{r}}_{\text{spin}}$ (see Equation (8.2)) are aligned.
- Seventh and final, it was reasoned in the first and second step that the mean motion in the R-T plane of the projections of both chaser position and spin-axis vector are equal. Therefore, an alignment of the two at $t = 0$ should lead to alignment at $t = 1500$, at least approximately.

The hypothesis is tested by calculating the expected open-loop ΔV values for a complete range for φ_{spin} from 0 to 360 degrees, with intervals of 1 degree, using a fixed value of φ, ϑ. The open-loop trajectory is computed once, resulting in a single expected open-loop ΔV value. For each φ_{spin} this computation is performed 5 times

and random noise with a very small amplitude is added to the initial conditions to prevent the sensitivity of the guidance algorithm to initial conditions discussed in Section 5.1.3 from influencing the results. The following settings for the relative orbit were adopted:

$$\begin{aligned} \varphi = \vartheta &= 0^\circ \\ a\delta a = a\delta\lambda &= 0 \\ a\delta e_x &= 50 \\ a\delta i_x &= 60 \\ a\delta e_y = a\delta i_y &= 0 \end{aligned}$$

which simply define a convenient and passively safe relative orbit. The initial argument of latitude u, at the start of the manoeuvre, is 0.7417 radians or 42.5 degrees. The resulting ΔV for all trajectories is shown in Figure 8.8 and the orientation of the most and least optimal spin-axis orientations are are visualised in the context of the reference orbit in Figure 8.9a.

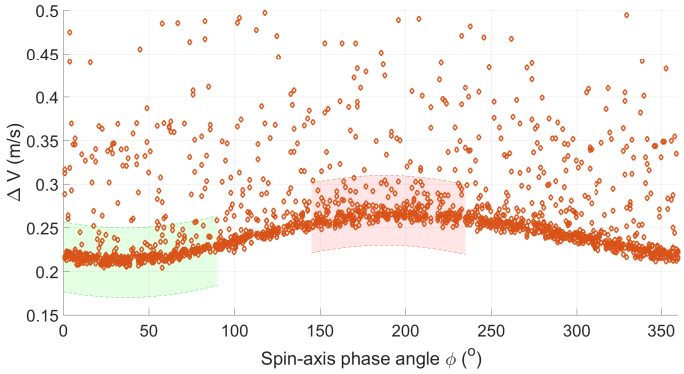

Figure 8.8: Open-loop ΔV for complete range of spin-axis phase angles ϕ. Green and red regions indicate the most and least optimal values of ϕ. The results show the sensitivity with respect to the initial conditions (Section 5.1.3), but also show a clear pareto front with optimal values.

Figure 8.8 shows that the hypothesis should at least partially be rejected, as the optimal configuration of the spin-axis is found around ϕ = 30 deg, which is not equal to the chaser phase angle φ (= 0 deg). However, Figure 8.8 shows that the total ΔV for the manoeuvre is definitely correlated to the spin-axis phase angle φ_{spin}. The most optimal configurations of the spin-axis are found close to the value of φ, centred around an optimal value at $\varphi_{\text{spin}} \approx 30$ deg. The spin-axis phase angle φ_{spin} should thus be relatively close to the chaser phase angle φ to allow the most optimal manoeuvre.

The differences in ΔV are not very significant and range from approximately 0.21 m/s around ϕ = 30 deg to approximately 0.26 m/s around ϕ = 190 deg, which is only a slight increase and likely negligible when the total mission ΔV is considered. However, the difference between minimum and maximum ΔV are dependent on the tilt angle of the spin-axis with respect to the orbital momentum axis N (see Section 2.2). The current simulation was performed with a tilt angle of 15°, resulting in small differences between maximum and minimum ΔV. When the tilt angle is 0 degrees (spin-axis aligned with N) there is no difference between minimum and maximum, while at a value of 90 degrees (spin-axis perpendicular to N) the difference between maximum and minimum ΔV increases to almost 100% (0.18 - 0.34 m/s). Therefore it is recommended to characterise the expected orientation of the spin-axis more accurately before commencing the mission.

The trajectories that belong to the pareto front of optimal solutions in Figure 8.8 are visualised in Figure 8.9 to further investigate their geometry.

Figure 8.9a shows that optimal configurations of the spin-axis at t = 1500 (green area) are situated just 'ahead' of the spacecraft initial position (orange cross) in the direction of motion. Additionally, Figure 8.9b shows that the reference trajectories with a final position in this green area require a smaller change of the relative orbital plane compared to those with a final position in the red area. This is attributed to the safety constraints, requiring a larger change in relative orbital plane to remain outside the KOS for the trajectories with final position in the red area. This required change of relative orbital plane is the main contributor to the

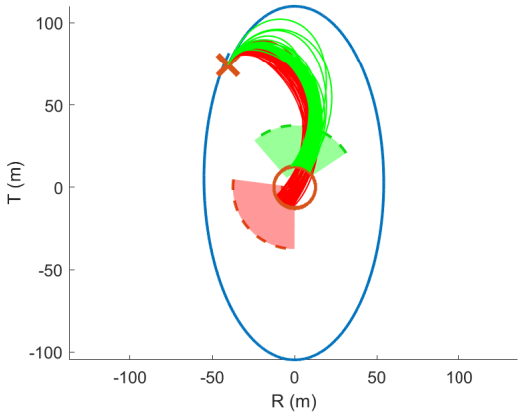

(a) Projection of relative observation orbit and most and least optimal spin-axis and trajectories, on the *R-T* plane. The green and red regions match those of Figure 8.8 and the trajectories that end in these regions are coloured accordingly. Cross indicates starting position for the manoeuvre.

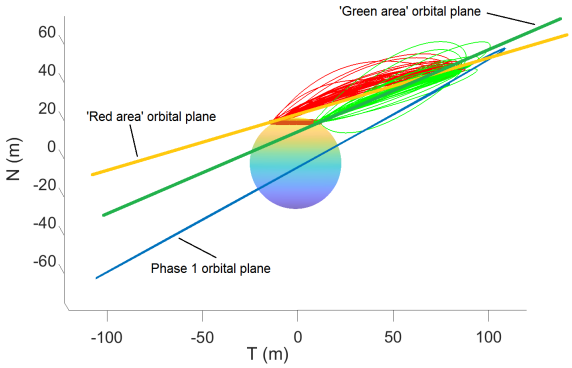

(b) Optimal reference trajectories for the complete range of ϕ, projected on the *T-N* plane. The green and red trajectories are the same as in Figure 8.9a. An approximation of the relative orbital plane of the trajectories is made by means of a straight line through their beginning and end point.

Figure 8.9: Projection on the *R-T* (left) and *T-N* planes (right) of the trajectories achieved in the best and worst scenarios identified in Figure 8.8.

increased ΔV and is logically increased when the tilt-angle increases. This may be imagined by visualising the blue band on the KOS in Figure 8.9b more towards the middle of the KOS. Consequently, reference trajectories to the red area are required to travel completely around the KOS and subsequently increasing the total ΔV.

In order to achieve the optimal initial conditions discussed in this section, in-plane reconfiguration would be required, changing the chaser phase angles φ, ϑ. This is possible with simple impulsive manoeuvres, at little ΔV cost, however, over extended periods of time (i.e. multiple orbits) [26]. The total ΔV costs for optimal in-plane transfers using two- or three-impulse manoeuvres were calculated by Gaias and D'Amico [26] and are expected in the order of 0.03 - 0.07 m/s. Possible benefits of this reconfiguration depend entirely on the spin-axis orientation. With the current 15° the differences between maximum and minimum ΔV are only 0.05 m/s, thus the cost of reconfiguration would be the same as the gain, rending such a reconfiguration useless. Therefore, reconfiguration is beneficial to the total expected mission ΔV only when the tilt-angle is sufficiently large.

8.3. Lighting conditions

Now that optimality with respect to mission geometry is explored, the optimality of the trajectory should be evaluated with respect to lighting conditions. As explained before, this considers the orientation of the camera boresight axis with respect to the incoming sun vector and is considered optimal when this angle is minimal, such that the sun is positioned directly behind the camera. This angle is influenced in different ways in the three different phases of the rendezvous process (see Section 4.2).

In phase 1 of the rendezvous process, the magnitude of this angle, χ_{cam}, is fully determined by the closed relative observation orbit that was selected, allowing the use of ρ and φ, ϑ together with φ_{sun} (see Section 8.1) to design this observation orbit optimally. In the second phase the angle $\chi_t extcam$ is fully dependant on the optimal manoeuvre, of which only the initial conditions can be controlled by manipulating φ, ϑ and t_0 of the manoeuvre. The third phase is completely dependant on the spin-axis, as the chaser is required to approach the target along its spin-axis, as described by Equation (5.15). Depending on the orientation of the spin-axis, which cannot be controlled, highly unfavourable lighting scenarios might arise.

8.3.1. Phase 1

The optimal design of the trajectory in the first phase of the rendezvous process is comprised of two steps. First, the optimal value of the angle ρ must be calculated and, second, the corresponding optimal values for φ, ϑ must be determined.

Angle of the relative orbital plane

The angle ρ was defined in Section 8.1 and can be used to align the reference trajectory with the incoming solar rays. The angle of the sun vector with the normal of Envisat's sun-synchronous orbit is $\approx 62°$. The angle

ρ should then be assigned an optimal value of

$$\rho = 90^\circ - 62^\circ = 28^\circ$$

The optimal ratio $\delta i/\delta e$ can then be derived from Equation (8.1) and has a value of approximately 1.06, with $\delta i > \delta e$, and an orbit with $a\delta i = 60$ and $a\delta e = 55$ is selected. This orbit has

$$\delta i/\delta e \approx 1.09$$

which is close to the optimal ratio, and exhibits a minimum and maximum inter-satellite distance of respectively

$$d_{\min} = a\delta e = 55m$$
$$d_{\max} = \sqrt{(2a\delta e)^2 + (a\delta i)^2} = \sqrt{110^2 + 60^2} \approx 125m$$

When using a passively safe orbit with parallel or anti-parallel e-/i-vectors, the relative orbital plane is tilted along the R-axis (see Figure 8.1). As the orientation of the R-axis in the inertial frame changes throughout the orbit, as shown in Figure 7.16, there are only two moments where the orbital plane can be perfectly aligned with the incidence angle of the solar rays. These two moments are found to be near the poles, where $u = 90$ deg (north pole) and $u = 270$ deg (south pole). More correct would be to define this moment for R perpendicular to the ecliptic plane, however, the choice is made to use the celestial poles, as these have well defined values of u, simplifying the analysis.

Since there are two poles, there are two optimal configurations, defined by $+\rho$ and $-\rho$. However, during eclipse the camera is not operational and the chaser cannot safely perform the manoeuvre. The eclipse period is found between $u \approx 280$ deg and $u \approx 40$ deg (see Figure 8.2). As the south pole is reached at $u = 270$ deg, this means that the optimal viewing conditions can only be exploited for a relatively short period of time, not sufficient to accommodate a 1500 second manoeuvre. This leaves the north pole, and accordingly $+\rho$, as only viable option.

Chaser phase angles

Despite the orientation of the relative orbit being fixed, the momentary lighting conditions still depend on the location of the chaser in the orbit, as explained in Section 8.1.2. It was found that the optimal aligned of the relative trajectory was for $\rho \approx +28^\circ$, aligning the reference trajectory with the incoming solar rays above the north pole. Figure 8.10 shows the geometry of this optimal relative orbit above the north pole, immediately identifying the optimal and least optimal position of the camera in this situation.

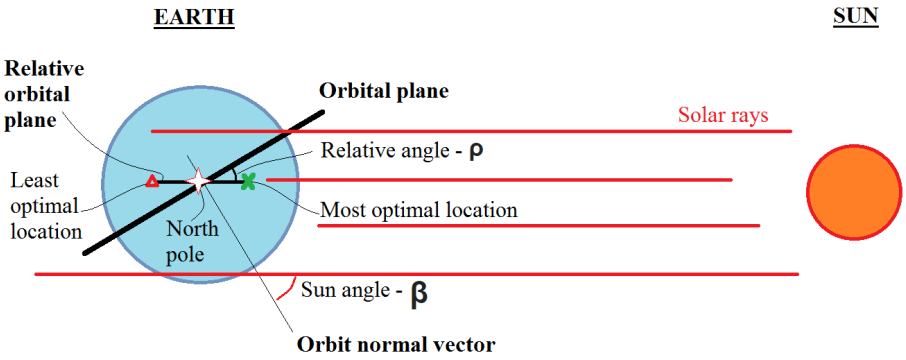

Figure 8.10: Top-view of the geometry created by the target orbital plane, relative orbital plane and sun position, projected on the ecliptic plane. The target is located above the north pole, at the centre of the reference orbit, marked by the white star. This geometry is a snapshot of the situation at $u = 90^\circ$.

The optimal position in Figure 8.10 is marked by a green cross and the sun-camera angle, χ_{cam}, is approximately 0 degrees at this instance. At the least optimal location $\chi_{\text{cam}} \approx 180$ degrees, and the sun is directly in front of the camera. Both the optimal and least optimal locations are found at the apsides of the relative orbit. The optimal position can be achieved using a parallel alignment of δe and δi, meaning $\varphi = \vartheta$ (see Section 3.3.4), with $\varphi = \vartheta = 0^\circ$. The least optimal position is found for $\varphi = \vartheta = 180^\circ$.

As the target orbital plane is not at an exactly right angle with the ecliptic plane, the optimal configuration identified in Figure 8.10 does not occur exactly above the north pole, as already shortly discussed at the end of the previous section. In order to select the most optimal value of φ, ϑ, the magnitude of the sun-camera angle, χ_{cam}, was examined over the course of one orbital period, for the previously determined optimal ratio $\delta i/\delta e$ and a range of φ, ϑ from -30 deg to +15 deg in steps of 5 degrees. The results of this analysis are presented in Figure 8.11,

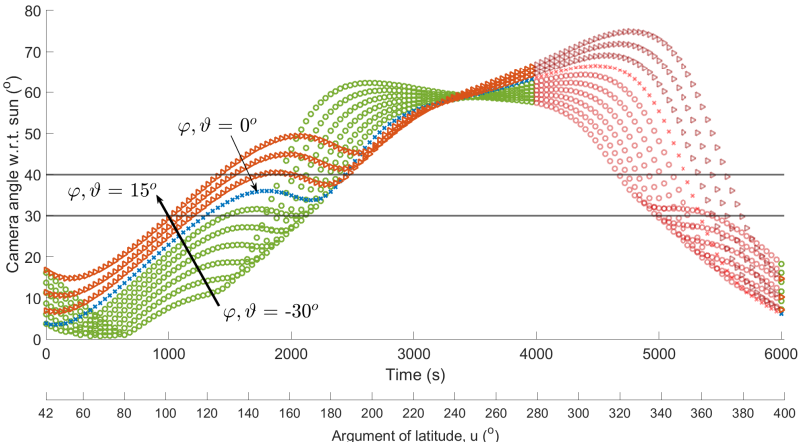

Figure 8.11: Sun-camera angle over the course of a single orbit, with δi = 60 and δe = 55. The red markers after t = 4000 identify the eclipse period. The thick arrow indicates the values of φ, ϑ represented by each line, starting with -30° at the bottom up to +15° at the tip of the arrow, following steps of 5° per line. The line for φ, ϑ is coloured blue and identified as reference. The black lines indicate a magnitude of χ_{cam} of 30 and 40 degrees respectively.

Figure 8.11 shows that she sun stays behind the camera (sun-camera angle < 90 deg) the entire orbit for all selected values of φ, ϑ. The thresholds of 30 and 40 degrees are selected as they are assumed to provide optimal lighting conditions. In the case of φ, ϑ = 0 deg, the sun-camera angle stays below 30 degrees for more than 1300 seconds and below 40 degrees for more than 2400 seconds, which is more than half of the useful orbit, excluding eclipse time. Using this case as a reference, it can be observed that increasing the value of φ, ϑ yields less desirable results, as the magnitude of the sun-camera angle is increased during almost the complete orbital period, and also the time period over which the magnitude is below 40 degrees is decreased.

Decreasing the value of φ, ϑ yields promising results, as the sun-camera angle magnitude is lower than for the reference case with φ, ϑ = 0 during most of the orbital period. A minimum value of nearly 0 deg is achieved for φ, ϑ between -10° and -30°, and the sun-camera angle stays below 30 degrees for a longer period of time. However, as the value of φ, ϑ decreases further to -25° and -30° a more rapid increase of the sun-camera angle is found at an earlier time. This results in reaching higher values earlier in the trajectory and strongly reducing the times at which the angle is below 30 or 40 deg with almost 1000 s between the reference case where φ, ϑ = 0° and the case where φ, ϑ = -30°. The choice of φ, ϑ therefore becomes a design choice, depending on the expected camera performance for different sun-camera angles.

Behaviour of the sun-camera angle

Considering the geometry expressed in Figure 8.4, it can be imagined that, after completing a full orbital period, the virtual motion of the sun from the perspective of the target may be described by a cone. The relative orbit of the chaser instead describes an elliptical plane from the perspective of the chaser. A completely optimal alignment of camera and sun is only possible when these virtual planes intersect, which is the case for less than half of the orbit, as demonstrated in Figure 8.12. This shows the plane that is formed by the trajectory of the chaser around the target as well as the cone that is formed from the virtual motion of the sun around the target. Therefore, in the best case, the camera is aligned with the solar rays for approximately half of the time in orbit and in the worst case for none of it.

Since the camera shall always be pointed at the target, the camera boresight axis is necessarily found within the relative orbital plane. Similarly, the sun-vector is always found in the cone described by the virtual motion of the sun around the target. The resulting relative motion of both camera and sun vectors is visualised in Figure 8.13 for φ, ϑ = 0°.

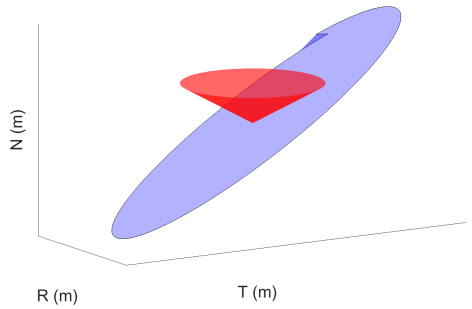

Figure 8.12: The surfaces created by the motion of respectively the chaser (blue) and the sun (red) around the target. The chaser motion describes a closed elliptical plane around the target, which is described by its relative orbit. The virtual motion of the sun described a 'cone' around the target, as may be visualised from Figure 8.4. Vectors describing the camera pointing are in the blue plane, while vectors describing the sun position are found in the red plane. Alignment of these vectors, and subsequently a minimisation of sun-camera angle χ_{cam}, can only occur upon the alignment of these two planes.

The motion that can be observed in Figure 8.13 can be explained from the different planes in Figure 8.12 as well as the velocity of the virtual motion of the chaser and sun around the target in the RTN frame. The sun travels with a constant motion due to the near-circular absolute target orbit. This can be observed from Figure 8.5, where the components of the unit vector produce a smooth sine wave. The camera, however, travels slower near the relative apsides and faster when it is near the *R*-axis, which may be observed from Figure 8.7, where the projection of the motion on the *R*-*T* is very unlike a sine wave.

As the orientation of the sun behind the camera changes continuously, both in the *R*-*T* and *T*-*N* planes. This causes the Envisat to be illuminated from different angles continuously from the perspective of the camera. This motion could both be beneficial or disadvantageous, something which will have to be shown in experiments that employ real pose estimation architectures.

8.3.2. Phase 3

It is useful to discuss the lighting conditions of phase 3 before phase 2, as the third phase is mainly concerned with the illumination conditions of the spin-axis, along which the chaser approaches the target in this third phase of the rendezvous process. It is shown that the lighting conditions of the trajectory in phase 2 are fully determined by the lighting of the relative orbit from phase 1 and the lighting of the spin-axis. As such a discussion of the spin-axis illumination, especially relevant for the third phase of the rendezvous process, is a logical next step.

Spin-axis illumination

Similar to the definition of χ_{cam}, the lighting conditions on the spin-axis are described by the angle between the negative spin-axis pointing vector and the sun pointing vector, represented by χ_{spin}. The spin-axis pointing vector is the vector pointing outward from the target along its axis of rotation, described by unit vector $\hat{\boldsymbol{\omega}}_{RTN}^{TBF/RTN}$. The spacecraft approaches the spin-axis along the spin-axis vector, meaning that the camera is approximately aligned with this vector in the opposite direction. Therefore the angle between the negative spin-axis pointing vector and the sun vector is approximately equivalent to the sun-camera angle that is experienced by the chaser in the third phase of the rendezvous.

Three scenarios for the orientation of the spin-axis in the inertial frame were described in Section 2.2, where the tilt-angle, between the spin-axis and *N*, was assumed to have a value of 0, 15 or 30 degrees. Due to the nutation, described in the same section, the spin-axis tilt-angle can be in any direction. In the inertial frame, the angle with *N* is thus fixed, while the angle with the Earth rotation axis *Z* (see Figure 2.4) is allowed to vary. This nutation has a period of several days, therefore the lighting conditions on the spin-axis during the approach are assumed constant, as this approach is expected to last less than 2000 seconds (see Section 4.2). The resulting lighting conditions on the spin-axis, in the form of χ_{spin} are presented in Figure 8.14.

Figure 8.14 shows that the angle χ_{spin} depends on the tilt-angle between the spin-axis and *N*. If this angle is 0, the spin-axis is constant with an angle of $\beta = 62°$, the sun-angle experienced by the sun-synchronous orbit. It is clear that the scenario with a 30 degree angle would be preferred, as the sun-angle χ_{spin} reaches lower values, however, the tilt-angle is however not a parameter which can be controlled. Furthermore, Figure 8.14

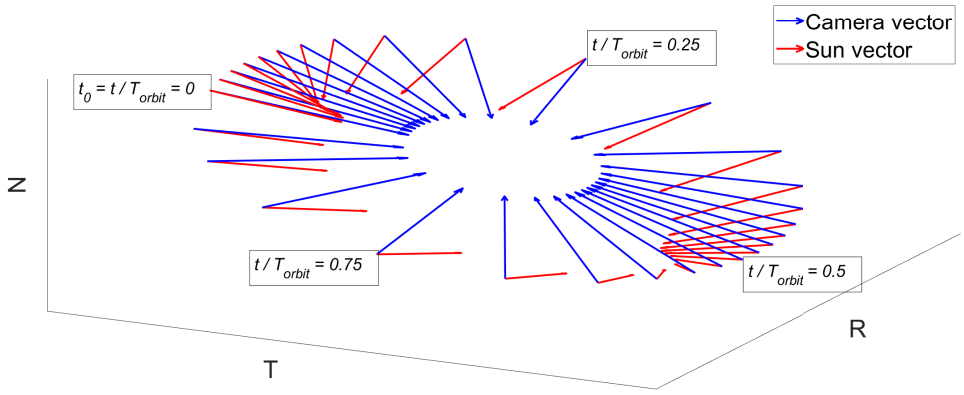

Figure 8.13: Time-lapse of pointing vectors from the sun and camera over the course of a single orbit. Vectors are plotted at a fixed time interval of 200 seconds and $a\delta i = 60$, $a\delta e = 50$, $\varphi, \vartheta = 0°$. The sun vector is aligned with the camera vector at the instant marked with t_0. Relative to the target, the sun vector virtually travels faster than the chaser and gets 'ahead' of the camera vector, leading to a misalignment of the two vectors in the R-T plane around $t/T_{orbit} = 0.25$. The camera vector then 'catches up' and, around $t/T_{orbit} = 0.5$, the vectors are again approximately aligned when projected on the R-T plane. However the relative orbit has passed through the orbital plane around $t/T_{orbit} = 0.25$, and the N-component of the camera vector becomes opposite that of the sun-vector. The reverse of this motion happens on the second half of the orbit, aligning the vectors again at $t/T_{orbit} = 1$.

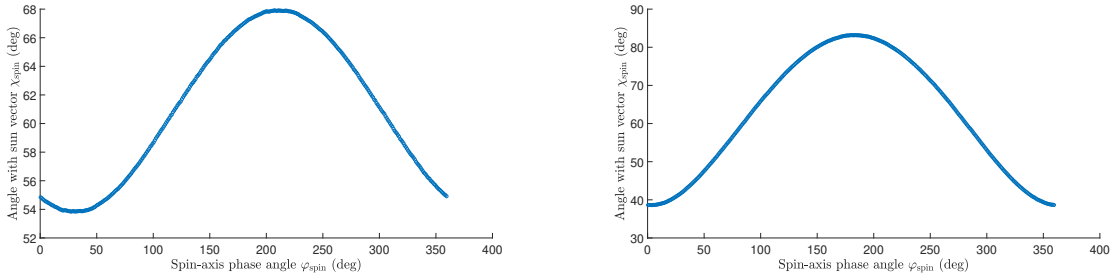

(a) 15 degree tilt-angle between spin-axis and N.

(b) 30 degree tilt-angle between spin-axis and N.

Figure 8.14: Mean spin-axis sun-angle χ_{spin} over a range of spin-axis phase angles φ_{spin}.

shows the mean value of the angle χ_{spin}, however, the actual value of χ_{spin} is not constant, but oscillating between ± 10 degrees of the mean value due to the wobbling motion. This can be seen in Figure 8.15.

Finally, Figure 8.14 shows that the minimal value of the χ_{spin} is not achieved when φ_{spin} is equal to φ_{sun}, which might be expected, as theoretically this should mean an alignment of the sun vector and the spin-axis vector. Repeating the analysis of χ_{spin} with the wobbling removed, learns that this 'mismatch' can be completely attributed to the wobbling of the spin-axis. When the rotations around the other two principle axes are set to 0, the wobbling due to inertia is largely removed and the minimal value of χ_{spin} is found at $\varphi_{\text{spin}} = 340°$, or -20°, which is consistent with the sun phase angle that was identified in Section 8.1.2.

It can be concluded that the expected attitude dynamics of the Envisat are favourable. If the spin-axis were directed in the opposite direction, values of χ_{spin} of 120° to 140° would be encountered. Furthermore, in the absence of the nutation, the spin-axis, in the worst case, could have a continuous χ_{spin} of 68° or 84°, the maximum values found in Figure 8.14. However, with the nutation acting on the target spin-axis, a desirable time for approach may be awaited, when the angle χ_{spin} is closer to its minimum achievable value of 54° or 38°, identified in Figure 8.14 for respectively a 15° and 30° tilt-angle. Once more it may be concluded that a more accurate characterisation of the Envisat spin-axis orientation, prior to the mission, is desirable.

8.3.3. Phase 2

The final part of the rendezvous process to consider is the optimal trajectory in the second phase. This trajectory resembles part of a closed, elliptical orbit [91], and is expected to closely follow the relative orbital

plane of the passive orbit. This was confirmed in Figure 8.9b, where it was shown that for the most optimal manoeuvres, the orbital plane of the optimal trajectory is close to the orbital plane of the relative orbit from phase 1.

This is a desirable property since it implies that lighting conditions during the optimal trajectory in phase 2 are similar to the relative observation orbit from phase 1. The facts are that, first, the sun-camera angle at the beginning of the phase 2 trajectory, χ_{cam,t_0}, is completely defined by the selected departure point from the orbit in phase 1 and, second, the sun-camera angle at the end of the trajectory, χ_{cam,t_f}, equals the value of χ_{spin}. All intermediate sun-camera angles, $\chi_{\text{cam},t}$, are expected to have a magnitude greater than χ_{cam,t_0} but smaller than χ_{spin}.

This expectation can be tested, and for this purpose an optimised design of the optimal trajectory is constructed. In this optimised design the relative orbit is defined from angle $\rho = 28$ deg, leading to $\delta e = 55$, $\delta i = 60$. Furthermore, the phase angles φ, ϑ are set to 0°, which was determined to yield desirable sun-camera angles in phase 1 (see Figure 8.11). Finally, φ_{spin} is set to 0° for a tilt-angle of 30° and to 30° for tilt-angles of 15° and 0°, which were determined the optimal values for minimising χ_{spin} (see Figure 8.14). Phase 2 was initiated at $u = 42°$, setting $t = t_0$ at this point. The lighting conditions for this trajectory are shown in Figure 8.15. This confirms the expectation that $\chi_{\text{cam},t_0}\ \chi_{\text{cam},t} < \chi_{\text{spin}}$.

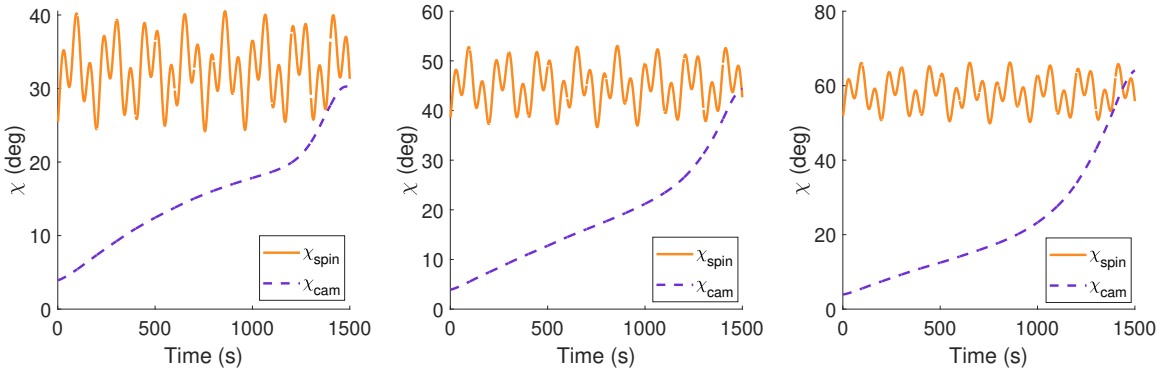

Figure 8.15: Angle of the sun-vector with the camera boresight vector in the optimal trajectory and with the spin-axis. Tilt angle of the spin-axis with the orbit normal is set to 30° (left), 15° (middle) and 0° (right).

This shows that by designing the rendezvous manoeuvre carefully, very favourable lighting conditions can be created. A slightly larger tilt angle would be favourable, as it results in smaller values of χ_{cam}, however, this value completely depends on the true orientation of Envisat and is not a design parameter.

Sun-camera angle optimization

One way to achieve control of the sun-camera angle, χ_{cam}, during the optimal manoeuvre, would be to add χ_{cam} as an objective or constraint in the trajectory optimization process described in Section 5.1. This, however, causes several difficulties with respect to multi-objective optimization and suitable constraint values.

The main challenge of multi-objective optimization is the determination of weighting factors for the objectives to be assessed [18], which, in this case, means determining weighting factors for ΔV and χ_{cam}. Since these two properties are physically unrelated, the determination of weighting factors would be completely arbitrary and experimental determination, often a laborious process, would be required. Furthermore, the relation between sun-camera angle χ_{cam} and measurement accuracy σ_{sun} (see Section 5.2.1) is completely based on assumptions. The optimal weighting, achieved through an experimental process, might therefore be useless, as it would heavily depend on these assumptions, which might be proven in the future not to be a good representation of real pose estimation systems. Therefore it is decided not to include χ_{cam} as an objective.

It would be mathematically easy to include χ_{cam} as a constraint:

$$\hat{\boldsymbol{r}}_{\text{sun}} \cdot \hat{\boldsymbol{r}}_{\text{cam}} + \|\hat{\boldsymbol{r}}_{\text{sun}}\| \cos \chi_{cam,max} \leq 0 \tag{8.5}$$

where $\hat{\boldsymbol{r}}_{\text{sun}}$ is the sun unit vector in the orbital frame, $\hat{\boldsymbol{r}}_{\text{cam}}$ is the camera unit pointing vector in the *RTN*-frame and $\chi_{\text{cam,max}}$ is the maximum allowable sun-camera angle. The problem with using χ_{cam} as a constraint arises

from the need for a proper value of $\chi_{\text{cam,max}}$. This value can not be smaller than the expected χ_{spin}, as this would create a conflict within the optimization process. Eventually this conflict would lead to divergence, as the final conditions of the trajectory would violate this constraint. Furthermore, as the constraint value should always obey $\chi_{\text{cam,max}} > \chi_{\text{spin}}$, while the value of χ_{cam} is not expected to exceed χ_{spin}, the constraint would not contribute anything to the optimization process and it is decided not to include a constraint either.

8.4. Illumination-based Performance

As a conclusion to this work, the performance of the vision-based GNC system is analysed for the most and least optimal lighting conditions that may be achieved. This demonstrates the working of the GNC algorithm and the dependence of its performance on illumination conditions. In both the optimal and least-optimal case, the relative observation orbit in phase 1 is characterised by:

$$\begin{aligned} a\delta a &= 0 \quad \text{m} \\ a\delta \lambda &= 0 \quad \text{m} \\ a\delta e &= 55 \quad \text{m} \\ a\delta i &= 60 \quad \text{m} \end{aligned}$$

As the closed orbit of phase 1 is designed completely around the sun angle (see Section 8.3.1), it is assumed that, on any mission, the satellite can be placed in the most optimal observation orbit, with phase angles φ, ϑ that reflect the most optimal χ_{cam}. Also, in both cases it is assumed that the approach in phase 2 commences directly after eclipse, as this is found to be a desirable location. These two assumptions lead to the following phase angles and argument of longitude:

$$\begin{aligned} \varphi, \vartheta &= 0 \quad \text{deg} \\ u &= 42 \quad \text{deg} \end{aligned}$$

For the most optimal case, it is assumed that the mission waits for the most optimal spin-axis configuration. The optimal lighting conditions are found by examining Figure 8.14, which shows a minimum mean χ_{spin} at

$$\varphi_{\text{spin}} \approx 0,\ 30 \quad \text{deg}$$

for tilt-angles of 30° and 15° respectively. To create the least optimal conditions, it is assumed that the mission approaches at the worst possible spin-axis configuration. For angles greater than 90° it could be decided to approach the satellite from the opposite side, to create better illumination conditions. Based on Figure 8.14, the maximum value of χ_{spin} is found for the following value of the spin-axis phase angle ϕ:

$$\varphi_{\text{spin}} \approx 180,\ 210 \quad \text{deg}$$

for tilt-angles of 30° and 15° respectively. For both the most and least optimal case, the tilt angle between the spin-axis and orbit normal N, is evaluated at 0, 15 and 30 degrees to create three different scenarios. The measurements are generated according to the theory outlined in Section 5.2, including standard deviation from both inter-satellite distance and sun-camera angle. To complete the framework, the strategies for recognition and mitigation, presented in Chapter 7, were also activated in this evaluation and the fitted estimate of $\boldsymbol{\omega}$ was used (see Section 7.3).

8.4.1. Phase 1: Passive observation

The rendezvous process begins with a period of passive observation, in which the chaser is moving on a closed, relative orbit with respect to the target. The chaser is not controlled and remains in this orbit over the course of one orbital period. The trajectory is presented in Figure 8.16, and the expected sun-camera angle for the satellite on this optimal closed orbit is shown in Figure 8.17.
It may be observed from Figure 8.17 that the sun angle is always behind the camera. As this first phase is not interesting from a guidance perspective, it is only shortly discussed. An overview of the expected performance

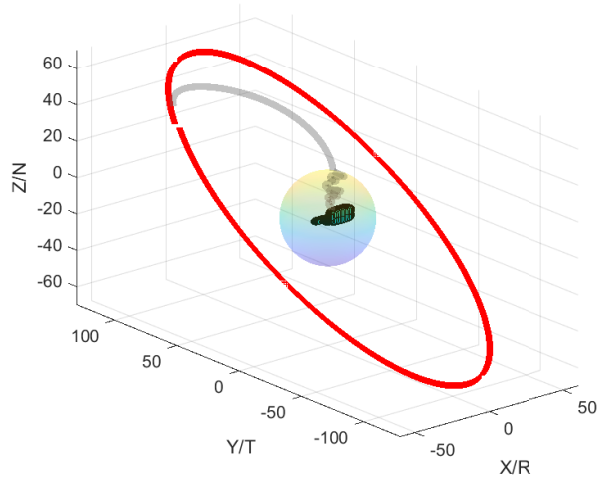

Figure 8.16: Highlighted in red is the trajectory of phase 1. It is a closed, elliptical orbit around the target which is passively save and allows optimal lighting conditions.

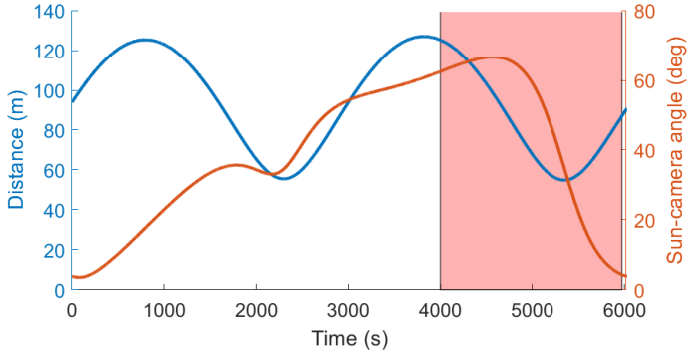

Figure 8.17: Inter-satellite distance and sun-camera angle for the first phase of the rendezvous trajectory, the closed relative orbit. The sun-camera angle is very favourable due to the trajectory design, as it stays below 40 degrees for over half the illuminated time and never exceeds 60 degrees. According to the assumptions from Section 5.2.1, this means that measurement error due to illumination should be low.

of the vision-based navigation system for the most optimal scenario is provided by Figures 8.18 and 8.19, showing the navigation and measurement errors respectively. It may be observed by comparing Figure 8.18 to Figure 8.17 that the distance is the main driver of the measurement accuracy in this phase.
In the most optimal case the performance of the navigation system shows small navigation errors for both the translational as well as the rotational components. Figure 8.18 shows that the position error is consistently below 0.5 meters, mostly below 0.2 meters. The velocity error during this period is at millimetre level. The attitude estimation error is around 2-3 degrees and the rotation estimate, presented separately in Figure 8.19, improved by the MMF, has an accuracy of 0.3 - 0.5 deg/s. As has been elaborately discussed throughout this work, the rotation error is crucial for the guidance system in the second phase.

Eclipse period
It can be seen that, during the eclipse period, the attitude errors grow to almost 360 degrees, indicating that the attitude estimate should not be used when no measurements are available, which was also concluded in Chapter 6 for the periods of decreased performance of the pose estimation system.

The performance of the navigation filter in the translational component allows to keep the camera pointed at the target during eclipse, as the position error remains smaller than 2 m during the period of eclipse. This means that the camera is still pointed at the target after the eclipse period, which enables the chaser to immediately resume measurements when the sunlight is returned, without the need for searching the target. This allows the second phase of the manoeuvre to commence quickly after the eclipse period has ended.

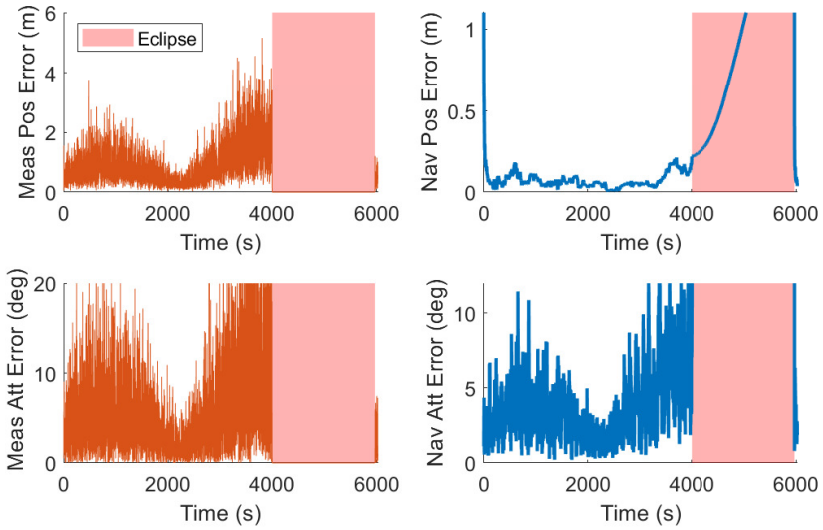

Figure 8.18: Navigation and measurement errors in the least optimal trajectory. As the measurements are accurate (mostly < 1m, 7 deg), correspondingly the navigation filter performs well in the estimation of both translational (errors < 0.3 m) and rotational (errors <5 deg) parameters.

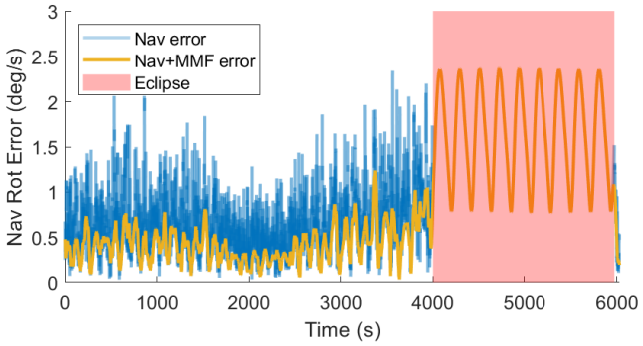

Figure 8.19: Navigation rotation error for the optimal orbit in phase 1. The accuracy of the estimate is significantly improved by the application of the moving mean filter discussed in Section 5.2.3.

8.4.2. Phase 2: Optimal manoeuvre

The rendezvous continues with the (near-)optimal manoeuvre. This phase and its challenges were already elaborately discussed in Chapter 6 and several forms of mitigation were investigated and proven in Chapter 7. The trajectory in the second phase, ending at the intersection of the spin-axis with the KOS of 25m radius, is visualised in Figure 8.20.

The trajectory is simulated for three different values of the tilt-angle between the spin-axis and the orbit normal of 0, 15 and 30 degrees. Furthermore, to demonstrate the working of the mitigation strategies from Chapter 7, three moments of failure were randomly introduced during this approach:

$t = 247s$	$\rightarrow$	$2s$	*Optimistic feedback failure*
$t = 839s$	$\rightarrow$	$30s$	*Pessimistic feedback failure*
$t = 1213s$	$\rightarrow$	$60s$	*Pessimistic feedback failure*

The definition of a failure period, in terms of measurement accuracy, was provided in Section 6.2.1 and an overview of the feedback definitions may be obtained from Section 4.3.1. The trajectory in this second phase is evaluated for both the best and worst final spin-axis orientation, considering illumination conditions.

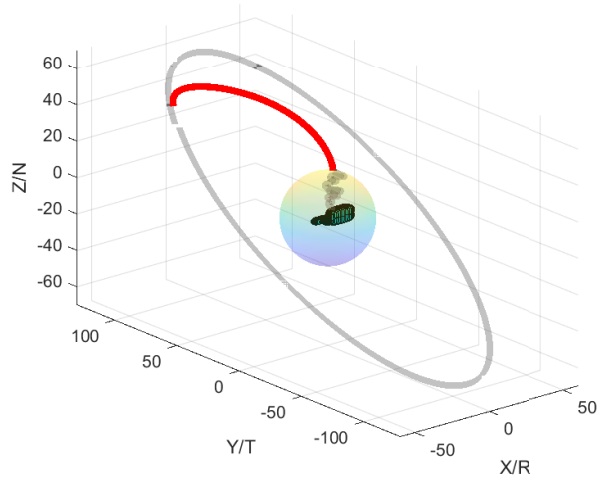

Figure 8.20: Highlighted in red is The trajectory of phase 2. It is the result of solving the minimisation problem described by Equation (5.8) and closely resembles a piece of a closed, elliptical orbit [91].

Most optimal conditions

The most important parameters of this phase are presented in Figure 8.21 for the most optimal conditions, showing the sun-camera angle, measurement error, navigation and guidance errors and open-loop and closed-loop ΔV respectively.

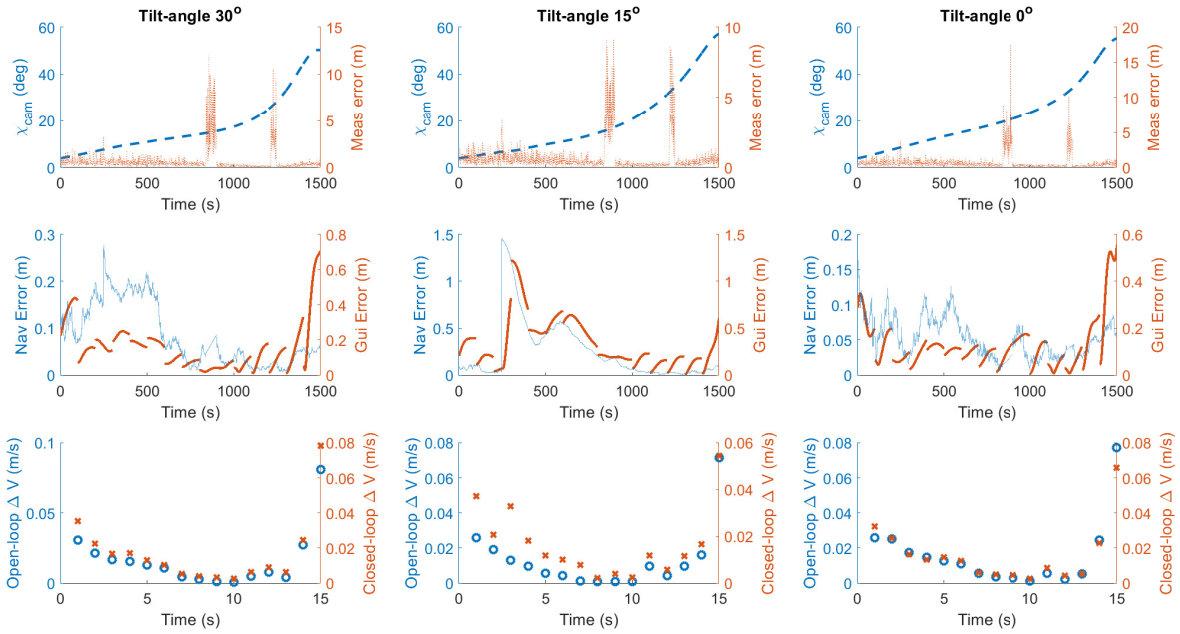

Figure 8.21: Overview of sun-camera angle χ_{cam}, measurement error, navigation and guidance error and open- and closed-loop ΔV for phase 2. Any large errors that were present in Section 6.2.1, especially for the optimistic feedback type, have been correctly mitigated. The increased amount of measurement error is still found in the measurements (top row), however, any sign of failure is completely absent from the navigation and guidance error (middle row), as well as from the ΔV estimate (bottom row).

Examination of the top row of Figure 8.21 learns that, in the optimal case where χ_{cam} is low, the measurement accuracy under nominal circumstances is influenced mainly by the inter-satellite distance. The sun-camera angle can be seen to grow more rapidly near the end of the trajectory, where a slight increase in the measurement error can be observed in the cases of 15° and 30° tilt-angle.

Further examination of Figure 8.21 learns that, under optimal lighting conditions and including all mitigation strategies, the GNC architecture performs satisfactorily. Despite the fact that some periods of decreased performance of the pose estimation system are present, as can be observed from the measurement error in the top row, the performance of the GNC system is stable, especially compared to the scenarios that were presented for optimistic feedback in Section 6.2.1. Only the navigation and guidance error, as well as the closed-loop ΔV, show a slight increase for the optimistic feedback scenario, in the case where the tilt-angle is 15°. This increase is however quickly restored, showing that the strategies for recognition and mitigation from Section 7.1 work properly.

Figure 8.22 shows the attitude measurement errors and corresponding rotation errors.

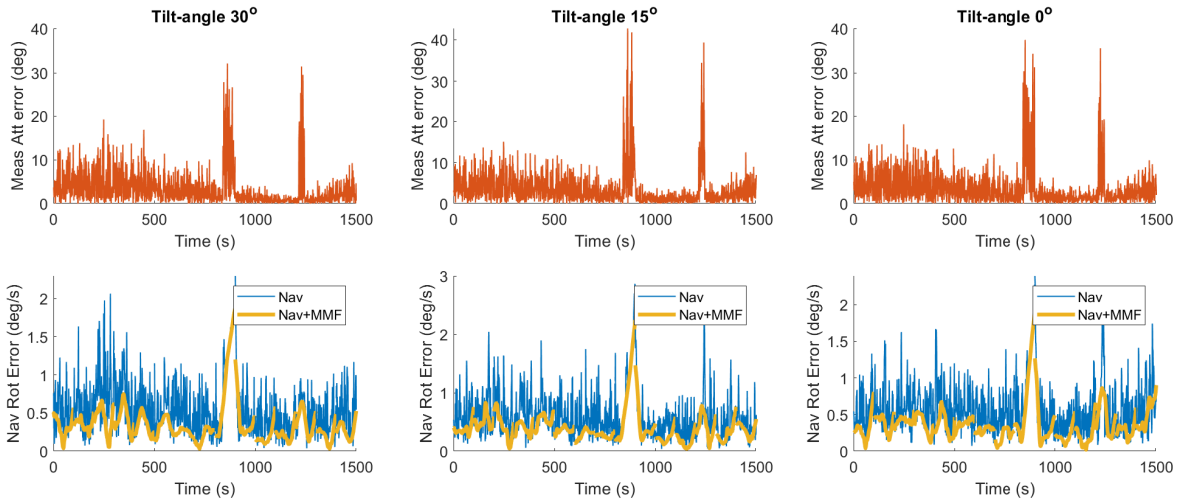

Figure 8.22: Attitude measurement error and navigation rotation error for the most optimal trajectory of phase 2.

Figure 8.22 shows how the navigation estimate of the rotation is influenced by the measurement error. Peaks may be observed in the bottom row of Figure 8.22 at the same moment as the peaks in the measurements occur in the top row. This again demonstrates the difficulty that the navigation filter has with estimating the target rotation. As may be observed in Figure 8.21, no such peaks occur in the navigation position error for peaks in the position measurement error. The accuracy that is achieved in the estimate of the target rotation is around 0.5 deg/s. This accuracy translates into the fitted and integrated final estimation errors in Table 8.2.

Table 8.2: Fitted, integrated and achieved final position error for the most optimal conditions in phase 2. The fitted estimate of the final position was used in the trajectory, and therefore the true final error should resemble the fitted error.

	Tilt-angle		
	30°	15°	0°
Fitted error (m)	4.050	5.274	5.096
Integrated error (m)	4.805	5.244	7.780
True final error (m)	4.634	5.807	4.534

Table 8.2 shows that the fitted estimate of the final state (Section 7.3) is more accurate than the integrated estimate (Section 7.2) in nearly every case. In some cases, when the accuracy of $\boldsymbol{\omega}$ and $\boldsymbol{J}$ are sufficiently high, the benefit of the fitted method is small compared to the integrated method. As the fitted method is used in the simulation, naturally the values of the true final error are closer to the fitted error than the integrated error.

Least optimal conditions

The least optimal conditions are characterised by a different final spin-axis orientation compared to the most optimal conditions. Similar to the data presented in Figure 8.21, Figure 8.23 presents the most important data for the trajectory with the least optimal conditions.

Figure 8.23 shows that despite the increase of χ_{cam} at the end of the trajectory, no significant differences are found when comparing it too the most optimal scenario. The same is true for the attitude measurement error

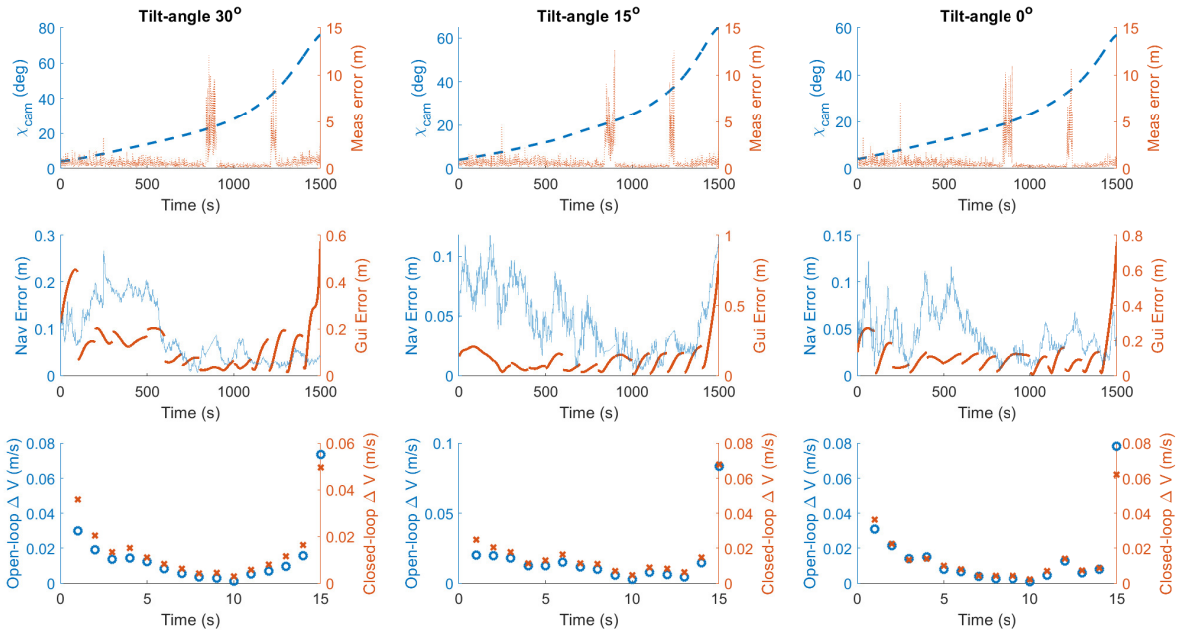

Figure 8.23: Overview of sun-camera angle χ_{cam}, measurement error, navigation and guidance error and open- and closed-loop ΔV for the least optimal conditions in phase 2. May be compared to Figure 8.21, upon which minimal differences are found.

and navigation rotation error, shown in Figure 8.24.

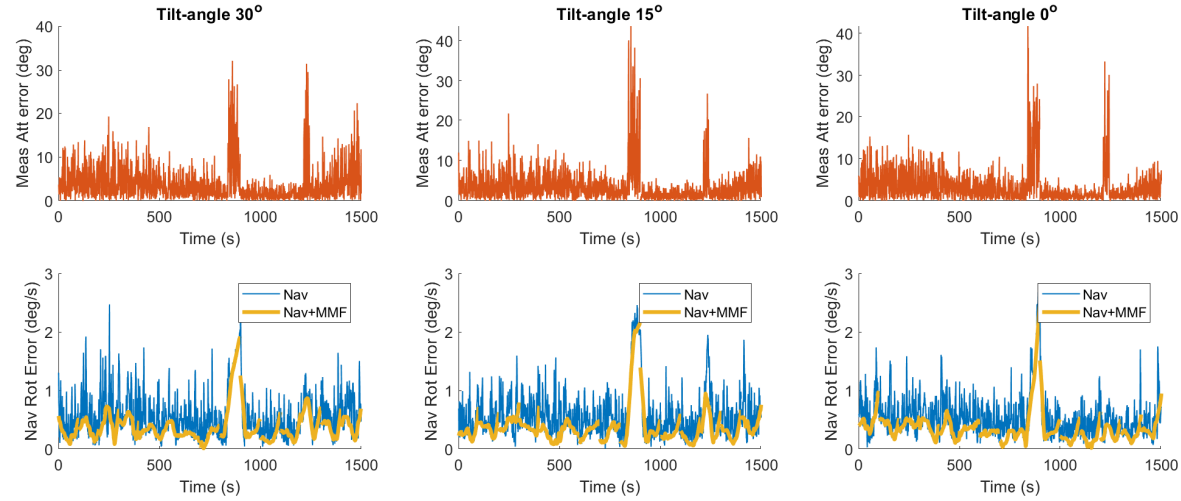

Figure 8.24: Attitude measurement error and navigation rotation error for the least optimal trajectory of phase 2. May be directly compared to Figure 8.22.

Finally, a table similar to Table 8.2 may be presented for the bad case, the result of which is Table 8.3. Surprisingly, Table 8.3, representing the least optimal case, reports lower values for all the errors, compared to the most optimal case from Table 8.2. This is a good example of the limited accuracy that is currently achieved on the final state estimate. The differences between the fitted and integrated cases are very small in the case of sufficiently accurate measurement, and it must also be considered that only a very small sample (3 runs) is used. Repeating this analysis with 100 runs per case would yield more trustworthy values, however, this would also take more time. Currently the evaluation of the 1500 second trajectory of phase 2, takes approximately 6 minutes on an Intel i7 dual core processor. Running 100 runs for all scenarios (3 tilt-angles, most and least optimal) would result in 600 runs and a total of 3600 minutes, the equivalent of 2.5 days. It is decided not to

Table 8.3: Fitted, integrated and achieved final position error for the least optimal conditions in phase 2. The fitted estimate of the final position was used in the trajectory. May be directly compared to Table 8.2.

	Tilt-angle		
	30°	15°	0°
Fitted error (m)	4.255	5.600	4.472
Integrated error (m)	5.624	5.710	5.315
True final error (m)	3.657	4.923	3.973

include this and might be left as a recommendation. The similarity between the achieved final error in the most and least optimal cases may be considered as another incentive, to develop more accurate methods for the estimation of the target's rotational dynamics.

8.4.3. Phase 3: Forced approach

The trajectory of the third and final phase of the rendezvous process is characterised by the need to follow the spin-axis, resulting in a spiralling motion due to the wobbling of the spin-axis, as shown in Figure 5.16. The reference trajectory in phase 3 is highlighted in red in Figure 8.25.

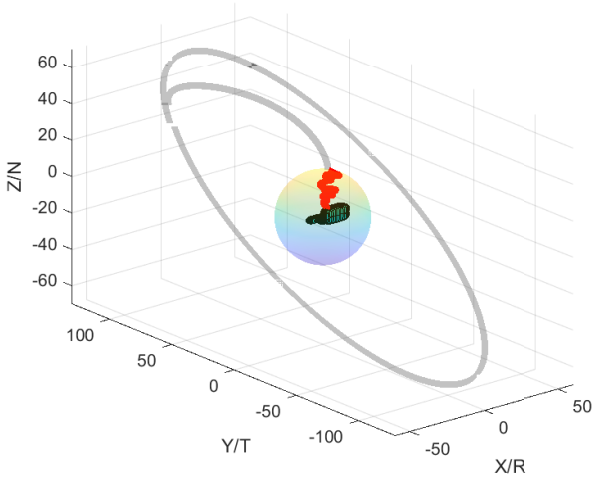

Figure 8.25: Highlighted in red is the trajectory of phase 3. As this trajectory is required to follow the spin-axis upon approach, it is characterised by a spiralling motion.

This is likely the most challenging part of the rendezvous trajectory, as the sun-camera angle is highest in this phase. On the other hand, the distance is decreased to a relatively low value. Because of the sun induced error, the error in the estimation of $\boldsymbol{\omega}_{TBF}^{RTN/TBF}$ increases. This complicates the trajectory, as the estimation of the desired state is fully dependent on $\boldsymbol{\omega}_{TBF}^{RTN/TBF}$, according to Equation (5.15).

Most optimal conditions

The most optimal conditions are characterised by the lowest possible value of χ_{cam} for the tilt-angle of the spin-axis. Figure 8.26 shows the sun-camera angle, measurement error and guidance and navigation errors for this phase.

It can be noticed that, despite the sun-angle growing to 60°/70°. The combination of sun-angle and distance is still favourable, as measurement error are in the same order as they were observed at the beginning of the optimal trajectory (see Figure 8.21), approximately 1 m. It may be observed that although navigation error is very low, the guidance error is much higher than in previous situations. This again stresses the difficulty that the controller has with following the spiralling trajectory. This spiral is guided based on the navigation estimate of $\boldsymbol{\omega}_{RTN}^{TBF/RTN}$, the error on which is presented in Figure 8.27, together with the measurement errors

By comparing Figure 8.27 and Figure 8.22 that the attitude measurement error has increased compared to phase 2. The resulting increase in the navigation rotation error may also be observed. This increase is not

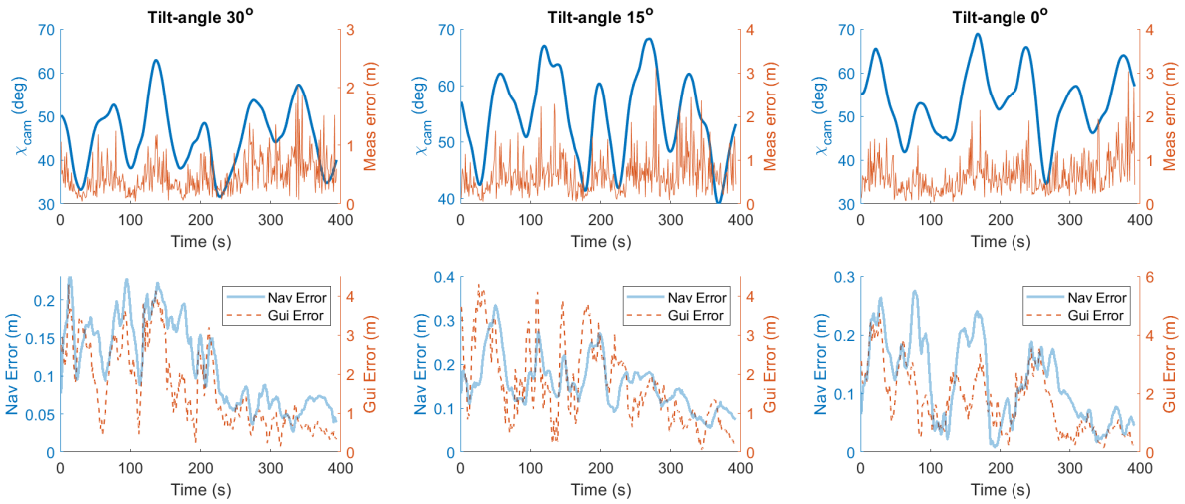

Figure 8.26: Overview of the sun-camera angle χ_{cam}, measurement error and guidance and navigation errors for phase 3.

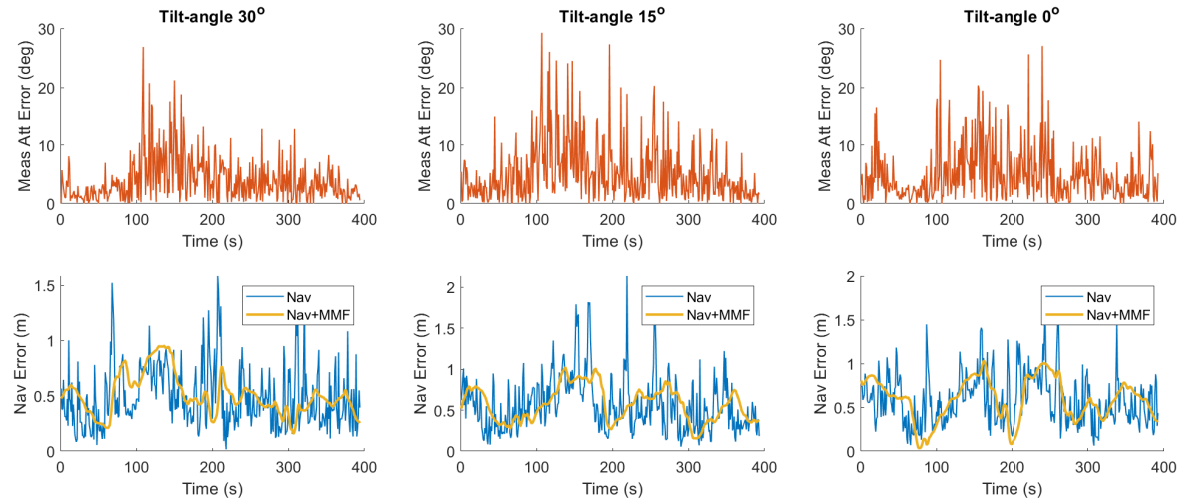

Figure 8.27: Attitude measurement error and navigation rotation error for the most optimal trajectory of phase 3.

a desirable development, as the guidance trajectory in phase is fully determined from it. Increased error inevitably leads to larger guidance errors and larger ΔV, as shown in Table 8.4.

Table 8.4: Control effort, mean guidance error and true final position error for the most optimal conditions in phase 3. The true final error is the difference between the final state achieved by the chaser and the true desired state, calculated from the true value of unit vector $\hat{\boldsymbol{\omega}}_{RTN}^{TBF/RTN}$ at a final distance of 5 meters.

	Tilt-angle		
	30°	15°	0°
ΔV (m/s)	10.356	12.414	11.473
Mean guidance error (m)	1.684	2.012	1.817
True final error (m)	0.759	0.708	1.151

It is found that all trajectories require in excess of 10 m/s of ΔV for completion, which is considered unacceptable. This is another strong incentive to either improve the estimation of $\boldsymbol{\omega}_{RTN}^{TBF/RTN}$ or to formulate the trajectory of phase 3 differently. This is further supported by the fact that the true final error, achieved at the end of phase 3,

Finally, the third phase also incorporates the synchronisation of the chaser rotation with the rotation of

the target. The results of this synchronisation are shown in Figure 8.28.

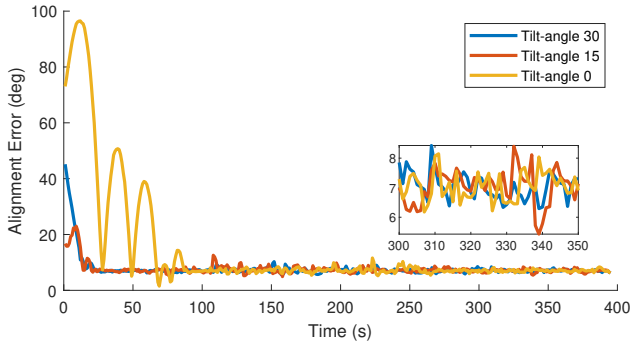

Figure 8.28: Synchronisation error for the chaser for the most optimal conditions in phase 3. The synchronisation error describes the angular difference between the chaser body frame and its intended orientation.

Surprisingly, all runs are able to reach a final attitude control error of 7 degrees, which was the threshold that was determined by the tuning of the controller in Section 5.3.3. This is explained by calculating the mean value of the navigation attitude error, which has a magnitude of around 4 deg, which is well below the 7 degree control error.

Least optimal conditions

The trajectory of phase 3 in the least optimal case is necessarily subject to a higher degree of error, due to the increased mean value of χ_{cam}. This increase may be observed in Figure 8.29, together with a slight increase of the measurement error and accordingly the navigation and guidance error.

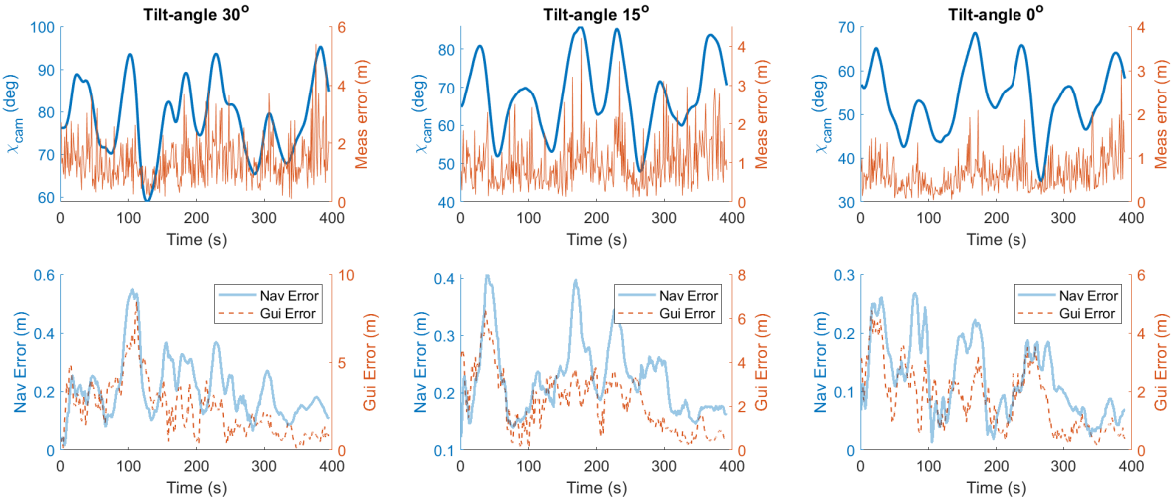

Figure 8.29: Overview of the sun-camera angle χ_{cam}, measurement error and guidance and navigation errors for the least optimal conditions in phase 3. An increase may be observed with respect to Figure 8.26.

Figure 8.29 shows that despite a significant increase in χ_{cam}, from 45° to 80° in the case of a 30° tilt-angle, the increase in the navigation error, from ≈ 0.15 m to ≈ 0.3 m is only marginal. Guidance error seems to be unaffected in magnitude, except for some spikes. Considering the relative distance of the chaser with respect to Envisat, decreasing from 25 m to 5 m, a guidance error of 4 m might be reason for worry, however, it can be shown that these errors arise mainly perpendicular to the Envisat spin-axis, ensuring safety of the chaser at all time. Also, the guidance error decreases with time and is at sub-meter level when the chaser is closest to the target.

The attitude and rotation of the target are displayed in Figure 8.30.

A similar increase from Figure 8.27 to Figure 8.30 may be observed, as was the case with Figure 8.29. The measurement accuracy decreases and the estimation error accordingly increases. The navigation rotation errors

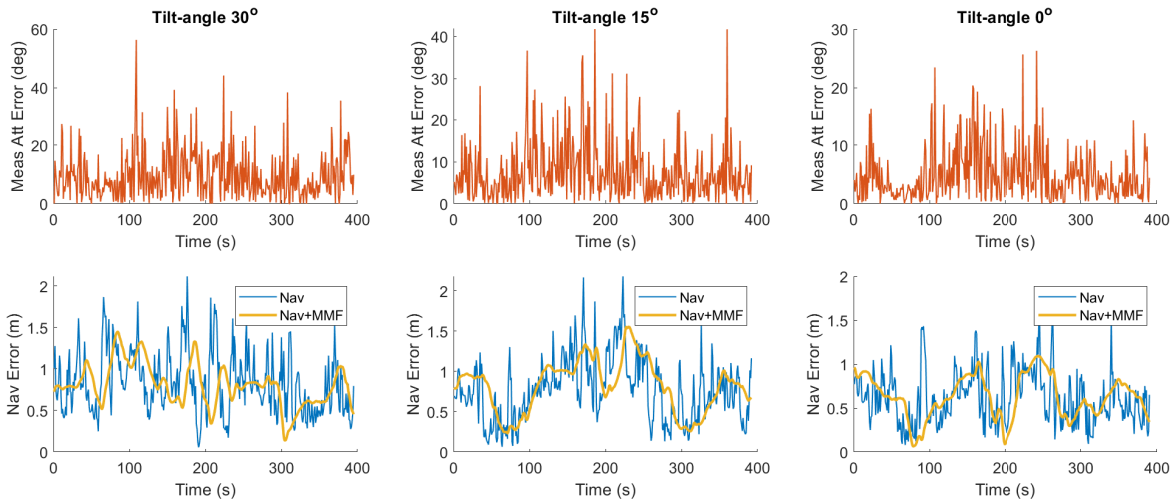

Figure 8.30: Attitude measurement error and navigation rotation error for the least optimal trajectory of phase 3. May be directly compared to Figure 8.27

.

assume a magnitude of almost 1 deg/s, which is insufficient for accurate guidance, as might be demonstrated from Table 8.5, showing even higher ΔV and mean guidance error compared to Table 8.4.

Table 8.5: Control effort, mean guidance error and true final position error for the least optimal conditions in phase 3. The true final error as in Table 8.4, to which this table may be directly compared.

	Tilt-angle		
	30°	15°	0°
ΔV (m/s)	14.824	13.207	11.541
Mean guidance error (m)	2.224	2.208	1.763
True final error (m)	1.125	1.216	1.105

Contrary to the comparison of Tables 8.2 and 8.3 for phase 2, the comparison of Tables 8.4 and 8.5 shows a clear increase of all variables presented in the table, as would be expected beforehand. Finally, the synchronisation errors achieved from the control law are presented in Figure 8.28.

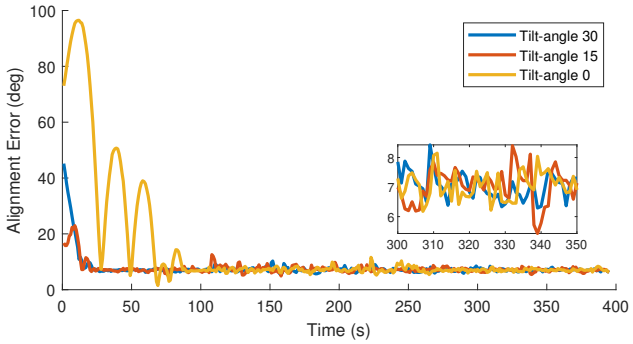

Figure 8.31: Synchronisation error for the chaser for the least optimal conditions in phase 3. May be directly compared to Figure 8.28.

This shows that, despite the decrease in measurement accuracy that was observed between Figures 8.27 and 8.30, no increase of synchronisation error is found when comparing Figure 8.31 to Figure 8.28. The reason for this becomes clear when the mean navigation attitude error is calculated, as this value is equal to 4.827 degrees, which is well below the minimum achievable control error.

It might be concluded from this section that the GNC architecture is surprisingly robust against the var-

ious lighting conditions, throughout all the phases. It was shown that, when designing the trajectory for the most optimal lighting conditions, the performance of the GNC system is always adequate, and navigation errors < 1 m, 5 deg, 0.5 deg/s may be achieved in almost any situation. The only exception being the third phase, where the navigation rotation error could not be established at < 0.5 deg/s.

The optimal trajectory in the second phase was proven efficient, robust to uncertainties and, using the mitigation strategies, robust to failures/decreased performance of the pose estimation system. This trajectory was shown to be efficient both under the most and least optimal conditions, showing similar efficiency and final error in both cases.

The third phase of the rendezvous process should receive the most attention in future research, as this phase exhibits very high ΔV values and is prone to high guidance errors. This may be attributed to the trajectory, which is required to follow the spin-axis, which asks a lot from the controller. A different trajectory might be considered that is more suitable for a tumbling target with large amounts of wobbling.

9

Conclusions and Recommendations

This chapter presents the conclusions that were reached from this research, the contribution of which can be divided into three categories. The first category is related to the investigation of performance of the guidance system, especially under decreased performance of the pose estimation system. The second category is concerned with the robust estimation and prediction of the target attitude dynamics. The third category is associated with trajectory design, aimed at designing for optimal lighting conditions.

9.1. Guidance performance

The first part of this research was aimed at finding out how the guidance system performs when the performance of the pose estimation system is decreased. The GNC algorithm was tested against several scenarios, most importantly against three types of measurement feedback. First, true feedback which is statistically perfect (σ^2). Second, pessimistic feedback, which assigns a measurement covariance that is higher than the true value ($> \sigma^2$) and, third, optimistic feedback, which assigns a covariance that is lower than the true value ($< \sigma^2$).

Failure of the system and need for mitigation were found in specific scenarios, in particular those with optimistic feedback. These scenarios cause a strong response and create navigation errors > 5m, whereas errors of 20 cm were achieved in nominal operation. The difficulty with optimistic feedback is that the navigation filter cannot identify it. As the assigned covariance is low, a decrease of the filter state covariance is caused and the filter thinks it has become more, rather than less accurate. A reference state is propagated without the measurement update that occurs in the filter, allowing the identification of divergences caused by measurements. Using a threshold, this reference allows to correctly identify 100% of the optimistic feedback scenarios, the detection lagging 1 or 2 seconds behind the true occurrence. Upon identification the navigation state is reset and takes the value of the reference, effectively mitigating these situations and keeping errors in the order of 20-40 cm.

In the case of true or pessimistic feedback, the main effect is a decreased accuracy of the attitude dynamics estimation. While the translational state proved to be robust, the attitude became considerably less accurate, such that the guidance system can not accurately calculate the desired final state and should not be updated using this attitude data. In these cases the navigation system recognises the error, as the filter state covariance serves as an indication of a loss of accuracy and can be used to identify the periods of decreased performance. A threshold on the attitude state covariance is used to identify periods of decreased performance, resulting in a 100% recognition rate, with a small detection lag of 3 to 6 seconds. The mitigation consists of withholding the guidance system from updating the optimal trajectory, which does not significantly improve the performance of the system.

9.2. Attitude Dynamics Estimation

It was found that the main weakness of vision-based pose estimation systems is in their ability to estimate the attitude dynamics of a tumbling object, especially when a future prediction of these dynamics is required, required by the guidance system to make an estimate of the desired final conditions for an optimal manoeuvre towards the spin-axis.

Currently, the standard technique for obtaining a prediction of attitude dynamics consists of the integration of the current attitude rates over the remaining time. However, when integrating the attitude dynamics over long integration times, final position errors of 5-8 m are found in the presence of uncertainties in target rotation and inertia as small as 0.5 deg/s and 4%. As the guidance error has a sub-meter magnitude, this estimation error can be identified as the largest source of error in the guidance system. Furthermore, this estimation error was found to have a large standard deviation, often exceeding 2 m, indicating a high level of unpredictability in the magnitude of this error.

These conclusions have raised the need to develop a more robust method for the prediction of target attitude dynamics. A method was developed based on the minimisation of a least squares problem, fitting the available attitude data obtained during a complete orbital period with a sinusoidal function. Future points may be extrapolated from this function as a form of prediction, which is found robust against uncertainties in the target attitude dynamics and inertia. Using this method slightly improves the accuracy of the estimate to 4-5 m, and greatly decreases the standard deviation of the estimates to below 20 cm. A combination of the fitting method with the standard integration has been attempted, however, no increase in performance could be observed.

9.3. Trajectory Designs for Optimal Lighting

The final part of this research focused on the design of trajectories in which the lighting conditions of the vision-based system are optimised. Concretely, this design aimed to minimise the angle χ_{cam} between the camera boresight vector and the sun vector, which was assumed to be the main driver of measurement accuracy. A Relative Orbital Element (ROE) parameterization was exploited to define a relative orbit for observation under optimal lighting conditions. It was found that an optimal trajectory is possible in each phase of the rendezvous.

The first phase consists of a passively safe, elliptical, relative orbit. By controlling the angle of this orbit with respect to the target orbital plane, as well as the position of the chaser on this orbit, $\chi_{\text{cam}} < 40^o$ for a period of at least 2000 seconds, allowing for a long period of accurate measurements. Subsequently, χ_{cam} in the second phase may be controlled by selecting a proper time of departure from the passively safe orbit. When an optimal departure time is selected, the angle $\chi_{\text{cam}} < 60^\circ$ during the entire optimal manoeuvre in the second phase.

For the third phase of the rendezvous, in which the chaser approaches the target along the spin-axis, the expected lighting conditions are determined by the spin-axis orientation, and the angle χ_{spin} was defined as the angle between the spin-axis vector and the sun vector. It was found that the most optimal values of χ_{spin} are encountered for a larger tilt angle between the spin-axis and N, which is expected between 0° and 30°. Due to nutation, the spin-axis moves between mean values of χ_{spin} = 40°-80°, with a margin of ±10° due to wobbling. By awaiting the right conditions, the spin-axis may be approached at a very favourable χ_{cam} = 30°-40°.

9.4. Recommendations

The first recommendation is for the construction of a more accurate prediction model of the expected rotational dynamics, as the largest challenge for vision-based systems remains the prediction of attitude dynamics. Currently the most accurate results achieved from the fitting method contain an error of 4-5 m, remaining the largest source of error in the GNC system. In parallel to the development of such a method, the rotation of the Envisat should be more accurately characterised, as the expected magnitude and orientation of the rotation still contain a large margin of uncertainty.

Second, depending on the tumbling and wobbling of the Envisat, the trajectory in the third phase of the rendezvous might need to be reconsidered. Constraining this trajectory to follow the spin-axis continuously was shown to require considerable control effort, which might not be necessary. A trajectory that approximately follows the spiral, but stays near the centre of it, might be a viable solution, as the chaser would consume less fuel following a straight line compared to a spiral. Alternatively, the use of a Keep Out Coat (KOC) instead of a Keep Out Sphere could be investigated, as this would bring the final position of the optimal manoeuvre closer to the target. A shorter distance in the third phase automatically reduces the fuel consumption. This would require an investigation of the safe use of a KOC, defining a minimum allowable distance from the target surface to ensure safety.

Third, the influence the sun-camera angle on the accuracy of pose estimation systems should be further investigated. Despite the fact that this angle is easy to model as a metric, very little information about its

relation to measurement accuracy is available. Defining how the performance of the pose estimation system depends on this angle will assist with error modelling in future experiments.

Finally, it might be interesting to research a camera pointing law based on the position of the target in the image, rather than based on the estimated relative position, as in this work. This would however require access to an operational pose estimation system.

Bibliography

[1] Brent W Barbee, J Russell Carpenter, Scott Heatwole, F Landis Markley, Michael Moreau, Bo J Naasz, and John Van Eepoel. A guidance and navigation strategy for rendezvous and proximity operations with a noncooperative spacecraft in geosynchronous orbit. *The Journal of the Astronautical Sciences*, 58(3): 389–408, 2011.

[2] Heike Benninghoff and Toralf Boge. Rendezvous involving a non-cooperative, tumbling target-estimation of moments of inertia and center of mass of an unknown target. In *25th international symposium on space flight dynamics*, volume 25, 2015.

[3] M Bhagat. *Convex Guidance for Envisat Rendezvous*. PhD thesis, Delft University of Technology, 2016.

[4] Robin Biesbroek, Tiago Soares, Jakob Husing, and Luisa Innocenti. The e. deorbit cdf study: A design study for the safe removal of a large space debris. In *64th International Astronautical Congress (IAC), Beijing*, 2013.

[5] Robin Biesbroek, Luisa Innocenti, Andrew Wolahan, and Sara Morales Serrano. e. deorbit–esa's active debris removal mission. In *Proceedings of the 7th European Conference on Space Debris*, page 10. ESA Space Debris Office, 2017.

[6] Robin Biesbroek et al. The e. deorbit cdf study. In *6th IAASS conference, Montréal, Canada*, 2013.

[7] James D Biggs and Nadjim Horri. Optimal geometric motion planning for a spin-stabilized spacecraft. *Systems & Control Letters*, 61(4):609–616, 2012.

[8] Christophe Bonnal, Jean-Marc Ruault, and Marie-Christine Desjean. Active debris removal: Recent progress and current trends. *Acta Astronautica*, 85:51–60, 2013.

[9] Louis Breger and Jonathan P How. Safe trajectories for autonomous rendezvous of spacecraft. *Journal of Guidance, Control, and Dynamics*, 31(5):1478–1489, 2008.

[10] Lorenzo Pasqualetto Cassinis, Robert Fonod, and Eberhard Gill. Review of the robustness and applicability of monocular pose estimation systems for relative navigation with an uncooperative spacecraft. *Progress in Aerospace Sciences*, 2019.

[11] Norad Celestrak. Catalogue number: 27386, Name: Envisat, Latest Data: TLE. `https://celestrak.com/satcat/tle.php?CATNR=27386`, 2020. [Online; accessed 19-September-2020].

[12] WH Clohessy and RS Wiltshire. Terminal guidance system for satellite rendezvous. *Journal of the Aerospace Sciences*, 27(9):653–658, 1960.

[13] John L Crassidis and F Landis Markley. Sliding mode control using modified rodrigues parameters. *Journal of Guidance, Control, and Dynamics*, 19(6):1381–1383, 1996.

[14] Simone D'Amico. *Autonomous formation flying in low earth orbit*. PhD thesis, Technische Universiteit Delft, 2010.

[15] Simone D'Amico, Eberhard Gill, and Oliver Montenbruck. Relative orbit control design for the prisma formation flying mission. In *AIAA Guidance, Navigation, and Control Conference and Exhibit*, page 6067, 2006.

[16] F de Bruijn, E Gill, and J How. Comparative analysis of cartesian and curvilinear clohessy-wiltshire equations. *Journal of Aerospace Engineering*, 3(2):1, 2011.

[17] J.A.F. Deloo. Analysis of the rendezvous phase of e.deorbit. Msc thesis, Delft University of Technology, December 2015.

[18] Dominic Dirkx and Erwin Mooij. *Conceptual shape optimization of entry vehicles*. Springer, 2016.

[19] Xiaodong Du, Bin Liang, Wenfu Xu, and Yue Qiu. Pose measurement of large non-cooperative satellite based on collaborative cameras. *Acta Astronautica*, 68(11-12):2047–2065, 2011.

[20] Simone D'Amico. Relative orbital elements as integration constants of hill's equations. *DLR, TN*, pages 05–08, 2005.

[21] Simone D'Amico, J-S Ardaens, Gabriella Gaias, Heike Benninghoff, Benjamin Schlepp, and JL Jørgensen. Noncooperative rendezvous using angles-only optical navigation: system design and flight results. *Journal of Guidance, Control, and Dynamics*, 36(6):1576–1595, 2013.

[22] Simone D'Amico, Mathias Benn, and John L Jørgensen. Pose estimation of an uncooperative spacecraft from actual space imagery. *International Journal of Space Science and Engineering 5*, 2(2):171–189, 2014.

[23] MC Eckstein, CK Rajasingh, and P Blumer. Colocation strategy and collision avoidance for the geostationary satellites at 19 degrees west. In *International Symposium on Space Flight Dynamics*, volume 6, 1989.

[24] Stéphane Estable, Clément Pruvost, Eugénio Ferreira, Jürgen Telaar, Michael Fruhnert, Christian Imhof, Tomasz Rybus, Gregory Peckover, Robert Lucas, Rohaan Ahmed, et al. Capturing and deorbiting envisat with an airbus spacetug. results from the esa e. deorbit consolidation phase study. *Journal of Space Safety Engineering*, 7(1):52–66, 2020.

[25] Alexandre Falcoz, Valerio Moro, Alexander Cropp, and Finn Ankersen. AGADiR: Advanced gnc for active debris removal. In *e.Deorbit Symposium*, Noordwijkerhout, The Netherlands, May 2014. European Space Agency.

[26] G Gaias and S D'Amico. Impulsive maneuvers for formation reconfiguration using relative orbital elements. *Journal of Guidance, Control, and Dynamics*, 38(6):1036–1049, 2015.

[27] Gabriella Gaias, Simone D'Amico, and J-S Ardaens. Angles-only navigation to a noncooperative satellite using relative orbital elements. *Journal of Guidance, Control, and Dynamics*, 37(2):439–451, 2014.

[28] Eberhard Gill, Simone D'Amico, and Oliver Montenbruck. Autonomous formation flying for the prisma mission. *Journal of Spacecraft and Rockets*, 44(3):671–681, 2007.

[29] John L Goodman. History of space shuttle rendezvous and proximity operations. *Journal of Spacecraft and Rockets*, 43(5):944–959, 2006.

[30] Tommaso Guffanti, Simone D'Amico, Michele Lavagna, et al. Long-term analytical propagation of satellite relative motion in perturbed orbits. In *27th AAS/AIAA Space Flight Mechanics Meeting*, pages 5–9. San Antonio, 2017.

[31] Michael A Henson and Dale E Seborg. Input-output linearization of general nonlinear processes. *AIChE Journal*, 36(11):1753–1757, 1990.

[32] Marko Jankovic, Jan Paul, and Frank Kirchner. Gnc architecture for autonomous robotic capture of a non-cooperative target: preliminary concept design. *Advances in Space Research*, 57(8):1715–1736, 2016.

[33] Donald J Kessler and Burton G Cour-Palais. Collision frequency of artificial satellites: The creation of a debris belt. *Journal of Geophysical Research: Space Physics*, 83(A6):2637–2646, 1978.

[34] Mate Kisantal, Sumant Sharma, Tae Ha Park, Dario Izzo, Marcus Märtens, and Simone D'Amico. Satellite pose estimation challenge: Dataset, competition design, and results. *IEEE Transactions on Aerospace and Electronic Systems*, 56(5):4083–4098, 2020.

[35] Adam W Koenig, Tommaso Guffanti, and Simone D'Amico. New state transition matrices for spacecraft relative motion in perturbed orbits. *Journal of Guidance, Control, and Dynamics*, 40(7):1749–1768, 2017.

[36] Daniel Kucharski, Georg Kirchner, Franz Koidl, Cunbo Fan, Randall Carman, Christopher Moore, Andriy Dmytrotsa, Martin Ploner, Giuseppe Bianco, Mikhailo Medvedskij, et al. Attitude and spin period of space debris envisat measured by satellite laser ranging. *IEEE Transactions on Geoscience and Remote Sensing*, 52(12):7651–7657, 2014.

[37] MK Ben Larbi and Enrico Stoll. Spacecraft formation control using analytical integration of gauss'variational equations. In *6th International Conference on Astrodynamics Tools and Techniques, ICATT*, 2016.

[38] Vincent Lepetit and Pascal Fua. *Monocular model-based 3D tracking of rigid objects*. Now Publishers Inc, 2005.

[39] Catherine Lewis. Linear programming: theory and applications. *Whitman College Mathematics Department*, 2008.

[40] Hongbin Li, Petre Stoica, and Jian Li. Computationally efficient parameter estimation for harmonic sinusoidal signals. *Signal Processing*, 80(9):1937–1944, 2000.

[41] J-C Liou. The top 10 questions for active debris removal. In *Proceedings of the 1st European Workshop on ADR*, June 2010.

[42] J-C Liou, Nicholas L Johnson, and NM Hill. Controlling the growth of future leo debris populations with active debris removal. *Acta Astronautica*, 66(5-6):648–653, 2010.

[43] JC Liou. An update on leo environment remediation with active debris removal. *Orbital Debris Quarterly News*, 15(2):4–6, 2011.

[44] Chang Liu and Weiduo Hu. Relative pose estimation for cylinder-shaped spacecrafts using single image. *IEEE Transactions on Aerospace and Electronic Systems*, 50(4):3036–3056, 2014.

[45] Huashan Liu, Xiaobo Lai, and Wenxiang Wu. Time-optimal and jerk-continuous trajectory planning for robot manipulators with kinematic constraints. *Robotics and Computer-Integrated Manufacturing*, 29 (2):309–317, 2013.

[46] Damiana Losa, Marco Lovera, Rémi Drai, Thierry Dargent, and Joël Amalric. Electric station keeping of geostationary satellites: a differential inclusion approach. In *Proceedings of the 44th IEEE Conference on Decision and Control*, pages 7484–7489. IEEE, 2005.

[47] David G Luenberger, Yinyu Ye, et al. *Linear and nonlinear programming*, volume 2. Springer, 1984.

[48] Yazhong Luo, Jin Zhang, and Guojin Tang. Survey of orbital dynamics and control of space rendezvous. *Chinese Journal of Aeronautics*, 27(1):1–11, 2014.

[49] Meysam Mahooti. High precision orbit propagator. MATLAB Central File Exchange, 2020. URL `https://www.mathworks.com/matlabcentral/fileexchange/55167-high-precision-orbit-propagator`. Retrieved on August 31, 2020.

[50] Olvi L Mangasarian. Absolute value equation solution via linear programming. *Journal of Optimization Theory and Applications*, 161(3):870–876, 2014.

[51] F Landis Markley and John L Crassidis. *Fundamentals of spacecraft attitude determination and control*. Springer, 2014.

[52] D Milligan, L Ventimiglia, Y Eren, D Mesples, F Diekmann, D Kuijper, and M Garcia-Matatoros. Envisat platform operations: Providing a platform for science. In *2007 Envisat Symposium, Montreux/Switzerland*, pages 23–27, 2007.

[53] O Montenbruck, M Kirschner, and Simone D'Amico. E-/i-vector separation for grace proximity operations. *DLR/GSOC TN*, pages 04–08, 2004.

[54] Bo J Naasz, Richard D Burns, Steven Z Queen, John Van Eepoel, Joel Hannah, and Eugene Skelton. The hst sm4 relative navigation sensor system: overview and preliminary testing results from the flight robotics lab. *The Journal of the Astronautical Sciences*, 57(1-2):457–483, 2009.

[55] M Navabi and MR Hosseini. Spacecraft quaternion based attitude input-output feedback linearization control using reaction wheels. In *2017 8th International Conference on Recent Advances in Space Technologies (RAST)*, pages 97–103. IEEE, 2017.

[56] Mark Nishimura, David B Lindell, Christopher Metzler, and Gordon Wetzstein. Disambiguating monocular depth estimation with a single transient. In *European Conference on Computer Vision*, pages 139–155. Springer, 2020.

[57] Roberto Opromolla, Giancarmine Fasano, Giancarlo Rufino, and Michele Grassi. Pose estimation for spacecraft relative navigation using model-based algorithms. *IEEE Transactions on Aerospace and Electronic Systems*, 53(1):431–447, 2017.

[58] Bob Palais and Richard Palais. Euler's fixed point theorem: The axis of a rotation. *Journal of fixed point theory and applications*, 2(2):215–220, 2007.

[59] Tae Ha Park, Sumant Sharma, and Simone D'Amico. Towards robust learning-based pose estimation of noncooperative spacecraft. *arXiv preprint arXiv:1909.00392*, 2019.

[60] Vincenzo Pesce, Michèle Lavagna, and Riccardo Bevilacqua. Stereovision-based pose and inertia estimation of unknown and uncooperative space objects. *Advances in Space Research*, 59(1):236–251, 2017.

[61] Vincenzo Pesce, Roberto Opromolla, Salvatore Sarno, Michèle Lavagna, and Michele Grassi. Autonomous relative navigation around uncooperative spacecraft based on a single camera. *Aerospace Science and Technology*, 84:1070–1080, 2019.

[62] Camille Pirat, Muriel Richard-Noca, Christophe Paccolat, Federico Belloni, Reto Wiesendanger, Daniel Courtney, Roger Walker, and Volker Gass. Mission design and gnc for in-orbit demonstration of active debris removal technologies with cubesats. *Acta Astronautica*, 130:114–127, 2017.

[63] Alexander B Roger and Colin R McInnes. Safety constrained free-flyer path planning at the international space station. *Journal of Guidance, Control, and Dynamics*, 23(6):971–979, 2000.

[64] Luc BM Sagnières and Inna Sharf. Long-term rotational motion analysis and comparison to observations of the inoperative envisat. *Journal of Guidance, Control, and Dynamics*, 42(2):364–376, 2019.

[65] Hanspeter Schaub, Lee EZ Jasper, Paul V Anderson, and Darren S McKnight. Cost and risk assessment for spacecraft operation decisions caused by the space debris environment. *Acta Astronautica*, 113:66–79, 2015.

[66] Tom Schouwenaars, Arthur Richards, Eric Feron, and Jonathan How. Plume avoidance maneuver planning using mixed integer linear programming. In *AIAA Guidance, Navigation, and Control Conference and Exhibit*, page 4091, 2001.

[67] Shai Segal, Pini Gurfil, and Kamran Shahid. In-orbit tracking of resident space objects: A comparison of monocular and stereoscopic vision. *IEEE Transactions on Aerospace and Electronic Systems*, 50(1): 676–688, 2014.

[68] Florian Sellmaier, Toralf Boge, Jörn Spurmann, Sylvain Gully, Thomas Rupp, and Felix Huber. On-orbit servicing missions: Challenges and solutions for spacecraft operations. In *SpaceOps 2010 Conference Delivering on the Dream Hosted by NASA Marshall Space Flight Center and Organized by AIAA*, page 2159, 2010.

[69] Yaroslav D Sergeyev, Dmitri E Kvasov, and Marat S Mukhametzhanov. On the least-squares fitting of data by sinusoids. In *Advances in Stochastic and Deterministic Global Optimization*, pages 209–226. Springer, 2016.

[70] Sumant Sharma and Simone D'Amico. Pose estimation for non-cooperative rendezvous using neural networks. *arXiv preprint arXiv:1906.09868*, 2019.

[71] Sumant Sharma and Simone D'Amico. Pose estimation of uncooperative spacecraft using monocular vision. Stanford University 2014 PNT Challenges and Opportunities Symposium, 2014.

[72] Sumant Sharma and Simone D'Amico. Reduced-dynamics pose estimation for non-cooperative spacecraft rendezvous using monocular vision. In *38th AAS Guidance and Control Conference, Breckenridge, Colorado*, 2017.

[73] Sumant Sharma and Simone D'Amico. Neural network-based pose estimation for noncooperative spacecraft rendezvous. *IEEE Transactions on Aerospace and Electronic Systems*, 56(6):4638–4658, 2020.

[74] Sumant Sharma, Connor Beierle, and Simone D'Amico. Pose estimation for non-cooperative spacecraft rendezvous using convolutional neural networks. In *2018 IEEE Aerospace Conference*, pages 1–12. IEEE, 2018.

[75] Sumant Sharma, Jacopo Ventura, and Simone D'Amico. Robust model-based monocular pose initialization for noncooperative spacecraft rendezvous. *Journal of Spacecraft and Rockets*, 55(6):1414–1429, 2018.

[76] Jian-Feng Shi, Steve Ulrich, Stephane Ruel, and Martin Anctil. Uncooperative spacecraft pose estimation using an infrared camera during proximity operations. In *AIAA SPACE 2015 conference and exposition*, page 4429, 2015.

[77] Leena Singh, Simone Bortolami, and Lance Page. Optimal guidance and thruster control in orbital approach and rendezvous for docking using model predictive control. In *AIAA Guidance, Navigation, and Control Conference*, page 7754, 2010.

[78] Joan Sola. Quaternion kinematics for the error-state kalman filter. *arXiv preprint arXiv:1711.02508*, 2017.

[79] Joern Spurmann and Simone D'Amico. Proximity operations of on-orbit servicing spacecraft using an eccentricity/inclination vector separation. In *22nd International Symposium on Spaceflight Dynamics*, 2011.

[80] Nathan Stacey and Simone D'Amico. Analytical process noise covariance modeling for absolute and relative orbits. *arXiv preprint arXiv:2105.06516*, 2021. Preprint submitted to Acta Astronautica on May 17, 2021.

[81] Joseph A Starek, Behçet Açıkmeşe, Issa A Nesnas, and Marco Pavone. Spacecraft autonomy challenges for next-generation space missions. In *Advances in Control System Technology for Aerospace Applications*, pages 1–48. Springer, 2016.

[82] Joshua Sullivan, Sebastian Grimberg, and Simone D'Amico. Comprehensive survey and assessment of spacecraft relative motion dynamics models. *Journal of Guidance, Control, and Dynamics*, 40(8):1837–1859, 2017.

[83] J Telaar, C Schlaile, and J Sommer. Guidance and navigation for rendezvous with an uncooperative target. *Progress in Flight Dynamics, Guidance, Navigation, and Control–Volume 10*, 10:3–20, 2018.

[84] Steve Tretter. Estimating the frequency of a noisy sinusoid by linear regression (corresp.). *IEEE Transactions on Information theory*, 31(6):832–835, 1985.

[85] Brent E Tweddle and Alvar Saenz-Otero. Relative computer vision-based navigation for small inspection spacecraft. *Journal of Guidance, Control, and Dynamics*, 38(5):969–978, 2015.

[86] Jacopo Ventura, Marco Ciarcià, Marcello Romano, and Ulrich Walter. Fast and near-optimal guidance for docking to uncontrolled spacecraft. *Journal of Guidance, Control, and Dynamics*, 40(12):3138–3154, 2017.

[87] B Bastida Virgili, S Lemmens, and H Krag. Investigation on envisat attitude motion. In *e. Deorbit workshop*, 2014.

[88] V Vittaldev, E Mooij, and MC Naeije. Unified state model theory and application in astrodynamics. *Celestial Mechanics and Dynamical Astronomy*, 112(3):253–282, 2012.

[89] Renato Volpe. *Choreography on Elliptical Orbit"*. PhD thesis, La Sapienza Università di Roma, 2016.

[90] Renato Volpe and Christian Circi. Optical-aided, autonomous and optimal space rendezvous with a non-cooperative target. *Acta Astronautica*, 157:528–540, 2019.

[91] Renato Volpe, Christian Circi, Marco Sabatini, and Giovanni B Palmerini. Gnc architecture for an optimal rendezvous to an uncooperative tumbling target using passive monocular camera. *Acta Astronautica*, 2020.

[92] Harvey M Wagner. Linear programming techniques for regression analysis. *Journal of the American Statistical Association*, 54(285):206–212, 1959.

[93] Gerhard Wanner and Ernst Hairer. *Solving ordinary differential equations II*, volume 375. Springer Berlin Heidelberg, 1996.

[94] James R Wertz. *Spacecraft attitude determination and control*, volume 73. Springer Science & Business Media, 2012.

[95] C Wiedemann, S Flegel, M Möckel, J Gelhaus, V Braun, C Kebschull, J Kreisel, M Metz, and P Vörsmann. Cost estimation of active debris removal. In *63rd International Astronautical Congress*. International Astronautical Federation Naples, Italy, 2012.

[96] Jacob Williams. Lvlh transformations, 2014. URL `http://degenerateconic.com/wp-content/uploads/2015/03/lvlh.pdf`. accessed: 02-10-2020.

[97] Kjetil Wormnes, Ronan Le Letty, Leopold Summerer, Rogier Schonenborg, Olivier Dubois-Matra, Eleonora Luraschi, Alexander Cropp, Holger Krag, and Jessica Delaval. Esa technologies for space debris remediation. In *6th European Conference on Space Debris*, volume 1, pages 1–8. ESA Communications ESTEC Noordwijk, The Netherlands, 2013.

[98] Dawei Zhang, Shenmin Song, and Run Pei. Safe guidance for autonomous rendezvous and docking with a non-cooperative target. In *AIAA guidance, navigation, and control conference*, page 7592, 2010.

[99] DJ Zimpfer, PS Spehar, F Clark, C D'Souza, and M Jackson. Autonomous rendezvous and capture guidance, navigation and control. In *Flight Mechanics Symposium,(Goddard Space Flight Center, Greenbelt, Maryland), Session*, volume 3, pages 18–20, 2005.